UNIVERSITY OF CALIFORNIA
Santa Barbara

Search for new physics in proton-proton collisions at 7 TeV in events with a single lepton, jets, and missing transverse momentum

A Dissertation submitted in partial satisfaction
of the requirements for the degree of

Doctor of Philosophy

in

Physics

by

Finn O'Neill Rebassoo

Committee in Charge:

Professor Jeffrey D. Richman, Chair

Professor Claudio Campagnari

Professor David Berenstein

August 2011

The Dissertation of
Finn O'Neill Rebassoo is approved:

Professor Claudio Campagnari

Professor David Berenstein

Professor Jeffrey D. Richman, Committee Chairperson

August 2011

Search for new physics in proton-proton collisions at 7 TeV in events with a single lepton, jets, and missing transverse momentum

by

Finn O'Neill Rebassoo

I would like to dedicate this to my father,

Vaho Rebassoo.

Acknowledgements

It's not over till it's over Yogi Berra

Well now it is finally over and it is a little hard to believe. I would like to first and foremost thank my parents, Maura O'Neill and Vaho Rebassoo, who gave me the vision from a young age that learning and higher education is something that is valuable. They also instilled in me a curiosity for mathematics and science that continued throughout my years. The rest of my family including my sister, Liisa O'Neill, gave me support throughout all these years, and I would like to thank them as well. Then there is of course my girlfriend Tiffany Myles, who made many sacrifices while I finished graduate school. She gave me the love, support, and perspective to help deal with the ups and downs of graduate school and Santa Barbara.

On the work and school side of things I would like to thank Jean-Roch Vlimant and Jake Ribnik for the crash courses in C^{++} and root (even though the four hour lectures by Jean-Roch on C^{++} straight through lunch were pretty rough). I certainly felt like I was thrown into the flames not having much computing experience. But in the end it all worked out. I would also like to thank Puneeth Kalavase for his help on my numerous random questions throughout the years. In addition, my advisor, Jeff Richman, helped give me a great perspective of the field and ways to think about different science questions.

Throughout the fifth of my life to this point that I have spent in graduate school, my many close friends helped me stay sane and in the end more focused by giving me breaks from the stresses (though luckily not too many breaks). This includes Nick Cross, Kwasi Gyane, Gabe Chipe, Kabir Randhava, Nick Leonard, Tyronne Martin, Seelye Arms, Robin Twelker, Sharla Dodd, Chris Evelyn, Dan Gargas, Anthony Cresci, Reggie Archer, and many more.

Lastly, there are many more people that have influenced me over the years and helped me make it to this point. You know who you are, thank you!

Curriculum Vitæ

Finn O'Neill Rebassoo

Education

2011	Doctor of Philosophy in Physics, University of California, Santa Barbara.
2008	Masters of Science in Physics, University of California, Santa Barbara
2003	Bachelor of Arts, Occidental College.

Experience

2005 – 2011	Graduate Research Assistant, High Energy Experiment, University of California, Santa Barbara.
2002	Undergraduate Research Assistant, Plasma Physics, Occidental College.

Selected Publications

CMS Collaboration: "Missing transverse energy performance of the CMS detector," arXiv:1106:5048v1.

CMS Collaboration: "Search for new physics in proton-proton collisions at $\sqrt{s} = 7$ TeV in events with a single lepton, jets, and missing transverse momentum," arXiv:1106:1870v1.

Abstract

Search for new physics in proton-proton collisions at 7 TeV in events with a single lepton, jets, and missing transverse momentum

Finn O'Neill Rebassoo

This thesis presents results for a search for new physics based on 36 pb^{-1} of data taken during 2010 by the CMS experiment at the Large Hadron Collider (LHC). We specifically look at the signature with a single isolated lepton, jets, and large missing transverse momentum ($\not\!\!E_T$). To predict the standard model backgrounds in this search, two separate and complementary methods are employed, each of which use control samples in the data. The standard model background predictions are consistent with the observed number of events in both the muon and electron channels and for both background prediction methods. In addition, the observed $\not\!\!E_T$ distribution agrees well with the standard model prediction. In the absence of a signal we proceed to set limits in the contrained minimal supersymmetric extension of the standard model (CMSSM) parameter space.

Professor Jeffrey D. Richman
Dissertation Committee Chair

Contents

Acknowledgements **v**

Curriculum Vitæ **vii**

Abstract **ix**

List of Figures **xiv**

List of Tables **xxvi**

1 Introduction **1**

2 Theory **6**
2.1 Physics of the standard model 6
2.2 Motivations for searching beyond the standard model 11
2.2.1 Dark Matter 12
2.2.2 Hierarchy Problem 16
2.3 Supersymmetric theory 18
2.3.1 Overview of theory 18
2.3.2 How SUSY solves some SM issues 21
2.3.3 CMSSM 25
2.3.4 SUSY production at the LHC 28
2.3.5 Decay of SUSY into lepton plus $\not{E}_T$ and jets 32
2.3.6 SM backgrounds to LHC single lepton SUSY searches . . 36

3 Experimental Hardware **40**
3.1 Large Hadron Collider 40
3.2 Compact Muon Solenoid 43

3.2.1 Overview . . . 43
3.2.2 Silicon tracking system . . . 47
3.2.3 Electromagnetic calorimeter . . . 57
3.2.4 Hadronic calorimeter . . . 61
3.2.5 Muon system . . . 74
3.2.6 Trigger and data acquisition . . . 81

4 Object Reconstruction 85
4.1 Muons . . . 85
4.2 Electrons and photons . . . 91
4.3 Jets . . . 99
4.4 Missing transverse momentum . . . 106

5 Search for supersymmetry 111
5.1 Overall search strategy and methods . . . 113
5.2 Event selection . . . 117
5.2.1 Overview of selection cuts and background composition . 117
5.2.2 Monte Carlo simulation samples used . . . 120
5.2.3 Data samples used and trigger requirements . . . 122
5.2.4 Event cleaning . . . 123
5.2.5 Preselection cuts . . . 125
5.2.6 Definition of analysis variables . . . 130
5.3 Event properties after preselection cuts . . . 132
5.4 Background determination using H_T and S_{MET} . . . 136
5.4.1 Introduction to method . . . 136
5.4.2 Definition of background determination procedure . . . 144
5.4.3 Lack of correlation between H_T and S_{MET} . . . 146
5.4.4 Monte Carlo and data distributions of H_T and S_{MET} . . 149
5.4.5 Results of background prediction in Monte Carlo, data . 154
5.4.6 Cross-check of method using lower jet multiplicity . . . 158
5.4.7 Systematic uncertainties . . . 159
5.4.8 Systematic error due to QCD contamination . . . 165
5.4.9 Summary of background prediction . . . 172
5.5 Background determination using lepton spectrum method . . . 174
5.5.1 Introduction to method . . . 174
5.5.2 Description of signal and control regions for single lepton prediction . . . 186
5.5.3 Effect of W polarization in $t\bar{t}$ and W+jets . . . 188
5.5.4 Effect of lepton p_T threshold . . . 199
5.5.5 Effect of $\not\!\!E_T$ resolution on background prediction . . . 201

5.5.6 Dilepton, single tau background predictions 206
5.5.7 QCD background prediction in signal region 217
5.5.8 QCD contamination to control regions 228
5.5.9 Single top and Z+jets background estimation 230
5.5.10 Scale factors applied to predictions 231
5.5.11 Results of background predictions 235
5.5.12 Systematics uncertainties 240
5.6 Signal efficiencies and uncertainties 252
5.7 Search results in terms of SUSY models 254

6 Conclusion **265**

Bibliography **268**

Appendices **277**

A $\not\!\!E_T$ resolution in CMS **278**
A.1 Samples and event requirements 278
A.2 $\not\!\!E_T$ resolution vs. ΣE_T without calibrations 280
A.3 Calibrated $\not\!\!E_T$ resolution vs. calibrated ΣE_T 285
A.4 Monte Carlo generator dependence of ΣE_T calibration 295
A.5 Conclusion 295

List of Figures

1.1 List of main contributors to this analysis and their institutions. 5

2.1 The fundamental particles in the standard model along with their mass, charge, and spin. Quarks are shown in purple, bosons in red, and leptons in green. Figure from Ref. [6]. 8
2.2 The "Bullet Cluster", which shows two galaxies colliding. The blue represents the amount of matter from gravitational lensing that is otherwise not seen and the red represents the amount of matter as measured by X-rays from galaxy remnants, mostly hydrogen gas. The interpretation is that the blue matter is the dark matter which interacts weakly and thus has passed through relatively easily. On the other hand the red matter represents the baryonic matter which has slowed down significantly due to electromagnetic interactions. Figure from Ref. [16]. 14
2.3 Quarks, leptons, and Higgs in the standard model and their corresponding superpartners in the MSSM. From Ref. [19]. 20
2.4 Gauge bosons in the standard model and their superpartners in the MSSM. The bino and wino are not mass eigenstate particles and thus mix to produce the charginos and neutralinos, which are the mass eigenstates. From Ref. [19]. 20
2.5 This plot shows how the different couplings constants for SM interactions evolve as a function of the energy. In the SM the couplings do not converge (dotted lines); however, in the MSSM the couplings do converge at a GUT scale of roughly 10^{16} GeV (bold lines). In the MSSM case sparticle masses are varied from 250 GeV to 1 TeV. Two loop effects are taken into account. From Ref. [19]. 22
2.6 One-loop corrections to the Higgs mass, m_H^2: (a) with fermion loop, (b) with scalar loop. 24

2.7 Renormalization group running of scalar and gaugino mass parameters with boundary conditions at 2.5 x 10^{16} GeV. The parameter values for this plots are $m_0 = 80$ GeV, $m_{1/2} = 250$, $A_0 = -500$ GeV, tan$\beta = 10$, and sign(μ)>0. Gaugino masses are labeled M_1, M_2, and M_3. The dashed lines for the squarks and sleptons are for the third generation and the solid lines are for the first and second generations. Plot from Ref. [19]. 26
2.8 Mass spectrum of LM0 signal point (from Ref. [28]). 29
2.9 Mass spectrum of LM1 signal point (from Ref. [28]). 29
2.10 Feynman diagrams for gluon-gluon and gluon-quark production of sparticles. Figure from Ref. [19]. 30
2.11 Feyman diagrams for quark-antiquark and quark-quark production of sparticles. Figure from Ref. [19]. 31
2.12 These plots show for $\sqrt{s} = 7$ TeV the distribution of SUSY particle types produced in the initial hard scattering process. For each model the total summed contribution is 1 and the y-axis gives the fraction of a certain process. (a) shows LM0, LM1, LM3, LM6, and LM9. (b) shows LM2, LM4, LM5, LM7, and LM8. All the models except LM7 and LM9 are dominated by strong production. LM7 and LM9 are dominated by weak production because in these models the squark masses are very high. 33
2.13 p_T distribution of the initial two SUSY particles for different LM points. For $\sqrt{s} = 7$ TeV. 34
2.14 Typical SUSY decay chain for benchmark point LM0. The two W^+'s are off-shell W's, denoted by $*$. This decay would end up giving a lepton, missing transverse momentum (from the neutrino and the two LSPs), and some large number of jets (if each jet from a quark in this diagram were within detector acceptance and had a p_T above whatever threshold the analysis is using you could get 7 jets in this event!!). 35
2.15 Distribution of the parent particle of the muon for different SUSY benchmark points. (a) LM0, LM1, LM3, LM6, LM9 (b) LM2, LM4, LM5, LM7, LM8. 37
2.16 Tree-level diagrams for $t\bar{t}$. At the LHC (a) is the dominant production process, while (b) is the dominant production process at the Tevatron. 38
2.17 Tree-level diagrams for W+jets. 39

3.1 Schematic (not to scale) showing the different detectors at the LHC. From Ref. [29]. 41

3.2 Schematic showing an expanded view of the CMS detector. Figure from Ref. [30]. 44
3.3 Schematic showing a transverse slice of the CMS detector. An overview of where different particles are measured in the detector is shown. From Ref. [31]. An interactive version of this schematic is shown in Ref. [32]. 44
3.4 Barrel of the CMS detector. From Ref. [33]. 46
3.5 One quarter longitudinal view of the CMS Experiment. Dimensions are in mm. Figure from Ref. [30]. 47
3.6 Schematic showing the layout of the tracker and the different layers. Double-sided layers are shown in blue and single-sided layers are shown in red. The double-sided layers are there to provide improved position measurement. Units on the x-axis and y-axis are in mm. Original figure from Ref. [34]. 50
3.7 (a) Single pixel module (from Ref. [30]), (b) installation of the pixel endcap disks (from Ref. [33]). 52
3.8 Different silicon modules in the tracker. Each module consists of two silicon wafers that are wire-bonded together, a harness, and readout electronics. The upper two modules are from the TOB and their length is approximately 25 cm. The upper right module is tilted with respect to the upper left module and used in the double-sided layers to obtain a more precise position measurement. The lower four modules are from the TEC and have different length and size depending on their location in the TEC. From Ref. [33]. 54
3.9 First three layers of tracker inner barrel. From Ref. [35]. 55
3.10 Resolution of different track parameters as a function of η: (a) transverse momentum, (b) transverse impact parameter, and (c) longitudinal impact parameter. Figures from Ref. [30]. 56
3.11 Material thickness in radiation lengths after the ECAL, HCAL and at the depth of each muon station. Figure from Ref. [30]. 58
3.12 Single crystal from ecal endcap. From Ref. [30]. 59
3.13 Transverse section through the ECAL, showing the geometrical configuration. Figure from Ref. [30]. 60

3.14 Resolution of ECAL supermodule as a function of energy. A supermodule is a cluster of many crystals. The barrel section of the ECAL has 36 identical "supermodules". The energy was measured in an array of 3 x 3 crystals with electrons impacting the central crystal. The upper series of points corresponds to events taken with a 20 x 20 mm^2 trigger and the lower series corresponds to events selected to fall within a 4 x 4 mm^2 region. From Ref. [30]. 62
3.15 Material thickness in interaction lengths after the ECAL, HCAL and at the depth of each muon station. Figure from Ref. [30]. 65
3.16 Russian workers sitting on artillery shells used to produce some of the brass absorber material. These artillery shells are from WW II and were obtained from the Russian Navy. From Ref. [33]. 66
3.17 Hadronic Barrel (HB) calorimeter. From Ref. [40]. 68
3.18 Hadronic Endcap (HE) calorimeter. From Ref. [30] 69
3.19 Schematic showing (a) the r-ϕ view of an HF wedge and (b) the expanded view of tower 13, long (red) and short (green) fibers alternate and are separated by 5 mm. Figures from Ref. [41]. 71
3.20 Wedge Module of the Forward Hadron Calorimeter (HF). From Ref. [42]. 72
3.21 Energy distributions of 20 GeV (upper plot) and 100 GeV (lower plot) pions after applying the HCAL vs. ECAL energy based cuts to remove backgrounds. Figures from Ref. [30]. 73
3.22 Schematic showing the layout of the muon chambers. The white boxes in the muon system are the iron used for the return yoke of the magnet. The green boxes are the DT chambers, the red boxes are the RPCs, and the blue boxes are the CSCs. Figure from Ref. [30]. . . . 76
3.23 The layout of a DT chamber inside a muon barrel station. Each DT chamber in the 3 innermost stations consists of 12 layers of drift tubes divided into 3 groups of 4 consecutive layers (called Superlayers). The tubes are staggered by half a tube for better position resolution. Two Superlayers have wires parallel to the beamline and measure the $r - \phi$ coordinate, while a third Superlayer is perpendicular to the two Superlayers and mesasure the z-coordinate running parallel to the beam. The Honeycomb plate between the Superlayers gives a longer lever arm to measure the track direction in the chamber. Figure from Ref. [30]. 78
3.24 Installation of DT chambers into one of the wheels in the barrel. From Ref. [30]. 79

3.25 Installation of CSC chambers onto one of the disks in the endcap. From Ref. [30]. 80
3.26 Schematic view of a CSC chamber. Wires running radially act as the anode and strips along the phi direction act as a cathode. Figure from Ref. [30]. 81
3.27 The muon momentum resolution versus momentum using the muon system only, the inner tracker only, or both. a) barrel, $|\eta|$ <0.2; b) endcap, 1.8< $|\eta|$ <2.0. Figures from Ref. [30]. 82

4.1 Tag-and-probe muon reconstruction efficiency as a function of p_T in data and simulation. The integrated luminosity for the data is 84 nb^{-1}. The upper left plot shows the global muon efficiency for $|\eta| < 1.2$, the upper right plot shows the tight muon efficiency for $|\eta| < 1.2$, the lower left plot shows the global muon efficiency for $1.2 < |\eta| < 2.4$, and the lower right plot shows the tight muon efficiency for $1.2 < |\eta| < 2.4$. From Ref. [45]. 89
4.2 Electron fake rate as a function of E_T (top) and η (bottom) for the "WP95" and "WP80" working points. From Ref. [50]. 97
4.3 Combined L1 pileup, L2 relative, and L3 absolute jet energy corrections as a function of jet η in Monte Carlo for jet p_T of 50 GeV (left) and 200 GeV (right). From Ref. [57]. 103
4.4 Jet energy corrections including L1, L2, L3 corrections from Monte Carlo and residual corrections from data as a function of η for two different jet p_T's, 50 GeV (left) and 200 GeV (right). From Ref. [57]. . . 104
4.5 Jet energy correction uncertainties for the different algorithms as a function of p_T for two different values of η, 0.0 (left), and 2.0 (right). From Ref. [57]. 105
4.6 calo$\not\!\!E_T$ distributions in a minimum-bias data sample with and without cleaning and filters, compared to simulation. The highest bin is an overflow bin. From Ref. [58]. 108
4.7 Calibrated $\not\!\!E_{Tx,y}$ resolution versus calibrated pfΣE_T for calo$\not\!\!E_T$, tc$\not\!\!E_T$, and pf$\not\!\!E_T$ in data and simulation. From Ref. [58]. 110

5.1 $\not\!\!E_T$ distribution for all events analyzed from muon and Calo $\not\!\!E_T$ triggers and for events identified as beam halo. Events recorded by collision muon triggers are shown by the red dashed curve while the subset which met the requirement of the beam halo filter are shown by the red inverted triangles. As can be seen from these distributions the halo muons overlapping with muon triggered events is very small. This is in contrast to Calo $\not\!\!E_T$ -triggered events, shown in blue solid curve, where there are many high $\not\!\!E_T$ events that pass the beam halo filter (blue triangles). Plot from Ref. [58]. 126
5.2 Muon channel: quantities related to missing transverse energy. 137
5.3 Electron channel: quantities related to missing transverse energy. 138
5.4 Muon channel: distributions describing jet transverse momenta. 139
5.5 Electron channel: distributions describing jet transverse momenta. 140
5.6 Muon channel: distributions describing global energy properties. 141
5.7 Electron channel: distributions describing global energy properties. 142
5.8 Distributions describing electron and muon properties. 143
5.9 Plots of H_T and S_{MET} for total Monte Carlo background in the μ-channel for the loose (top) and tight (bottom). In each case, the distribution is shown in two slices of the complementary variable. Figures from Ref. [80]. 147
5.10 Plots of H_T and S_{MET} for total Monte Carlo background in the e-channel for the loose (top) and tight (bottom). In each case, the distribution is shown in two slices of the complementary variable. Figures from Ref. [80]. 148
5.11 Two-dimensional distributions of H_T vs. S_{MET} for simulation and data samples in the μ channel. The definition of the regions for the tight selection are indicated on the figures. Figures from Ref. [80]. 151
5.12 Two-dimensional distributions of H_T vs. S_{MET} for simulation and data samples in the e channel. The definition of the regions for the tight selection are indicated on the figures. Figures from Ref. [80]. 152
5.13 Distributions of variables in the ABCD-regions for the μ channel. H_T with a cut $S_{MET} > 2.5$ and S_{MET} with a cut $H_T > 300$. Figures from Ref. [80]. 153
5.14 Distributions of variables in the ABCD-regions for the e channel. H_T with a cut $S_{MET} > 2.5$ and S_{MET} with a cut $H_T > 300$. Figures from Ref. [80]. 154

5.15 The ratio of events in the high and low regions in H_T (left) and S_{MET} (right) as a function of the second variable for the loose (top) and tight (bottom) selections in the μ channel. The points correspond to data while the lines and the shaded regions represent the SM MC predictions. These prediction have been normalized to data in the control region. These rescaling corrections were smaller than $\pm 25\%$. The definitions of the low (control) and high regions can be found in Table 5.2. Figures from Ref. [80]. 166
5.16 The ratio of events in the high and low regions in H_T (left) and S_{MET} (right) as a function of the second variable for the loose (top) and tight (bottom) selections in the electron channel. The points correspond to data while the lines and the shaded regions represent the SM MC predictions. These prediction have been normalized to data in the control region. These rescaling corrections were smaller than $\pm 25\%$. The definitions of the low (control) and high regions can be found in Table 5.2. Figures from Ref. [80]. 167
5.17 Relative isolation distributions for QCD control and signal region. Figures from Ref. [80]. 170
5.18 RelIso distributions in the ECAL barrel region for the QCD control region (black) and the ABCD signal regions (blue). Left: distributions from QCD MC simulation. Right: Data for values of RelIso > 0.2. Figures from Ref. [80]. 172
5.19 Reconstructed $\not\!\!E_T$ distribution of different standard model processes in Monte Carlo simulation normalized to 36.1 pb^{-1}. The requirements for this plot are a reconstructed muon with $p_T > 20$ GeV, and at least 4 reconstructed jets with $p_T > 30$ GeV. Generator level information is used to classify the different contributions. The lepton spectrum method tries to predict the tail of this distribution for the different background components using data-driven methods. The dominant background is W+jets and $t\bar{t}$ events with a single lepton. . 175
5.20 MC composition of background in loose and tight selection signal regions. The "Other" slice includes QCD, single top, and Z+jets. . . 177
5.21 Monte Carlo $t\bar{t}$ events: reconstructed $\not\!\!E_T$ vs. generated $\not\!\!E_T$ from neutrinos. This plot demonstrated that for the event selection used in the single-lepton analysis, most of the reconstructed $\not\!\!E_T$ corresponds to true missing transverse momentum. 178

5.22 Generator level μ and ν p_T distributions in $t\bar{t}$ and W+jets, with and without a $p_T(\mu)$ >20 threshold. Other requirements include at least 4 reconstructed jets and exactly 1 generator level muon from a W boson, where the geneartor muon must have $|\eta| < 2.1$. The neutrino and muon p_T distributions are very similar to each other in both $t\bar{t}$ and W+jets. The p_T threshold on the muon tends to remove events in the high $p_T(\nu)$ tail, while keeping the high $p_T(\mu)$ tail the same. 179
5.23 Distributions of muon p_T vs. $\not\!\!E_T$ in the μ channel for (a) Monte Carlo $t\bar{t}$ events and (b) the LM1 SUSY benchmark model. In $t\bar{t}$ events, the lepton p_T and $\not\!\!E_T$ in a given event are anticorrelated, but their distributions are very similar overall. In the LM1 benchmark model, which is typical of many SUSY models, the $\not\!\!E_T$ distribution is much harder than the lepton spectrum, since it is dominated by the production of two LSPs. Figures from Ref. [80]. 181
5.24 LM1: generator level lepton p_T distribution (black) and generator level $\not\!\!E_T$ (red), where the $\not\!\!E_T$ is calculated from the vector sum of the transverse momentum of the LSPs in the event. For these distributions no $p_T(\mu)$ threshold is required; however, the muon must have $|\eta|$ <2.1 and four reconstructed jets are also required. 182
5.25 Flow-chart showing the different data-driven background determinations and the control samples used for each. The small Z+jets and single top contribution is not included in this flow-chart since it is very small and estimated from the MC. The last row of the flow-chart specifies whether a scale factor from the MC is applied to correct for known effects. 185
5.26 Distributions plotted at generator level with requiring exactly 1 muon from a W boson and no other generator level or reco level requirements. The angular distribution of the muon results in a quantifiable difference in the muon and neutrino p_T distributions. 194
5.27 Test of re-weighting procedure for W polarization in $t\bar{t}$ events. Distributions plotted at generator level with requiring exactly 1 muon from a W boson and no other generator level or reco level requirements. Differences in the neutrino and muon p_T go away at generator level when reweighting the angular distribution to be purely longitudinal. . 196
5.28 $p_T(W)$ after the preselection cuts (black) and after an additional $\not\!\!E_T$ cut (red), W+jets Madgraph MC. 197
5.29 $dN/d\cos\theta^*_\ell$ (SM) in W + jets, $100 < p_T(W) < 300$ GeV, Alpgen MC. Distributions plotted at generator level, with requirement of exactly 1 muon from a W boson and no other requirements. 199

5.30 Leading jet p_T for different single-jet triggers. 203
5.31 Examples of $\not\!\!E_T$ templates from the data. The templates are produced in bins of H_T. Both these templates are for the ≥ 4 jet bin. Template (a) has $H_T = 310 - 320$ GeV and uses the Jet Trigger HLT_Jet50U. Template (b) has $H_T = 360 - 370$ GeV and Jet Trigger HLT_Jet100U. 204
5.32 Smearing effect on a single event. 205
5.33 Smearing effect on the muon p_T distribution in 36 pb^{-1} of data. 206
5.34 The p_T response function for muons from τ decays, normalized to unity in $t\bar{t}$ MC. Figures from Ref. [80]. 210
5.35 The p_T response function for jet(s) from τ decays with 20 GeV$<$ $p_T(\tau)$ $<$50 GeV. Distribution normalized to unity in $t\bar{t}$ MC. Figure from Ref. [80]. 211
5.36 Monte Carlo dilepton feed-down: comparison of actual $\not\!\!E_T$ distribution with prediction based on dilepton control sample. Figures from Ref. [80]. 212
5.37 Data dilepton feed-down: prediction of $\not\!\!E_T$ distribution based on dilepton control sample; comparison is with Monte Carlo dilepton background. Figures from Ref. [80]. 213
5.38 Monte Carlo τ background: comparison of actual $\not\!\!E_T$ distribution with prediction based on single-lepton control sample. Figures from Ref. [80]. 215
5.39 Data τ background: prediction of $\not\!\!E_T$ distribution based on single-lepton control sample; comparison is with Monte Carlo τ background samples. Figures from Ref. [80]. 216
5.40 Relative isolation in data and SM Monte Carlo samples in events with $\geq 1\mu$, $0e$, and at least four jets with $p_T > 30$ GeV. The requirement that the muon satisfy $\Delta R > 0.3$ with respect to all jets above threshold is not applied here because it biases the distribution. This plot also uses lower muon p_T threshold, 15 GeV, to obtain a larger event sample in the low RelIso tail of the distribution. 219
5.41 QCD Monte Carlo: $\not\!\!E_T$ in slices of RelIso (RelIso$<$ 0.1 and 0.2 $<$ RelIso $<$ 0.5 for muons. 220
5.42 Monte Carlo samples in the muon channel: relative isolation vs. $\not\!\!E_T$ distributions. 222
5.43 Distribution of muon relative isolation (RelIso) vs. $\not\!\!E_T$ in data (36 pb^{-1}) 223

5.44 Data in the electron channel: Relative isolation vs. $\not\!\!E_T$. (a) is used to make the QCD prediction in the loose selection, (b) is used to make the QCD prediction in the tight selection. Figures from Ref. [80]. 226
5.45 Distribution showing th ratio of $\not\!\!E_T$ in electron and muon channels. We fit this ratio in order to obtain a scale factor for using the muon p_T to predict the electron $\not\!\!E_T$. Figures from Ref. [80]. 230
5.46 Measured vs. predicted $\not\!\!E_T$ distributions in muon and electron channels, with loose selections. The data are shown as points with error bars, while the prediction from the resolution-smeared lepton spectrum is shown as the red curve. 235
5.47 Measured vs. predicted $\not\!\!E_T$ distributions in muon and electron channels, with tight selections. The data are shown as points with error bars, while the prediction from the resolution-smeared lepton spectrum is shown as the red curve. 236
5.48 Display of muon event passing the tight selection. 238
5.49 Display of muon event passing the tight selection. 239
5.50 $dN/d\cos\theta^*_\ell$ (SM) and $\pm 5\%$ polarization shifts in $t\bar{t}$ Monte Carlo. 242
5.51 $dN/d\cos\theta^*_\ell$ (SM) and polarization shifts in W + jets from reweighting W polarization fractions, $100 < p_T(W) < 300$ GeV, Alpgen MC. . 244
5.52 Determination of the variation of the MC top p_T that results in a MC $p_T(W)$ distribution that is no longer consistent with the data. Figures from Ref. [80]. 246
5.53 Event display of the ECAL hits in an area surrounding one of the jets in Run 142928 Event 503363075 (one of our two signal events). Inside the jet there is a missing 5 x 5 ECAL crystal cluster that is either dead or masked out. It turns out that in this event the signal muon points very close to the jet axis (ϕ_μ =3.05, η_μ =0.52) but passes the relative isolation requirement. This happens because the crystals with the largest energy are within the inner veto cone of the muon isolation and the crystals outside the inner veto cone that would have the largest energy and make the muon fail the relative isolation requirement are either dead or masked out. Thus, this is a pathological event where dead or masked ECAL channels result in high $\not\!\!E_T$ and a lepton within a jet passing our relative isolation requirement. Algorithms were developed to remove events like this in the 2010 data. However, due to a bug in the algorithm this event actually passes this filter. This bug has been fixed and this event would be rejected in the 2011 data analysis. 251
5.54 Exclusion region for $\tan\beta = 3$, loose selection, lepton spectrum method. 258

5.55 Exclusion region for $\tan\beta = 3$, tight selection, lepton spectrum method. 259
5.56 Exclusion region for $\tan\beta = 10$, loose selection, lepton spectrum method. 260
5.57 Exclusion region for $\tan\beta = 10$, tight selection, lepton spectrum method. 261
5.58 Exclusion region for $\tan\beta = 50$, loose selection, lepton spectrum method. 262
5.59 Exclusion region for $\tan\beta = 50$, tight selection, lepton spectrum method. 263

A.1 Minimum bias MC ΣE_T for different $\not\!\!E_T$ algorithms (pythia 8). . 280
A.2 Minimum bias MC $\not\!\!E_T$ for different $\not\!\!E_T$ algorithms (pythia 8). The plot on the left is linear and the plot on the right is log. 281
A.3 $\not\!\!E_T$ Resolution from RMS versus ΣE_T in data and MC for different $\not\!\!E_T$ algorithms. The upper left plot shows for type I calo$\not\!\!E_T$. The upper right plot shows for type II calo$\not\!\!E_T$. The lower left plot shows for pf$\not\!\!E_T$. The lower right plot shows for tc$\not\!\!E_T$. 282
A.4 $\not\!\!E_T$ Resolution vs. ΣE_T for pf$\not\!\!E_T$ in the case of requiring two calojets (left) and in the case of requiring two pfjets (right). 283
A.5 $\not\!\!E_T$ Resolution from gaussian fit versus ΣE_T in data and MC for different $\not\!\!E_T$ algorithms. The upper left plot shows for type I calo$\not\!\!E_T$. The upper right plot shows for type II calo$\not\!\!E_T$. The lower left plot shows for pf$\not\!\!E_T$. The lower right plot shows for tc$\not\!\!E_T$. 284
A.6 Scatter plots of reco ΣE_T vs. gen ΣE_T for different algorithms. . 285
A.7 Mean reco ΣE_T vs. gen ΣE_T for different algorithms. Each distribution is fitted to a linear shape. 286
A.8 Correction factors for $\not\!\!E_T$ and ΣE_T in MC (pythia), versus average dijet p_T. The upper left plot shows for type I calo$\not\!\!E_T$. The upper right plot shows for type II calo$\not\!\!E_T$. The lower left plot shows for pf$\not\!\!E_T$. The lower right plot shows for tc$\not\!\!E_T$. 288
A.9 Calibrated $\not\!\!E_T$ resolution vs. calibrated ΣE_T compared to calibrated $\not\!\!E_T$ resolution vs. genΣE_T. The black points are vs. genΣE_T, the red points are vs. calibrated ΣE_T. The circles are for type1, the squares are for type2, the right side up triangles are for tc$\not\!\!E_T$ and the upside down triangles are for pf$\not\!\!E_T$. 289

A.10 Calibrated $\not\!\!E_T$ resolution vs. calibrated particle flow ΣE_T compared to calibrated $\not\!\!E_T$ resolution vs. genΣE_T. The black points are vs. genΣE_T, the red points are vs. particle flow calibrated ΣE_T. The circles are for type1, the squares are for type2, the right side up triangles are for tc$\not\!\!E_T$ and the upside down triangles are for pf$\not\!\!E_T$. 290
A.11 Calibrated $\not\!\!E_T$ resolution vs. calibrated pfΣE_T for the different algorithms in data (points), MC (lines). 291
A.12 Ratio of calibrated type II, pf, and tc $\not\!\!E_T$ resolution to type I $\not\!\!E_T$ resolution as a function of calibrated pfΣE_T, for data (points) and MC (lines). 292
A.13 Calibrated $\not\!\!E_T$ resolution vs. calibrated pfΣE_T for raw calo$\not\!\!E_T$, typeI calo$\not\!\!E_T$, and typeII calo$\not\!\!E_T$. The points are for data and the lines are for MC. 293
A.14 Calibrated $\not\!\!E_T$ resolution vs. calibrated pfΣE_T for different pythia samples and different $\not\!\!E_T$ algorithms. The different colors represent different algorithms, and the different style points represent different minimum bias MC samples. 294
A.15 Difference of pythia tunes calibrated $\not\!\!E_T$ resolution and pythia8 calibrated $\not\!\!E_T$ resolution vs. calibrated pfΣE_T for different algorithms. 296

List of Tables

2.1 Parameters for different low mass (LM) benchmark points at CMS. For all these points the sign of μ is positive. The cross sections are leading order and given for $\sqrt{s} = 7$ TeV. In addition the k-factors going from leading order to next-to-leading order are given. 27

3.1 Location of pixel detector layers with respect to the center of the detector. From Ref. [30]. 51
3.2 Detector Types. From Ref. [30]. 53

4.1 Electron efficiency for different working points using the "tag-and-probe" method on $Z \to ee$ events. Numbers taken from Ref. [50]. 98

5.1 Event yields SM backgrounds in Monte Carlo samples, data, and in SUSY Monte Carlo samples after applying the pre-selection requirements. The Monte Samples are normalized to the integrated luminosity of the data sample, 36 pb^{-1}. The yields are given for the muon and electron channels, and combined, both before and after a loose requirement on the minimium transverse energy of the event, $\not\!\!E_T > 25$ GeV. For the SUSY models LM0 and LM1, the NLO cross sections are used. The LM0 model is a benchmark model near the current Tevatron limits in the mSUGRA plane. Table from Ref. [80]. 134
5.2 Definition of loose and tight regions for H_T vs. S_{MET} method. Table from Ref. [80]. 145
5.3 S_{MET} vs. H_T, muon channel: Overview of Monte Carlo and data yields in each of the ABCD regions and the corresponding background prediction in the signal region, for both loose and tight selection. Table from Ref. [80]. 156

5.4 S_{MET} vs. H_T, electron channel: Overview of Monte Carlo and data yields in each of the ABCD regions and the corresponding background prediction in the signal region, for both loose and tight selection. Table from Ref. [80]. 157
5.5 Muon channel: predicted (SM) backgrounds for the ABCD method with H_T and S_{MET} for events with exactly 3 jets. Table from Ref. [80]. 158
5.6 Electron channel: predicted (SM) backgrounds for the ABCD method with H_T and S_{MET} for events with exactly 3 jets. Table from Ref. [80]. 159
5.7 Estimated systematic uncertainties on the background prediction for the ABCD method using the loose selection, expressed as variations on $\kappa = AD/BC$. The MC prediction is $\kappa = 1.08 \pm 0.04$ for the muon channel and $\kappa = 1.03 \pm 0.05$ for the electron channel, respectively. The observed variations of κ are at the limit of statistical significance. For all components the maximum deviation was assigned as a systematic error. Table from Ref. [80]. 161
5.8 Estimated systematic uncertainties on the background prediction for the ABCD method using the tight selection, expressed as variations on $\kappa = AD/BC$. The MC prediction is $\kappa = 0.98 \pm 0.06$ for the muon channel and $\kappa = 1.16 \pm 0.08$ for the electron channel, respectively. The observed variations of κ are at the limit of statistical significance. For all components the maximum deviation was assigned as a systematic error. Table from Ref. [80]. 162
5.9 Results for the data-driven estimation of the QCD contribution to the regions in H_T and S_{MET} for the μ and e channels. The regions are defined in Table 5.2. Table from Ref. [80]. 169
5.10 QCD estimates from the alternative method for the loose and tight ABCD regions in the ECAl barrel and endcap and for the sum of both. The regions are defined in Table 5.2. Table from Ref. [80]. . 173
5.11 Summary of results in the tight selection for the S_{MET} vs. H_T background prediction. Numbers from Ref. [80]. 173
5.12 Lepton spectrum method with loose cuts applied to Monte Carlo: tests of data-driven background determination. Pre-selection cuts are applied, and the signal region corresponds to $\not\!\!E_T > 150$ GeV. Note that the predictions for the dilepton feed-down and tau to lepton are underestimated by this method and are determined separately. 187

5.13 Lepton spectrum method with tight cuts applied to Monte Carlo: tests of data-driven background determination. Pre-selection cuts are applied, and the signal region corresponds to $\not\!\!E_T > 250$ GeV and $H_T > 500$ GeV. Note that the predictions for the dilepton feed-down and tau to lepton are underestimated by this method and are determined separately. 189
5.14 Loose Selection: Dilepton feed-down yields for Monte Carlo truth, Monte Carlo prediction, and data prediction. Only statistical uncertainties are shown. Numbers from Ref. [80]. 211
5.15 Tight Selection: Dilepton feed-down yields for Monte Carlo truth, Monte Carlo prediction, and data prediction. Only statistical uncertainties are shown. Numbers from Ref. [80]. 212
5.16 Loose Selection: single $\tau \to \ell$ yields for Monte Carlo truth, Monte Carlo prediction, and data prediction. Only statistical errors are shown. Numbers from Ref. [80]. 217
5.17 Tight Selection: single $\tau \to \ell$ yields for Monte Carlo truth, Monte Carlo prediction, and data prediction. Only statistical errors are shown. Numbers from Ref. [80]. 217
5.18 QCD background study in Monte Carlo using the two-dimensional distribution of RelIso vs. $\not\!\!E_T$. The regions are defined as A: 0.2<RelIso<0.5, $\not\!\!E_T$ <25 GeV, B: RelIso<0.1, $\not\!\!E_T$ <25 GeV, C: 0.2<RelIso<0.5, $\not\!\!E_T$ >25 GeV, D: RelIso<0.1, $\not\!\!E_T$ >25 GeV. Because there are so few QCD events in the signal region, even with the loose selection requirements, the test region D starts at $\not\!\!E_T > 25$ GeV, compared with $\not\!\!E_T > 150$ GeV for the loose selection and $\not\!\!E_T > 250$ GeV for the tight selection. Furthermore, we perform a test with a lower muon p_T threshold to gain additional statistics. 221
5.19 Data (muon channel): QCD background determination in the space of RelIso vs. $\not\!\!E_T$ for loose and tight selections, 36 pb^{-1}. 224
5.20 Data (electron channel), Loose Selection: QCD background determination in the space of RelIso vs. $\not\!\!E_T$. These numbers are for the 8 pb^{-1} of data with no isolation requirements on the single electron triggers. For the final prediction the number predicted in Region D is scaled from 8 pb^{-1} to 36 pb^{-1} to obtain $0.0^{+0.38}_{-0.0}$. Numbers from Ref. [80]. 226

5.21 Data (electron channel), Tight Selection: QCD background determination in the space of RelIso vs. $\not\!\!E_T$. To calculate the uncertainty of the prediction we assume there is one event in Region C and assign a Poisson uncertainty to this one event, which we propagate to region D. The H_T requirement for the tight selection is loosened from 500 GeV to 300 GeV to gain more statistics in Regions A and B. With the loosened H_T requirement this prediction is more conservative. Numbers from Ref. [80]. 227
5.22 Muon channel: scale factors for single lepton, dilepton, and tau predictions. Numbers are for the tight selection and come from Monte Carlo. The errors on the actual and predicted numbers are statistical only. However, for the scale factor both statistical and systematic uncertainties are shown. See Sec. 5.5.12 for information on how the systematic uncertainties are determined. These numbers were calculated using the W+jets alpgen sample. The prediction for the single lepton component includes resolution smearing and the small overlap with the other predictions. 234
5.23 Electron channel: scale factors for single lepton, dilepton, and tau predictions. Numbers are for the tight selection and come from Monte Carlo. The errors on the actual and predicted numbers are statistical only. However, for the scale factor both statistical and systematic uncertainties are shown. See Sec. 5.5.12 for information on how the systematic uncertainties are determined. These numbers were calculated using the W+jets alpgen sample and the prediction is from the muon p_T spectrum. The prediction for the single lepton component includes resolution smearing and the small overlap with the other predictions. 234
5.24 Loose cuts applied to data: yield from data-driven background determination and yield in signal region. Pre-selection cuts are applied, and the signal region corresponds to $\not\!\!E_T > 150$ GeV. 237
5.25 Tight cuts applied to data: yield from data-driven background determination and yield in signal region. Pre-selection cuts are applied, and the signal region corresponds to $\not\!\!E_T > 250$ GeV and $H_T > 500$ GeV. 240
5.26 Systematic uncertainties for the lepton spectrum method. Each uncertainty is expressed as a change in the ratio of predicted to the true number of events (evaluated in Monte Carlo). The total uncertainty is the individual uncertainties summed in quadrature. 241

5.27 Muon quantities in events in the loose signal region, $\not\!\!E_T > 150$ GeV. Events with * are those which are also in the tight signal region ($H_T > 500$ GeV and $\not\!\!E_T > 250$ GeV). $\Delta\phi$ is the angle between the muon and the $\not\!\!E_T$. Table from Ref. [80]. 248
5.28 Distribution of charge and btag for data events in the muon channel with $\not\!\!E_T > 150$ GeV. Table from Ref. [80]. 249
5.29 Muon quantities in events in the loose control region, $p_T(\mu) > 150$ GeV. Events with * are those which also are in the tight control region ($H_T > 500$ GeV and $p_T(\mu) > 250$ GeV). $\Delta\phi$ is the angle between the muon and the $\not\!\!E_T$. Table from Ref. [80]. 249
5.30 Distribution of charge and btag for data events in the muon channel with $p_T(\mu) > 150$ GeV. Table from Ref. [80]. 250

Chapter 1

Introduction

In particle physics we strive to determine the fundamental particles in the universe (particles that are not made of other particles) and their fundamental interactions. These reductionist methods in science have a long history, reaching all the way back to the ancient Greeks, who believed everything was made of four fundamental elements. These days physicists have discovered that the fundamental particles are quarks (which make up the proton and neutron), leptons (such as the electron), and bosons (such as the photon), all which obey four fundamental forces. These forces, in decreasing order of strength, are the strong force, the electromagnetic force, the weak force, and the gravitational force. The strong force is responsible for the binding of the nuclei in atoms. Electromagnetic forces are present all around us in the form of electricity and magnetism. The weak force is generally not as intuitive, but is responsible for many different radioactive decays (such as beta decay). Lastly, gravity, which is very intuitive

since we can easily visualize how it impacts us on a daily basis, is responsible for the celestial movement of large objects.

The standard model theory of particle physics is a framework where these fundamental particles and all the interactions except gravity can be understood in a precise quantitative way. The standard model (SM) is described in more detail in Sec. 2.1. With the standard model it is possible to understand the nature of much of the universe and how it evolved. However, there are places where the standard model is either not complete or does not describe certain phenomena. For instance, for the standard model to be a complete theory we must understand the so-called Higgs mechanism that gives masses to all the particles. So far we have not found the Higgs boson which could explain this. In addition to not having found the Higgs boson we also know that there must be other particles in the universe that the standard model does not predict. One strong reason to believe this is the observation of large amounts of "dark matter" in the universe that cannot be explained by any standard model particle. More explanation of "dark matter" and other reasons to believe the standard model must be supplemented by additional theories is given in Sec. 2.2.

Supersymmetry (SUSY) is one of the theoretical models that is very interesting because it can possibly fill in places where the standard model falls short. SUSY postulates a doubling of the number of fundamental particles in the uni-

verse and one of these particles could be responsible for the "dark matter". An overview of SUSY, including the strong theoretical and experimental motivations for it, is given in Sec. 2.3.

This paper describes a search for SUSY at the Compact Muon Solenoid (CMS) experiment at the Large Hadron Collider (LHC) particle accelerator. In order to perform any search in particle physics these days one must understand the complex hardware and software that goes into detecting the particles. Gone are the days of simple table-top experiments to discover new particles, such as visually detecting cosmic ray tracks going through cloud-chamber detectors.[1] As physicists wanted to explore shorter and shorter length scales they needed higher energy particles that could not be provided from cosmic rays (at least at a high enough rate) or other natural phenomena. Thus, physicists started building particle accelerators that could generate high-energy collisions. Currently the LHC is the highest energy collider in the world and when particles collide and are detected by the CMS experiment there are all kinds of complications that must be taken into account. A detailed description of the LHC and the CMS detector is given in Chapter 3. Chapter 4 then describes the software algorithms that take the hardware signals and reconstruct the different particles.

[1] This is how the positron was discovered.

The parameter space for SUSY is very large and thus there are many different ways to search for it. The searches for SUSY at CMS are signature based searches, meaning they are focused on understanding a particular event sample after requiring certain reconstructed objects in the event (such as leptons, $\not\!\!E_T$, jets, or photons). In this paper we focus on the search mode requiring a single isolated lepton, jets, and $\not\!\!E_T$. The results of this search have been presented in Ref. [1]. A detailed description of this search, including motivations for this signature, is given in Chapter 5. Conclusions are stated in Chapter 6 and a study of the $\not\!\!E_T$ resolution at CMS is described in the Appendix.

The search described in Chapter 5 was done within the CMS collaboration with three main institutions involved: UCSB, Institut für Hochenergiephysik der ÖAW (located in Vienna, Austria), and Cornell University. Our colleagues at Vienna and Cornell focused on the S_{MET} vs. H_T ABCD method while UCSB focused on the lepton spectrum method. My work was mostly on the lepton spectrum method, though I performed cross-checks and optimization studies of the S_{MET} vs. H_T ABCD method. Within the work done for the lepton spectrum method the dilepton and tau predictions were done by Chris Justus and the QCD prediction for the electrons was done by Wing To. In addition, Victor Pavlunin helped with the systematic studies for the lepton spectrum method and the

Search for new physics in proton-proton collisions at 7 TeV in events with a single lepton, jets, and missing transverse momentum

W. Adam[3], A. Chatterjee[1], T. Danielson[2], M. Duenser[3], C. Justus[2], W. Kiesenhofer[3], R. Patterson[1], V. Pavlunin[2], F. Rebassoo[2], J. Richman[2], R. Schoefbeck[3], D. Stuart[2], W. To[2], W. Waltenberger[3], and E. Widl[3]

[1] Cornell University, Ithaca, NY, USA
[2] University of California, Santa Barbara, CA, USA
[3] Institut für Hochenergiephysik der ÖAW, Wien, Austria

Figure 1.1: List of main contributors to this analysis and their institutions.

overall implementation (the method was first proposed by him). A complete list of the main contributors to this work is given in Figure 1.1.

I should also mention that in the published paper for this search (see Ref. [1]), the variable S_{MET} is referred to as Y_{MET}. The variable name was changed just before publication to be more consistent with other SUSY searches at CMS.

Chapter 2

Theory

2.1 Physics of the standard model

The standard model of particle physics is made up of the Glashow-Weinberg-Salam theory describing the weak and electromagnetic forces and the Quantum Chromodynamics (QCD) theory describing the strong force. [1] It explains almost all data pertaining to the strong, weak, and electromagnetic forces, but does not incorporate gravity (as mentioned before). The standard model was developed using quantum field theory (QFT), which is able to reconcile quantum effects with special relativity, and to describe how particles can be created and annihilated. The technical description is that the standard model is a gauge theory based on the group $SU(3) \times SU(2) \times U(1)$. This nomenclature gives a description of the internal symmetries that are responsible for the different

[1] For information on the Glashow-Weinberg-Salam theory see Refs. [2] [3] [4]. For a review of QCD theory see Ref. [5].

forces. Quantum Chromodynamics (QCD), which has a $SU(3)$ symmetry associated with a new quantum number called color, is responsible for the strong force. The electroweak part of the theory, which has a $SU(2) \times U(1)$ symmetry which is broken (more about this later), is responsible for the electromagnetic and weak forces.

The fundamental particles in the standard model are shown in Figure 2.1 and separated into two main groups: fermions and bosons (fermions have half-integer spin and bosons have integer spin). There are four fundamental spin 1 bosons: the photon, the Z and W bosons, and the gluon. In the standard model the forces are a result of particle exchange of these bosons. The photon mediates the electromagnetic force, the W^+, W^-, and Z^0 bosons mediate the weak force, and the gluon mediates the strong force.[2]

The fermions are divided up into quarks and leptons, both of which come in three different generations as shown in the first three columns in Figure 2.1. Quarks interact via the strong, electromagnetic, and weak force and they are the constituents, along with gluons, of hadrons (particles that are bound together strongly). In fact, quarks are only found in hadronic bound states called mesons (two quarks in a bound state such as a pion or kaon) and baryons (three quarks in a bound state such as a proton or neutron). The absence of single isolated

[2]There are in fact 8 different gluons, all with different color composition, that mediate the strong force. This is a result of the 8 degrees of freedom of the SU(3) symmetry group.

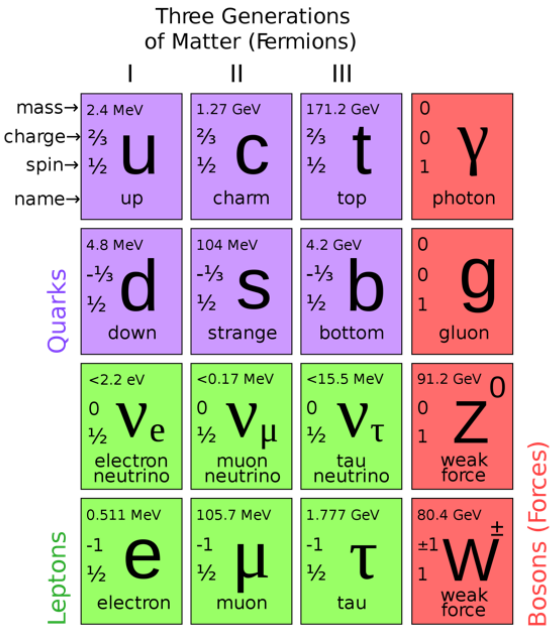

Figure 2.1: The fundamental particles in the standard model along with their mass, charge, and spin. Quarks are shown in purple, bosons in red, and leptons in green. Figure from Ref. [6].

quarks in nature is due to the fact that the strong force increases in strength as a function of distance. As a single quark starts to get further away from another quark the potential energy between the two quarks increases enough (it goes roughly like $V(r) \approx r$ as opposed to the Couloumb field that goes like $V(r) \approx 1/r$) that quark anti-quark pairs are created out of the vacuum. These quark pairs essentially follow the same direction as the original quark and form bound states that include the original quark. This process is called hadronization. Because of this it is not possible to isolate a single quark and it will always be in a multi-quark bound state (such as a proton, neutron or pion) when detected experimentally. Technically, this effect is called "infrared slavery" and comes from the fact that QCD is a non-Abelian theory where the gluons can interact with each other. This effect is seen everyday at particle accelerators, where high energy quarks and gluons hadronize to produce jets, a spray of collimated particles along the direction of the initial quark or gluon. Many years have been spent studying the bound states of the quarks; for a detailed review see Ref. [7].

The leptons are divided up into charged and neutral leptons, where the charged leptons are the electron, muon, and tau, and the neutral leptons are their corresponding neutrinos. Because the neutrinos are neutral, they interact only through the weak force, whereas the electron, muon, and tau have electric

charge and thus interact through both the electromagnetic and weak force. The strength of the electroweak force decreases as a function of distance, so unlike quarks, leptons can be isolated.

All the particles in Figure 2.1 have corresponding anti-particles as well. For instance, the electron's anti-particle is the positron and the up quark's anti-particle is the anti-up quark. An anti-particle has the same mass and spin but opposite value of charge and conserved quantities like baryon number and lepton number. Most of the known matter in the universe is made of matter not anti-matter and is from the first generation. The reason why our universe is largely matter and not anti-matter is still unknown and cannot be explained in the standard model. The reason most matter is from the first generation is that these particles have lower masses and thus are stable, while the second and third generation particles are unstable.

The part of the standard model theory missing in Figure 2.1 is the Higgs boson. The Higgs boson is a consequence of the Higgs mechanism [8] [9] [10], which is responsible for electroweak symmetry breaking that gives mass to all the standard model particles. The Higgs boson has not been found experimentally yet, and ongoing searches at the Tevatron and LHC are looking for it. If it isn't found, the mechanism for electroweak symmetry breaking will have to be something different. Another postulated particle, the graviton, is not shown in

Figure 2.1 and is a spin 2 boson that could be the mediator of the gravitational force.

2.2 Motivations for searching beyond the standard model

In the previous section we gave a brief overview of the standard model and its properties. It cannot be emphasized enough how well this theory predicts the strong and electroweak phenomena seen by experiments. However, there are several theoretical and experimental reasons to believe that it must be supplemented by additional theoretical framework. Some of the significant experimental observations that cannot be explained within the framework of the standard model include the large amount of observed dark matter in the universe, the existence of neutrino masses, and the domination of matter over anti-matter in the universe. Some of the theoretical issues with the standard model are that it contains many arbitrary masses and parameters, the different generations of the fermions cannot be explained, and the mass of the Higgs boson is subject to quadratically divergent quantum corrections (hierarchy problem). In addition, the standard model does not describe gravity and does not provide the unification of the strong, electromagnetic, and weak forces at some GUT scale. Of

the different theories that try to explain these phenomena, supersymmetry can give possible solutions to the dark matter and hierarchy problems, and can also provide unification of all the forces except gravity.[3] Since we are focusing on supersymmetry in this paper we will give a detailed explanation of the dark matter and hierarchy issues (the unification of the forces is much simpler to explain and thus will be described in the context of SUSY) and leave the other issues for the reader to investigate.

2.2.1 Dark Matter

It turns out that the matter in the standard model, specified in Figure 2.1, only makes up a small piece of the total energy density of the universe. The additional energy density comes in the form of dark matter and dark energy. The exact fraction of baryonic matter (B), dark matter (DM), and dark energy (Λ) in the universe is given by:

$$\Omega_B \simeq 0.0456 \pm 0.0016, \tag{2.1}$$

$$\Omega_{DM} \simeq 0.227 \pm 0.014, \tag{2.2}$$

$$\Omega_\Lambda \simeq 0.728 \pm 0.015, \tag{2.3}$$

[3]This means that at some very high energy the strong, weak, and electromagnetic forces will all have the same strength. The electroweak theory in the SM already unifies the weak and electromagnetic forces. However, the SM cannot unify the strong force with these forces.

where the values are taken from Ref. [11]. Ordinary baryonic matter[4] only makes up roughly 5% of the universe and there is about 5 times as much dark matter than baryonic matter (the dark energy term which is roughly 75% is also very perplexing but is out of the scope of this paper).

The fact that there is additional matter in the universe that we don't understand was first seen by Fritz Zwicky in 1933. He was looking at the Coma cluster of galaxies and observed that the velocity of the galaxies would require much more luminous mass than was seen [12]. Additional studies by Rubin and collaborators [13] [14] and Bosma [15] in the 1970s looking at individual galaxies found that the rotation velocity at large radii from the center of the galaxy was significantly underpredicted by considering only the luminous mass. Many different observations based on gravitational interaction have since confirmed the presence of dark matter. One particularly spectacular result is the picture of the so called "bullet cluster", shown in Figure 2.2. The "bullet cluster" shows two clusters of galaxies colliding (just the fact that we are able to photograph two clusters of galaxies colliding is pretty incredible). By using gravitational lensing and X-ray measurements it is possible to look at the dark matter in the galaxies (the matter seen by gravitational lensing but not through X-rays) and the normal baryonic matter in the galaxies (the matter seen through X-rays).

[4]This is matter that can be described by the SM.

Figure 2.2: The "Bullet Cluster", which shows two galaxies colliding. The blue represents the amount of matter from gravitational lensing that is otherwise not seen and the red represents the amount of matter as measured by X-rays from galaxy remnants, mostly hydrogen gas. The interpretation is that the blue matter is the dark matter which interacts weakly and thus has passed through relatively easily. On the other hand the red matter represents the baryonic matter which has slowed down significantly due to electromagnetic interactions. Figure from Ref. [16].

Figure 2.2 shows that the inferred dark matter (blue) of the two galaxies interacts very weakly and thus passes through very easily. This is in contrast to the normal baryonic matter (red) of the two galaxies, which passes through slower because of electromagnetic interactions.

Though many experiments have seen dark matter from gravitational interactions, no direct observation of the particles responsible for dark matter has been made. There are many criteria that a particle must satisfy to be a dark matter

candidate. It must be weakly-interacting (or else we would see its radiation), stable on cosmological timescales, and give the correct relic density. Most cosmologists also differentiate between "cold" and "hot" dark matter, where "cold" means that the particles were not moving at relativistic velocities at the time of galaxy formation and "hot" means they were. "Cold" dark matter is favored by most cosmological models for several reasons, one of which is that it explains the distribution of structure we see in the universe better than "hot" dark matter [17]. However, there is the possibility that dark matter could have both a "cold" and a "hot" component [7].

None of the particles in the SM can be a good DM candidate. Most of the particles are unstable and decay and thus would not survive on cosmological timescales. For some of the stable particles, such as protons, neutrons, and electrons, their energy density is taken into account by the baryonic energy density (for electrons to contribute to dark matter they must be bound with the protons and thus would be taken into account by Ω_B). Neutrinos cannot be the dark matter because the current upper bounds on the neutrino masses, $\Sigma_i m_\nu = 0.58\text{eV}$ [18], imply that the relic neutrino density, $\Omega_\nu = \Sigma_i m_\nu/47$ eV, must be much smaller than the required dark matter density given in Equation (2.3).

Some dark matter candidates that are in theories beyond the standard model include WIMPs (weakly-interacting massive particles), axions, and black holes. As will see soon enough SUSY provides a natural candidate for a WIMP. For a thorough review of different dark matter candidates see Ref. [11].

2.2.2 Hierarchy Problem

One of the strong theoretical motivations for expecting new physics at around the TeV scale is called the hierarchy problem and has to do with quantum corrections to the Higgs mass. In quantum field theory we perform pertubative expansions to calculate quantitatively the amplitude for certain processes. For instance when calculating the Higgs mass, m_H^2, the mass is given by:

$$m_H^2 = m_{H0}^2 + \delta m_H^2 + ..., \tag{2.4}$$

where m_{H0} is the tree level mass (sometimes called the bare mass), δm_H^2 is the one-loop correction to the mass, and the ellipses represent higher order corrections. It turns out that the one-loop correction is quadratically divergent [19]:

$$\delta m_H^2 = \frac{-|\lambda|^2}{8\pi^2}\Lambda^2 + ..., \tag{2.5}$$

where λ is the coupling constant of the Higgs fermion vertex and Λ is a energy cutoff scale where new physics applies. This quadratically divergent term is a direct result of the Higgs boson being a spin 0 particle and does not afflict other

particles in the standard model (there are no other fundamental spin 0 particles in the SM).

If there is no new physics until the Planck scale (where quantum fluctuation of the gravitational fields becomes important and there is a good chance Quantum Field Theory just breaks down) the cutoff scale of the theory, Λ, will be 10^{19} GeV and the one-loop correction term must cancel the tree-level term at roughly one part in 10^{32} to give a Higgs mass below 1 TeV (a Higgs mass above 1 TeV violates pertubative unitarity for WW scattering). This is technically not a problem for the theory but seems like a very nasty feature. It is called the hierarchy problem because unless there is new physics present at roughly the TeV scale we do not know why the Higgs mass is so much smaller than the Planck mass or GUT scale.

The hierarchy problem is eliminated by either taking the Higgs to be a composite structure (for instance, in technicolor theory) or by requiring a new symmetry. As we will see supersymmetry provides a nice theoretical structure to eliminate this problem.

2.3 Supersymmetric theory

As stated previously Supersymmetric theory is able to fix some of the issues with the standard model. Its provides a natural dark matter candidate, fixes the hierarchy problem, and unifies the QCD and electroweak coupling constants. Before going into detail about exactly how it does this we need to first give an overview of its basic properties. For a more detailed review of supersymmetry see Ref. [19]. Additional information can be found in Refs. [20], [21], [22],[23], and [24].

2.3.1 Overview of theory

Supersymmetry is a symmetry relating bosonic degrees of freedom to fermionic degrees of freedom. It was first developed in the 1970s when theorists were investigating early versions of string theory and later applied to develop a supersymmetric extension to the standard model. The simplest extension of the standard model is the Minimal Supersymmetric Model (MSSM). In the MSSM each standard model particle has a partner particle with the exact same quantum numbers except spin, which differs by 1/2. These SUSY partner particles are called "sparticles" (for supersymmetry partners) and SUSY predicts a whole plethora of new fundametal particles. For instance for every lepton and quark

there is a bosonic partner (i.e., for a muon there is a scalar muon, called a smuon) and for every gauge boson there is a fermionic partner called a gaugino. The Supersymmetric particles are usually denoted with a tilde above, so a smuon is denoted as $\tilde{\mu}$, a sneutrino is denoted as $\tilde{\nu}$, a stop quark is denoted as $\tilde{t}$, etc.

In order for the spin degrees of freedom to be consistent in the MSSM, each quark or charged lepton has two superpartners, one for each chiral component. For instance the electron is made up of a left-handed piece, e_L, and a right-handed piece, e_R, each which has a spin 0 superpartner, called $\tilde{e}_L$ and $\tilde{e}_R$, respectively. Figure 2.3 lists the superpartners of the quarks, leptons, and Higgs boson. Figure 2.4 lists the superpartners of the vector bosons (gauginos). All the gauginos except the gluino (the partner of the gluon) are not mass eigenstates and so they mix to produce charginos, $\tilde{\chi}_1^{\pm}$, $\tilde{\chi}_2^{\pm}$, and neutralinos, $\tilde{\chi}_1^0$, $\tilde{\chi}_2^0$, $\tilde{\chi}_3^0$, $\tilde{\chi}_4^0$. The different subscript numbers on the charginos and neutralinos corresond to their mass ordering. Thus, the $\tilde{\chi}_1^{\pm}$ and $\tilde{\chi}_1^0$ are the lightest chargino and neutralino, respectively.

If these "sparticles" had the same mass as their standard model partners we would have already observed them. However, no experiments have observed any of these particles and as a result SUSY must be a broken symmetry of nature. The doubling of particles in supersymmetry might seem a little weird but something similar has been seen before when anti-particles were first postulated.

Names		spin 0	spin 1/2
squarks, quarks	Q	$(\widetilde{u}_L \;\; \widetilde{d}_L)$	$(u_L \;\; d_L)$
($\times$3 families)	$\overline{u}$	$\widetilde{u}^*_R$	$u^\dagger_R$
	$\overline{d}$	$\widetilde{d}^*_R$	$d^\dagger_R$
sleptons, leptons	L	$(\widetilde{\nu} \;\; \widetilde{e}_L)$	$(\nu \;\; e_L)$
($\times$3 families)	$\overline{e}$	$\widetilde{e}^*_R$	$e^\dagger_R$
Higgs, higgsinos	H_u	$(H^+_u \;\; H^0_u)$	$(\widetilde{H}^+_u \;\; \widetilde{H}^0_u)$
	H_d	$(H^0_d \;\; H^-_d)$	$(\widetilde{H}^0_d \;\; \widetilde{H}^-_d)$

Figure 2.3: Quarks, leptons, and Higgs in the standard model and their corresponding superpartners in the MSSM. From Ref. [19].

Names	spin 1/2	spin 1
gluino, gluon	$\widetilde{g}$	g
winos, W bosons	$\widetilde{W}^\pm \;\; \widetilde{W}^0$	$W^\pm \;\; W^0$
bino, B boson	$\widetilde{B}^0$	B^0

Figure 2.4: Gauge bosons in the standard model and their superpartners in the MSSM. The bino and wino are not mass eigenstate particles and thus mix to produce the charginos and neutralinos, which are the mass eigenstates. From Ref. [19].

In this case anti-particles were a result of going from three-dimensional space to four-dimensional space. In SUSY the "sparticles" are a result of going from four-dimensional space to superspace. The fact that supersymmetry adds many more parameters to the standard model is not too disconcerting because it is an effective theory that must be replaced at some higher energy scale by a more complete theory (such as string theory) that can explain the different parameter values in the theory.

2.3.2 How SUSY solves some SM issues

In the MSSM framework with sparticle masses between 100 GeV to 1 TeV several issues are solved. The quadratically divergent terms in the Higgs mass calculation are no longer present and the coupling constants are unified at a higher energy scale. (If the sparticle masses increase above approximately 1 TeV these issues are no longer solved). In addition, if a new quantum number is introduced, called R-parity, supersymmetry gives a natural dark matter candidate.

Figure 2.5 shows the coupling constants as a function of energy. In the standard model the coupling constants do not converge (dotted lines). However, in the MSSM (bold lines) this unification is possible at around 10^{16} GeV, the so-called Grand Unified Theory (GUT) scale. The reason the slopes of the

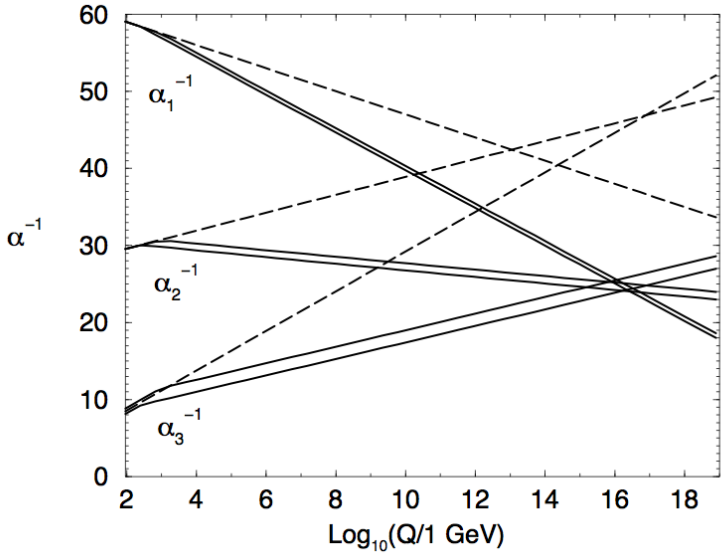

Figure 2.5: This plot shows how the different couplings constants for SM interactions evolve as a function of the energy. In the SM the couplings do not converge (dotted lines); however, in the MSSM the couplings do converge at a GUT scale of roughly 10^{16} GeV (bold lines). In the MSSM case sparticle masses are varied from 250 GeV to 1 TeV. Two loop effects are taken into account. From Ref. [19].

coupling constants is different between SUSY and the SM is that in SUSY there is additional particles that can appear in the loop diagrams that effect the running of the coupling constant.

The hierarchy problem is solved by the addition of new scalar particles that appear in the higher order corrections to the Higgs mass. Figure 2.6 shows the one-loop diagrams with fermion and bosonic propagators. These diagrams have opposite signs (there is an additional -1 factor between bosons and fermions) and if $\lambda_S = |\lambda_f|^2$ the quadratic sensitity to the cutoff in Equation 2.5 can be eliminated. In addition, it happens to work out that this cancellation of the divergences works at all orders in perturbation theory.

In most theories of SUSY a discrete multiplicative quantum number R-parity must be conserved. The technical definition of R-parity is $R = (-1)^{2j+3B+L}$, where j is spin, B is baryon number, and L is lepton number. SUSY particles have R-parity -1 and SM particles have R-parity 1. The reason that R-parity is so common is that SUSY theories without it have problems protecting the proton lifetime ($p \rightarrow e^+\pi^0$) or conserving lepton number ($\tilde{\gamma} \rightarrow \gamma + \nu$). To be consistent with experimental observations the R-parity violating terms in any SUSY theory would have to be very small. The consequences of requiring R-parity is that SUSY particles must be produced in pairs. Additionally, there must be a lightest supersymmetric particle (LSP) that is stable because it cannot decay

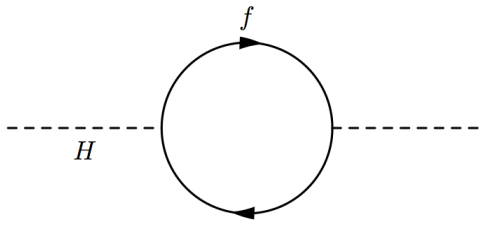

(a)

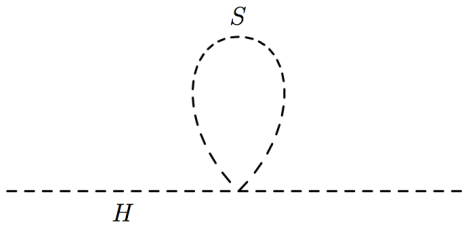

(b)

Figure 2.6: One-loop corrections to the Higgs mass, m_H^2: (a) with fermion loop, (b) with scalar loop.

to any standard model particle. This LSP can be a nice dark matter candidate because in most models it is weakly-interacting, heavy, and stable.

2.3.3 CMSSM

The MSSM has over 100 parameters, and while many of these can be eliminated using known experimental measurements, the parameter space is still extremely large for experimentalists to investigate. To help reduce the number of parameters the constrained Minimal Supersymmetric Model (CMSSM) was developed. By making certain assumptions the CMSSM reduces the number of parameters to five. Two of the main assumptions of the CMSSM is that the gaugino masses unify at the GUT scale and the scalar masses unify at the GUT scale. While the first assumption is well motivated because of the unification of the coupling constants at the GUT scale, the second is not as well motivated and there is no strong theoretical justification for making the scalar masses unify at the GUT scale. The five parameters include $m_{1/2}$, m_0, $\tan\beta$, A_0, and sign(μ) and are defined at the GUT scale of roughly 10^{16} GeV. The definitions of these parameters are the following: $m_{1/2}$ is the univeral gaugino mass, m_0 is the universal scalar mass, A_0 is the universal trilinear coupling, $\tan\beta$ is the ratio of the two Higgs-doublet vacuum expectation values, and sign(μ) is the sign of the Higgs mixing parameter. These parameters are then run down to the electroweak

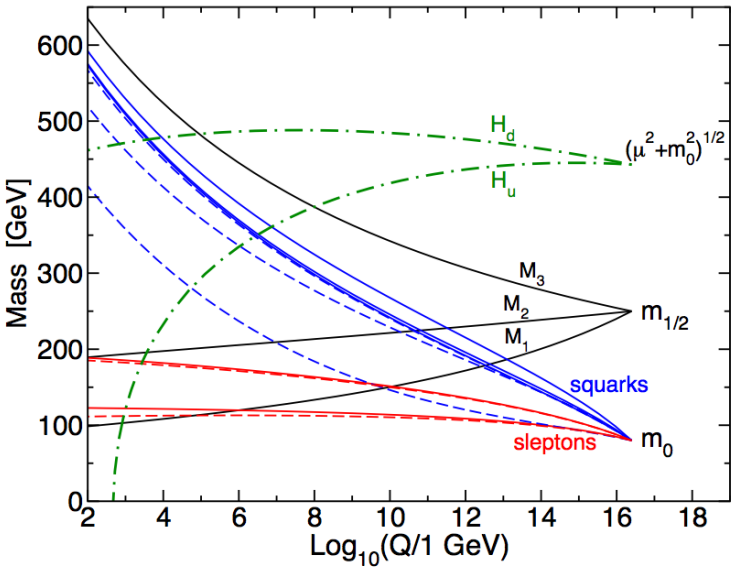

Figure 2.7: Renormalization group running of scalar and gaugino mass parameters with boundary conditions at 2.5 x 10^{16} GeV. The parameter values for this plots are m_0 = 80 GeV, $m_{1/2}$ = 250, A_0 = −500 GeV, tanβ = 10, and sign(μ)>0. Gaugino masses are labeled M_1, M_2, and M_3. The dashed lines for the squarks and sleptons are for the third generation and the solid lines are for the first and second generations. Plot from Ref. [19].

scale (where we perform our experiments) to obtain the sparticle masses, decay branching ratios and production cross sections.

Figure 2.7 shows the running of the GUT scale parameters to the electroweak scale for a particular model point in CMSSM. The parameters M_1, M_2, and M_3 are the U(1), SU(2), and SU(3) gaugino masses respectively and they determine the different gluino, neutralino, and chargino masses. The gluino mass is determined by M_3 while the neutralino and chargino masses are a function of M_1, M_2, and μ. The gluino mass is roughly $2.7m_{1/2}$ while the slepton masses

Table 2.1: Parameters for different low mass (LM) benchmark points at CMS. For all these points the sign of μ is positive. The cross sections are leading order and given for $\sqrt{s} = 7$ TeV. In addition the k-factors going from leading order to next-to-leading order are given.

Model	σ (pb)	k = NLO/LO	m_0 (GeV)	$m_{1/2}$ (GeV)	A_0	tanβ
LM0	38.9	1.41	200	160	-400	10
LM1	4.89	1.34	60	250	0	10
LM2	0.60	1.33	185	350	0	35
LM3	3.44	1.40	330	240	0	20
LM4	1.88	1.35	210	285	0	10
LM5	0.47	1.34	230	360	0	10
LM6	0.31	1.30	85	400	0	10
LM7	1.21	1.11	3000	230	0	10
LM8	0.73	1.41	500	300	-300	10
LM9	7.13	1.48	1450	175	0	50

are to a good approximation $m^2_{\tilde{\ell}_R} \approx m_0^2 + 0.15 m_{1/2}^2$ and $m^2_{\tilde{\ell}_L} \approx m_0^2 + 0.5 m_{1/2}^2$. For the first two generations of squarks the masses are approximately given by $m^2_{(\tilde{u},\tilde{d})_L} \approx m_0^2 + 5.0 m_{1/2}^2$ and $m^2_{(\tilde{u},\tilde{d})_R} \approx m_0^2 + 4.5 m_{1/2}^2$. We should mention that the assumptions of the CMSSM limits the phenomenology, most importantly by making the gluino and LSP have an approximately fixed mass ratio. Additional phenomenological models, called simplified models [25] [26], have been developed to help broaden the searches at the CMS and ATLAS experiments.

In the CMS experiment we have defined different benchmark points for low mass (LM) CMSSM, with the cross sections ranging from the order of 1 to 100 pb. Table 2.1 shows the CMSSM parameters for ten of these different model points.

All these benchmark points were beyond the reach of previous experiments at the time the LHC started running.[5] The mass spectrum of the sparticles for the mass points LM0 and LM1 is shown in Figures 2.8 and 2.9 respectively. For LM0 one of the stop quarks is the heaviest particle[6] and in the case of LM1 the gluino is the heaviest particle. In both cases the lightest neutralino, $\tilde{\chi}_1^0$, is the lightest supersymmetric particle (LSP), and this is generally the case for most CMSSM models. Usually the LSP is on the order of 100 GeV for these models. In the next section we will discuss the production of SUSY models (including these benchmark points) at the LHC. For a more detailed description of the CMSSM framework see Ref. [27].

2.3.4 SUSY production at the LHC

At the LHC the center-of-mass energy is enough to probe SUSY models with sparticles of the order of hundreds of GeV. For most SUSY models the strong production will dominate since the cross section at the LHC for strong processes is much higher than electroweak processes. However, as we will show later in

[5]Since the LHC started running some of these points have been excluded by LHC SUSY searches, such as the one described in this paper.

[6]The third generation quarks are labeled with indices 1 and 2 instead of L and R because for their mass eigenstates there is some mixing between left and right chiral states (which is not the case for the first two generations).

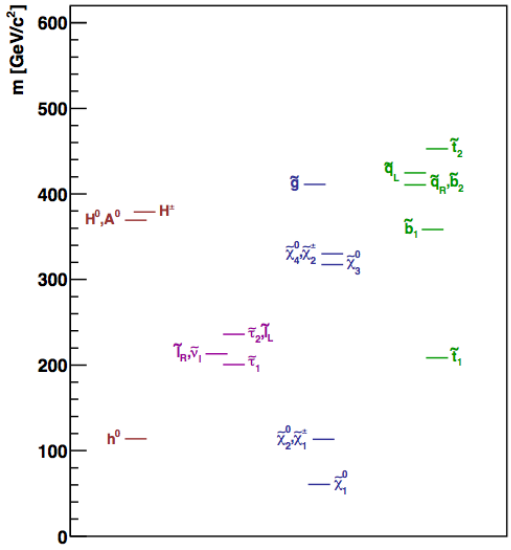

Figure 2.8: Mass spectrum of LM0 signal point (from Ref. [28]).

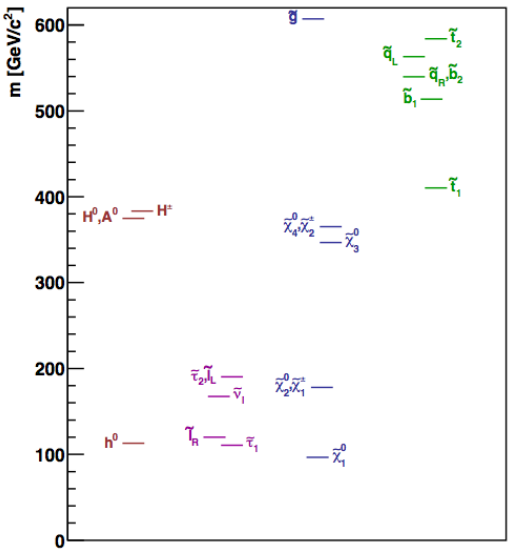

Figure 2.9: Mass spectrum of LM1 signal point (from Ref. [28]).

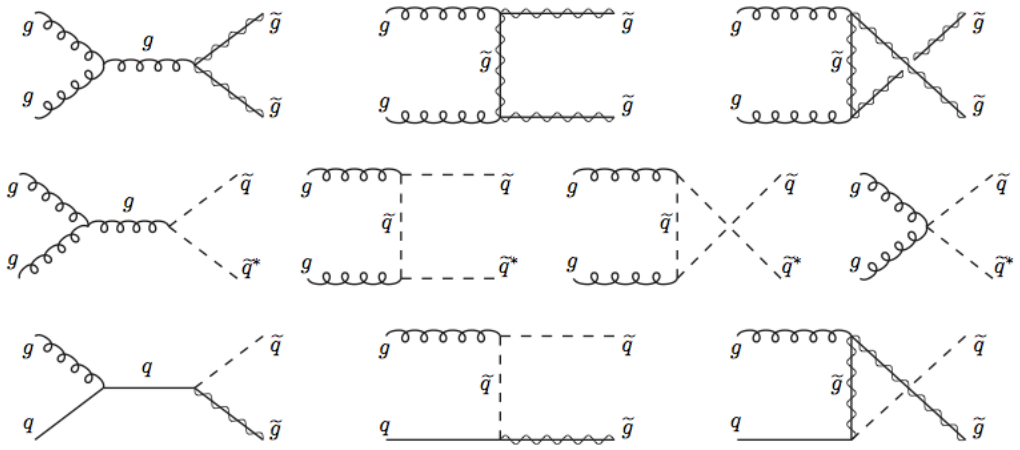

Figure 2.10: Feynman diagrams for gluon-gluon and gluon-quark production of sparticles. Figure from Ref. [19].

this section, for some regions of parameter space (for instance, when the squark masses are extremely high) electroweak production dominates.

Figures 2.10 and 2.11 show the Feynman diagrams for different SUSY strong production processes at the LHC. All the diagrams start with either gg, gq, qq, or $q\bar{q}$ and then proceed through s,t, or u channels to produce gluinos and squarks or anti-squarks with the following final state: $\tilde{g}\tilde{g}$, $\tilde{g}\tilde{q}$, $\tilde{q}\tilde{q}$, and $\bar{\tilde{q}}\tilde{q}$. There are additional diagrams for strong production that are not shown in Figures 2.10 and 2.11 that come from $g\bar{q}$ and $\bar{q}\bar{q}$ scattering. However, because the LHC is a pp machine anti-quarks have to be sea quarks and these diagrams are highly suppressed.

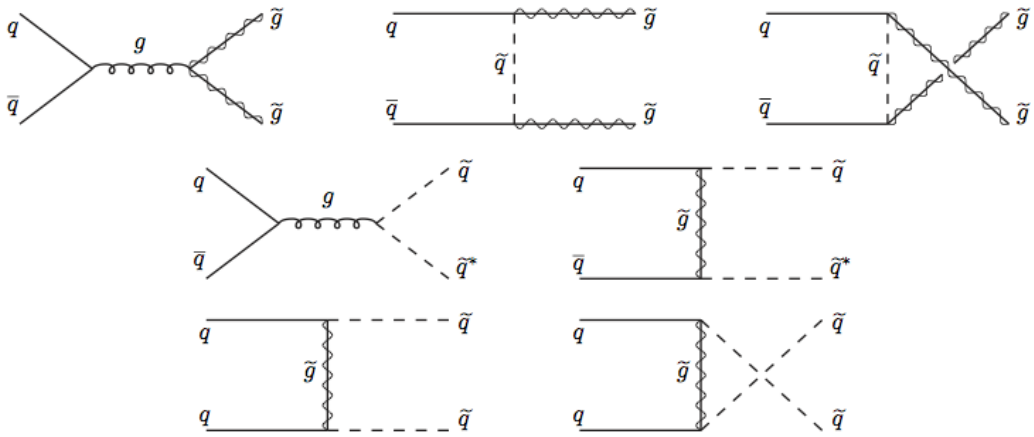

Figure 2.11: Feyman diagrams for quark-antiquark and quark-quark production of sparticles. Figure from Ref. [19].

We will now investigate the different SUSY production for the LM benchmark models specified in the previous section. Figure 2.12 shows the distribution of initial hard-scattering sparticles for different LM masses. For LM0-LM6, and LM8 the production of sparticles is dominated by $\tilde{q}\tilde{q}$ and $\tilde{q}\tilde{g}$. For LM7 and LM9 the paradigm is quite different. For these models the production is dominated by electroweak production and the initial sparticles are neutralinos or charginos more than 80 percent of the time. This happens because in both LM7 and LM9 the squark masses are very high compared to the gluino mass, and the neutralino

and chargino masses are low compared to the gluino mass.[7] The production then happens through an electroweak process such as $d\bar{u} \to \tilde{\chi}_i^0 \tilde{\chi}_j^-$.

Figure 2.13 shows the p_T distribution of the initial SUSY particles produced for different LM points. For the points besides LM7 and LM9 the distribution peaks at around 100 GeV to 200 GeV with a large tail. For LM7 and LM9 the peaks are at much smaller values and there are smaller tails. This is again due to the fact that these signal points are dominated by electroweak production. For electroweak production there has to be an anti-quark in the initial state, and since this anti-quark has to be a sea quark (as stated earlier) it will typically have less momentum and the initial SUSY particles will thus have less momentum.

2.3.5 Decay of SUSY into lepton plus $\not{E}_T$ and jets

Once SUSY particles are created, their decay is specified by the mass spectrum of sparticles, in particular the splitting of these masses, and the couplings. Though there are large variations in decay processes a few general comments can be made. For all the LM points the decay of the sparticles will result in two LSPs (due to R-parity) that interact weakly and thus will not interact with the detector (like neutrinos), creating missing transverse momentum. In addition,

[7] In LM7 the lowest squark mass is 1790 GeV whereas the gluino mass is 637 GeV and the neutralino and chargino masses are on the order of 100-400 GeV. For LM9 the lowest sqark mass is 882 GeV, the gluino mass is 488 GeV and the neutralino and chargino masses are on the order of 65-225 GeV.

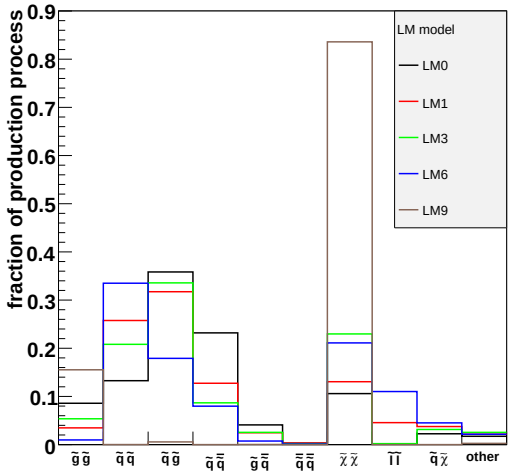

(a)

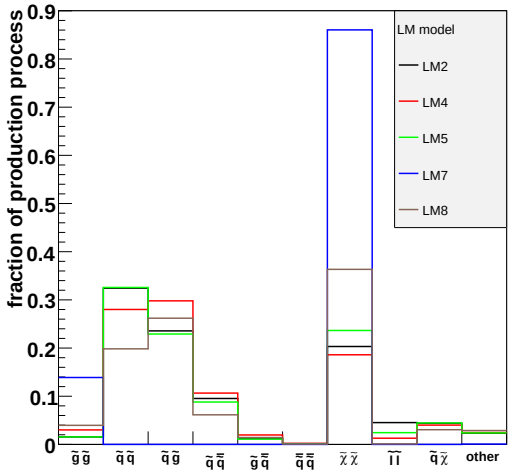

(b)

Figure 2.12: These plots show for $\sqrt{s} = 7$ TeV the distribution of SUSY particle types produced in the initial hard scattering process. For each model the total summed contribution is 1 and the y-axis gives the fraction of a certain process. (a) shows LM0, LM1, LM3, LM6, and LM9. (b) shows LM2, LM4, LM5, LM7, and LM8. All the models except LM7 and LM9 are dominated by strong production. LM7 and LM9 are dominated by weak production because in these models the squark masses are very high.

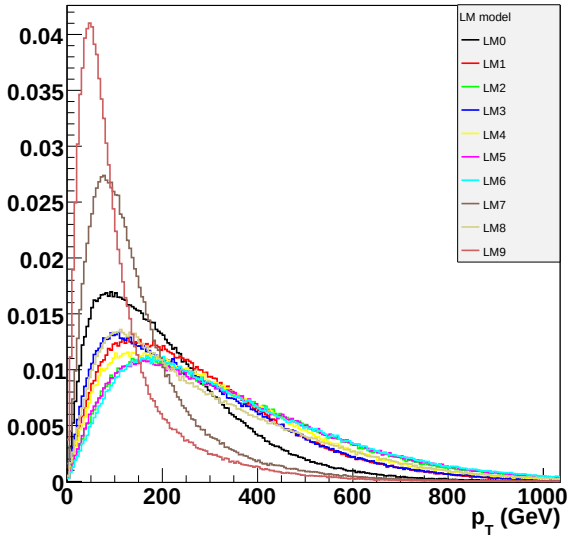

Figure 2.13: p_T distribution of the initial two SUSY particles for different LM points. For $\sqrt{s} = 7$ TeV.

most SUSY decays chains are somewhat long and thus produce a large number of jets. Thus, most SUSY searches at the LHC require looking for large missing transverse momentum after applying some requirement on the number of jets. For this paper we focus on requiring an additional observable, exactly 1 lepton in the event, where a lepton can either be a muon or an electron (taus are not considered for this paper). A typical Feynman diagram for the full SUSY production and decay giving a lepton, jets and missing transverse momentum is shown in Figure 2.14.

So how are charged leptons produced in SUSY? Figure 2.15 shows the mother particle of the muon in different SUSY LM benchmark points. There are two

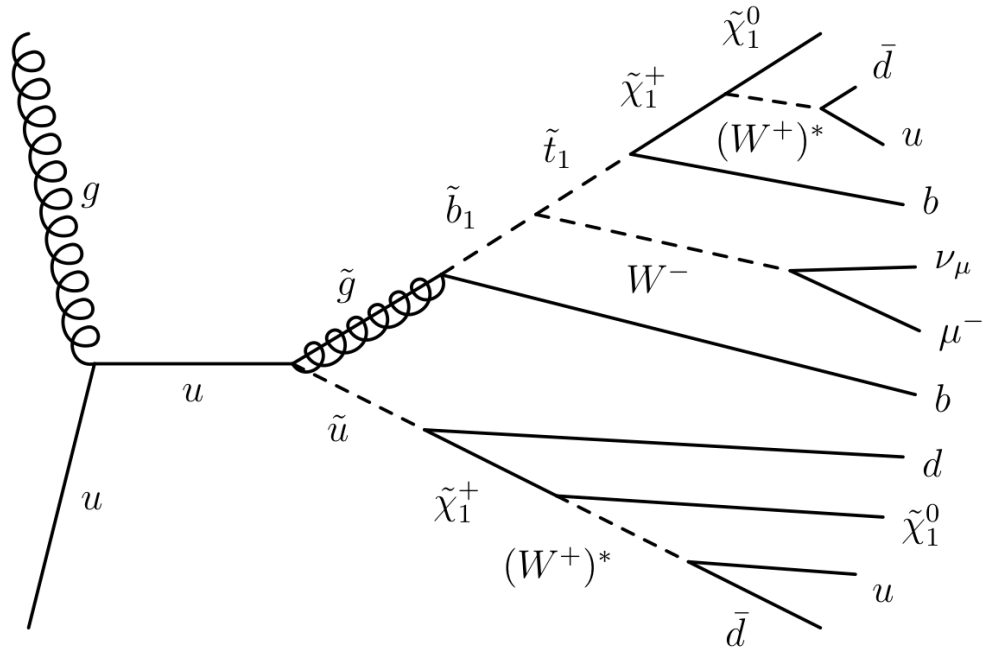

Figure 2.14: Typical SUSY decay chain for benchmark point LM0. The two W^+'s are off-shell W's, denoted by $*$. This decay would end up giving a lepton, missing transverse momentum (from the neutrino and the two LSPs), and some large number of jets (if each jet from a quark in this diagram were within detector acceptance and had a p_T above whatever threshold the analysis is using you could get 7 jets in this event!!).

typical classes, one where the muons are dominantly from a W or Z and one where the muons are dominantly from a chargino or neutralino. In addition some smaller amount of the time muons can also come from smuons (in LM6 this is a sizable contribution, approximately 35 percent of total). The decay processes to electrons is essentially the same as to muons and similar conclusions can be made.[8]

2.3.6 SM backgrounds to LHC single lepton SUSY searches

Though requiring a lepton reduces the number of SUSY events (because the efficiency to produce at least one lepton is on the order of ten percent) it can help with the background prediction. Leptons are generally clean signatures in the detector and can be used to reduce the QCD background, which generally has larger uncertainties than other SM backgrounds from electroweak and $t\bar{t}$ processes. These other SM backgrounds become dominant when you require a single lepton in the event.

Once requiring exactly one lepton, at least a few jets ($\geq$ 3), and some amount of missing transverse momentum ($\not\!\!E_T$), the dominant standard model backgrounds to SUSY searches at the LHC are $t\bar{t}$ and W+jets. Figure 2.16

[8]The muon and electron masses are so much smaller than all the sparticle masses. This means the fact that the muon mass is 200 times larger than the electron mass doesn't really matter. This is similar to the fact that the branching fraction for a W to an e or μ is essentially the same because the W is so much heavier than both the e and μ.

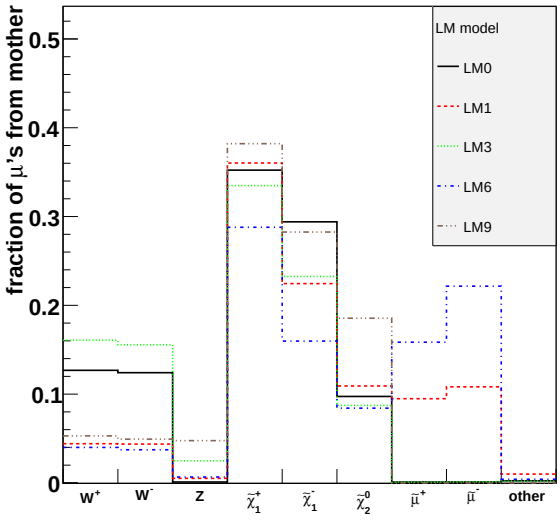

(a)

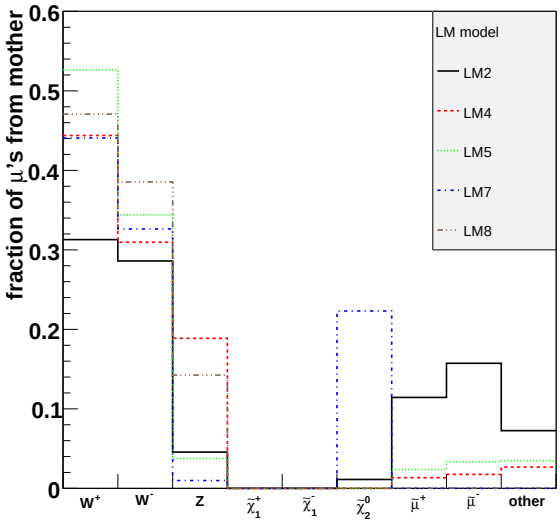

(b)

Figure 2.15: Distribution of the parent particle of the muon for different SUSY benchmark points. (a) LM0, LM1, LM3, LM6, LM9 (b) LM2, LM4, LM5, LM7, LM8.

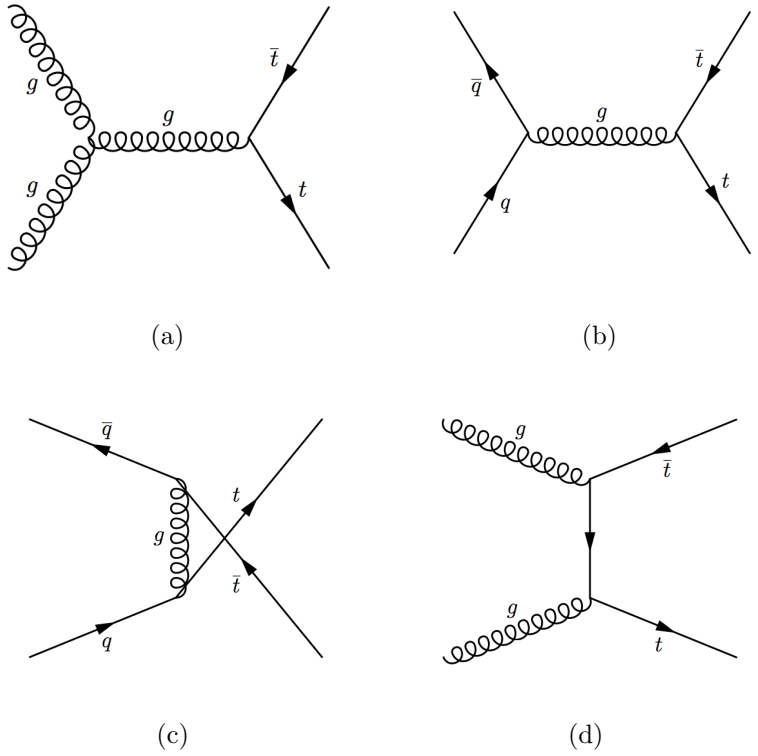

Figure 2.16: Tree-level diagrams for $t\bar{t}$. At the LHC (a) is the dominant production process, while (b) is the dominant production process at the Tevatron.

shows the Feynman diagrams for $t\bar{t}$ production at the LHC. The production of $t\bar{t}$ at the LHC is dominated by gluon-gluon fusion, in sharp contrast to production at the Tevatron where quark anti-quark annihilation dominates. Once the two top quarks are produced each decays to a b quark and a W boson. If one of the W boson decays to a lepton and a neutrino then there will typically be one lepton, four jets (two from the b quarks and two from the other W boson), and some amount of $\not\!\!E_T$ from the high p_T neutrino.

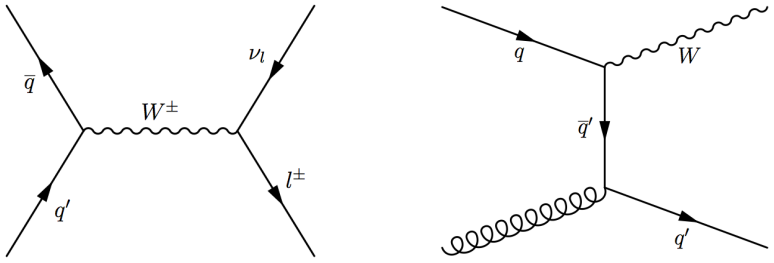

(a) (b)

Figure 2.17: Tree-level diagrams for W+jets.

The leading-order diagram for the other large SM background, W+jets, is shown in Figure 2.17. For this background, like for $t\bar{t}$, the lepton and neutrino come from a W boson and will produce the lepton and large $\not\!\!E_T$. For the leading-order diagrams in Figure 2.17 there will typically be only one or zero jets. However, initial or final state radiation or more complicated diagrams (i.e. loop diagrams) can give many more jets along with the W boson.

Chapter 3

Experimental Hardware

3.1 Large Hadron Collider

The Large Hadron Collider (LHC) was built to probe physics at the TeV energy scale, including for instance the mechanism for electroweak-symmetry breaking (which can be explained by the Higgs mechanism). In addition, there are many other extensions of the standard model theory that have not been seen by previous experiments but could manifest themselves at the higher energy regions explored by the LHC.[1] The LHC was designed to collide two beams of protons or heavy ions (hence the name hadron collider) with a beam energy[2] (7 TeV) and luminosity (10^{34} cm^{-2} s^{-1}) 7 and 100 times larger, respectively, than any other previous hadron collider.[3] For part of the year (on average about one

[1] One example is supersymmetry, which is described in Sec. 2.3.

[2] The LHC is currently running at a energy of 3.5 TeV per beam. The plan is to reach 7 TeV per beam in 2014.

[3] The closest being the Tevatron at Fermilab that collides protons and anti-protons with a beam energy of 980 GeV and $\sqrt{s} = 1.96$.

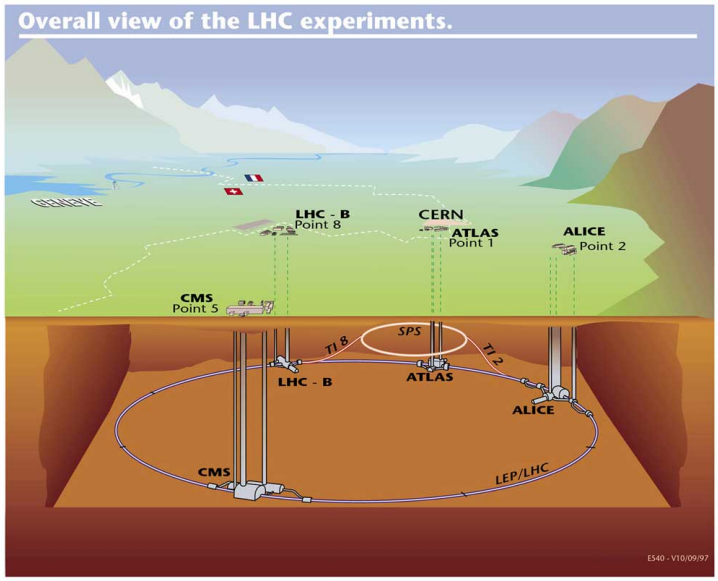

Figure 3.1: Schematic (not to scale) showing the different detectors at the LHC. From Ref. [29].

month) the LHC will also collide high energy heavy-ion beams to investigate the quark-gluon plasma which existed in the early universe.

The LHC lies just outside Geneva, Switzerland on the French-Swiss border at the CERN laboratory. Figure 3.1 shows a schematic of the LHC, which has a circumference of 27 km. Radiofrequency (RF) cavities accelerate the protons along the beam direction and magnets steer the protons along the loop and keep the beam focused. The combination of the powerful magnets and large circumference make it possible to keep the high-energy protons circling around the collider (if a larger circumference were used the strength needed for the magnets would be less). To facilitate the construction of the LHC the accelerator

machine was built in the already existing tunnel used for the Large Electron-Positron Collider (LEP), which stopped running in 2001. The tunnel is on average 100 meters underground to prevent cosmic radiation from hitting the detectors and also to prevent any radiation from the machine and experiments from reaching ground level and having a harmful environmental impact.[4]

There are 1232 dipole magnets that steer the protons around the 27 km loop. At a beam energy of 7 TeV the magnetic field strength of these magnets is roughly 8 Tesla (T). An additional 392 quadrupole magnets keep the beam focused. Superconducting magnets are used to reach the high field strength[5] and liquid helium is used to keep the magnets at their operating temperature of 1.9 K. The proton beams are in a vacuum with a pressure of approximately 10^{-7} Pascals (Pa), approximately 10 times less than the pressure on the moon. The low pressure is necessary to avoid collisions between the protons and gas molecules in the beam pipe. Closer to the interaction points the pressure is even less, approximately 10^{-9} Pa.

The proton beams are made up of bunches of protons, where at design luminosity the bunches will be separated by 25 ns or 7 m (the protons are traveling at essentially the speed of light), with 2808 bunches per beam. In some cases

[4]In fact, another reason to build it underground is that it is a lot cheaper to build a tunnel than buy the equivalent land above ground.

[5]Non-superconducting magnets would use a lot more energy and would be much harder to cool.

the bunch distance is larger than 25 ns to allow for beam dumping if there is a problem. Each bunch has 1.1 x 10^{11} protons and bunches from two different beams are collided at four different interaction points around the machine where the major detectors are placed. Figure 3.1 shows the four different major detectors: ATLAS, CMS, LHCb and ALICE. ATLAS and CMS are general purpose detectors that can perform many general physics searches and complement each other. ALICE is designed specifically to study the heavy-ion interactions and LHCb is designed to study rare b-hadron decays to measure the CP-violating processes.

3.2 Compact Muon Solenoid

3.2.1 Overview

The Compact Muon Solenoid (CMS) is designed to measure the many different highly energetic particles coming from the interaction point of the proton beams. The detector is massive, with a diameter of 14.6 m, length of 21.6 m, a weight of 12,500 tons, and more iron than the Eiffel Tower. This large a detector is needed to accurately measure the momentum and energy of the particles while also containing most of the particles.[6]

[6]As we will see later in this section containment is important for measuring the particles' energy correctly and also to be able to differentiate muons from other particles.

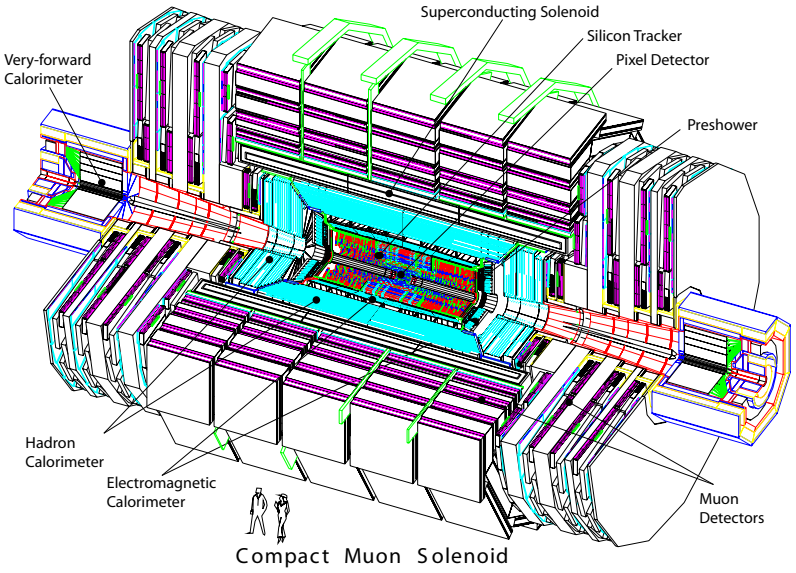

Figure 3.2: Schematic showing an expanded view of the CMS detector. Figure from Ref. [30].

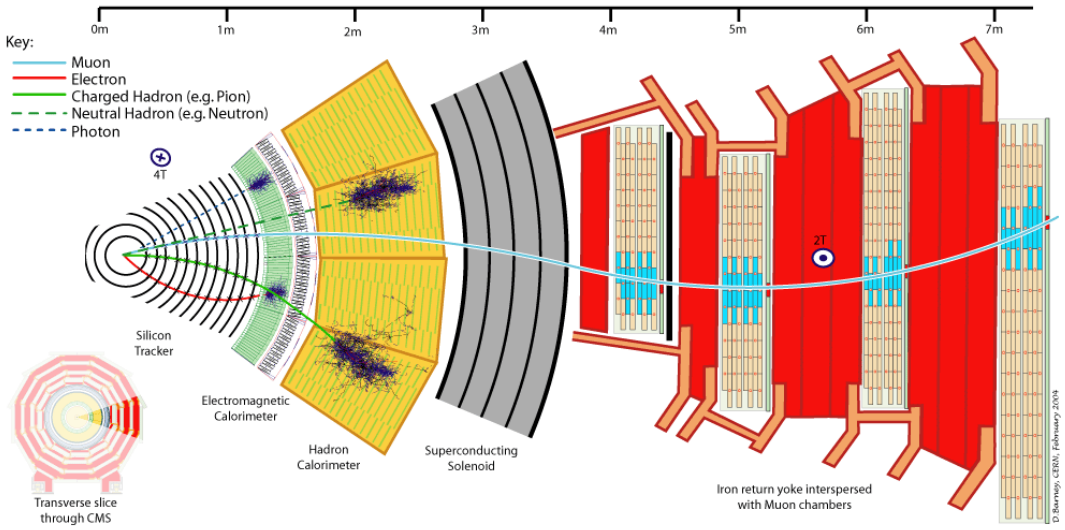

Figure 3.3: Schematic showing a transverse slice of the CMS detector. An overview of where different particles are measured in the detector is shown. From Ref. [31]. An interactive version of this schematic is shown in Ref. [32].

The layout of the CMS detector is strongly constrained by the superconducting solenoid magnet. To obtain the best resolution on the particle's momentum the strongest possible magnet was used (in fact CMS has the largest superconducting magnet ever built). The CMS magnet is 13 m long with a inner diameter of 5.9 m[7] and design strength of 4 T.[8]

The tracker and calorimeter system are inside the CMS magnet. Figure 3.2 shows a schematic of the CMS detector, and Figure 3.3 shows a transverse slice of the detector and how different particles go through the detector. As particles leave the interaction point they first hit the tracker, which measures the momentum of charged tracks. The tracker is not meant to stop the particles. In fact it is designed to have as little material as possible so that the momentum measurement is not effected by interactions of the particles with the tracker material. Outside of the tracker is the electromagnetic calorimeter, which stops electrons and photons and measures their energy. The hadronic calorimeter, which lies right outside the electromagnetic calorimeter stops hadronic particles and measures their energy. The calorimeters allow for the inference of neutrinos or other weakly interacting particles (such as the lightest supersymmetric particle (LSP)

[7]For the sake of efficiency the magnet was not built at CERN. However, in order for it to be transferred to Cessy, where CMS is located, it had to be less than 7 m in diameter so it could fit through the streets.

[8]The actual magnetic field value used for CMS is slightly less, 3.8 T. The lower value is used for safety reasons.

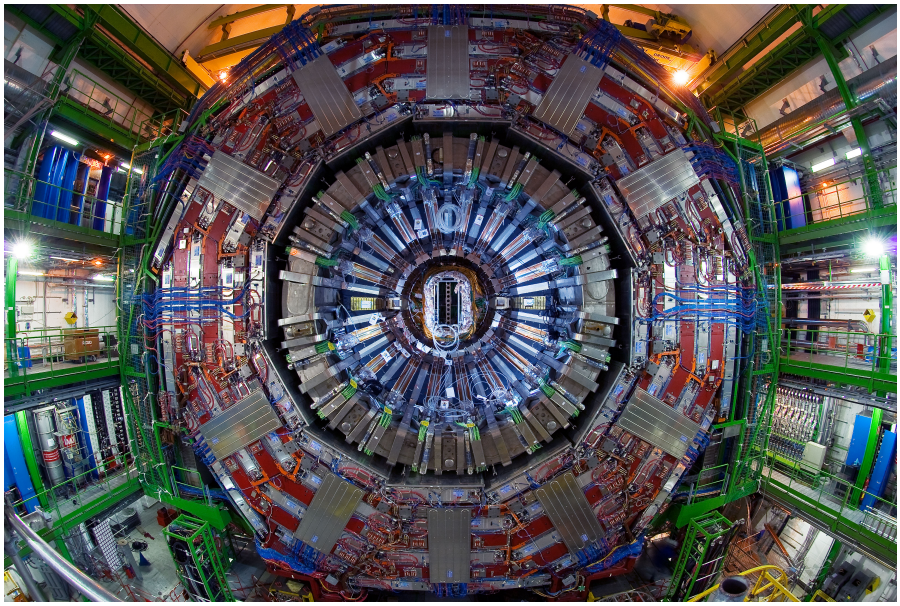

Figure 3.4: Barrel of the CMS detector. From Ref. [33].

in SUSY models), which will show up as an imbalance of momentum transverse to the beam direction.

The calorimeters stop essentially all known particles except for neutrinos and muons (there is a small probability that a hadron will make it all the way through the calorimeter to the muon system). The last part of the CMS detector is the muon detector system, which lies outside the solenoid and measures the presence of muons.[9] Figure 3.4 shows a picture of the barrel of the CMS detector (the

[9]If you are wondering why such a large part of the detector is devoted to a single particle, muons, it is because they are very important objects for many different physics analyses. This is because muons indicate an electroweak process since they don't interact via the strong force.

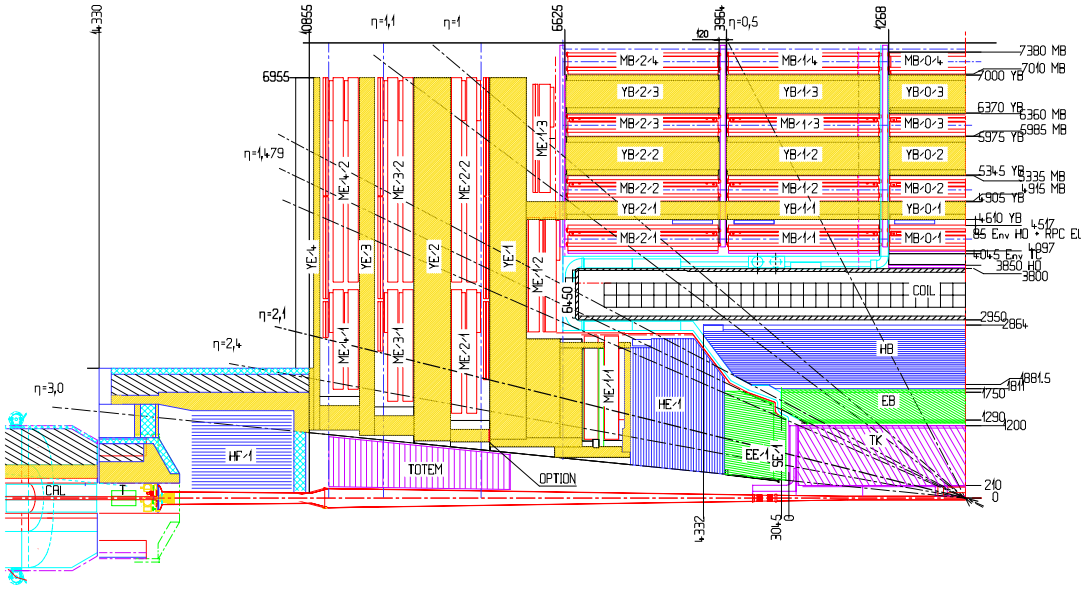

Figure 3.5: One quarter longitudinal view of the CMS Experiment. Dimensions are in mm. Figure from Ref. [30].

CMS detector is divided up into the barrel and two endcaps in order to give as full coverage as possible).

Figure 3.5 shows a technical layout of the different sub-detector components, which will each be described in detail throughout the rest of this chapter.

3.2.2 Silicon tracking system

The innermost part of the CMS detector is the tracker, so called because it tracks the trajectories of charged particles as they leave the interaction point. As a charged particle traverses the tracker it deposits energy in each layer of the

tracker (these deposits are called hits) and a trajectory of the particle is built, called a track. The magnetic field bends this track and makes it possible to measure precisely the momentum of the particle.[10] Specifically, the tracker measures precisely the momentum of high-energy electrons, muons and charged hadrons. In addition, long-lived b-quarks will decay in the tracker and the displacement of the tracks from this decay can be used to identify b-jets.

The design of the tracker is motivated by a few points. The tracker needs to have good position resolution and fast response time but also be light enough to not disturb the particles path as they traverse the tracker (through for instance inelastic scattering off a nucleus). The tracker is made of silicon semiconductor devices, which satisfy these criteria. The silicon modules are essentially solid-state ionization chambers. As a charged particle traverses the device, it ionizes electrons off the lattice, creating electron/hole pairs that are guided by an electric field to electrodes and then read out as an electric signal.

Since the tracker is the part of the detector closest to the interaction point it must also be able to withstand large particle fluxes. The high magnetic field and steeply falling p_T distribution of particles from the interaction means that the track density falls rapidly with an increasing radius from the interaction point.

[10]For instance, the transverse momentum of the track is directly related to the track curvature by the following equation: $p_T(\mathrm{GeV}) = 0.3 * \mathrm{B(T)} * \mathrm{r(m)}$, where $B(\mathrm{T})$ is the magnetic field strength in Tesla, and r is the radius of curvature of the track in meters.

The tracker has been designed for a maximum occupancy of approximately 3% per LHC crossing.[11] To keep the occupancy low, the tracker is divided up to essentially three regions where slightly different technologies and geometrical configurations are used. In the part of the tracker closest to the interaction point ($r < 10$ cm), where the particle flux is the highest, silicon pixel detectors are used with a size of 100 x 150 μm^2, giving an occupancy of approximately 10^{-4} per LHC crossing. In an intermediate region between radius 20 cm to 55 cm, silicon strip detectors with a minimum cell size of 10 cm x 80 μm are used, giving an occupancy of approximately 2-3% per LHC crossing. Lastly, in the outermost region of radius 55 cm to 110 cm, silicon strip detectors with a larger pitch are used, with a maximum cell size of 25 cm x 180 μm, keeping the occupancy to approximately 1% per LHC crossing.

The total area of the pixel detector is 1 m^2, and the total area of the silicon strip detector is 200 m^2. The coverage of the tracker extends to $|\eta| < 2.4$. Figure 3.6 shows a schematic picture of the tracker layout (the pixel detector layers are not shown in this figure). The outer radius extends to nearly 110 cm and the total length is approximately 540 cm. The pixel detector has 3 barrel layers with 2 endcap disks on each side. Table 3.1 gives the location of the different pixel barrel and endcap layers with respect to the center of the

[11] During heavy ion running the occupancy will be much larger and will be up to 20% in outer parts of the tracker.

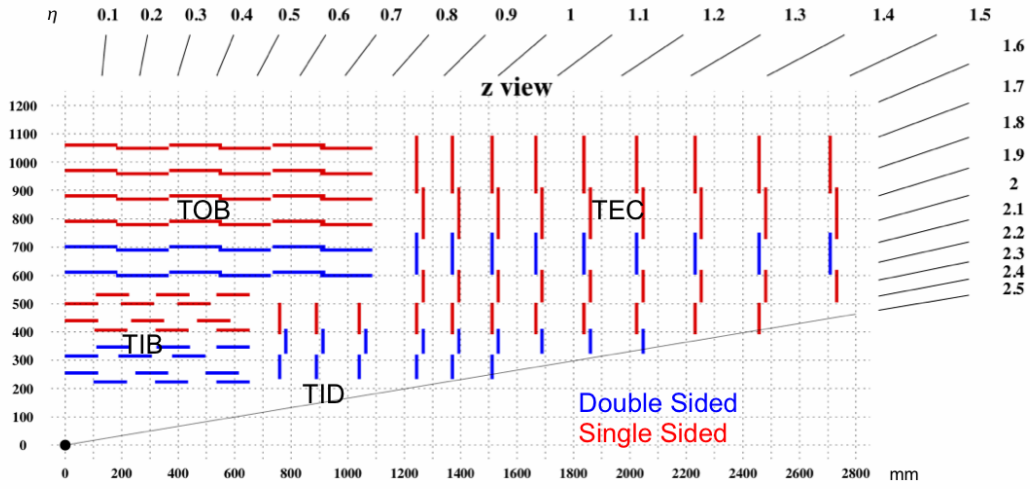

Figure 3.6: Schematic showing the layout of the tracker and the different layers. Double-sided layers are shown in blue and single-sided layers are shown in red. The double-sided layers are there to provide improved position measurement. Units on the x-axis and y-axis are in mm. Original figure from Ref. [34].

Table 3.1: Location of pixel detector layers with respect to the center of the detector. From Ref. [30].

Barrel Layer	radius (cm)	length (cm)
Layer 1	4.4	53
Layer 2	7.3	53
Layer 3	10.2	53
Endcap Layer	radius (cm)	z (cm)
Layer 1	6-15	34.5
Layer 2	6-15	46.5

detector. Figure 3.7 shows one pixel module and the installation of the forward pixel detector. There are 768 pixel modules in the barrel and 672 pixel modules in the endcap disks.

The silicon strip tracker has several different components, the tracker inner barrel (TIB), the tracker outer barrel (TOB), the tracker end cap (TEC), and the tracker inner disks (TID). The TIB makes up the first 4 layers of silicon modules in the barrel, whereas the TOB makes up the remaining 6 layers. The TEC comprises 9 disks that extend from the region 120 cm $< |\eta| <$ 150 cm and the TID comprises 3 small disks that fill the area between the TIB and the TEC.

The silicon strip tracker consists of roughly 15400 modules, where each module is composed of two silicon wafers (the size of the wafers is roughly 15 cm x 15 cm), a harness, and readout electronics. Figure 3.8 shows the various single silicon strip modules in the TEC and TOB. Table 3.2 breaks down the number

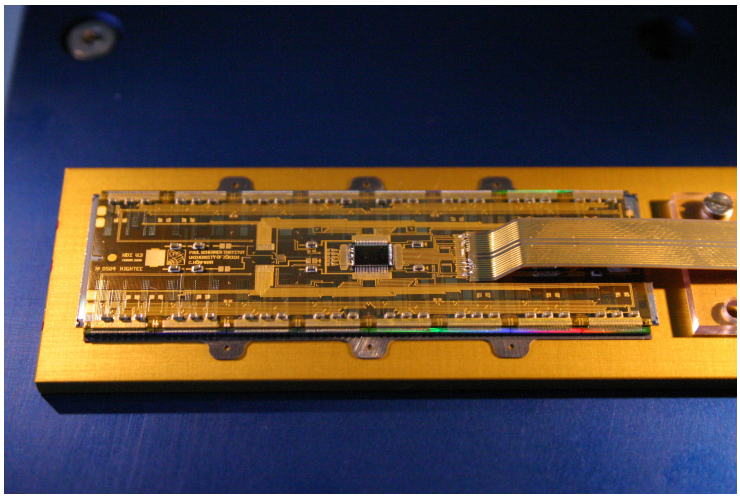

(a)

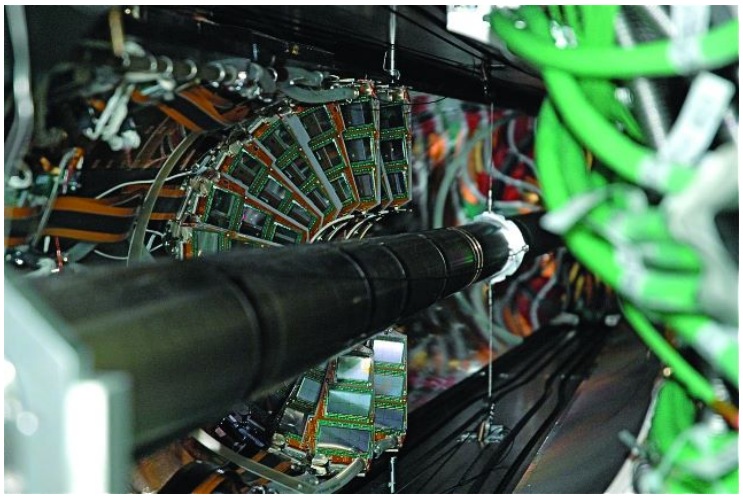

(b)

Figure 3.7: (a) Single pixel module (from Ref. [30]), (b) installation of the pixel endcap disks (from Ref. [33]).

Table 3.2: Detector Types. From Ref. [30].

part	No. modules	thickness (μm)	mean pitch (μm)
TIB	2724	320	81/118
TOB	5208	500	81/183
TID	816	320	97/128/143
TEC inner	2512	320	96/126/128/143
TEC outer	3888	500	143/158/183

of modules, the thickness of the modules, and mean pitch of the strips for each of the different tracker components. The innermost part of the tracker, namely the TIB, TID, and TEC have smaller mean pitch than the outermost part of the tracker due to the higher number of particles traversing this part of the tracker. Since the mean pitch and strip length is larger in the outer part of the tracker the thickness of the silicon wafer has been increased to maintain a good S/N ratio.

To improve the measurement in the $r-\phi$ and $r-z$ coordinates some of the layers of the tracker are double-sided with two modules back-to-back in a single layer. The angle between the two modules is 100 mrad. Figure 3.6 shows the layers that are double-sided, including the first two layers of the TIB, the first two layers of the TOB, the first two rings of the TID, and the innermost 2 rings and fifth ring of the TEC. The double-sided layers lead to a single point

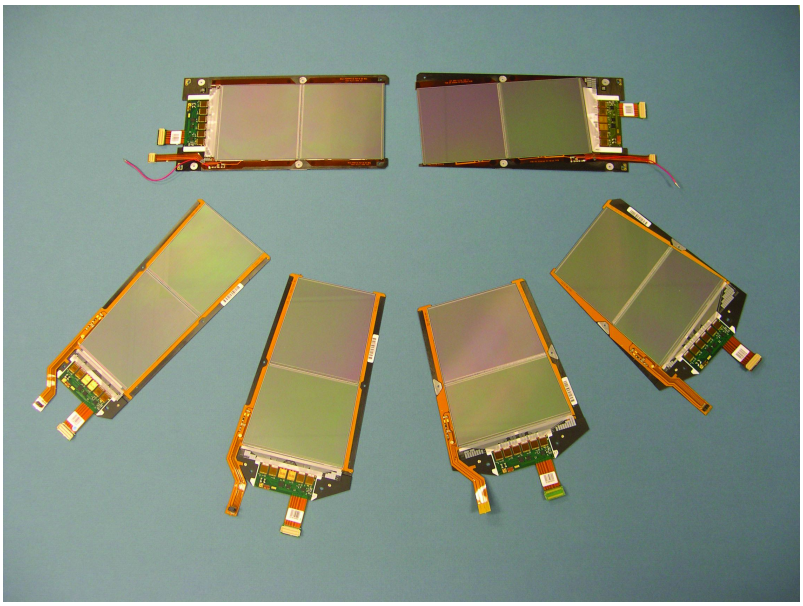

Figure 3.8: Different silicon modules in the tracker. Each module consists of two silicon wafers that are wire-bonded together, a harness, and readout electronics. The upper two modules are from the TOB and their length is approximately 25 cm. The upper right module is tilted with respect to the upper left module and used in the double-sided layers to obtain a more precise position measurement. The lower four modules are from the TEC and have different length and size depending on their location in the TEC. From Ref. [33].

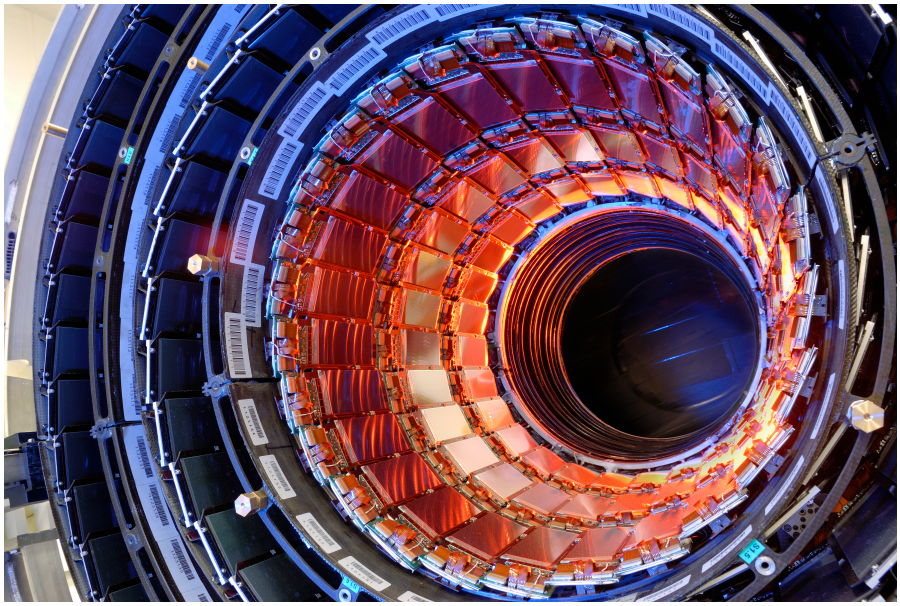

Figure 3.9: First three layers of tracker inner barrel. From Ref. [35].

resolution in the TIB (TOB) of between 23–34 (35-52) μm in the $r-\phi$ direction and 230 (530) μm in the z direction.

Figure 3.10 shows the performance of the tracker for single muons with transverse momenta of 1, 10, and 100 GeV. For a 10 GeV muon the transverse momentum resolution is approximately 1%. The resolution on the transverse momentum decreases as the momentum of the muon increases because with higher momentum the track has less curvature. Other track parameters such as the transverse impact parameter and longitudinal impact parameter also have decreasing resolution as the muon momentum increases.

For more information on the tracker in CMS see Refs. [36],[37], and [30].

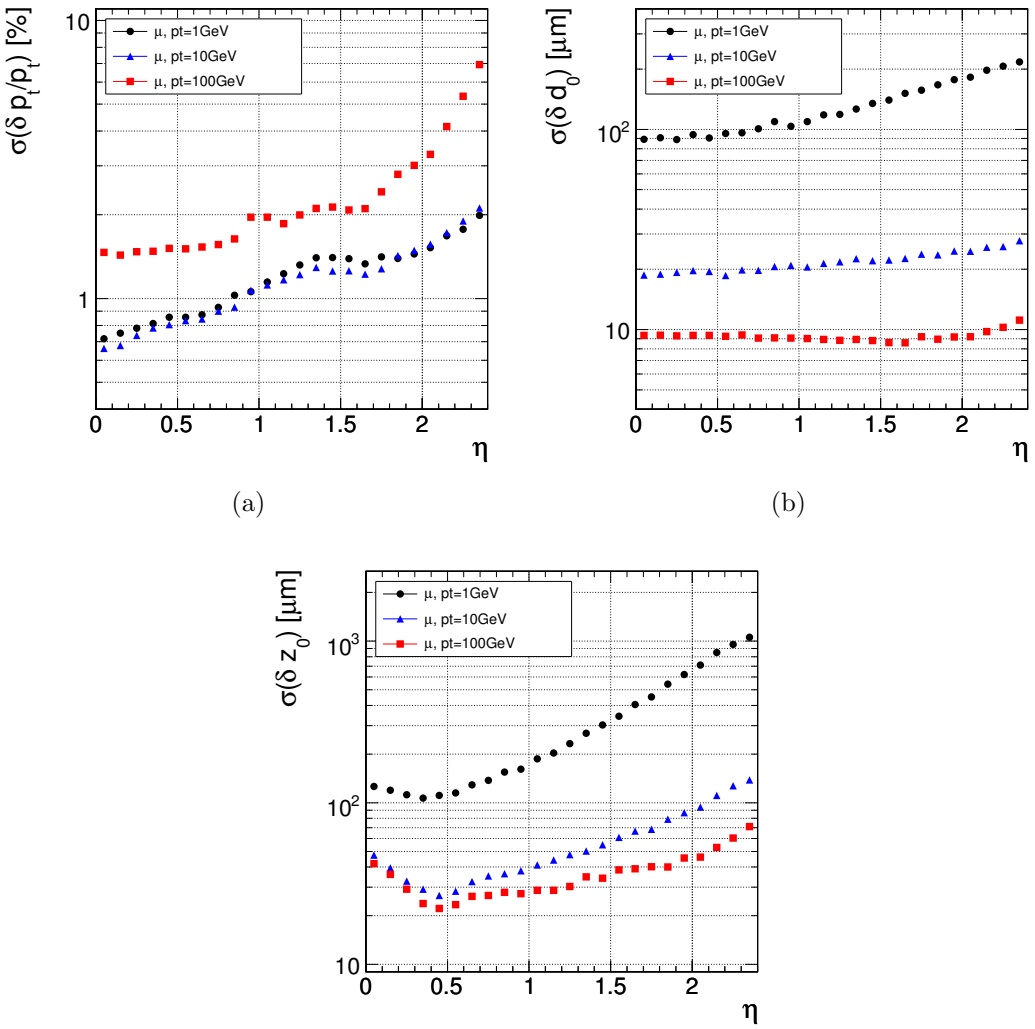

Figure 3.10: Resolution of different track parameters as a function of η: (a) transverse momentum, (b) transverse impact parameter, and (c) longitudinal impact parameter. Figures from Ref. [30].

3.2.3 Electromagnetic calorimeter

The electromagnetic calorimeter (ECAL) uses lead tungstate ($PBWO_4$) scintillating crystals with the main purpose of precisely measuring the energy of electrons and photons. As the electrons and photons traverse the ECAL they interact with the heavy nuclei in the crystals, creating a shower of lower energy photons and electrons via pair production and bremsstrahlung. Once the energy of the electrons and photons is below some critical energy they no longer shower, but deposit energy in the lead tungstate via ionization and excitation of electrons. This energy is then transferred to the luminescent center of the crystal and photons are released ("scintillated"). The light is produced in short bursts of photons[12] that are read out by photodetectors and proportional to the particles energy. An important feature of the ECAL is that it must be kept at the same temperature ($\pm 0.05\%$) because the light output decreases as the temperature increases.

Lead tungstate is a dense material (density = 8.28 g/cm^3) with a short radiation length (X_0=0.89 cm) and short Moliere radius (2.19 cm). The radiation length is the appropriate scale for measuring high energy electromagnetic cascades and is the mean distance over which a high energy electron loses 1/e of its energy by bremsstrahlung or 7/9 the mean free path for pair production by a

[12] About 80% of the light is emitted in 25 ns.

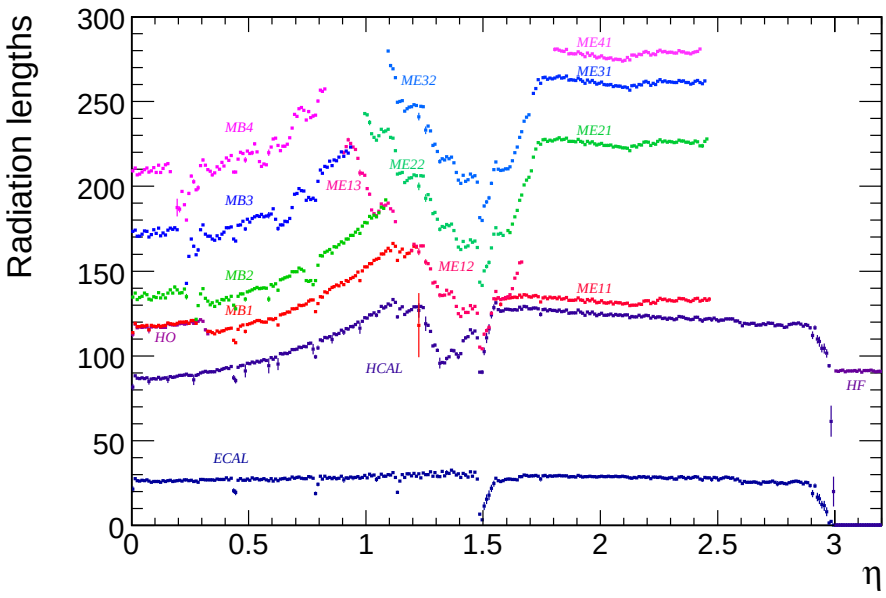

Figure 3.11: Material thickness in radiation lengths after the ECAL, HCAL and at the depth of each muon station. Figure from Ref. [30].

high-energy photon [30]. The Moliere radius is the radius of a cylinder where on average 90% of the electromagnetic cascade is contained. Thus a short radiation length means the ECAL can be compact and the short Moliere radius means it can have fine granularity. The dimensionless quantity X_d/X_0, where X_d is the thickness of a detector component, gives a measure of the detector thickness in terms of EM interactions. Figure 3.11 shows the material thickness in radiation lengths after each of the calorimeters and the muon stations as a function of η.

Figure 3.12 shows a single lead tungstate crystal being assembled. The ECAL has 61200 crystals mounted in the central barrel region of the detector ($|\eta|$ <1.479) and 7324 crystals mounted in each of the endcaps (1.479 < $|\eta|$ <

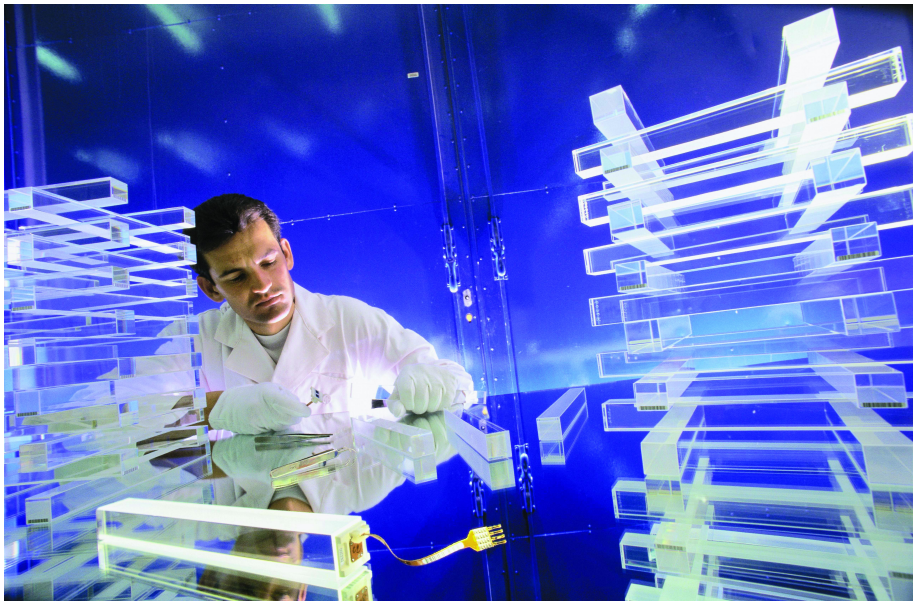

Figure 3.12: Single crystal from ecal endcap. From Ref. [30].

3.0). Figure 3.13 shows the geometry of the ECAL in y-z plane. The crystals in the barrel are 22 x 22 mm^2 at the front face and 26 x 26 mm^2 at the rear face. In the barrel the crystal length is 230 mm, which corresponds to a dimensionless radiation length of 25.8. The center of the front face of the crystals in the barrel are at a radius of 1.29 m from the the beamline. In the endcap the crystals have a slightly larger cross section, 28.6 x 28.6 mm^2 at the front face and 30 x 30 mm^2 at the rear face. However, the endcap crystals have a slightly smaller length, 220 mm, which is due to the presence of the preshower (3 X_d/X_0) in the endcap. The preshower is placed in front of the endcap to help identify neutral pions and also to improve the position measurement of electrons and photons.

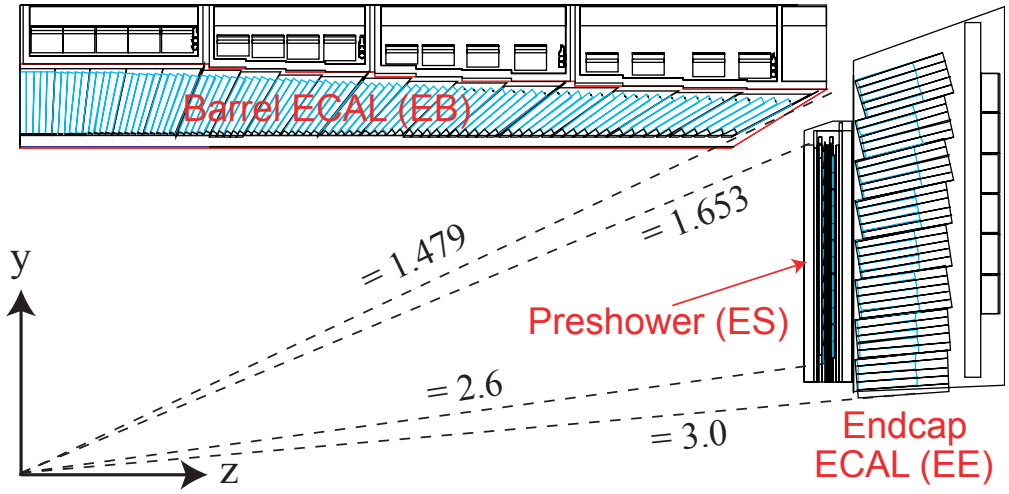

Figure 3.13: Transverse section through the ECAL, showing the geometrical configuration. Figure from Ref. [30].

The lead tungstate crystals emit blue-green scintillating light at a broad maximum of 420 nm. However, the light output of lead tungstate is rather low compared to other inorganic crystal scintillators. Precise photodectors that can work in a large magnetic field are needed. In the barrel the photodectors used are avalanche photodiodes (APDs). Each APD has an active area of 5 x 5 mm^2 and two are glued to the back of each crystal. In the endcap the photodectors used are vacuum phototriodes (VPTs) which each have a diameter of 25 mm. A single VPT is glued to the back of each crystal. VPTs are chosen for the endcap because they can withstand the large neutron flux, while the APDs are much more sensitive to ionizing radiation.

Figure 3.14 shows the ECAL energy resolution as a function of the electron energy in a test beam. The resolution can be parameterized as a function of energy using the following equation:

$$(\frac{\sigma}{E})^2 = (\frac{S}{\sqrt{E}})^2 + (\frac{N}{E})^2 + C^2, \tag{3.1}$$

where S is the stochastic term, N is the noise term, and C is the constant term. The parameter's values after fitting to data are shown in Figure 3.14, where S is approximately 3%, N = 124 MeV, and C = 0.26%. The resolution of the ECAL is quite good, with high energy electrons ($E > 100$ GeV) having a energy resolution of less than 0.5%.

More detailed information on the ECAL can be found in Refs. [38], [39], and [30].

3.2.4 Hadronic calorimeter

The purpose of the hadronic calorimeter (HCAL) it to measure the energy of hadrons, particles made up of quarks and gluons, and also to infer the presence of weakly interacting particles, which do not deposit energy in the calorimeter. The missing transverse energy, which measures the imbalance of energy in the transverse plane with respect to the beamline[13], can be used to detect the

[13] A precise definition of missing transverse energy is given in Sec. 4.4.

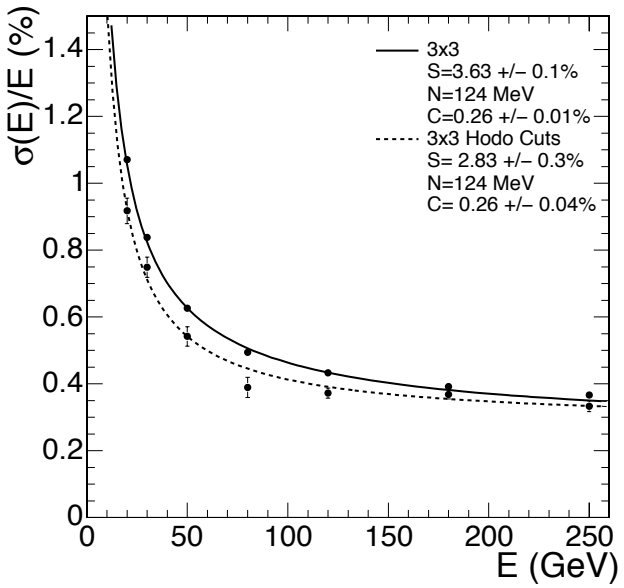

Figure 3.14: Resolution of ECAL supermodule as a function of energy. A supermodule is a cluster of many crystals. The barrel section of the ECAL has 36 identical "supermodules". The energy was measured in an array of 3 x 3 crystals with electrons impacting the central crystal. The upper series of points corresponds to events taken with a 20 x 20 mm^2 trigger and the lower series corresponds to events selected to fall within a 4 x 4 mm^2 region. From Ref. [30].

presence of neutrinos or new physics with weakly-interacting particles.[14] To increase the resolution on the missing transverse energy it is important to make the calorimeter as hermetic as possible. Other important design features include fine transverse granularity, minimizing non-Gaussian tails in the energy resolution, and containment of the hadronic shower.

As a hadron traverses the HCAL it will interact strongly with the absorbing material in the HCAL and initiate a shower of particles that can be used to measure the energy of the incident hadron. The interactions of the hadron in the HCAL are characterized by the nuclear cross section, and the relevant variable is the interaction length, λ_{int}. The interaction length is defined to be the mean free path between inelastic collisions and the probability for a hadron to have a nuclear interaction is $P = 1 - e^{-(\mathrm{X_d}/\lambda_{\mathrm{int}})}$, where $\mathrm{X_d}$ is the distance traveled by the particle. A shorter interaction length is optimal for the HCAL since it means a higher probability for an inelastic collision. Thus, a hadron will have to traverse less material before starting a shower. The dimensionless quantity $\mathrm{X_d}/\lambda_{\mathrm{int}}$ gives a measure of the detector thickness in terms of strong interactions. Figure 3.15 shows the material thickness in interaction lengths after each of the calorimeters and muon stations and as a function of η. Since the ECAL has

[14] One example is R-parity conserving supersymmetry, where the lightest supersymmetric particle is usually weakly-interacting and can create a large amount of missing transverse energy.

some material thickness the hadrons will deposit energy in the ECAL before they reach the HCAL.[15] The probability for a hadron to have a nuclear interaction in the ECAL is roughly $P = 1 - e^{-1} = 0.63$ (where the 1 in the exponential comes from the amount of dimensionless interaction lengths in the ECAL). Though this might seem like a large probability, even if a hadron has a nuclear interaction by the time it leaves the ECAL the full hadronic shower will take longer to develop and will not be contained in the ECAL. Thus, the majority of the energy from the hadron is within the HCAL. The probability for a hadron to have a nuclear interaction in the HCAL is roughly $P = 1 - e^{-10} = 0.99995$.[16]

The HCAL consists of several different components including the hadronic barrel (HB), hadronic endcap (HE), hadronic outer (HO), and the forward hadronic (HF) calorimeters. The hadronic barrel (HB) and hadronic endcap (HE) cover the $|\eta| = 0 - 3$ region, and the gap between the HB and HE is inclined at 53 degrees and away from the center of the detector so that the HB and HE are essentially joined hermetically.[17] The HO is an additional calorimeter in the central region ($|\eta| < 1.26$) that is outside of the solenoid and is used to measure any energy leaks out of the back of the hadronic barrel. The HF was designed to increase the hermicity of the HCAL by covering the region from

[15] In fact the tracker has some material thickness that is roughly 20-40% that of the ECAL and must be taken into account as well.

[16] Though of course the probability to create a shower and contain the shower is not this high.

[17] This incline between the HB and HE is shown in Figure 3.5.

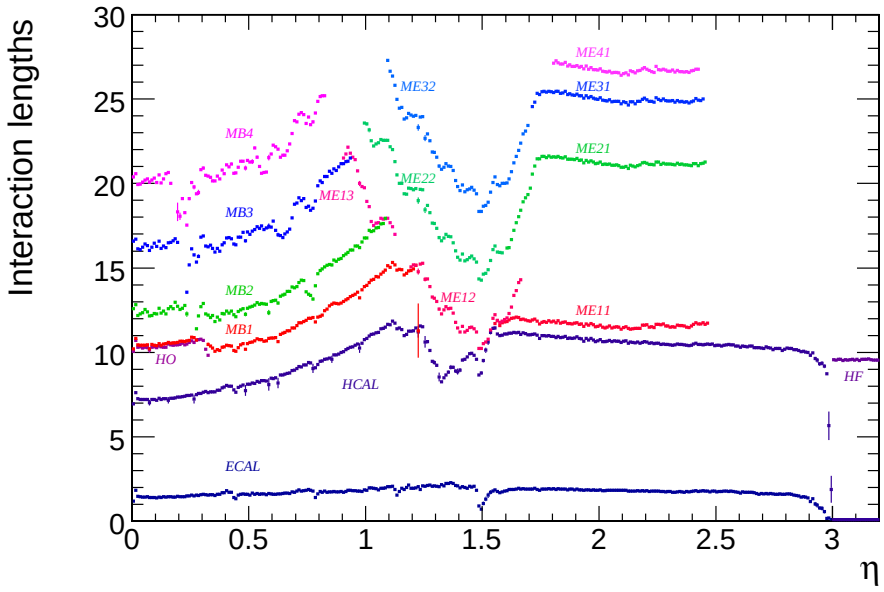

Figure 3.15: Material thickness in interaction lengths after the ECAL, HCAL and at the depth of each muon station. Figure from Ref. [30].

$|\eta| = 3 - 5$. The location of the different calorimeters within the detector is shown in Figure 3.5. The HCAL completely surrounds the ECAL and the HB and HE are fully immersed in the high magnetic field of the solenoid.

Brass is chosen as the main absorbing material for the HB and HE because it has a relatively short interaction length, it is non-magnetic, and it is easy to machine. The brass used is a copper alloy with 90% copper and 10% zinc. This is chosen instead of pure copper due to its better machinability. Brass was also chosen because of its shorter interaction length than for instance iron (15 cm for copper vs. 17 cm iron), which allows for more dimensionless interaction lengths packed within the solenoid magnet. Much of the brass for the HCAL was taken

Figure 3.16: Russian workers sitting on artillery shells used to produce some of the brass absorber material. These artillery shells are from WW II and were obtained from the Russian Navy. From Ref. [33].

from Russian artillery shells from World War II, shown in Figure 3.16. This brass was very high quality and over 1 million shells were melted to produce some of the absorber material used in the hadronic calorimeter.

To provide good containment of the hadronic showers in the HB and HE, the maximum amount of absorber (brass) is used with the minimum amount of space devoted to the active medium (plastic scintillator tiles) which measures the energy. The HB and HE hadronic calorimeters are sampling calorimeters that alternate layers of absorber and scintillator.[18] As a particle passes through

[18]The makeup of the HO and HF are slightly different and are described below.

the absorber it produces a shower of particles, and the particles' energy is measured as a rapid light pulse in the scintillator. This light pulse is read out with special fiber optics and then carried to a photodection readout system, hybrid photodiodes (HPDs).

The HB covers the η range from 0 to 1.4 and has two half barrels each composed of 18 identical 20 degree wedges in ϕ. Each wedge weighs approximately 26 tons and Figure 3.17 shows a half barrel of the HB with the 18 wedges labeled. Each wedge consists of 17 active plastic scintillators interspersed between the absorber, which is either brass or steel. The innermost and outermost absorbers of each wedge are stainless steel for structural strength. The rest of the absorbers are brass and there is 50–56.5 mm of brass interspersed with 3.7 mm of scintillating plastic. The lateral granularity of the HB is $\delta\eta$ x $\delta\phi$ = 0.087 x 0.087, which matches the granularity of the ECAL (though the granularity of the HB is exactly 5 times worse than the granularity of the EB). The innermost position of the HB is 1777 mm from the beamline and the outermost position is 2876.5 mm, leaving about a meter of material for the hadrons to shower in.

The HE covers the η range from 1.3 to 3.0 and in each endcap there are 18 wedges to match the composition of the HB. The basic makeup of the HE is very similar to the HB though the HE is composed entirely of brass absorber plates. The HE has 19 active scintillator layers for each wedge, where the thickness of

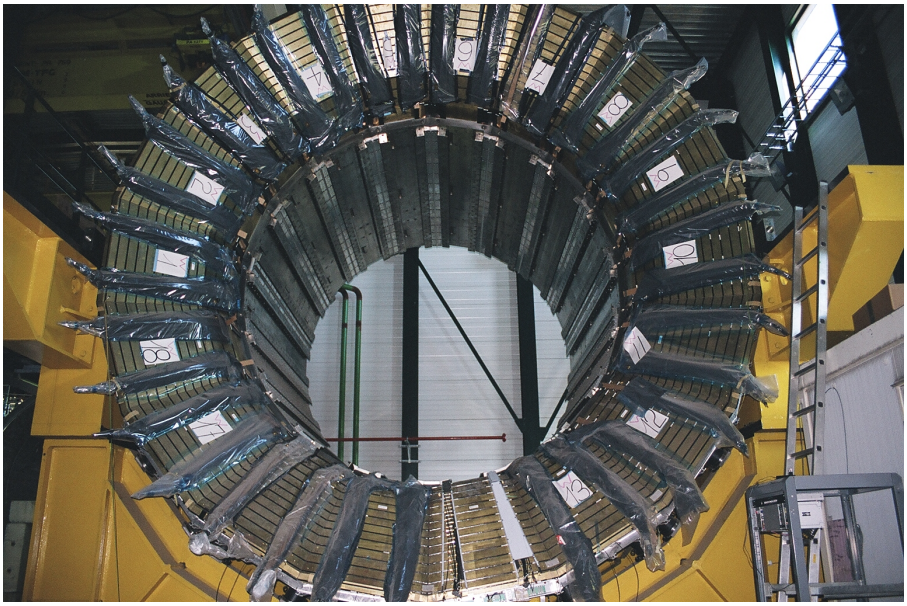

Figure 3.17: Hadronic Barrel (HB) calorimeter. From Ref. [40].

the brass absorbing plates is 78 mm and the scintillator thickness is 3.7 mm. Figure 3.18 shows a picture of one of the two HE's.

The HO is located outside the magnetic field just before the barrel muon system at $|\eta| = 0 - 1.26$. The purpose of the HO is to reduce the tails in the energy resolution function by "catching" the remaining energy leaking through the rear of the calorimeter. This also leads to an improved resolution of the missing transverse energy. The HO is made of scintillators 10 mm thick and the granularity of the HO matches the HB, $\delta\eta$ x $\delta\phi$ = 0.087 x 0.087. The entire assembly is divided into 5 rings each having 12 sectors which exactly correspond to the 5 wheels and 12 sectors in the muon barrel system. As shown

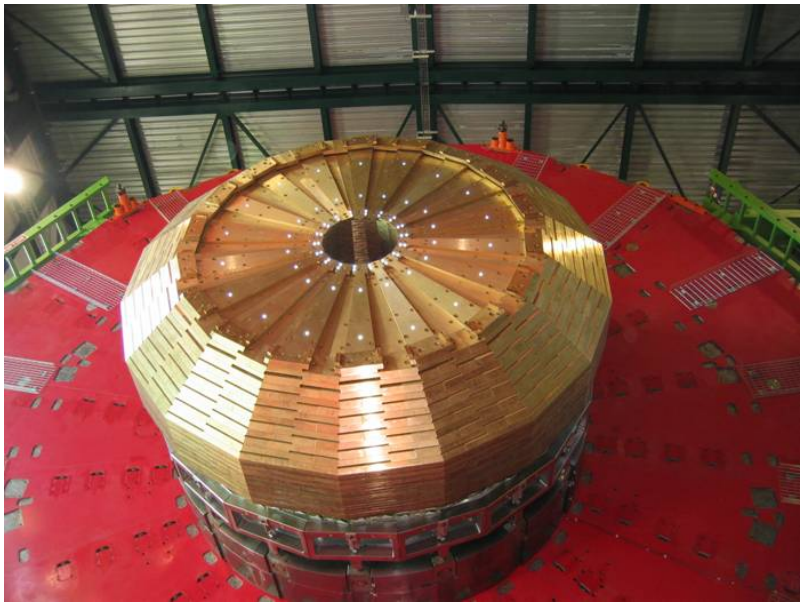

Figure 3.18: Hadronic Endcap (HE) calorimeter. From Ref. [30]

in Figure 3.15 the HO increases the total material in the calorimeter system to 11.6 dimensionless interaction lengths in the barrel, thus making it possible to contain more of the hadronic showers.

The HF is a steel/quartz fiber calorimeter that is located at 11.2 meters from the interaction point and measures particles at high rapidity, $|\eta| = 3 - 5$. Because it lies at high rapidity, it must withstand the large particle fluxes in this forward region. The HF was designed to be radiation resistant and for this reason quartz fibers are used as the active material. The quartz fibers use Cherenkov light to measure the energy of the particles and since the Cherenkov effect is insensitive to neutrons (because they have no charge) the quartz fibers

are radiation resistant. In addition, the Cherenkov effect is almost instantaneous so the detector response is very fast.

Steel is used as the absorber in the HF and it has a total depth of 1.65 m. A schematic of an HF wedge is shown in Figure 3.19(a). Grooves of 1mm x 1mm are machined into the steel absorber, and the quartz fibers are run along the length of the steel absorber in these grooves, parallel to the beam line. Figure 3.19(b) shows a schematic of the steel absorber and the grooves with the quartz fibers in them. The quartz fibers are placed 5 mm apart in a square grid and two different lengths of quartz fibers are used, long (1.65 m) and short (1.43 m). The beginning of the short fibers is 0.22 m into the steel absorber, whereas the long fibers run the full length of the steel absorber. This is done because electrons and photons will deposit a large fraction of their energy in the first 22 cm (so only in the long fibers), while hadrons will deposit energy in both the short and long fibers. This makes it possible to differentiate between electrons/photons and hadrons in the HF. Figure 3.20 shows a picture of the HF calorimeter.

Now that we have looked at the different components of the HCAL we can look at how well it works, i.e., what is the energy resolution. In 2002 a HCAL test beam experiment was designed to study the performance of the HCAL. The

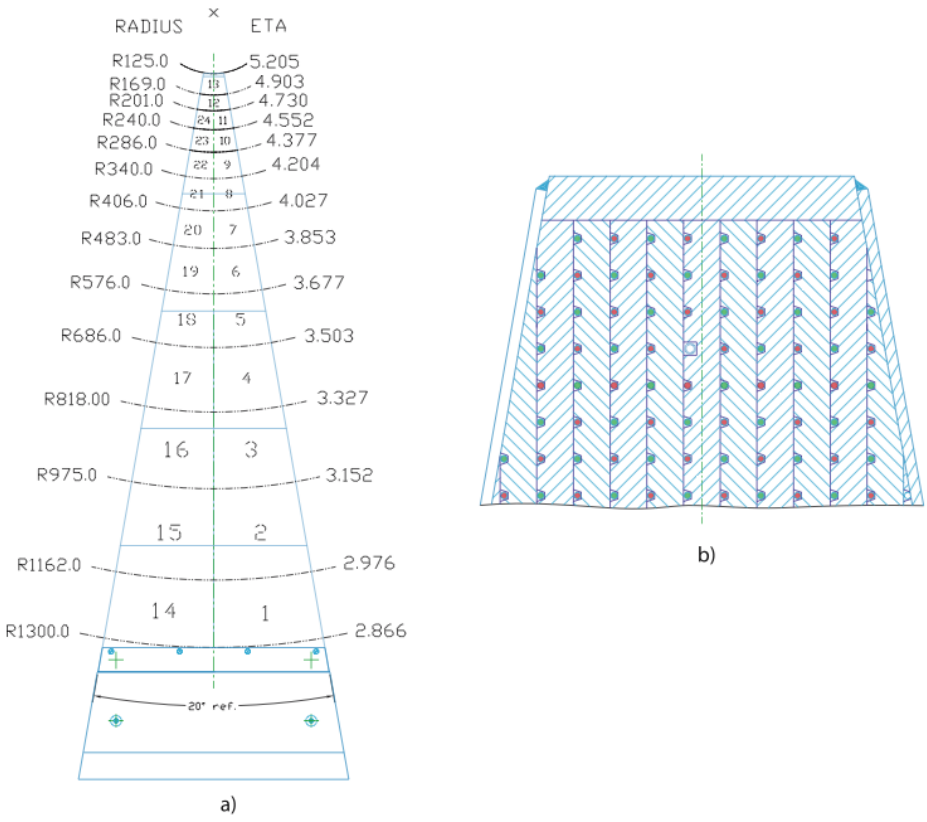

Figure 3.19: Schematic showing (a) the r-ϕ view of an HF wedge and (b) the expanded view of tower 13, long (red) and short (green) fibers alternate and are separated by 5 mm. Figures from Ref. [41].

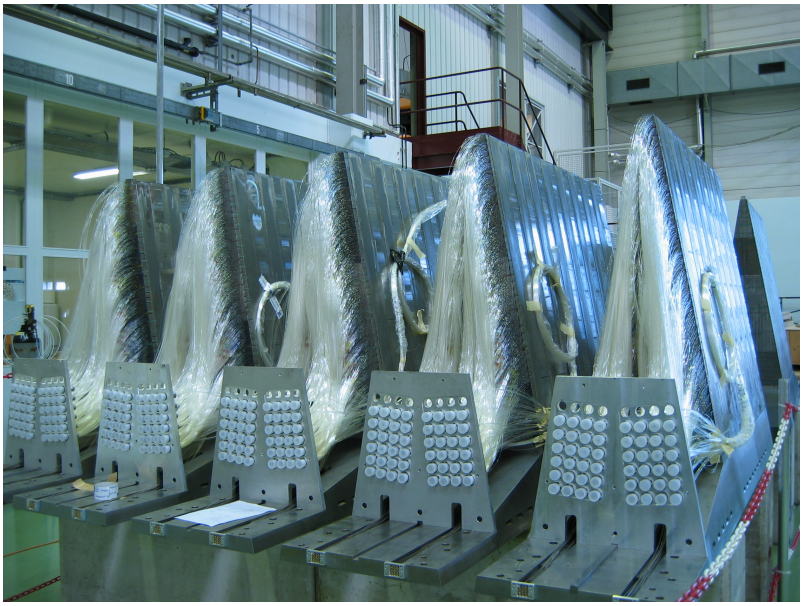

Figure 3.20: Wedge Module of the Forward Hadron Calorimeter (HF). From Ref. [42].

detector was exposed to beams of π^- (20, 30, 50, 100, 300 GeV).[19] A total of 144 HB and 16 HO channels were tested using an aluminum slab to represent the solenoid material and along with a prototype of the ECAL. Figure 3.21 shows the energy distributions of 20 and 100 GeV pions. The non-gaussian tails at low energy in the energy distribution of 100 GeV pions come from energy leakage beyond the HB outer limits (the HO was added to decrease these tails). The non-gaussian tails at high energy in the energy distribution of 20 GeV pions come from the non-compensating nature of the CMS calorimeters.[20] To calculate

[19] In this test beam experiment the detector was also exposed to muon and electron beams; however, we do not consider those cases here.

[20] This means that the calorimeter signals for hadrons is generally smaller than for electrons, impacting the linearity of the response function.

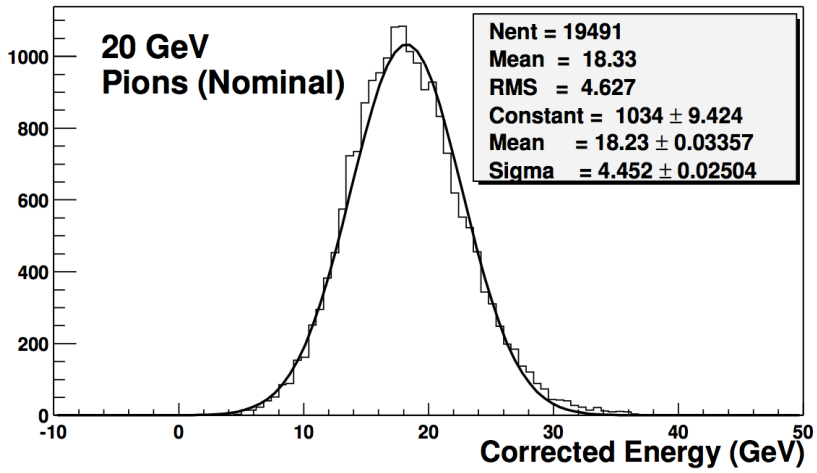

(a)

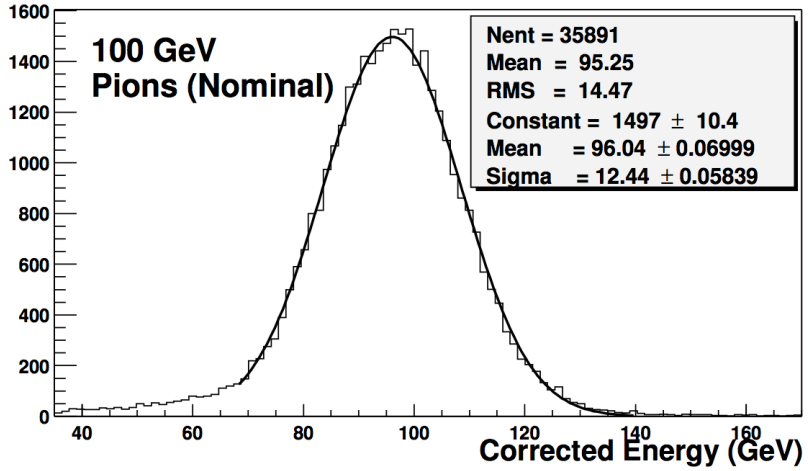

(b)

Figure 3.21: Energy distributions of 20 GeV (upper plot) and 100 GeV (lower plot) pions after applying the HCAL vs. ECAL energy based cuts to remove backgrounds. Figures from Ref. [30].

the approximate resolution we take the RMS and divide by the mean. For the 20 GeV pion beam the resolution is approximately 22% and for the 100 GeV pion beam the resolution is approximately 12%. This roughly agrees with the resolution function $\sigma/E = 100\%/\sqrt{(E)} \oplus 4.5\%$ obtained from earlier test beam studies [43]. An important feature of the HCAL is that the energy resolution increases as the energy of the hadron increases.

Though we have described the resolution of single pions in the HCAL the measurement object we are often concerned with is a jet, which is a collection of hadrons along the same direction. A jet comes from the hadronization of a quark or gluon and is created by the hard scattering processes. Different jet algorithms and their resolution are described in detail in Sec. 4.4.

More detailed information on the HCAL can be found in Refs. [43] and [30].

3.2.5 Muon system

As muons traverse the detector, they are typically not stopped by the tracker, calorimeter, or solenoid, and dedicated muon chambers are placed outside the solenoid to measure their presence. Muons do not radiate and create a shower in the ECAL like electrons because of their much larger mass (approximately 200 times more massive than the electron)[21] and they do not interact via the

[21]The radiation cross section goes roughly like $1/\mathrm{m}^2$, so the fact that the muon is 200 times heavier means its radiation cross section will be approximately 40000 times less.

strong force so they do not create a hadronic shower in the HCAL. In addition, muons are minimum ionizing particles (particles that have mean energy loss rates close to the minimum), so they deposit very little energy via ionization. These properties allow the muon to penetrate through many meters of very dense material (such as iron) without being stopped.

The muon system is made up of three detector subsystems including the Drift Tube Chambers (DTs), the Cathode Strip Chambers (CSCs), and the Resistive Plate Chambers (RPCs). DTs are used in the barrel region ($|\eta| < 1.2$) where the rate is expected to be small and the magnetic field has a relatively low intensity. In the forward region ($1.2 < |\eta| < 2.4$), where there is a large amount of radiation and the magnetic field is uneven, CSCs are used. The RPCs are placed in both the barrel and endcap, and provide better time resolution but worse position resolution than the DTs and CSCs.[22] The RPCs and either the DTs or CSCs provide a combined trigger object in the first level of the trigger system, making the trigger system more robust and precise. The different muon chambers are interspersed between iron, which is used as the return yoke for the magnet and also stops any additional particles (besides muons) that make it through the calorimeters. Figure 3.22 shows a schematic of the muon detector and its different components.

[22]The RPCs are able to determine the correct bunch crossing unambigiously.

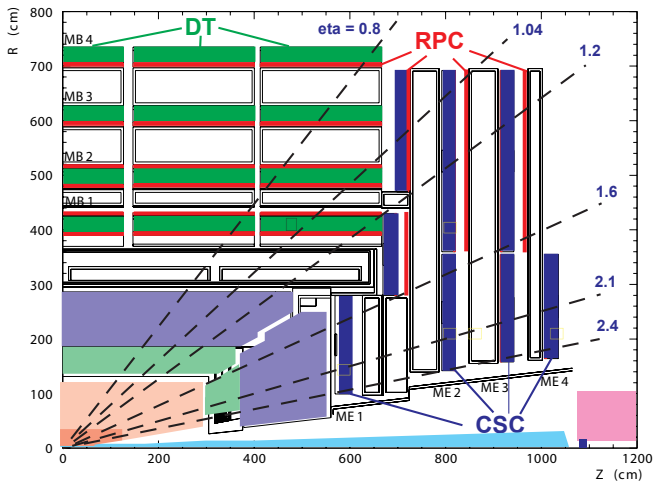

Figure 3.22: Schematic showing the layout of the muon chambers. The white boxes in the muon system are the iron used for the return yoke of the magnet. The green boxes are the DT chambers, the red boxes are the RPCs, and the blue boxes are the CSCs. Figure from Ref. [30].

In the barrel of the detector there are 250 DT chambers divided up into four concentric "stations" and 5 wheels each having 12 sectors, where a single sector covers a 30 degree azimuthal angle.[23] Figure 3.22 shows the DT chambers in green and the four stations are labeled as MB1, MB2, MB3, and MB4. Each DT chamber is made up of 12 layers of drift tubes and the layout is shown in Figure 3.23. A single drift tube is around 2.5 m long and 4 cm wide. The width of the drift tube is constrained by the maximum drift length of 2 cm which allows for a negligible occupancy. Each drift tube is essentially a gas cell with a wire

[23] A naive calculation of the number of chambers yields 4 x 5 x 12 = 240, which is slightly less than 250. However, this does not take into account that in the last "station" the sectors at 90 and 270 degrees (at the very top and bottom of the detector) are divided up into two DT chambers instead of one DT chamber like the rest of the sectors. This gives the additional 10 DT chambers.

running through it. The tubes are operated at atmospheric pressure, and the gas is a Ar/CO_2 mixture, with the amount of CO_2 between 10-20%. As a muon passes through the drift tube it knocks electrons off the gas molecules. Electric fields in the tube then force these electrons towards the wire, producing a signal in the wire. For each station the measurement of the muon vector gives a ϕ precision better than 100 μm in position and approximately 1 mrad in direction. Figure 3.24 shows a picture of the installation of some of the DT chambers into one of the the wheels in the barrel.

RPC detectors are interspersed between the layers of the DT in the barrel. The RPC detectors are shown in red in Figure 3.22. In the first two stations in the barrel two RPCs layers sandwich each DT chamber; however, in the last two stations only one RPC layer lies before the DT chamber. The RPCs consist of two parallel high-resistivity plates (in this case Bakelite) separated by a 2 mm width gas volume. As a muon traverses a RPC it creates an electric discharge in the gas. This discharge then creates a signal in external aluminum strips via capacitive coupling. In the barrel these aluminum strips run along the beam direction. A RPC is able to tag an ionizing particle within a time scale of less than 25 μm, the time between bunch crossings at design luminosity. In total there are 610 RPCs in the full detector, 480 which are in the barrel.

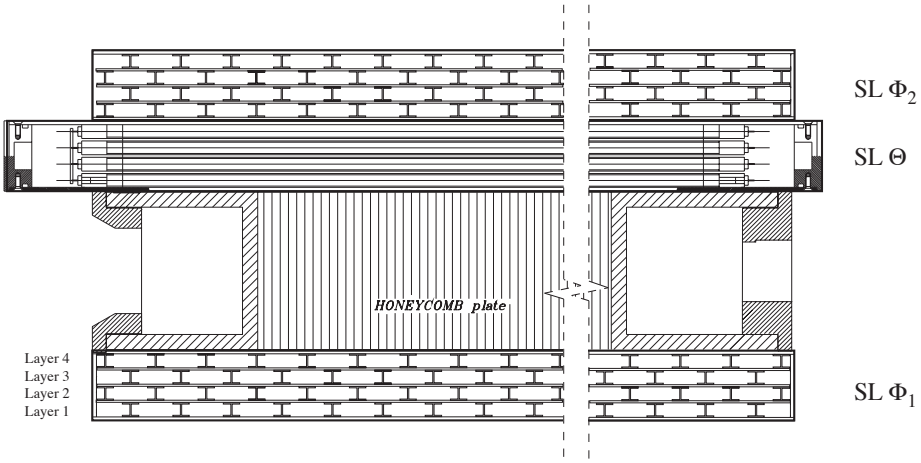

Figure 3.23: The layout of a DT chamber inside a muon barrel station. Each DT chamber in the 3 innermost stations consists of 12 layers of drift tubes divided into 3 groups of 4 consecutive layers (called Superlayers). The tubes are staggered by half a tube for better position resolution. Two Superlayers have wires parallel to the beamline and measure the $r - \phi$ coordinate, while a third Superlayer is perpendicular to the two Superlayers and mesasure the z-coordinate running parallel to the beam. The Honeycomb plate between the Superlayers gives a longer lever arm to measure the track direction in the chamber. Figure from Ref. [30].

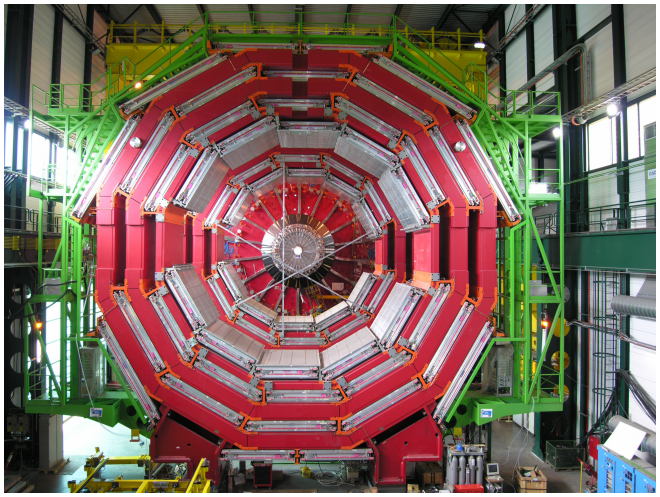

Figure 3.24: Installation of DT chambers into one of the wheels in the barrel. From Ref. [30].

The endcaps of the muon system are made up of 468 Cathode Strip chambers which are mounted onto 4 disks enclosing the CMS magnet. For each disk there are 2 concentric rings around the beam axis (except the first disk where there is 3 concentric rings) and for each ring there is either 18 or 36 chambers. Figure 3.25 shows the installation of the CSCs onto one of the disks in the endcap. Each CSC is trapezoidal in shape with maximum length 3.4 m and maximum width 1.4 m. Figure 3.26 shows a schematic view of a single CSC chamber. Each CSC chamber is made up of 7 trapezoidal panels with 6 gas gaps. Each panel has wires running radially along it and strips running along the ϕ direction. The wires act as anodes and the strips as cathodes; thus, when a particle ionizes electrons in the gas gaps it produces a charge on the anode wire and an image charge on the

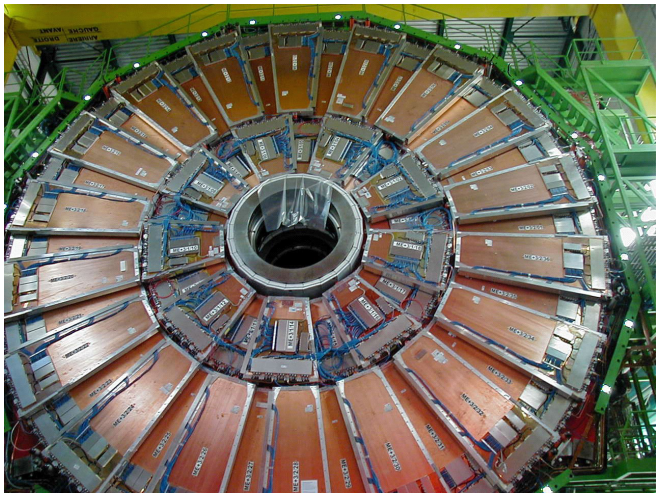

Figure 3.25: Installation of CSC chambers onto one of the disks in the endcap. From Ref. [30].

cathode strips. The spatial resolution of the CSC strips is roughly 100 μm and the angular resolution in ϕ is on the order of 10 mrad. RPCs are interspersed between the iron and CSCs in the endcap to help with the triggering of muons.

Both the muon system and tracker provide a momentum measurement of a muon. Figure 3.27 shows the muon momentum resolution as a function of momentum for just the tracker, just the muon system, and the combined system. Sec. 4.1 discusses the details of how the tracker and muon system information is combined. The momentum measurement in the muon system is determined by the muon bending angle at the exit of the magnetic field coil, constraining the track to have come from the interaction point. Below muon p_T of roughly 200 GeV multiple scattering dominates the error on this measurement in the muon

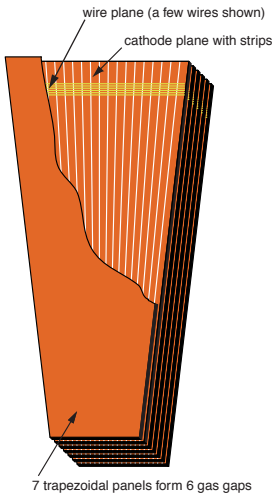

Figure 3.26: Schematic view of a CSC chamber. Wires running radially act as the anode and strips along the phi direction act as a cathode. Figure from Ref. [30].

system. Thus, for low p_T muons the best momentum measurement comes from the tracker, where the contribution from multiple scattering is much smaller. For high p_T muons the momentum of the tracker can be improved using the additional track measurements in the muon system.

For more information on the muon system see Refs. [30] and [44].

3.2.6 Trigger and data acquisition

At design luminosity the LHC will have a bunch crossing rate of 40 MHz, leading to roughly 10^9 interactions per second.[24] Of the 40 million crossings per second only about 100 can be written out to disk. This means that the

[24]There will be approximately 20 interactions per crossing.

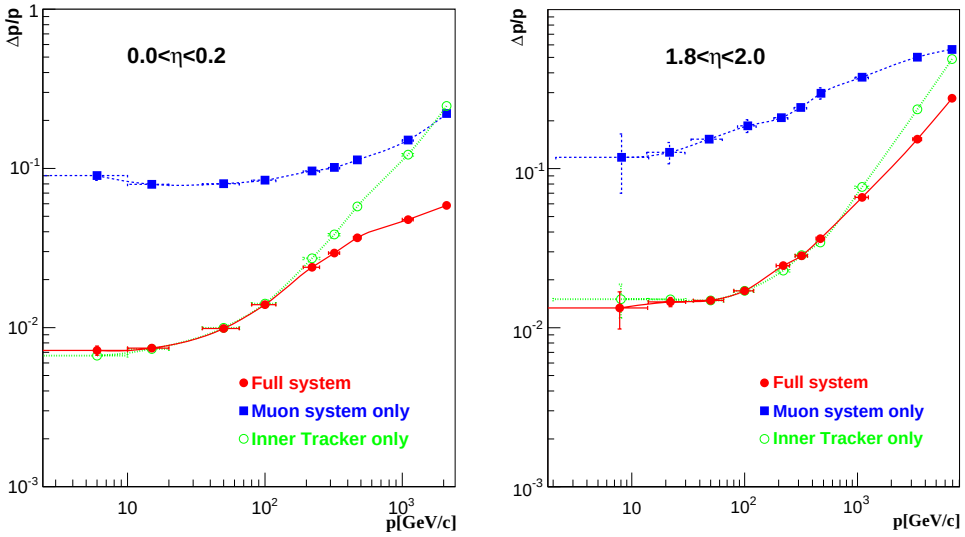

(a) (b)

Figure 3.27: The muon momentum resolution versus momentum using the muon system only, the inner tracker only, or both. a) barrel, $|\eta|$ <0.2; b) endcap, 1.8< $|\eta|$ <2.0. Figures from Ref. [30].

trigger and data acquisition system has the tough job of recording only 1 in 10^6 crossings. The trigger decision must be made on a very short time scale and the events that are triggered must contain the most exciting physics. [25] These requirements make it essential to have a data acquisition system that can synchronize signals from millions of channels very fast (to provide information about whether signals from different sub-detectors are from the same event) and a trigger acquisition system that is robust, flexible and fast.

The trigger system at CMS is split up into two main pieces, the Level 1 (L1) trigger and the High Level Trigger (HLT). The L1 is a custom hardware processor that reduces the rate to roughly 100 kHz (100,000 crossings per second). The L1 trigger takes information only from the calorimeter and muon system and uses trigger primitive objects such as photons, electrons, muons, jets to calculate whether the event is interesting enough to keep. The L1 trigger has 3.2 μs to decide to keep an event. Roughly 2 μs of this time is used to transfer the trigger information from the front-end electronics to the L1 services cavern and back. The remaining 1 μs is used for the actual L1 hardware calculation.

The HLT uses software to perform more complicated calculations by combining different trigger primitive objects and additional detector information (for

[25] Most events are minimum bias events, where the collision is a low-energy glancing hit. We are most interested in the events where the collision creates particles with high transverse momentum, which could come from new physics.

instance, information in the tracker). The HLT is run on a farm of more than 1000 standard computers and reduces the rate from the L1 output of 100 kHz to the 100 Hz that is written to disk. The nominal amount of time the HLT has to make a decision is on the order of 100 ms.

Chapter 4

Object Reconstruction

4.1 Muons

In hadron colliders muons provide a clean signature for many rare physics processes and thus their identification is extremely important. As a muon produced at or near the interaction point traverses the detector, it generates hits along its trajectory in the silicon tracker and with enough momentum it will deposit some minimum ionizing energy in the calorimeter and then a track in the muon system.[1] Most muons of interest are produced at or near the interaction point. Such muons can arise from the decay of the following particles: W, Z, b, c, J/ψ, and Υ. There are other categories of muons that we consider backgrounds because they do not usually signify rare physics processes. For instance, decays of light-flavour particles such as pions or kaons are very common in a hadron

[1] For low momentum muons, less than a few GeV, the magnetic field curves the track enough that it won't make it to the calorimeters.

collider, and they can decay to real muons that travel through the detector. Muons from pions or kaons can be created near the interaction point; however, due to the longer lifetime of pions or kaons oftentimes these muons are created further from the interaction point. These types of muons are called decays-in-flight. Another muon source, which happens less frequently than these other types, occurs when a calorimeter shower or nuclear interaction in the detector creates a real muon that traverses the muon chambers. The last source of real muons arises when a cosmic muon overlaps with a collision event. In addition to these cases where a real muon is created, there are cases where a hadron looks like a muon in the detector because it travels through the calorimeter without showering and creates a track in the muon chambers. These type of events are called hadron "punch-through" events.

Before going into detail about how we actually differentiate between these different sources of muons we must understand exactly how a muon is initially reconstructed in the detector. A typical muon has two tracks, one in the silicon tracker (called the tracker-track), and one in the muon system (called the standalone-muon track), both of which are made by performing a fit to the "hits" (energy deposits) in the sub-detector. There are two reconstruction approachs commonly used in CMS: global muon reconstruction and tracker muon reconstruction. The global muon reconstruction starts from a standalone-muon track

and extrapolates it to the tracker to find hits in the tracker that are consistent with the muon track. Then a combined fit is made to the hits in the silicon tracker and the muon system. As described in Sec. 3.2.5, for muons below p_T of 200 GeV the silicon tracker information provides the best resolution of the momentum. For muons with p_T >200 GeV the standalone-muon track information can help improve the resolution.

The tracker muon reconstruction starts from the tracker-track and extrapolates it to the muon chamber, looking for segments [2] in the muon chamber that are consistent with this tracker-track. Tracker muon reconstruction only requires a single muon segment in the muon system as opposed to the global muon reconstruction which typically requires two or more segments. For this reason the tracker muon reconstruction has higher efficiency for low momentum muons ($p < 5$ GeV). For higher momentum muons the efficiencies of the tracker muon and global muon reconstruction are comparable.

Now that we have described the muon reconstruction, we can explain the different identification variables used to identify muons from heavy particle decays. An important variable for rejecting cosmic muons and decay-in-flights is the transverse impact parameter, d_0. Typically a requirement of d_0 <2 mm is made (w.r.t. the primary vertex), which preserves the efficiency for muons from

[2] A muon segment is a collection of hits in a chamber.

beauty and charm mesons (and W and Z bosons) but rejects a large fraction of muons from pions and kaons (since they typically decay further from the interaction point). For cosmic muons, the distribution of d_0 is roughly uniform (in contrast to muons from collision events where it peaks at zero) and, in fact, this variable could be used to estimate this background.[3] Other discriminating variables for decay-in-flights are the number of hits in the tracker fit and the χ^2 value for the tracker fit. Since decay-in-flight muons tend to be created further from the interaction point the number of hits on the tracker fit will be less and the tracker fit will be worse.[4] To reject hadron "punchthrough" events requirements are made on the hits and track in the muon system. For instance, generally at least 2 segments in the muon system must match to a global muon. This rejects most hadron "punchthroughs" because they usually don't penetrate as far into the muon system as real muons due to the additional iron in the muon system. Early studies at CMS [45] have shown that the probability for protons with momentum between 5 and 10 GeV to "punchthrough" and create a global muon is approximately 5 x 10^{-4}, in agreement with expectations from Monte Carlo studies.

[3]For this analysis the background from cosmic muons is so low that we assume it is negligible.

[4]Typical values for these cuts are $N_{hits} \geq 11$ and $\chi^2 < 10$.

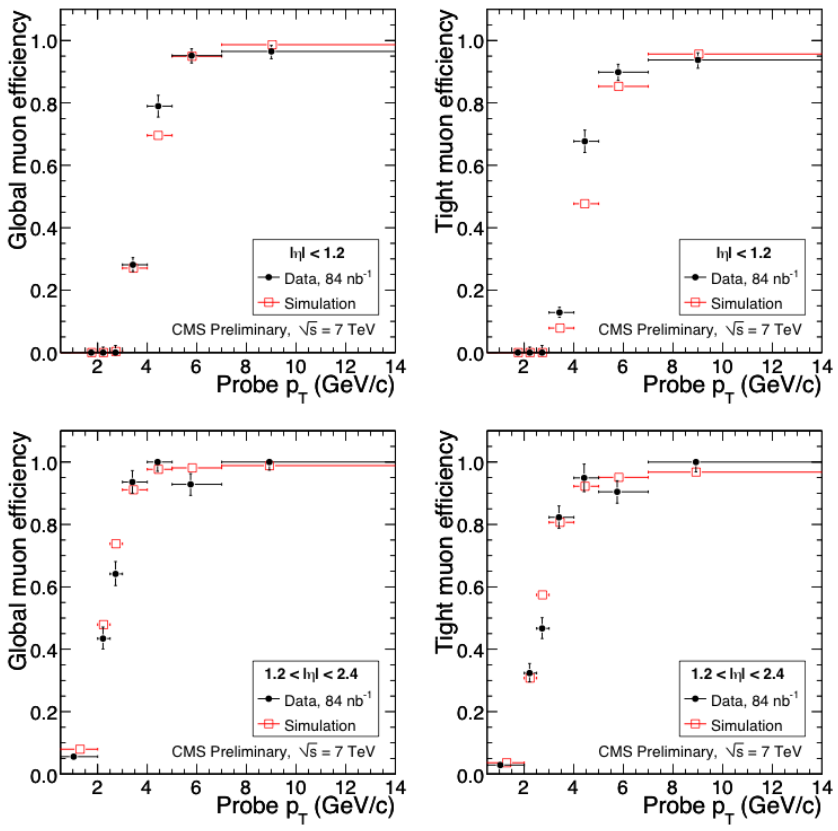

Figure 4.1: Tag-and-probe muon reconstruction efficiency as a function of p_T in data and simulation. The integrated luminosity for the data is 84 nb^{-1}. The upper left plot shows the global muon efficiency for $|\eta| < 1.2$, the upper right plot shows the tight muon efficiency for $|\eta| < 1.2$, the lower left plot shows the global muon efficiency for $1.2 < |\eta| < 2.4$, and the lower right plot shows the tight muon efficiency for $1.2 < |\eta| < 2.4$. From Ref. [45].

Figure 4.1 shows in early data the muon reconstruction efficiency for a global muon and tight muon, where the tight muon is a global muon with some additional identification requirements.[5] The efficiency is calculated using a "tag-and-probe" method with events from the $J/\psi \to \mu\mu$ resonance.[6] The tag (tight selection) is defined to be a global muon that tags the event as a having a $J/\psi \to \mu\mu$ resonance (this global muon is used along with a silicon track to calculate the resonance mass). The probe (loose selection) is defined to be a tracker track with a minimum ionizing signature (to help remove backgrounds to the method). The efficiency is then calculated as the number of probes that pass the global muon or tight muon selection. The global muon efficiency reaches a plateau value of 95-100% at roughly 6 GeV for $|\eta| < 1.2$ and at roughly 4-5 GeV for $1.2 < |\eta| < 2.4$. The tight muon efficiency reaches peak efficiency at a slightly higher muon p_T because of the additional identification requirements. These plots only show muon efficiencies up to 14 GeV; efficiencies for higher p_T muons can be determined by doing a similar tag-and-probe method using the Z-boson resonance.

More information on the muon identification in CMS can be found in Ref. [45].

[5]Specifically the tight muon requirements are: $N_{hits} \geq 11$, $\chi^2 < 10$, 2 segments matched to a global muon, d_0 <2 mm, at least one hit in the muon chamber, $p_T \geq 3$ GeV.

[6]The di-muon mass must be between 2.8 to 3.5 GeV (the mean value of the mass of the J/ψ is 3.1 GeV).

4.2 Electrons and photons

The identification of high p_T electrons and photons is very important for Higgs searches ($H \to \gamma\gamma$ or $H \to ZZ \to 4\ell$) and new physics searches with leptons or photons. The electromagnetic calorimeter measures most of the energy of high p_T electrons and photons with sometimes some small amount of spill-over into the hadronic calorimeter. The presence of a charged track in the silicon tracker can help differentiate between a photon and an electron. Electrons have charge and thus will create a track in the silicon tracker, whereas photons do not have charge and will not create a track in the silicon tracker.[7] To discriminate an electron or photon from a jet, identification requirements (described below in detail) are placed on the electron or photon object. In general the misidentification rate for electrons and photons is much higher than for muons because it is much easier for a jet to look like an electron or photon than a muon. Since in this analysis we focus on leptons and do not explicitly look at photons for our search signature we will skip a detailed description of the photon reconstruction and identification. Suffice to say that the reconstruction and identification of the photon is similar to the electron with the main difference being that there

[7] In fact, a photon can convert to an electron and positron via interaction with the material in the tracker and these electron and positron will have tracks. This is called photon conversion and is described in detail later in this section.

must be no pixel hits consistent with the energy deposit of the photon in the ECAL. For more information on photon reconstruction see Refs.[46][47].

There are many different sources of high p_T electrons at CMS. The electrons we are most interested in come from decays of particles such as a W, a Z, or a beauty or charm meson. The number of electrons from light flavour decays is small (this is in sharp contrast to the large number of muons from light flavour decays) due to the small branching fractions of a pion or kaon to an electron.[8] However, real electrons from a photon converting in the silicon tracker must be studied. In addition, there are many fake electrons from jets, where for instance a charged hadron can overlap with a π_0 (which decays to two photons), or the charged hadron is mostly contained in the ECAL. Identification requirements on the electron candidates are applied to try to remove all the electron sources except the heavy flavour decays.

[8] A charged pion decays roughly 99.99% of the time to a muon, and roughly 1 x 10^{-4} to an electron. This follows from the fact that the pion has a much larger mass than the electron and in the limit that $m_e = 0$ helicity must be conserved during the decay. However for helicity to be conserved you need a right handed neutrino and left handed electron or left-handed anti-neutrino and right-handed positron, both of which do not conserve angular momentum due to the pion having $J = 0$. In the case of the muon its mass is approximately 200 times larger than the electron so the helicity conservation is not as strong and you can have a right-handed neutrino and right-handed muon or left-handed anti-neutrino and left-handed anti-muon which both satisfy angular momentum conservation. This explanation follows similarly for the charged kaon decay $K \to e\nu_e$, and its branching fraction is 1 x 10^{-5}. However, in the case of a charged kaon decay there is a roughly 5% chance for the process $K \to \pi^0 e\nu_e$, so there is some small chance of a decay to an electron. In addition, electrons can be produced in K^0_L decays.

Before describing the identification requirements we will explain exactly how the electron reconstruction works. There are two main electron reconstruction schemes within CMS, "ECAL driven" and "track driven". The "ECAL driven" method looks for clusters of clusters of energy in the ECAL (called Superclusters) taking into account the fact that the electron can lose energy via the bremsstrahlung of photons as it travels through the silicon tracker. The bremsstrahlung of photons results in the energy in the calorimeter being spread out in ϕ but narrow in η (the photons are not charged so they have a different trajectory through the magnetic field then the electron, effecting the ϕ direction with respect to the electron but not the η direction with respect to the electron). Superclusters with transverse energy of greater than 4 GeV are taken and propagated back through the magnetic field (using both charge hypotheses) to the pixel detector where pixel hits are looked for. If two pixel hits are found they serve as a seed for building a silicon track. A Gaussian Sum Filter algorithm is then used to reconstruct the electron tracks [48]. The electron energy is determined as a weighted combination of the supercluster energy and tracker momentum. The "track driven" algorithm takes a track and looks for energy deposits in the ECAL that could be consistent with an electron. The "track driven" method was developed as part of the particle-flow reconstruction at CMS and is more efficient for low momentum electrons and electrons within

jets. For low momentum electrons the "ECAL driven" method is inefficent because it requires a Supercluster of E_T >4 GeV. For more information on the "track driven" method see Ref. [49].

At CMS a simple cut based selection criteria is used to select primary electrons.[9] The selection criteria for electrons fall into three classes: 1) electron identification cuts, 2) conversion rejection, and 3) isolation requirements. The electron identification cuts are used to discriminate between an electron and a jet and are different for the barrel and the endcap. Hadron showers are longer and wider than electromagnetic showers so shower shape variables and a precise matching of the track and the cluster can be used for discrimination purposes. The variable $\sigma_{i\eta i\eta}$ provides an expression for the η spread of the supercluster. It is calculated by the following expression:

$$\sigma^2_{i\eta i\eta} = \frac{\sum_i^{5x5} w_i(\eta_i - \bar{\eta}_{5x5})^2}{\sum_i^{5x5} w_i}, w_i = max(0, 4.7 + ln\frac{E_i}{E_{5x5}}), \tag{4.1}$$

where E_i and η_i are the energy and pseudorapidity of the i_{th} crystal within the 5 x 5 electromagnetic cluster and E_{5x5} and η_{5x5} are the energy and η of the entire 5 x 5 cluster [47]. The value of this variable should be smaller for an electron or photon than for instance a π_0, which decays to two photons, and can be used to discriminate between these objects. Another measure of the shower shape is

[9] Ideally, in the future a multi-variate method or likelihood fit should be used for the electron selection.

the variable H/E, the hadronic energy over the electromagnetic energy, which gives you a sense of how much of the total energy is in the HCAL vs. the ECAL. For a jet there will tend to be much more energy in the HCAL due to its longer shower length. In addition to shower shape variables two variables that match the track to the supercluster in η and ϕ, called $\Delta\eta$ and $\Delta\phi$, provide additional discrimination against jets.

Dedicated cuts have been developed for photon conversions that create real electrons. Electrons from photon conversions in the tracker will have some number of missing hits on the track in the silicon detector and this can be used to discriminate against conversions. In addition, looking for a partner track of the electron that has an opposite charge, small polar angle with respect to the electron track and small distance at the point where the two tracks are parallel leads to rejection of conversions. Isolation requirements are placed on electrons to try to reject electrons from semi-leptonic b and c decays. The energy and momentum in the calorimeters and tracker surrounding the electron are used to postulate whether the electron was within a jet. More details on exact isolation requirements are in Sec. 5.2.5.

Different electron identification working points were developed at CMS to obtain specific efficiencies and fake rates. Each working point places slightly different requirements on the identification variables listed above. An example

is "WP80", which was chosen so that the efficiency in Monte Carlo for prompt electrons with p_T >20 GeV from W decays would be 80%. A higher efficiency point with looser identification requirements, "WP95", was chosen to have a 95% efficiency for the same criteria; however, the fake rate for this working point is higher because of the loose requirements. Additional working points "WP60", "WP70", "WP85", and "WP90" use slightly different cuts on the variables to obtain varying efficiencies. We will only discuss "WP80" and "WP95" in further detail.

To determine the efficiency in data for "WP80" and "WP95" a "tag-and-probe" method using Z decays is used [50]. The "tag" in this case is an electron that passes standard identification and isolation cuts and has a supercluster E_T >20 GeV. The "probe" is a supercluster with $E_T > 20$ GeV that along with the "tag" gives an invariant mass at the Z mass. The efficiency is then determined by the number of "probes" that pass the "WP80" point. The efficiency for "WP80" and "WP95" were determined using this "tag-and-probe" method with the first 200 nb^{-1} of data at 7 TeV. Table 4.1 shows these efficiencies in data and Monte Carlo for the ECAL barrel and ECAL endcap. The efficiencies agree between data and Monte Carlo within errors.

To determine the fake rate (the ratio of electron candidates passing the background selection and electron ID over the total number of electron candidates in

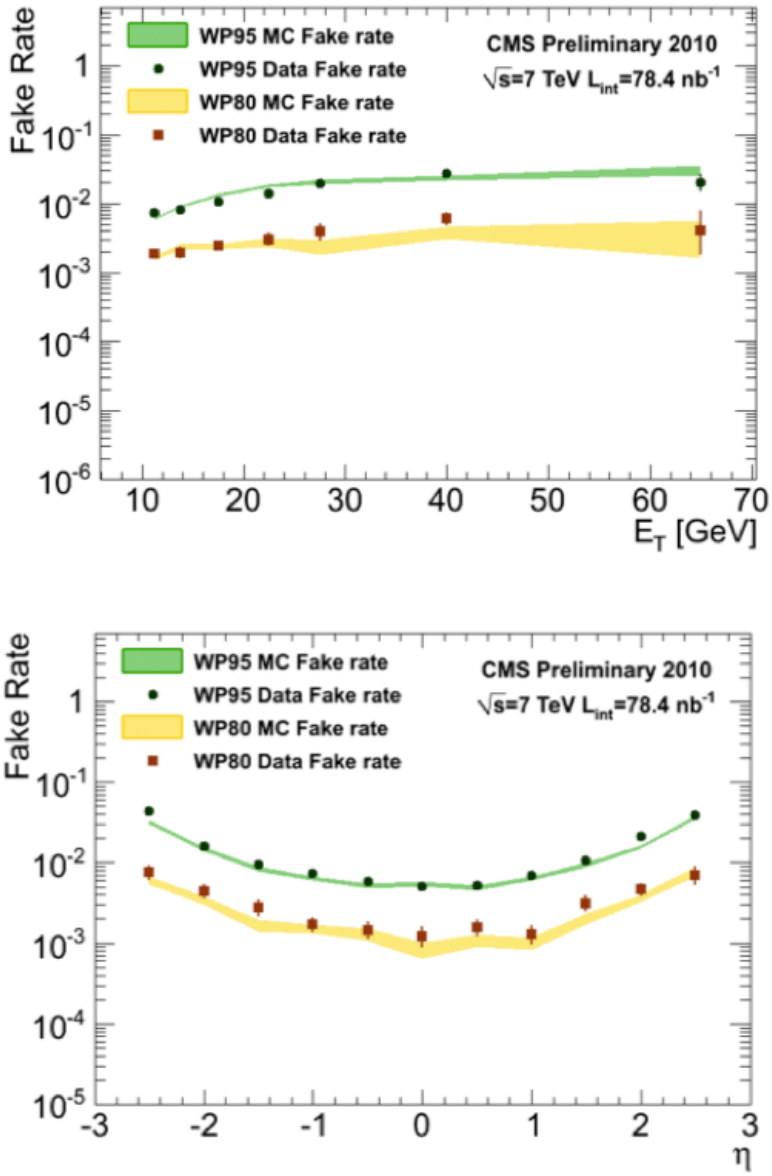

Figure 4.2: Electron fake rate as a function of E_T (top) and η (bottom) for the "WP95" and "WP80" working points. From Ref. [50].

Table 4.1: Electron efficiency for different working points using the "tag-and-probe" method on $Z \to ee$ events. Numbers taken from Ref. [50].

	ECAL barrel			ECAL endcaps		
Selection	Efficiency data	Error (stat.+sys.)	Efficiency MC	Efficiency data	Error (stat.+sys.)	Efficiency MC
WP95%	92.5%	3.2%	95.4%	86.4%	6.7%	92.9%
WP80%	77.5%	4.7%	85.1%	75.1%	8.6%	76.2%

the background selection) for these working points a sample of QCD events is used. The sample for this study is 78 nb^{-1} of 7 TeV data using a jet trigger with an uncorrected jet energy of 15 GeV. The event must have an electron candidate with E_T >10 GeV that is separated from the closest jet by a $\Delta R > 0.4$. To eliminate tagging due to real electrons the value of the electromagnetic fraction of the jet must be less than 90%. An additional $\not\!\!E_T$ requirement of 30 GeV is placed to remove contamination from W+jets events. Figure 4.2 shows the fake rate vs. E_T and η for "WP95" and "WP80" in Monte Carlo and data. As expected the fake rate for "WP95" is higher due to the looser identification requirements. The agreement between data and Monte Carlo is quite good.

4.3 Jets

The hard scattering of partons in the proton collisions at the LHC leads to high momentum quarks and gluons traversing the detector. As described in Sec. 2.1, these quarks and gluons cannot be free and as a single quark or gluon leaves the interaction point it hadronizes, making an observable collimated spray of bound particles, called a jet. By studying these jets experimentalists can determine properties of the original hard scattering process and not only test pertubative QCD predictions but probe for new physics, which oftentimes can have more jets on average than Standard Model processes. Both the calibration and the resolution of the jet energy must be understood in detail since these can be some of the largest systematic uncertainties for many analyses.[10]

At CMS four different types of jet reconstruction are performed: particle-flow jets (PFjets), calorimeter jets (calojets), jet-plus-track jets (JPT jets), and track-jets. Each type of reconstruction uses the jet clustering algorithm anti-kt [51], with a size parameter of 0.5. PFjets, calojets and JPT jets are used for most analyses at CMS. The particle-flow jets and JPT jets both have better resolution than the calojets because they use both tracker and calorimeter information while the calojets use only calorimeter information. The track-jets reconstruction

[10] In fact, for the analysis in this paper the largest systematic error is the uncertainty on the jet energy scale.

uses only tracker information to reconstruct jets and is specific to analyses that want to look at very low p_T jets or to cross-check jet reconstruction with the calorimeter. We will now describe the PFjets, calojets, and JPT algorithms in more detail. For more information on track-jets see Ref. [52].

Calorimeter jets are reconstructed using energy deposits in the ECAL and HCAL, specifically the calorimeter towers defined by one of more HCAL cell and multiple ECAL cells. For each cell there is a energy threshold to avoid building towers from noise. In the barrel ($|\eta|$ <1.4) each tower has one HCAL cell and a 5 x 5 unit of ECAL crystals. In the endcap the association between the HCAL and ECAL for the tower reconstructed is more complicated. The calorimeter jets do not use any tracker information during the reconstruction.

The JPT jet reconstruction uses the tracker information to improve the energy measurement (both the response and the resolution). Jets are first reconstructed using the calorimeter jet reconstruction. Then they are corrected using the tracks in the silicon tracker. Tracks that are associated to the jet vertex at the interaction point are extrapolated to the calorimeter and defined to be either out-of-cone or in-cone depending on whether the magnetic field bent the particle out of the jet cone in the calorimeter. For out-of-cone tracks their energy is added to the jet energy. For in-cone tracks their energy is added to the jet

energy and the energy the track would have deposited (based on Monte Carlo single particle studies) is subtracted.

The particle-flow algorithm tries to reconstruct all the particles in every event (i.e. muons, photons, charged hadrons, neutral hadrons, electrons) using each of the sub-detectors at CMS. For instance, to reconstruct a charged hadron the algorithm looks for tracks in the silicon detector that when extrapolated to the calorimeter will match an energy cluster. To reconstruct neutral hadrons the algorithm looks for energy deposits in the calorimeter that don't match any silicon tracks. If there is some overlap between neutral and charged hadrons the algorithm takes the charged hadron energy to be consistent with the associated momentum of the track and the excess energy is taken to be the neutral hadron energy. Once all particles in the the event are reconstructed the jet clustering is done using these particles. By using the excellent granularity of the ECAL and the tracker information the particle-flow algorithm is able to reconstruct and resolve charged hadrons and photons in jets very well, which is approximately 90 percent of the total jet energy. This improves the jet momentum and spacial resolution measurements compared to pure calojets. For more detailed information on the particle-flow algorithm see Refs. [53] and [54].

For each jet algorithm identification criteria are used to help remove jets from spurious noise. For a detailed description of jet id requirements for JPT jets and calojets see Ref. [55] and for PFjets see Ref. [56].

Corrections to the reconstructed raw jet energy must be made to take into account the non-uniform and non-linear response of the CMS calorimeters. The corrections are made initially from studying Monte Carlo samples and then used to correct the jet energy in both the Monte Carlo and data. For the data additional small residual corrections are added based on MC and data differences. The corrections determined from Monte Carlo studies change the mean jet energy to be match the particle jet energy, where a particle jet is defined with the same clustering algorithm but performed on the generator level Monte Carlo particles. There are three corrections typically applied: L1 offset, L2 relative, and L3 absolute. The L1 offset corrects for electronics noise and pile-up. This correction was not as important for 2010 data taking because the level of pile-up was pretty low. However, it will become more important as the luminosity of the LHC increases. The L2 relative correction removes variations in response across η and the L3 absolute correction removes variations in response in p_T. Figure 4.3 shows the combined L1L2L3 corrections determined from Monte Carlo. Because JPT jets and PFjets use tracker information to help measure the jet energy more correctly their corrections are much smaller than for calojets.

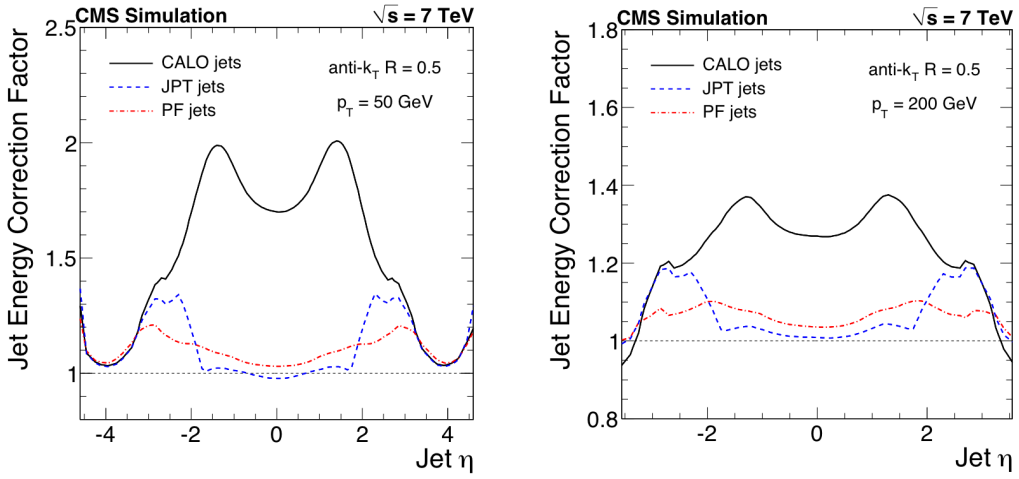

Figure 4.3: Combined L1 pileup, L2 relative, and L3 absolute jet energy corrections as a function of jet η in Monte Carlo for jet p_T of 50 GeV (left) and 200 GeV (right). From Ref. [57].

The additional residual corrections for the data are determined by looking at γ/Z+jets data events to obtain the variation in response in p_T and dijet data events to obtain the variation in response in η. In γ/Z+jets events the photon or Z energy can be measured very precisely in the ECAL (γ,$Z \to ee$) or the tracker and muon detector ($Z \to \mu\mu$) and this energy can be used to calibrate the jet energy using momentum conservation. Dijet events provide a sample where two jets should have the same p_T (if the calorimeter correctly measures their energy) even at different η due to the nature of hadron collisions and that we don't know the z-component of the momentum of the initial partons. Using this dijet sample the response at any η is calibrated to the jet energy response in

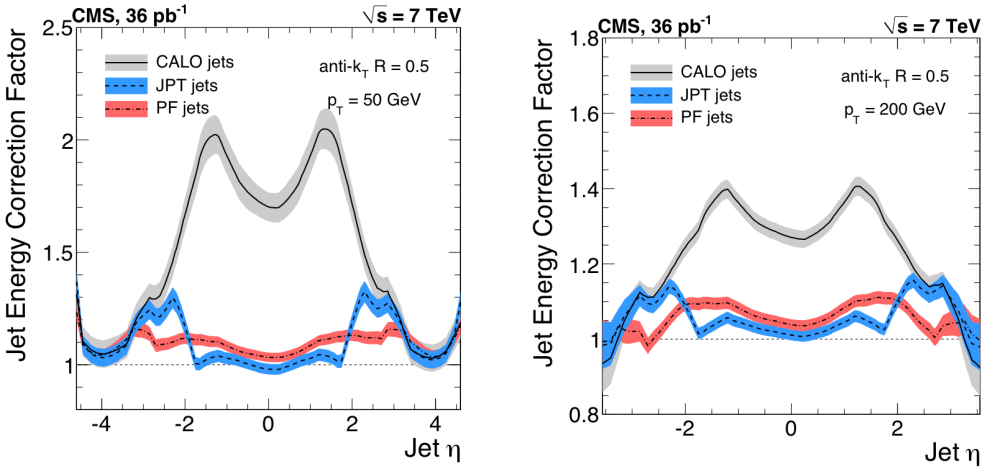

Figure 4.4: Jet energy corrections including L1, L2, L3 corrections from Monte Carlo and residual corrections from data as a function of η for two different jet p_T's, 50 GeV (left) and 200 GeV (right). From Ref. [57].

the $\eta < 1.3$ region (which is mostly flat). The total correction factor including residual corrections and L1L2L3 MC corrections is shown in Figure 4.4, where the residual corrections have been made based on studying dijet and γ/Z+jets events with 36 pb^{-1} of data. As can be seen by comparing Figure 4.4 to Figure 4.3 the residual corrections are very small. This is because the Monte Carlo does a very good job at predicting the appropriate corrections.

Figure 4.5 shows the jet-energy scale uncertainty as a function of jet p_T for two different η values and for the three different algorithms. These uncertainties are constrained by the dijet and γZ+jets studies described in the previous

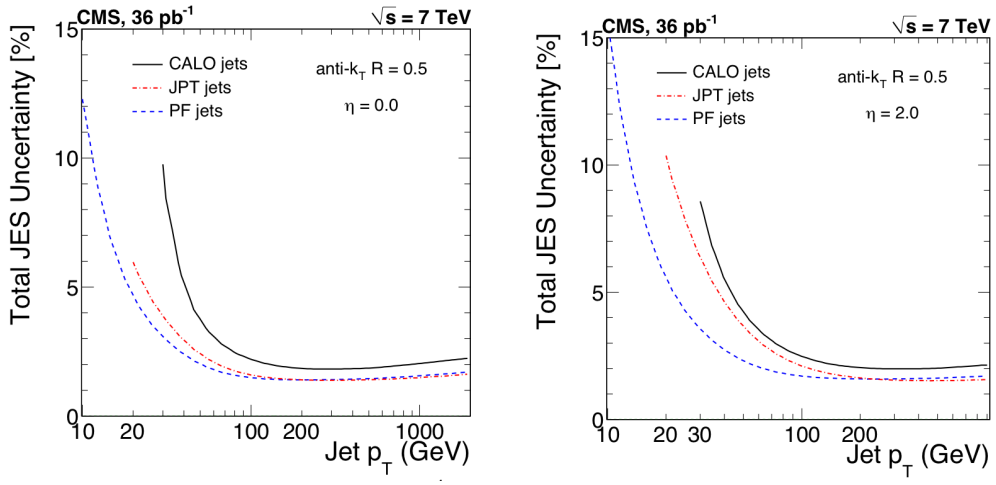

Figure 4.5: Jet energy correction uncertainties for the different algorithms as a function of p_T for two different values of η, 0.0 (left), and 2.0 (right). From Ref. [57].

paragraph. The uncertainty for PFjets is smaller, especially at lower jet p_T. For all jet types the uncertainty is less than 3% for jets with p_T larger than 50 GeV.

In addition to the jet energy scale the jet energy resolution is important as well for many physics studies. As expected, the JPT jet and PFjet resolution is better than the calojet resolution. For JPT jets or PFjets of 100 GeV in the central region, $\eta < 0.5$, their resolution has been determined to be roughly 10% and 8-9%, respectively. For calojets the resolution of a 100 GeV jet in the central region is roughly 12-13%. These numbers come from jet resolution studies with 36 pb^{-1} of data. For more information on the jet resolution and jet energy scale studies see Ref. [57].

4.4 Missing transverse momentum

The missing transverse momentum, $\not\!\!E_T$, is generally defined to be the negative vector sum of the transverse energy of all particles in the event.[11] It is very important for many SM measurements and new physics searches (as evidenced by this thesis) because it is a sign of weak decays to neutrinos or other new weakly-interacting particles (such as a WIMP). However, since the $\not\!\!E_T$ is a variable that is inferred from many different measured quantities in the calorimeter and sometimes in the tracker and muon systems[12] it is very sensitive to all types of detector effects. There are three different algorithms that reconstruct the $\not\!\!E_T$: calorimeter $\not\!\!E_T$ (calo$\not\!\!E_T$), track-counting $\not\!\!E_T$ (tc$\not\!\!E_T$), and particle-flow $\not\!\!E_T$ (pf$\not\!\!E_T$).

The calo$\not\!\!E_T$ is calculated using the calorimeter towers and their directions while trying to exclude from the calculation energy deposits that could arise from noise. The calo$\not\!\!E_T$ is corrected for muons, which are minimum ionizing particles and thus will only deposit a few GeV of energy even for a very high p_T muon. In the calo$\not\!\!E_T$ calculation the energy corresponding to the muon is removed and replaced with the muon p_T from the tracker and muon system. The tc$\not\!\!E_T$ starts with the calo$\not\!\!E_T$ and uses the higher resolution tracker to make corrections.[13] For

[11] It is sometimes called the missing transverse energy but this can be a little misleading because energy quantities are not vectors, whereas the missing transverse energy is. So it is more proper to call it missing transverse momentum.

[12] This depends on the algorithm used as we will explain later.

[13] The way the tc$\not\!\!E_T$ corrects the calo$\not\!\!E_T$ is similar to how the JPT algorithm corrects the caloJets.

charged tracks in the silicon tracker that are not muons or electrons and have $2 < p_T < 100$ GeV their corresponding energy in the calorimeter is removed (based on simulated pion response in the calorimeter) and replaced by their track p_T. For tracks with $p_T > 100$ GeV no correction is applied since the calorimeter is assumed to measure the energy well enough. For tracks with $p_T < 2$ GeV, that wouldn't reach the calorimeter because of the magnetic field, their energy is added to the $\not\!\!E_T$ calculation and no energy in the calorimeter is removed. The pf$\not\!\!E_T$ is calculated as the negative vector sum of all the particle flow particles in the event. A description of how the particle-flow algorithm reconstructs particles is given in the previous section along with some references.

For each of these algorithms there are additional corrections, called type I and type II, which can be applied to try to correct for the fact that the magnitude of the $\not\!\!E_T$ is generally underestimated. The magnitude of the $\not\!\!E_T$ can be underestimated for a variety of reasons including the nonlinearity of the calorimeter, neutrinos from semi-leptonic decays, and p_T thresholds and inefficiencies. The type I correction tries to correct the clustered energy in the event by replacing it by the jet corrected energy (jet corrections are explained in the previous section). The type II correction tries to correct for the unclustered energy that falls below the jet threshold and this correction is determined from $Z \to ee$ events. The corrections for calo$\not\!\!E_T$ are typically larger than for either tc$\not\!\!E_T$ or pf$\not\!\!E_T$ since

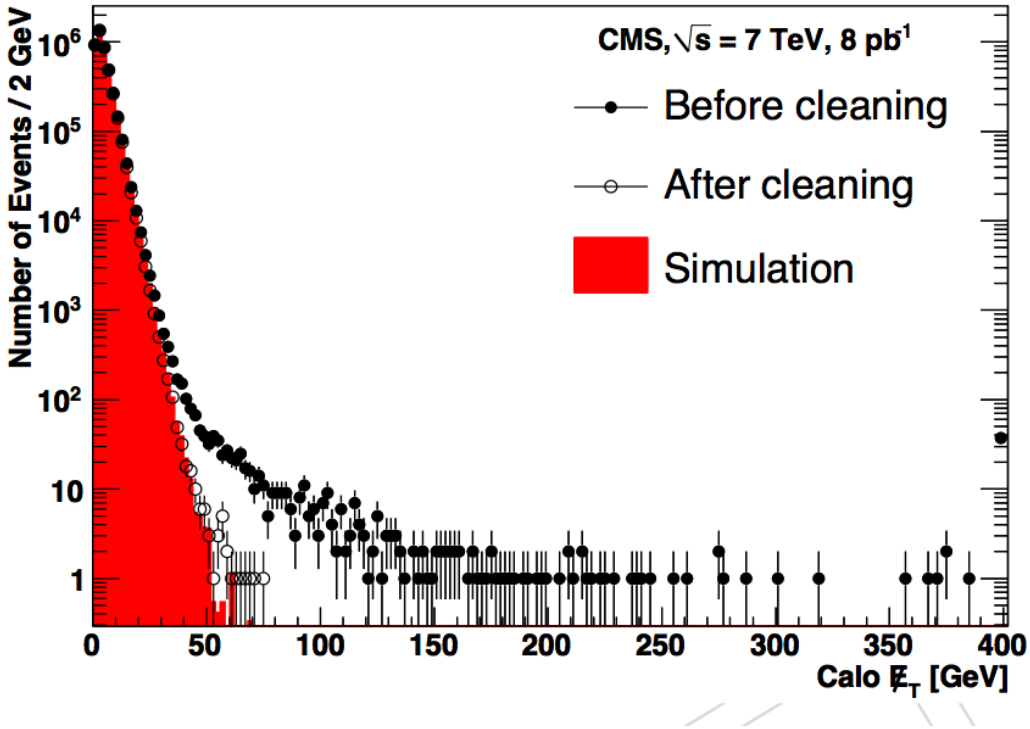

Figure 4.6: calo$\not\!\!E_T$ distributions in a minimum-bias data sample with and without cleaning and filters, compared to simulation. The highest bin is an overflow bin. From Ref. [58].

calo$\not\!\!E_T$ tends to underestimate the magnitude of the $\not\!\!E_T$ the most. Typical correction factors for calo$\not\!\!E_T$ can reach a factor of 2 whereas for pf$\not\!\!E_T$ they are less than 1.4. In general either just the type I correction or both type I and type II corrections are applied to the calo$\not\!\!E_T$. For tc$\not\!\!E_T$ neither of the corrections is typically applied and for pf$\not\!\!E_T$ type I corrections are sometimes applied.

In order for the $\not\!\!E_T$ variable to be used in physics analyses to measure the existence of high p_T neutrinos or other weakly-interacting particles it is impor-

tant that noise and anomalous detector effects can be filtered out. Anomalous detector effects that produce high $\not\!\!E_T$ can happen in a variety of ways, including spikes of energy in single crystals in the ECAL or particles hitting the transducers. For more detailed studies of these effects see Refs. [59] and [60]. If only a small number of channels is effected these channels are cleaned (i.e. removed) and the event can stay in the data sample. However, if a large number of channels is effected the event is filtered and tagged as not good for physics analyses. Figure 4.6 shows the calo$\not\!\!E_T$ distribution in data before and after cleaning and filtering versus simulation in minimum bias events. The large $\not\!\!E_T$ tail is removed by the cleaning and filtering and compares well with simulation, which does not include any of these anomalous events. The effect of the $\not\!\!E_T$ cleaning for the other algorithms is similar.

In addition to removing noise and spurious detector activity it is also important for physics analyses using $\not\!\!E_T$ resolution to have the best resolution possible. To compare the resolution of the different algorithms is slightly tricky since the $\not\!\!E_T$ and ΣE_T energy scales are different for each of the algorithms. To correct for this we calibrate the $\not\!\!E_T$ scale and ΣE_T scale of each algorithm to what the generator level scale should be. Figure 4.7 shows a comparision of the $\not\!\!E_T$ resolution vs. ΣE_T in minimum bias events with the first 11.7 nb^{-1} of data. Intrinsically the $\not\!\!E_T$ resolution for all algorithms becomes poorer as a function of ΣE_T because

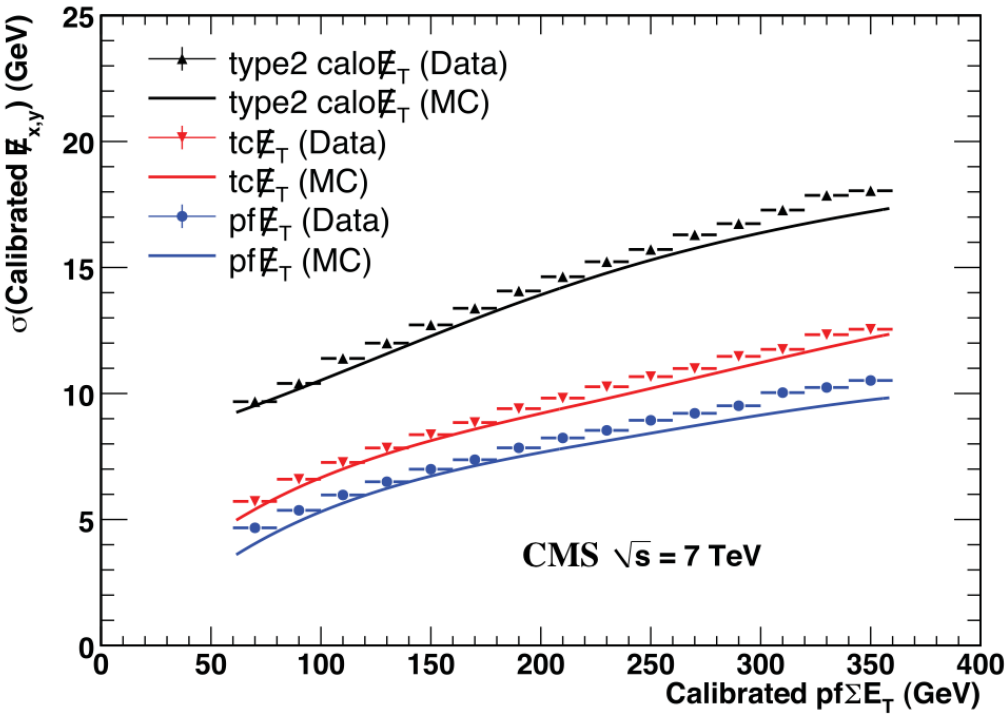

Figure 4.7: Calibrated $\not\!\!E_{Tx,y}$ resolution versus calibrated pfΣE_T for calo$\not\!\!E_T$, tc$\not\!\!E_T$, and pf$\not\!\!E_T$ in data and simulation. From Ref. [58].

there is more event activity and so greater chance for resolution problems. The resolution functions in Figure 4.7 match well between Monte Carlo and data and the pf$\not\!\!E_T$ algorithm has the best resolution of the three algorithms. For a detailed description of this $\not\!\!E_T$ resolution study see the Appendix. For more information on $\not\!\!E_T$ performance at CMS see Ref. [58].

Chapter 5

Search for supersymmetry

In this analysis we perform a search for supersymmetry at CMS using 36 pb^{-1} of data taken during the 2010 run. We specifically look at an event signature with a single isolated lepton (where for this analysis a lepton refers to an electron or a muon[1]) and at least four jets (with low p_T thresholds). Though the single isolated lepton requirement reduces the SUSY signal efficiency (for most SUSY models the branching fraction to leptons is 5-15%[2]), it has the nice feature of making QCD the sub-dominant background. QCD is very hard to predict and by making it one of our smaller backgrounds we don't have to worry as much

[1]Taus are not as clean objects in the detector as muons or electrons so they have been avoided for this analysis.

[2]See Sec. 2.3 for a more detailed explanation of how leptons are created in SUSY models

about weird detector effects.[3] In addition, the lepton channel is a probe of a distinctive SUSY decay chain where there has been an electroweak decay.

The four jet requirement reduces the amount of QCD further while also reducing other standard model backgrounds such as W+jets, Z+jets, and single top. In addition to the basic lepton and jet requirements we use variables such as $\not\!\!E_T$ and H_T, where $\not\!\!E_T$ is the transverse missing momentum and H_T is the scalar sum of jets in the event (see Sec. 5.2.6 for the exact definitions) to try to discriminate between supersymmetry and standard model physics. On an event-by-event basis we cannot tell whether an event was the result of standard model or supersymmetry production. However, SUSY models tend to have higher $\not\!\!E_T$ and H_T due to the higher mass scales of the SUSY particles compared to the standard model particles. Thus, an excess in events in the tails of these distributions could be a sign of supersymmetry.

Though there are nice theoretical motivations for supersymmetry (discussed in detail in Sec. 2.3) no evidence for it has been found at previous experiments. Supersymmetry searches at collider experiments such as the Tevatron [61, 62, 63] and LEP [64] have found no excess of events beyond the standard model and

[3]The QCD background is hard to predict for a couple reasons. First, the QCD contribution has a very large cross section so even if there is a small chance for certain anomalous events, such as a jet going through a crack in the detector and causing large $\not\!\!E_T$, the large cross section gives some chance for these to happen. Requiring a lepton removes almost all of these events because there is a very small probability that one of these anomalous events will overlap with a good event that has an isolated lepton. Second, there is a large uncertainty on the QCD cross section and we do not trust many of the Monte Carlo shapes of kinematic distributions.

have set limits in the CMSSM. Other searches at CMS [65, 66, 67, 68, 69] (using different event signatures than this analysis) and ATLAS [70, 71, 72, 73], based on the 2010 LHC run, have also found no evidence for supersymmetry.

5.1 Overall search strategy and methods

The strategy of this search is to reduce the amount of standard model background to only a handful of events (by making requirements on H_T and $\not\!\!E_T$) and then to predict, using data-driven background methods, the remaining small standard model contribution. The use of data-driven background methods is important, since we do not trust the Monte Carlo to model all effects that could result in standard model events passing our selection requirements and having large $\not\!\!E_T$ and H_T. In fact, for any discovery of supersymmetry the prediction from the simulation is not going to be enough to convince the world of the discovery, it will only convince the world that there is some effect that the Monte Carlo is not modeling correctly.[4] The Monte Carlo is very good in general but has some limitations when predicting all the complex detector and software performance. In addition, the kinematic distributions and cross sections of different standard model processes are not exactly known. Our data-driven methods rely minimally

[4] Even with data-driven methods people might say there is some effect we don't understand. However, at least with data-driven background methods we are trying to model things we don't know as much as possible.

on the Monte Carlo, mostly requiring that the data-driven method works well when tested on the Monte Carlo and that any deviations in the prediction in the Monte Carlo can be understood using a precise physical interpretation.

Since the parameter space for SUSY is very large and any discovery of new physics will need many cross-checks, we use multiple background determination methods. This helps ensure that we fully understand our event sample and that effects such as a bias or signal contamination in one method can be cross-checked with another method.[5] Also, different background determination methods can be sensitive to different kinematic regions and thus different SUSY models.

This analysis uses two separate methods that both use control samples in the data for the predictions but emphasize different objects in the event when making the prediction. The first method uses the variables H_T and $\not\!\!E_T/\sqrt{H_T}$ to look specifically at the jets and $\not\!\!E_T$ in the event and see if they are consistent with what the standard model predicts. To make the prediction this method relies on the empirical observation that H_T and $\not\!\!E_T/\sqrt{H_T}$ are uncorrelated in the major standard model backgrounds, $t\bar{t}$ and W+jets. When making the prediction this method does not separate the different standard model contributions, since all the major backgrounds show little to no correlation in the variables and they can be lumped together without effecting the prediction. However, the small QCD

[5] All methods have some issues that make them imperfect. This is what makes data-driven methods so difficult to come up with.

contribution (which does have a correlation in these variables) is estimated using separate control regions in the data.

The second method, called the lepton spectrum method, predicts the $\not\!\!E_T$ distribution in the largest backgrounds, $t\bar{t}$ and W+jets events with a single lepton from a W, using the lepton p_T spectrum. In these events the $\not\!\!E_T$ is dominated by the high p_T neutrino (as opposed to detector mismeasurement) and because both the lepton and neutrino come from a W-boson their spectra are very similar. Differences in the lepton and neutrino spectra are corrected for and can come from effects such as the W-polarization, resolution, and other effects that are discussed in detail below. For SUSY models the $\not\!\!E_T$ generally comes from the two lightest supersymmetric particles (LSPs), not a high p_T neutrino. For this reason the $\not\!\!E_T$ and lepton p_T are not related in the same way as for $t\bar{t}$ and W+jets events. In SUSY events the lepton p_T tends to be much less than the $\not\!\!E_T$ from the LSPs and a deviation in the $\not\!\!E_T$ tail from SUSY would not be predicted from the lepton p_T distribution.[6] The separate smaller standard model contributions including dilepton $t\bar{t}$ events feeding down to the single lepton sample, $\tau \to \ell$ ($\ell = e$, μ) decays in $t\bar{t}$ and W+jets events, and the QCD background, can not be accurately predicted using the lepton p_T spectrum and must be estimated using separate control samples.

[6]We have to be a little careful here. In SUSY models where the $\not\!\!E_T$ comes from a high p_T neutrino this method will not be able to differentiate between SUSY and standard model.

Both methods have nice features and drawbacks. The method using the H_T and $\not\!\!E_T/\sqrt{H_T}$ variables is very simple and because of this is very robust to many different systematic effects. However, it is hard to understand the underlying physics reason why the two variables should be uncorrelated and the empirical observation that they are uncorrelated must be trusted. In addition, signal contamination of the control regions can be a real issue if the mass scale of the SUSY models is just above the standard model. The lepton spectrum method is nice because there is an underlying physical explanation for why the lepton and neutrino spectra are similar and because it is very robust to SUSY signal contamination of the control regions in most SUSY models. However, the lepton spectrum method is much more complicated (employing different predictions for the different background contributions and making corrections for some of the predictions) than the H_T and $\not\!\!E_T/\sqrt{H_T}$ method and has larger systematic uncertainties. The lepton spectrum method also will have large signal contamination if the $\not\!\!E_T$ and lepton p_T are similar in SUSY. Overall the two methods provide complementary predictions that will provide a cross-check for each other.

For each method we employ two selection criteria for the search regions, a first called loose selection and a second called tight selection. The loose selection was chosen to give a larger statistics sample where the background determination

methods can be examined. The tight selection was motivated by the fact that for models with higher mass scales, the $\not\!\!E_T$ and H_T distributions are shifted upwards, but the production cross sections fall rapidly. In such scenarios, tighter cuts on $\not\!\!E_T$ and H_T can improve the sensitivity to these higher mass models.

5.2 Event selection

In this section we describe the basic event selection (i.e. preselection) for the single lepton SUSY search and the motivation for this selection.

5.2.1 Overview of selection cuts and background composition

Our selection requirements are only loosely determined by SUSY models since the number of SUSY models is large and choosing a specific model to base our selection on might hurt our sensitivity to other models. To give the most general SUSY results the basic event selection for different analyses in CMS is determined by requiring the presence of basic measurement objects such as leptons, jets, or photons and then understanding the event sample with these requirements in place. In our analysis the requirement of a single lepton and four jets determines our signature and changes our event sample with respect to these

other analyses, which require different signatures (such as a lepton, photon and jets, or two leptons and two jets, etc.). Once we understand our event sample with this basic signature in place we can add additional requirements on objects such as $\not\!\!E_T$ and H_T to give better discriminating power between the standard model and SUSY. Explanation of the signal regions in $\not\!\!E_T$ and H_T will be saved until later sections, where the background determination methods are described.

After requiring a single isolated lepton and four jets the dominant background is $t\bar{t}$. The next largest background is W+jets and the other backgrounds (QCD, single top, Z+jets) are very small. The QCD contribution is reduced by a large amount by requiring a single isolated lepton. Leptons from QCD events can arise from semi-leptonic decays of a b or c hadron or from the misidentification of a hadron as a lepton. Usually the leptons from a semi-leptonic b or c decay are close by many other particles in a jet and are easily rejected by an isolation cut, which requires that only a limited amount of transverse energy surrounds the particle. The identification requirements of the lepton, described in detail in Sec.5.2.5, remove most of the hadrons that are misidentified as leptons. The small leftover contribution from both these types of events are estimated using data-driven methods described in detail below. For electrons there is some additional number of events where a photon conversion in the material can create an electron and this must be rejected using additional identification cuts.

In order to avoid overlap with other searches performed at CMS we require that there be exactly one lepton, and veto any events with more than one lepton. In addition to avoiding the statistical overlap with other searches at CMS this requirement also provides a large rejection factor to backgrounds with two leptons, such as Z+jets events, where the Z boson decays into two leptons or no leptons (hadronic decay). Even with a veto on a second lepton there are still a few cases where dilepton events escape the veto and feed-down to our single lepton sample. This feed-down contribution must be understood since in dilepton events there are two neutrinos, and thus there can be a large amount of $\not\!\!E_T$. Events from $W \to \tau \to \ell$ are also present after the final selection and their small contribution must be determined as well.

The jet requirements reduce many of the electroweak and QCD backgrounds. When requiring several jets in processes such as Z+jets, W+jets or QCD the additional jets come from QCD corrections to the leading order processes, which decrease the overall cross section due to the extra coupling constant factor(s). Thus, the cross section for backgrounds such as Z+jets, W+jets, and QCD decreases sharply as you increase the number of jets. For $t\bar{t}$ events the story is slightly different since in a semi-leptonic $t\bar{t}$ decay there are already four jets at leading order (though whether these jets fall within the detector acceptance or above the p_T requirement is another question), two of which come from a b quark

and two of which come from the hadronic decay of one of the W bosons. For most SUSY models the multiplicity of jets is high since there are two massive objects created intially and the long decay chain of these objects creates many jets.

5.2.2 Monte Carlo simulation samples used

Though we try to limit our dependence on Monte Carlo simulation in this analysis, using simulation is important to determine the analysis procedures and to check the validity of the background methods. We use Monte Carlo event samples based on a variety of event generators, including MadGraph [74], Alpgen [75], and Pythia [76]. After the production with the event generator the detector performace and other effects are simulated using the GEANT package [77]. The detector geometry description with GEANT includes realistic subdetector conditions such as dead channels. For our largest background, $t\bar{t}$, we use a Madgraph sample with tune Z2 [78] tauola and assume a cross section of 157 pb. For the electroweak samples, W+jets and Z+jets, both MadGraph and Alpgen samples are used. For the W+jets sample there is a requirement placed at generator level that the W boson decay into a lepton (τ, μ, or e). The NNLO cross section used for this process has been determined to be 31.3 nb. For the Z+jets sample there is a requirement at generator level that the

Z boson decay to a dilepton pair [7] with an invariant mass larger than 50 GeV. The NNLO cross section used for this process has been determined to be 3.05 nb. The QCD and single top samples are generated using Pythia Monte Carlo generator with tune Z2.

To investigate signal properties different SUSY benchmark models within the CMSSM parameter space are generated using Pythia and GEANT. The CMSSM space benchmark points are chosen for historical reasons (to be able to compare to previous experiments such as D0 and LEP) and because of the simplicity of the models (there are very few parameters). Two of the more common model points in CMS, LM0 and LM1, are described in detail in Sec. 2.3. These model points are beyond the reach of the Tevatron and LEP and have leading cross sections of 38.9 pb for LM0 and 4.89 pb for LM1. Additional process-by-process k-factors are applied to the leading order cross section to obtain the NLO cross sections. Monte Carlo scans over the CMSSM parameter space were used for the final CMSSM exclusion plots. The CMS fast simulation package, which performs the detector simulation by making some simplifying assumptions to increase the speed of the simulation, was used to greatly reduce the amount of time to produce these scans.

[7] This includes $\mu\bar{\mu}$, $e\bar{e}$, $\tau\bar{\tau}$. This sample does not include $Z \to \nu\bar{\nu}$.

5.2.3 Data samples used and trigger requirements

The data samples used for this analysis were collected from March through November, 2010 and consist of pp collisions at a center-of-mass energy $\sqrt{s} = 7$ TeV. Of the data collected, 36 pb^{-1} was designated as good, meaning that all subdetectors of CMS were on and working properly.

The trigger paths used to obtain the data require a lepton above a certain p_T threshold and in some cases a certain amount of jet energy in conjunction. For the muon channel there is no isolation requirement made at the trigger level. In the muon channel for the first 3 pb^{-1} of data the p_T threshold at trigger level was 9 GeV. For the next 14 pb^{-1} of data this threshold was raised to 11 GeV due to the increase in luminosity. For the remaining 19 pb^{-1} of data in the muon channel the LHC luminosity increased above 2 x 10^{32}cm^{-2}s^{-1} and a cross trigger was implemented with the requirements that $p_T(\mu) > 5$ GeV and $H_T^{trigger} > 70$ GeV, where $H_T^{trigger}$ is the scalar sum of the uncorrected jet E_T values measured at trigger level. These online requirements are compatible with our offline muon p_T thresholds of either 15 or 20 GeV.

In the electron channel many different triggers are used, all requiring a single electron with p_T ranging from 10–17 GeV, depending on the luminosity. In addition, for some of the higher luminosity runs there are isolation and identification requirements made on the electron to reject fake electrons and electrons

from QCD events. All single electron triggers are compatible with our offline threshold, $p_T(e) > 20$ GeV, and offline identification and isolation requirements.

In the electron channel in some cases it is important to use the isolation variable as a handle to estimate the QCD background. For this reason, certain QCD estimates in this analysis use hadronic based triggers, where there is no electron requirements at trigger level. These hadronic triggers require $H_T^{trigger} >$ 100–160 GeV, where again the H_T is calculated using uncorrected jet E_T. For there to be no bias from these triggers, the offline H_T, which is calculated using corrected jet p_T and defined explicitly in Sec. 5.2.6, must be greater than around 300 GeV.

5.2.4 Event cleaning

For the data considered we apply certain event cleaning requirements with goal of eliminating anomolous events that can be produced in various ways and can effect our physics studies. We require that in each event there be at least one good primary vertex (PV). A primary vertex is defined to be good if its z position is less than 24 cm away from the nominal center of the detector and its transverse distance, ρ, is less than 2 cm away from the nominal center of the detector. These requirements ensure that the particles coming from the interaction of the protons are contained within the detector.

In addition to requiring a good primary vertex we also apply a scraping filter. Early on in the 2010 data taking there were certain events that caused a shower of hundreds of tracks in one side of the silicon tracker. This effect was determined to come from the proton beam scraping the pipe surrounding it and creating many particles that would subsequently reach one half of the detector. To avoid these anomolous events we require that if there are more than 10 tracks in the event, 25% or more of them have to be defined as "high purity", which gives some requirements on the track quality. This filter essentially removes these type of events because most of the tracks from the beam scraping are poorly defined tracks and thus not defined as "high purity".

We apply an additional filter called the Hadronic Barrel Hadronic Endcap (HBHE) noise filter. This filter rejects events that record anomalous signals in the hadronic calorimeter. These anomalous signals can come from effects such as particles hitting the transducers or from rare random discharges. Some of these effects were observed very early on in the 7 TeV data taking, and in some cases even prior to this, during past test beams and cosmic data taking [59]. Detailed studies of these effects in the hadronic calorimeter are described in Ref. [60].

Another effect that must be considered is beam halo, which can cause large $\not\!\!E_T$ due to asymmetric energy deposits in the detector. Beam halo is caused by the production of muons, via proton collisions, upstream from the interaction point.

These muons then subsequently continue down the beamline and hit the forward muon detector, the Cathode Strip Chambers, and then the Electromagnetic and Hadronic calorimeters. Dedicated filters have been developed at CMS to reject beam halo events [79]. However, as Figure 5.1 shows, once you apply any muon trigger these beam halo events are negligible and a beam halo filter is not necessary. Thus, we do not apply any filter on beam halo events.

5.2.5 Preselection cuts

With the pre-selection requirements we obtain a sample that is dominated by our main backgrounds, $t\bar{t}$ and W+jets. With this sample we will have a significant number of data events and can investigate basic properties of the sample. The pre-selection requirements are defined to be slightly tighter than our trigger requirements to avoid trigger bias. However, we do not make the pre-selection requirements significantly tighter than the trigger requirements in order to have enough events to understand the basic event properties.

The jet and $\not\!\!E_T$ reconstruction is performed using the particle-flow algorithm [53]. The jet clustering is done using the anti-k_T clustering algorithm [51], with a cone size of 0.5. Corrections to the raw jet energies are applied to establish a relative uniform response across the detector in η and an absolute calibrated response in p_T. Additional jet energy corrections are applied to the

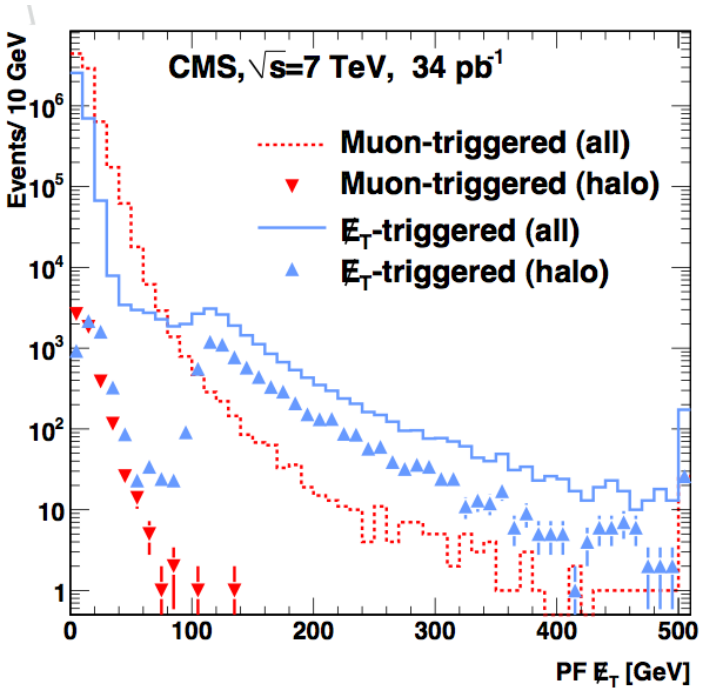

Figure 5.1: $\not\!\!E_T$ distribution for all events analyzed from muon and Calo $\not\!\!E_T$ triggers and for events identified as beam halo. Events recorded by collision muon triggers are shown by the red dashed curve while the subset which met the requirement of the beam halo filter are shown by the red inverted triangles. As can be seen from these distributions the halo muons overlapping with muon triggered events is very small. This is in contrast to Calo $\not\!\!E_T$ -triggered events, shown in blue solid curve, where there are many high $\not\!\!E_T$ events that pass the beam halo filter (blue triangles). Plot from Ref. [58].

data to take into account residual differences between the jet energy calibration in data and MC. Quality criteria are placed on the jets to reject noise and spurious energy deposits. More details on the jet reconstruction are in Sec. 4.4. The $\not\!\!E_T$ is defined to be the negative vector sum of all particles reconstructed by the particle-flow algorithm in the event (see Sec. 4.4 for more details on the $\not\!\!E_T$ reconstruction). For the preselection cuts we require 4 jets of p_T greater than 30 GeV and $|\eta| < 2.4$. We make no requirements on the $\not\!\!E_T$ in the event for the preselection.

In the muon channel we require a muon candidate with $p_T > 15$ GeV and $|\eta| < 2.1$. The $|\eta|$ requirement on the muon is determined by the muon triggers. Though the tracker has coverage out to $|\eta| < 2.4$ the Level 1 muon triggers do not cover the range between $2.1 < |\eta| < 2.4$, so we do not use this range. Several different quality requirements are placed on the muons to reject fake muons and muons that come from QCD processes. A detailed description of the muon reconstruction is given in Sec. 4.1. We require that the reconstructed track have at least 11 hits in the tracker and that the tracker fit have a χ^2 less than 10. We also require that the reconstructed track have an impact parameter in the transverse plane with respect to the beam spot satisying $d_0 < 0.02$ cm and an impact parameter in the z direction with respect to the primary vertex satisfying $d_z < 1$ cm. These impact parameter requirements help remove cosmic ray events

with a muon (after these cuts the cosmic ray background is determined to be negligible). An additional requirement on the muon track is that it must have at least 1 hit in the inner part of the silicon tracker where the silicon pixels are used. The muon must also have at least one segment in the muon chamber that is associated with the global track of the muon.

The isolation of the muon can be used to reject many background events where the muon originates in the semileptonic decay of a b or c jet. The isolation variable used in this analysis is called relative isolation and defined to be $I/p_T(\mu)$, where I is the sum of the transverse momentum in the tracker and the energy deposited in the electromagnetic and hadronic calorimeters in a cone around the muon. The cone is defined in η–ϕ space and its size is $\Delta R = 0.3$, where $\Delta R = [\Delta\eta^2 + \Delta\phi^2]^{1/2}$. To exclude the energy from the muon an inner veto cone is defined where the energy doesn't contribute to I. This inner veto cone size is $\Delta R = 0.01$ in the tracker, $\Delta R = 0.07$ in the ECAL, and $\Delta R = 0.10$ in the HCAL. We require that the ratio $I/p_T(\mu)$ be smaller than 0.10 for this analysis.

In the electron channel the electron candidates must have $p_T > 20$ GeV and $|\eta| < 2.4$, but with the barrel endcap overlap region of $1.4442 < |\eta| < 1.5660$ excluded due to the large number of fake electrons in this region. In addition, certain quality criteria were used to reject fake electrons and electrons from QCD. The quality criteria used in this analysis come from a set of common working

points developed in CMS that look at quantities such as the shower shape of the electron in the calorimeter, the ratio of energy in the hadronic calorimeter to the electromagnetic calorimeter and other quantities. The working point chosen for this analysis gives an electron reconstruction efficiency of 80% in W+jet events. A higher efficiency working point was not chosen because of the increase in fake electrons due to the looser identification and isolation requirements. A detailed description of the electron reconstruction is given in Sec. 4.2. The relative isolation cut in the electron channel is placed at 0.07 in the barrel and 0.06 in the endcap. The cone size for the isolation calculations is the same as for the muon; however, the inner veto cones are slightly different. The size of the inner veto cones for the electron are $\Delta R = 0.015$ in the tracker and $\Delta R = 0.15$ in the HCAL. For the ECAL the inner cone is roughly 3 single crystals centered on the electron track, where we say roughly because it is a function of the η of the electron track. Additional variables, such as the number of hits missing from the innermost part of the track, are used to reject conversion events, where a photon converts into an e^+e^- pair.

In order to ensure that there is only one lepton in the event we require that there be exactly one muon or one electron with the criteria listed above. If there is a second muon or electron in the event passing the above criteria the event is rejected.

Lastly, there is the issue of overlap between different particle-flow objects in the event. For instance, it is common for an electron to be reconstructed as a jet and a muon can also be reconstructed as a jet. To remove this overlap we apply a cross cleaning of the event objects. First, we disregard a jet if there is an electron (satisfying all cuts) within a $\Delta R <= 0.3$. Second we disregard a jet if there is a muon (satisfying all cuts) within $\Delta R <= 0.1$. Third, we disregard a muon if there is a jet within $\Delta R <= 0.3$.[8]

In summary the event criteria for the preselection is exactly one good lepton and 4 jets with $p_T > 30$ GeV, in addition to the event cleaning and trigger requirements. The preselection is used as the common starting point for the different background determination methods, with additional kinematic cuts placed to obtain the signal and control samples.

5.2.6 Definition of analysis variables

This section defines different kinematic variables that we use to make sure that we understand our event sample, some of which we use to define the different control and signal regions. These kinematic variables include $\not{E}_T$, H_T, H_{T2}, M_T, M_3, and S_{MET}.

[8]This last cut is used less so because of overlaps and more so to provide an additional check that the isolation requirement on the muon is working and rejecting muons in jets.

The $\not\!\!E_T$ is the magnitude of the missing momentum vector in the event:

$$\not\!\!E_T = |\mathbf{p_T^{miss}}|, \tag{5.1}$$

and is intended to estimate the magnitude of the momentum carried by unobserved particles in the plane transverse to the beam direction. However, in some cases this quantity can be dominated by detector effects that give rise to asymmetries in the event reconstruction. A more detailed explanation of how the $\not\!\!E_T$ is exactly calculated at CMS is given in Sec. 4.4.

The H_T quantity is the scalar sum of the transverse energies of jets j above a threshold of $p_T^j > 20$ GeV:

$$H_T = \sum_{j=\text{jets}} E_T^j, \tag{5.2}$$

The variable H_{T2} is exactly the same as H_T but with the highest p_T jet in the event removed from the sum over jets. H_{T2} is less sensitive than H_T to mismeasurements of the highest p_T jet in the event since this jet is removed from the sum.

The variable M_T is a measure of the transverse invariant mass of the lepton and $\not\!\!E_T$. It is defined to be:

$$M_T = \sqrt{2(p_T(\mu)\not\!\!E_T - p_x(\mu)p_x(\nu) - p_y(\mu)p_y(\nu))}, \tag{5.3}$$

and in events where the lepton and $\not\!\!E_T$ are a result of a W boson decay the M_T distribution peaks at around the W mass and has a sharp falloff at values larger than the W mass.

M_3 is the invariant mass of the combination of three jets for which the resulting transverse momentum is highest. This variable effectively tries to reconstruct the top mass in $t\bar{t}$ events. In other standard model samples the peak in M_3 at the top mass is much smaller than in $t\bar{t}$.

The quantity S_{MET} is defined to be:

$$S_{MET} \equiv \not\!\!E_T / \sqrt{H_T}, \tag{5.4}$$

where again the sum in the denominator is over all jets with $p_T > 20$ GeV. S_{MET} is sometimes called $\not\!\!E_T$ significance because it offers an event-by-event assessment of whether the $\not\!\!E_T$ in a given event is consistent with the known measurement resolutions of the jets [79].

5.3 Event properties after preselection cuts

We will now investigate the event properties of our sample after the preselection requirements. In particular, we want to make sure that the event yields and kinematic distributions are consistent with an event sample dominated by $t\bar{t}$ and W+jets, as expected from the Monte Carlo. This is important because

our data-driven background methods rely on the fact that the samples we are studying are dominated by $t\bar{t}$ and W+jets and that the kinematic distributions of these variables are not totally different than in the Monte Carlo. If the event composition or kinematic distributions of our data sample was significantly different than what we expect from the Monte Carlo (for instance if $t\bar{t}$ and W+jets weren't our largest backgrounds or our sample was dominated by anomalous detector events) we would not trust our data-driven methods to make predictions of the tails of the $\not\!\!E_T$ and H_T distributions.

Table 5.1 shows the event yields in Monte Carlo and data after the preselection cuts in both the muon and electron channels. As stated previously our largest backgrounds after the preselection cuts are $t\bar{t}$ and W+jets. The other smaller backgrounds include QCD, Z+jets, and single top (all other SM backgrounds are negligible). The amount of QCD in the electron channel is about twice as much as the muon channel due to the larger number of fake electrons than fake muons. Event yields for the two signal benchmark points, LM0 and LM1, are also shown. Table 5.1 also shows the yield numbers after requiring $\not\!\!E_T > 25$ GeV, which reduces the number of QCD events by roughly a factor of 5.

In both the muon and electron channel and before and after the $\not\!\!E_T > 25$ GeV cut there are more data events than total SM Monte Carlo events. It turns out

Table 5.1: Event yields SM backgrounds in Monte Carlo samples, data, and in SUSY Monte Carlo samples after applying the pre-selection requirements. The Monte Samples are normalized to the integrated luminosity of the data sample, 36 pb^{-1}. The yields are given for the muon and electron channels, and combined, both before and after a loose requirement on the minimium transverse energy of the event, $\not\!\!E_T > 25$ GeV. For the SUSY models LM0 and LM1, the NLO cross sections are used. The LM0 model is a benchmark model near the current Tevatron limits in the mSUGRA plane. Table from Ref. [80].

Sample	μ	μ ($\not\!\!E_T > 25$ GeV)	e	e ($\not\!\!E_T > 25$ GeV)	tot	tot ($\not\!\!E_T > 25$ GeV)
QCD	57	13	120	21	177	34
W + jets	137	110	110	87	247	197
Z + jets	27	10	31	8.4	59	18
$t\bar{t}$	289	249	237	201	525	450
single top	15	13	12	10	27	23
total SM MC	525	395	510	327	1035	722
data	580	444	581	391	1161	835
SUSY LM0	103	99	82	80	185	179
SUSY LM1	7.4	7.2	5.2	5.2	12.6	12.4

that this is due to the Monte Carlo underestimating the amount of W+jets with ≥ 4 jets by roughly 40% (this disagreement is not seen in lower multiplicity bins). This effect was first noticed in the $t\bar{t}$ single lepton cross section measurement at CMS, and their analysis [81] describes this effect in more detail. In fact, this disagreement between Monte Carlo and data backs up our earlier point regarding the importance of data-driven methods. Though the Monte Carlo simulation has done remarkably well at CMS you don't know where differences will pop up.

We will now compare the data and Monte Carlo for many different kinematic distributions after the preselection and $\not\!\!E_T > 25$ GeV requirement[9] to see if they agree. To correct for the W+jets Monte Carlo underestimate and so that we can compare shapes of the distributions correctly we increase the W+jets cross section with respect to its NNLO value of 31.3 nb by 40% while keeping the Monte Carlo cross section of $t\bar{t}$ at its nominal value of 157 pb (the other backgrounds are kept at their nominal values as well[10]). This increase in cross section for W+jets is applied in both the electron and muon channel and only to distributions in this section unless otherwise stated. In our data-driven methods presented later in this Chapter we do not use the fact that the Monte Carlo underestimates the W+jets contribution. This is because these methods are based on control samples in the data and should take this into account.[11]

Figure 5.2 shows for the muon channel different energy related quantities such as $\not\!\!E_T$, S_{MET}, and M_T. Thes shapes of these distributions agree well between the Monte Carlo and data. Figure 5.3 shows the same distributions for the electron channel and similar conclusions can be made. We have scanned many different distributions and they all show reasonably good agreement between

[9] The $\not\!\!E_T > 25$ GeV requirement reduces the amount of QCD so that we are comparing data and Monte Carlo in a sample dominated by basically just $t\bar{t}$ and W+jets.

[10] Some people have asked why we don't float the QCD cross section as well. It is because after the $\not\!\!E_T > 25$ GeV requirement there is very little QCD and variations in the QCD cross section will make a very little effect

[11] There is a small caveat. With a different fractional amount of W+jets and $t\bar{t}$ the methods might perform differently. This is addressed in the systematic studies.

the data and Monte Carlo. Figure 5.4 (5.5) shows the jet p_T quantities for the muon (electron) channel and Figure 5.6 (5.7) shows the event quantities H_T, H_{T2}, and M_3 (defined in Sec. 5.2.2) for the muon (electron) channel. Finally, Figure 5.8 shows lepton quantities such as the lepton momentum and lepton relative isolation for both muons and electrons.

Having looked at many different basic distributions with the preselection cuts we conclude that the event sample is dominated by $t\bar{t}$ and W+jets as expected and that there are no large discrepancies between the kinematics in the data and Monte Carlo. Since the basic shapes of the kinematic distributions agree well between data and Monte Carlo we can proceed to make background predictions of the tails of these distributions to look for excesses from SUSY.

5.4 Background determination using H_T and S_{MET}

5.4.1 Introduction to method

The first data-driven background method uses two kinematic variables, H_T and $S_{MET} \equiv \not{E}_T/H_T$ (both defined in detail in Sec. 5.2.6), to differentiate between the standard model background and SUSY. Since these variables are nearly uncorrelated for the major backgrounds in this analysis, the ratio of high S_{MET} to low S_{MET} is nearly independent of the value of H_T, and this property can

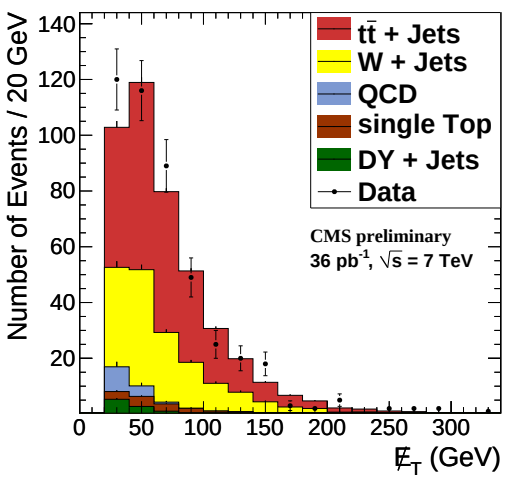

(a) $\not\!\!E_T$ (μ channel)

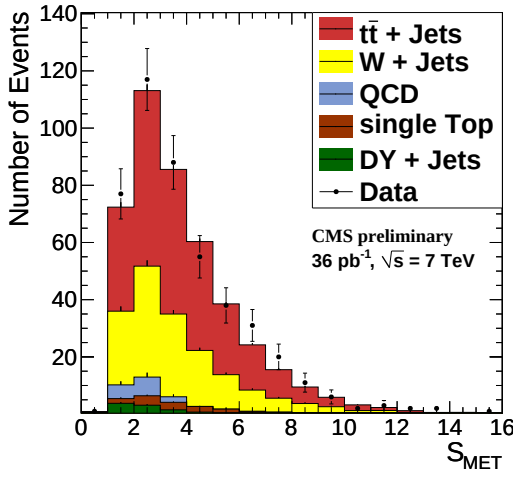

(b) S_{MET} (μ channel)

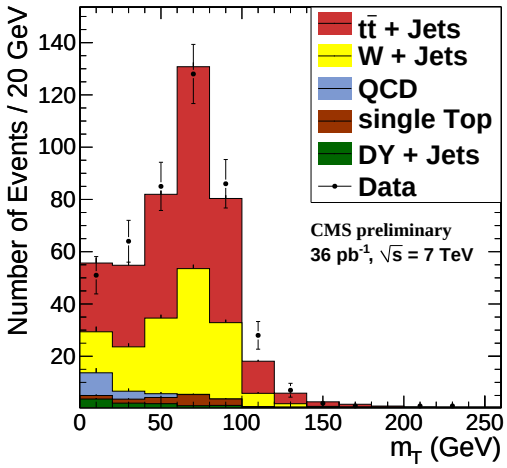

(c) M_T (μ channel)

Figure 5.2: Muon channel: quantities related to missing transverse energy. The data are shown by points with error bars; the Monte Carlo prediction is displayed as the histogram with the individual components summed. Figures from Ref. [80].

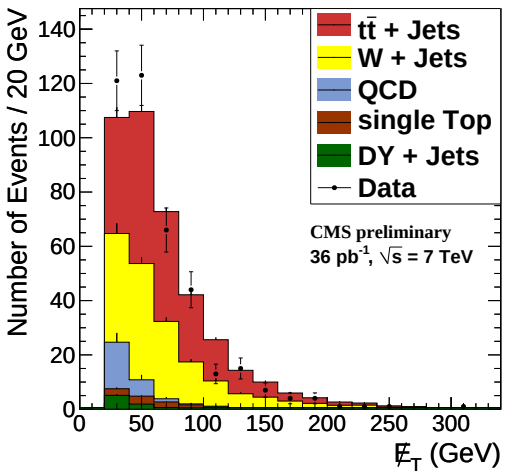

(a) $\not\!\!E_T$ (e channel)

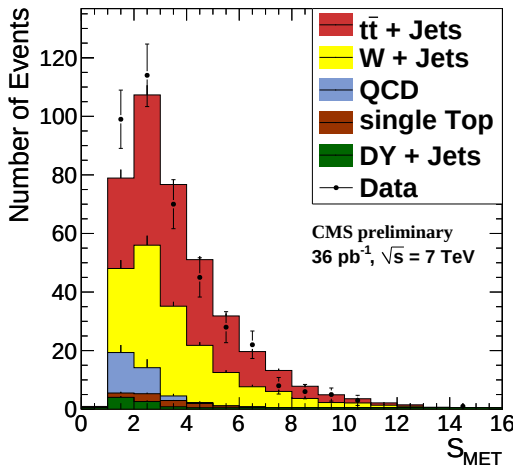

(b) $\not\!\!E_T$ significance (e channel)

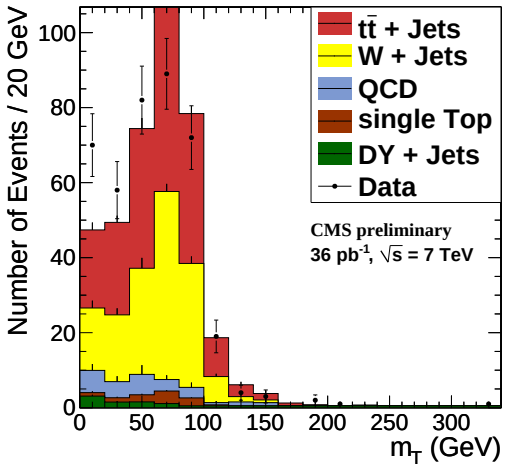

(c) M_T (e channel)

Figure 5.3: Electron channel: quantities related to missing transverse energy. The data are shown by points with error bars; the Monte Carlo prediction is displayed as the histogram with the individual components summed. Figures from Ref. [80].

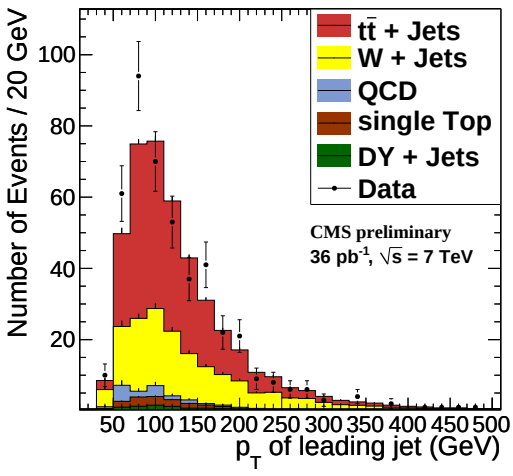

(a) p_T of leading jet

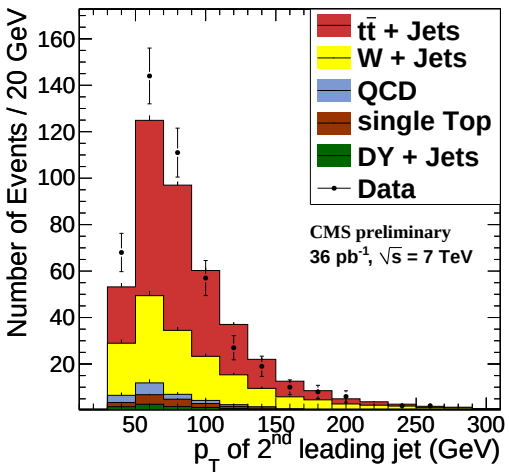

(b) p_T of 2nd leading jet

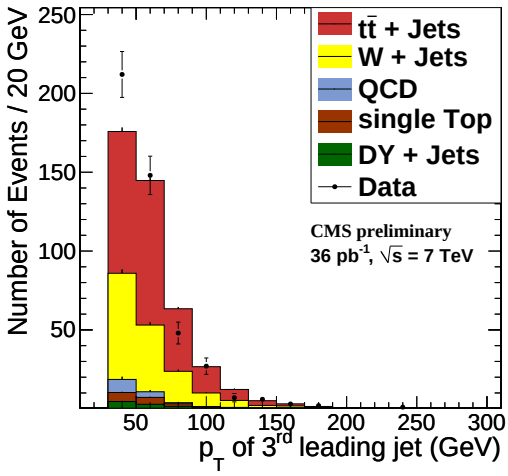

(c) p_T of 3rd leading jet

Figure 5.4: Muon channel: distributions describing jet transverse momenta. Figures from Ref. [80].

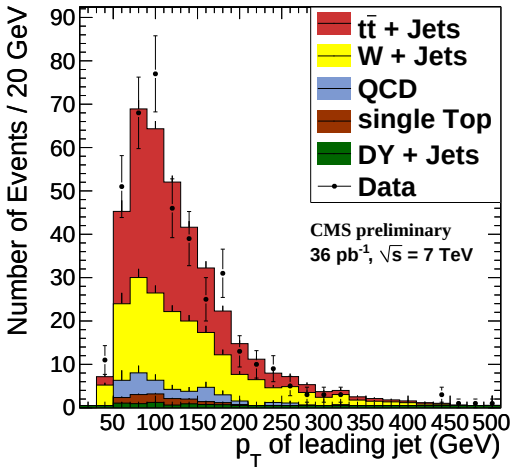

(a) p_T of leading jet

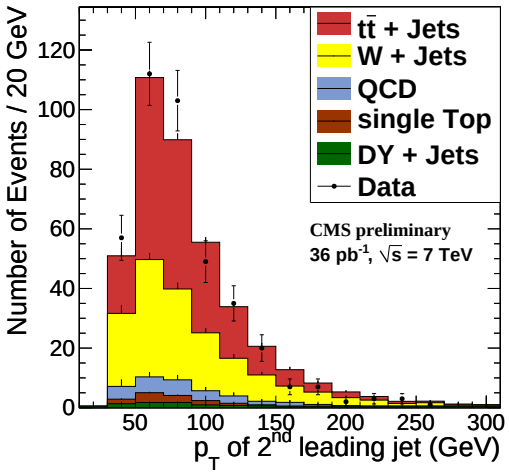

(b) p_T of 2nd leading jet

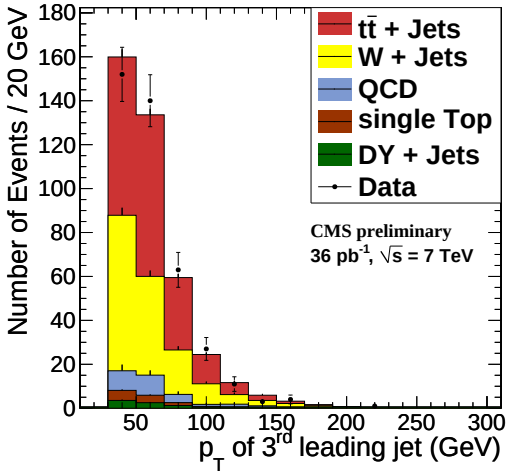

(c) p_T of 3rd leading jet

Figure 5.5: Electron channel: distributions describing jet transverse momenta. Figures from Ref. [80].

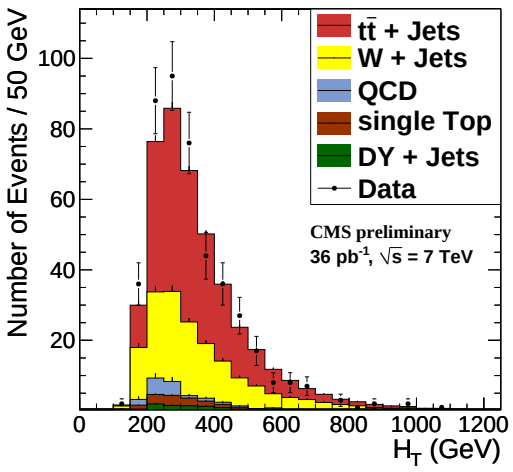

(a) H_T

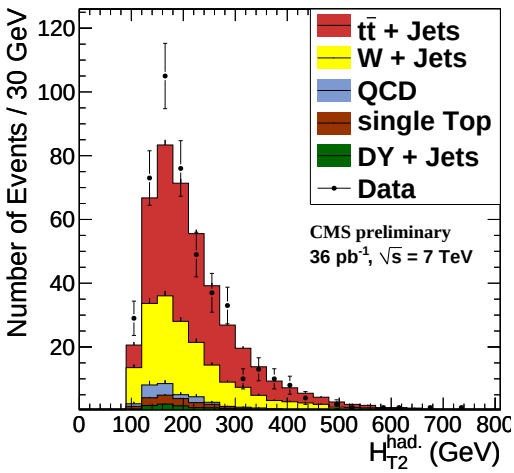

(b) H_{T2}

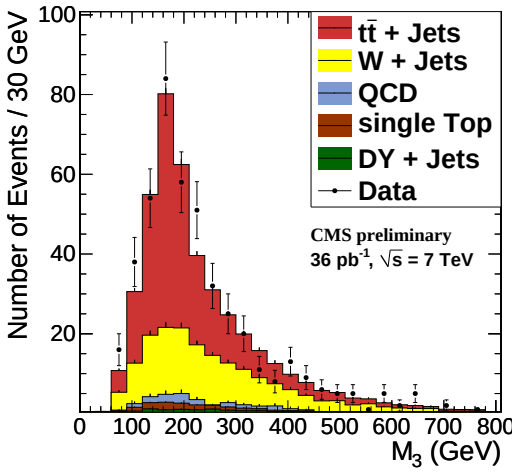

(c) M_3

Figure 5.6: Muon channel: distributions describing global energy properties. Figures from Ref. [80].

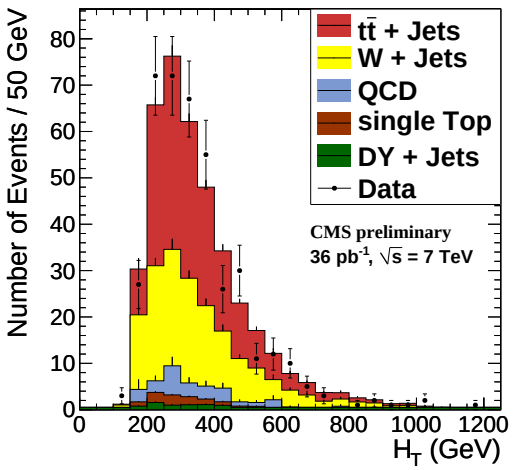

(a) H_T

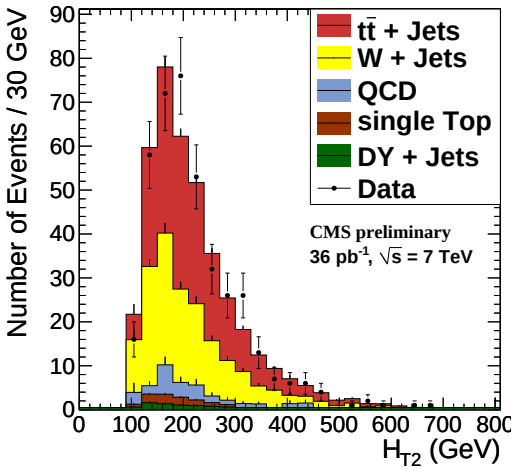

(b) H_{T2}

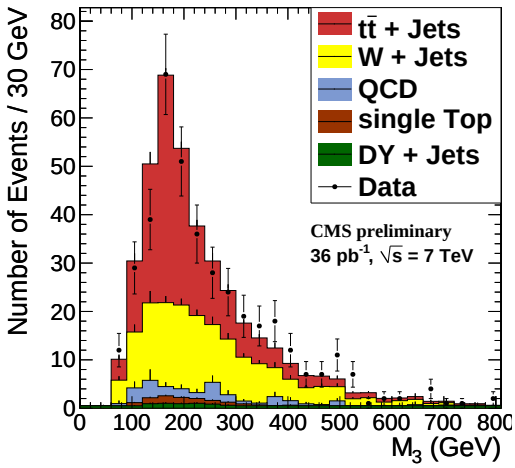

(c) M_3

Figure 5.7: Electron channel: distributions describing global energy properties. Figures from Ref. [80].

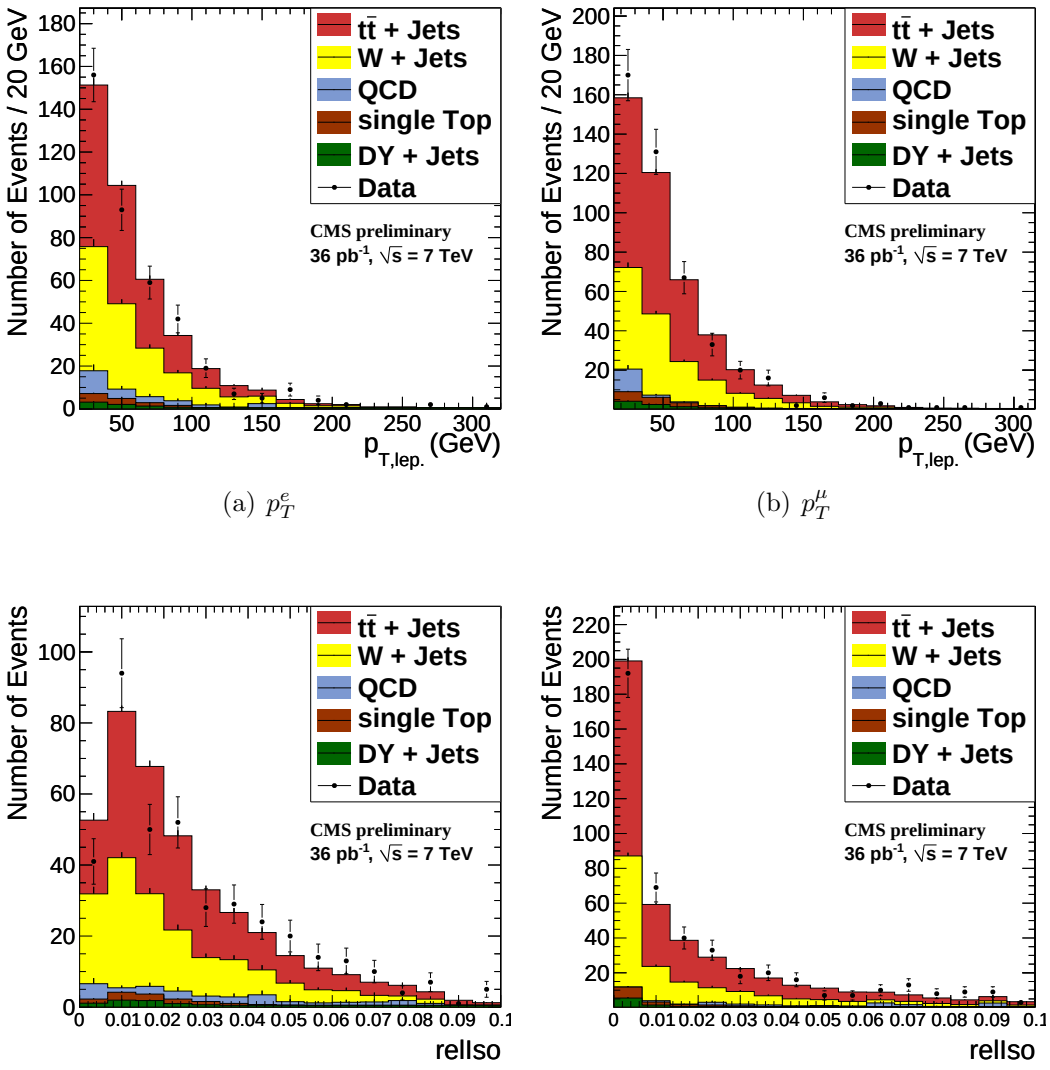

(a) p_T^e

(b) p_T^μ

(c) Relative isolation e

(d) Relative isolation μ

Figure 5.8: Distributions describing electron and muon properties. Figures from Ref. [80].

be used to make a background prediction in the signal region. These variables and a similar procedure were also used in the CMS opposite-sign dilepton SUSY search [82].

5.4.2 Definition of background determination procedure

In this method we first define four different kinematic regions for both a loose and tight selection. The signal region is at high H_T and S_{MET}, where the number of background events is small and where typical SUSY events should lie. The three control regions have either low S_{MET} or H_T or both, and should be dominated by the standard model background.[12] Table 5.2 shows the definition of the control regions (regions A, B, and C) and the signal region (region D) for both the loose and tight selection. The selection criteria for the regions is the same for both the electron and muon channel.

The tight selection was designed for higher mass SUSY models and the control and signal regions were chosen so that only a few SM background events would remain in the signal region. The loose selection was designed for SUSY models with a higher cross section and to gain more statistics in the different control and signal regions. With higher statistics in each of the different regions it gives

[12]Since the range of models in SUSY is vast, depending on the model, there can be some signal contamination in the control regions. Signal contamination is described in more detail later.

Table 5.2: Definition of loose and tight regions for H_T vs. S_{MET} method. Table from Ref. [80].

	Loose selection		Tight selection	
Region	H_T	S_{MET}	H_T	S_{MET}
A	$300 < H_T < 350$	$2.5 < S_{MET} < 4.5$	$300 < H_T < 650$	$2.5 < S_{MET} < 5.5$
B	$400 < H_T$	$2.5 < S_{MET} < 4.5$	$650 < H_T$	$2.5 < S_{MET} < 5.5$
C	$300 < H_T < 350$	$4.5 < S_{MET}$	$300 < H_T < 650$	$5.5 < S_{MET}$
D	$400 < H_T$	$4.5 < S_{MET}$	$650 < H_T$	$5.5 < S_{MET}$

additional events to understand the standard model background and avoids large statistical fluctuations present in the tight selection.

Once the different signal and control regions are chosen it is possible to make an estimate of the amount of standard model background in the signal region in the following way. If the correlation between H_T and S_{MET} is very small (which we will show in the next section) the ratio of high S_{MET} to low S_{MET} is nearly independent of H_T. Thus, the number of events in the signal region D can be estimated from $N(D) = [N(C)/N(A)]N(B)$, where $N(i)$ denotes the number of events in region i.

5.4.3 Lack of correlation between H_T and S_{MET}

As stated previously the two variables H_T and S_{MET} show a lack of a significant correlation in the major backgrounds in the analysis and this will be explicitly shown in this section. This lack of correlation is an empirical statement and it is difficult to understand from fundamental physics properties exactly why this is. However, we apply many different tests to the event sample in Sec. 5.4.7 and quantify the resulting changes in the correlation as the systematic uncertainty of the measurement.

Figure 5.9 shows the distribution of H_T and S_{MET} in slices of each other for the muon channel for both the loose and tight selection in the full Monte Carlo simulation for the background samples. These distributions show that for the total Monte Carlo background sample there is a lack of correlation between S_{MET} and H_T since the shape of each variable is independent of the other variable. In fact, we have also looked at the individual Monte Carlo samples and we find that for the major backgrounds, $t\bar{t}$ and W+jets this lack or correlation holds as well.

Figure 5.10 shows the same distributions of H_T and S_{MET} in slices of each other but for the electron channel. These distributions show that the lack of correlation holds true in the electron channel as well.

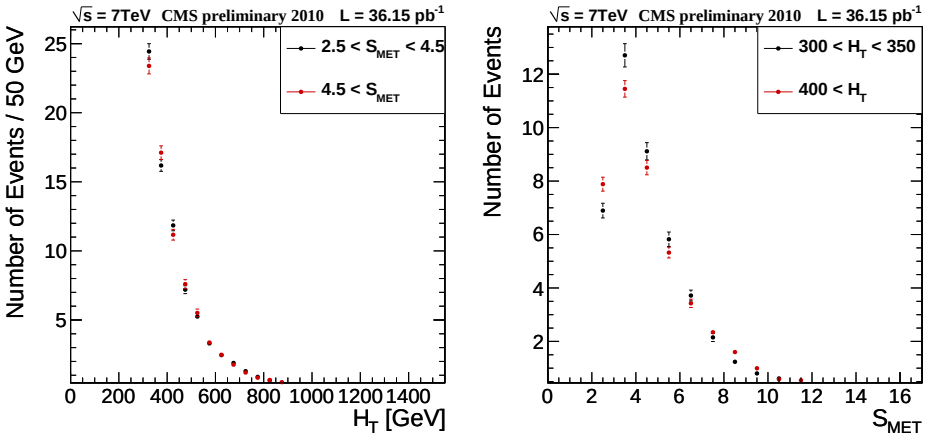

(a) H_T in slices of S_{MET} (loose)

(b) S_{MET} in slices of H_T (loose)

(c) H_T in slices of S_{MET} (tight)

(d) S_{MET} in slices of H_T (tight)

Figure 5.9: Plots of H_T and S_{MET} for total Monte Carlo background in the μ-channel for the loose (top) and tight (bottom). In each case, the distribution is shown in two slices of the complementary variable. Figures from Ref. [80].

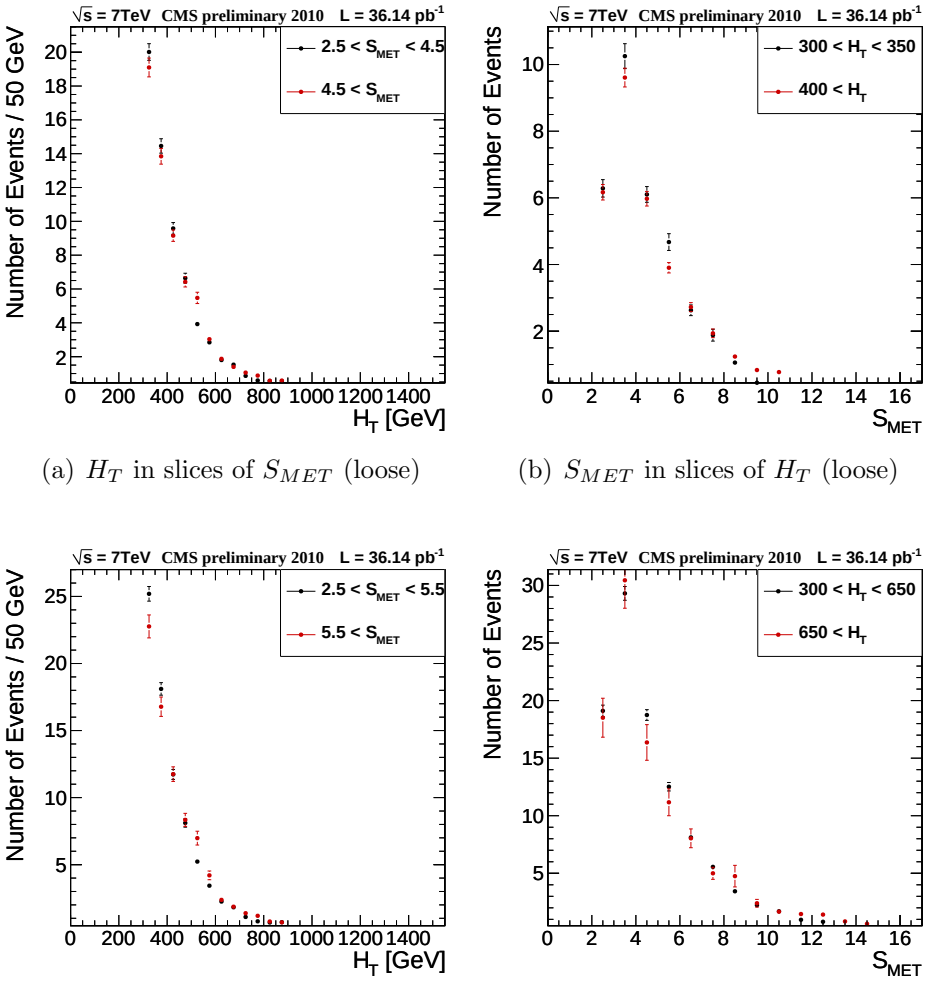

(a) H_T in slices of S_{MET} (loose)

(b) S_{MET} in slices of H_T (loose)

(c) H_T in slices of S_{MET} (tight)

(d) S_{MET} in slices of H_T (tight)

Figure 5.10: Plots of H_T and S_{MET} for total Monte Carlo background in the e-channel for the loose (top) and tight (bottom). In each case, the distribution is shown in two slices of the complementary variable. Figures from Ref. [80].

Though S_{MET} is a slightly more complicated variable to interpret than $\not\!\!E_T$, $\not\!\!E_T$ shows a significant correlation with H_T and thus can not be used in this method instead of S_{MET} to make a background prediction.[13]

5.4.4 Monte Carlo and data distributions of H_T and S_{MET}

Before discussing the explicit background prediction for the Monte Carlo and the data we first look at different H_T and S_{MET} distributions to get an idea of the shape differences between SM and SUSY (in Monte Carlo) and also to compare what is observed in the data to what the Monte Carlo simulation predicts.

Figure 5.11 shows the two dimensional distributions of S_{MET} vs. H_T in the muon channel for different Monte Carlo background samples, the data, and the two SUSY signal models, LM0 and LM1. The different regions for the tight selection are drawn on the distributions and all distributions are normalized to 36 pb^{-1}. The data tend to lie at lower H_T and S_{MET} as would be expected from the SM Monte Carlo simulation. The SUSY model LM1 lies at significantly higher H_T and S_{MET} than the background samples. The SUSY model LM0 does not lie at as high values of H_T and S_{MET} as LM1 due to its lower mass scale.

[13]In fact, we could try to measure the correlation between $\not\!\!E_T$ and H_T but we decided against this to keep the method as simple as possible. Even though the lack of correlation between S_{MET} and H_T is hard to understand from a basic physics perspective, the simplicity of this method is what makes it so nice. This is in contrast to the lepton spectrum method, which is much more complicated, but much easier to understand from basics physics arguments.

In the tight selection the control regions would in fact have large contamination from LM0, which can be seen from the two dimensional distributions. This signal contamination would still exist even in the loose selection in the presence of LM0 due to its large cross section and the fact that LM0 does not lie at much higher H_T and S_{MET} than the background samples. In the case of LM1 there is relatively little signal contamination because of its high mass scale and low cross section. Signal contamination can bias the background prediction but it is quite complicated to take into account due to the fact that there is not a single signal model that can represent all possible scenarios and that the cross sections of different models vary widely. This is a main reason we use multiple methods to cross-check our results.

Figure 5.12 shows similar two dimensional distributions of S_{MET} vs. H_T for the electron channel. The distributions look very much the same as those in the muon channel, and similar conclusions can be made.

The individual distributions of H_T and S_{MET} in the muon channel are shown in Figure 5.13. These distributions are plotted in the combined A, B, C, and D regions and the W+jets cross section has been scaled with the same factor as in Sec. 5.3. The standard model background samples are summed and the SUSY models, LM0 and LM1 are not summed. The observed data distributions agree well with the summed Monte Carlo background distributions. Figure 5.14

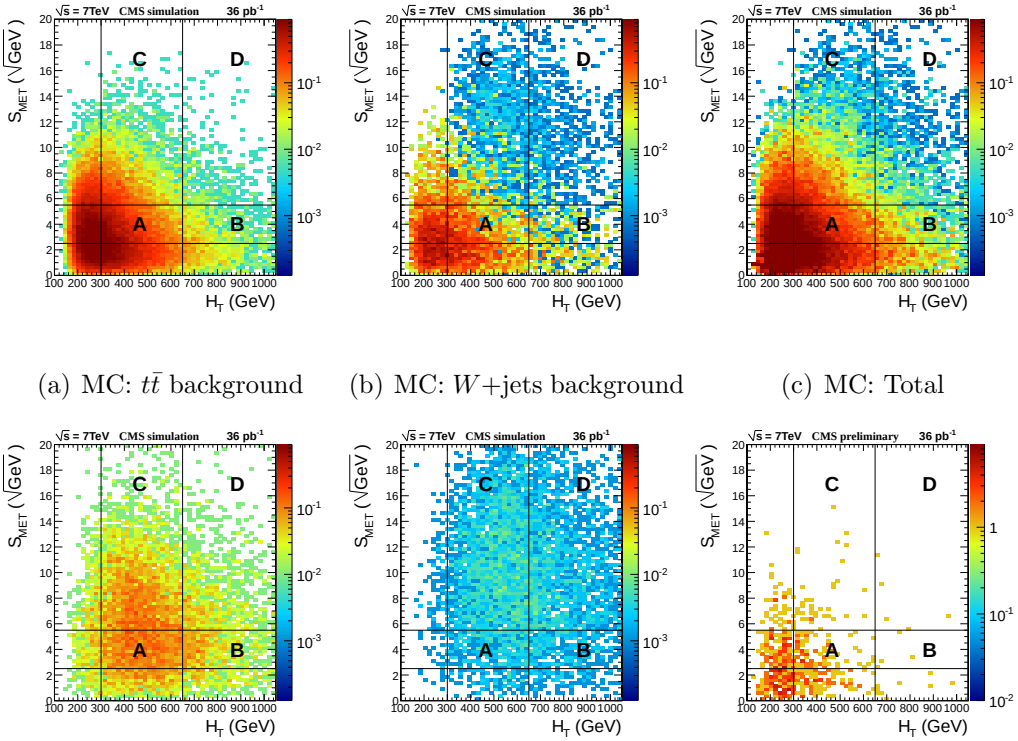

(a) MC: $t\bar{t}$ background (b) MC: W+jets background (c) MC: Total

(d) MC: SUSY LM0 (e) MC: SUSY LM1 (f) Data

Figure 5.11: Two-dimensional distributions of H_T vs. S_{MET} for simulation and data samples in the μ channel. The definition of the regions for the tight selection are indicated on the figures. Figures from Ref. [80].

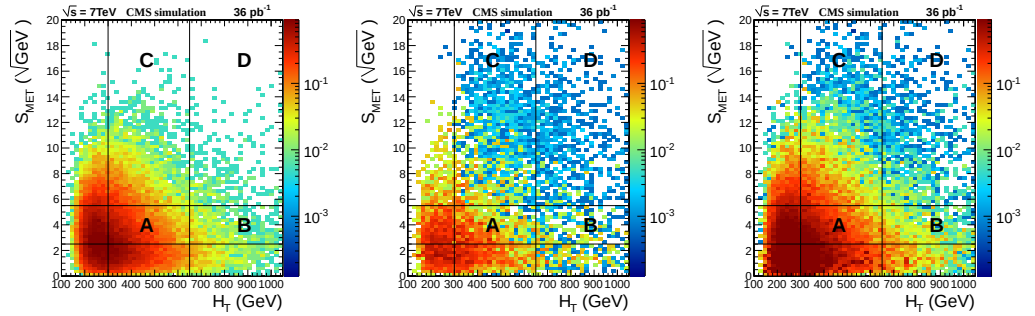

(a) MC: $t\bar{t}$ background (b) MC: W+jets background (c) MC: Total

(d) MC: SUSY LM0 (e) MC: SUSY LM1 (f) Data

Figure 5.12: Two-dimensional distributions of H_T vs. S_{MET} for simulation and data samples in the e channel. The definition of the regions for the tight selection are indicated on the figures. Figures from Ref. [80].

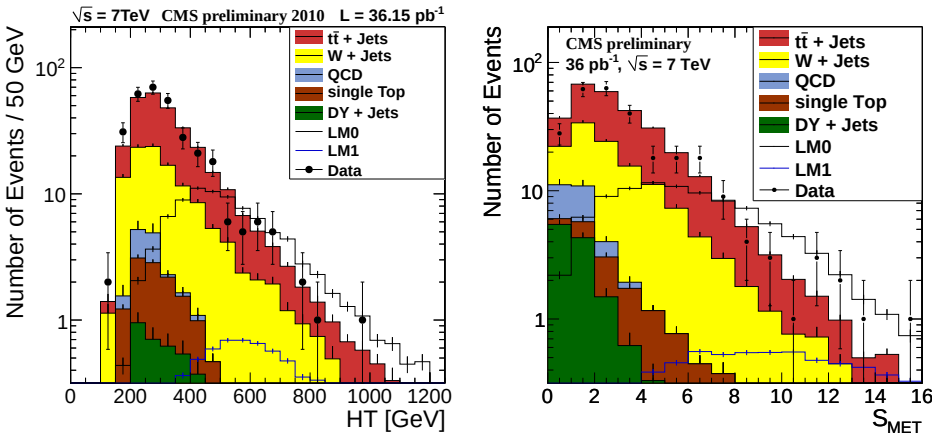

Figure 5.13: Distributions of variables in the ABCD-regions for the μ channel. H_T with a cut $S_{MET} > 2.5$ and S_{MET} with a cut $H_T > 300$. Figures from Ref. [80].

shows similar H_T and S_{MET} distributions in the electron channel (where again the W+jets contribution has been scaled by the same factor as in Sec. 5.3). The observed data distributions and the summed Monte Carlo distributions agree well here also..

Next we will look at the explicit numbers in each of the control and signal regions and the prediction for the background in both the loose and tight selection in Monte Carlo and data.

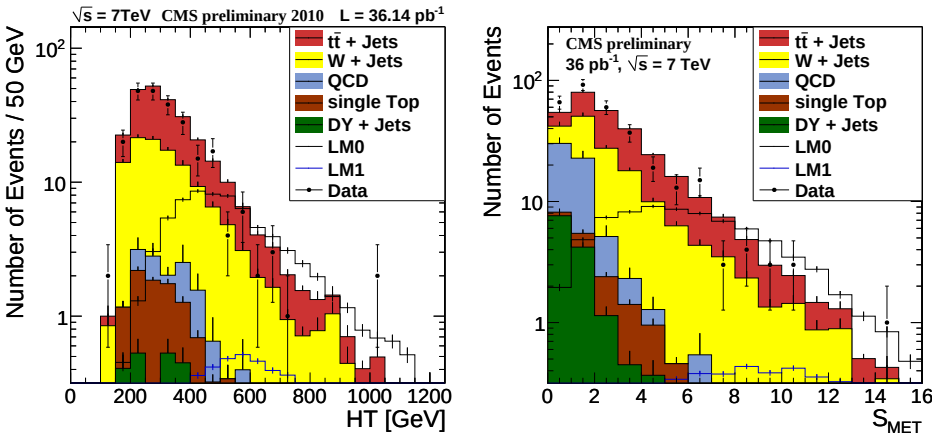

Figure 5.14: Distributions of variables in the ABCD-regions for the e channel. H_T with a cut $S_{MET} > 2.5$ and S_{MET} with a cut $H_T > 300$. Figures from Ref. [80].

5.4.5 Results of background prediction in Monte Carlo, data

In the previous section we looked at many different distributions involving H_T and S_{MET} to get an idea of where different samples lie in these distributions and how the shapes of the data and Monte Carlo compare. In this section we will look at individual numbers in each of the control and signal regions and at the background prediction in the signal region using the S_{MET} vs. H_T method.

Table 5.3 shows the event yields in the muon channel and in both the loose and tight selection for each of the regions and the prediction for the signal region, all in Monte Carlo simulation and data. Several different conclusions can

be made from these tables and they generally hold true whether looking at the loose or the tight selection and either the muon or electron channel (the yields in the electron channel are shown in Table 5.3). The first is that if you look at the total standard model Monte Carlo the predicted number of events, $N(D)_{pred}$, is statistically consistent with the actual number of events, $N(D)$. This agreement between the predicted and actual number of events holds true in the Monte Carlo even when considering individual backgrounds such as $t\bar{t}$, W+jets, and single top. For the QCD sample there is simply not enough statistics in the Monte Carlo to draw any conclusions about whether the method predicts the background correctly. However, the QCD contribution is expected to be very small, and we estimate its effect in a data-driven procedure described in Sec. 5.4.8. The Z+jets contribution is not predicted well by this method, but the number of events in each region from this background is very small (less than one event) even for the loose selection.

Another conclusion to draw from Table 5.3 is that the observed number of events in each region in the data is statistically consistent with the number predicted by the total SM MC. Lastly, in the data, the predicted number of events in signal region D, N_D, is statistically consistent with the observed number of events. In the muon channel for the loose (tight) selection we observe 30 (5) events in the data while we predict $29.2 \pm 9.3 \pm 4.1$ ($1.7 \pm 0.9 \pm 0.3$) events.

Table 5.3: S_{MET} vs. H_T, muon channel: Overview of Monte Carlo and data yields in each of the ABCD regions and the corresponding background prediction in the signal region, for both loose and tight selection. Table from Ref. [80].

sample	$N(A)$	$N(B)$	$N(C)$	$N(D)$	$N(D)_{\text{pred}}$
			Loose selection		
$t\bar{t}$	17.58 ± 0.29	24.77 ± 0.35	13.6 ± 0.26	20.33 ± 0.32	19.16 ± 0.55
W + jets	5.95 ± 0.48	10.92 ± 0.59	4.91 ± 0.4	9.04 ± 0.47	9.01 ± 1.14
single top	0.9 ± 0.03	0.83 ± 0.03	0.66 ± 0.03	0.64 ± 0.03	0.61 ± 0.04
Drell-Yan	0.54 ± 0.15	0.46 ± 0.14	0.08 ± 0.06	0.54 ± 0.15	0.07 ± 0.06
QCD	0.1 ± 0.1	0.1 ± 0.1	0.0 ± 0.0	0.0 ± 0.0	0.0 ± 0.0
total SM MC	25.07 ± 0.59	37.08 ± 0.71	19.25 ± 0.48	30.56 ± 0.58	28.47 ± 1.11
data	30	35	25	30	29.17 ± 9.31
			Tight selection		
$t\bar{t}$	65.28 ± 0.56	4.76 ± 0.15	26.01 ± 0.36	2.05 ± 0.1	1.9 ± 0.07
W + jets	23.27 ± 0.88	3.62 ± 0.34	10.05 ± 0.53	1.28 ± 0.1	1.56 ± 0.18
single top	2.85 ± 0.06	0.08 ± 0.01	1.09 ± 0.04	0.02 ± 0.01	0.03 ± 0.0
Drell-Yan	1.41 ± 0.24	0.21 ± 0.09	0.5 ± 0.14	0.04 ± 0.04	0.07 ± 0.04
QCD	0.3 ± 0.17	0.0 ± 0.0	0.0 ± 0.0	0.0 ± 0.0	0.0 ± 0.0
total SM MC	93.1 ± 1.09	8.67 ± 0.38	37.64 ± 0.66	3.39 ± 0.15	3.5 ± 0.17
data	98	4	41	5	1.67 ± 0.89

Table 5.4: S_{MET} vs. H_T, electron channel: Overview of Monte Carlo and data yields in each of the ABCD regions and the corresponding background prediction in the signal region, for both loose and tight selection. Table from Ref. [80].

sample	$N(A)$	$N(B)$	$N(C)$	$N(D)$	$N(D)_{\text{pred}}$
			Loose selection		
$t\bar{t}$	13.95 ± 0.26	19.94 ± 0.31	10.02 ± 0.22	15.62 ± 0.28	14.33 ± 0.47
W + jets	4.93 ± 0.4	9.12 ± 0.54	3.66 ± 0.34	7.19 ± 0.4	6.77 ± 0.93
single top	0.73 ± 0.03	0.65 ± 0.03	0.49 ± 0.02	0.48 ± 0.02	0.43 ± 0.03
Drell-Yan	0.41 ± 0.13	0.29 ± 0.11	0.12 ± 0.07	0.29 ± 0.11	0.09 ± 0.06
QCD	0.0 ± 0.0	1.51 ± 0.66	0.27 ± 0.27	0.0 ± 0.0	0.0 ± 0.0
total SM MC	20.01 ± 0.49	31.51 ± 0.91	14.56 ± 0.5	23.57 ± 0.5	22.92 ± 1.17
data	19	33	19	17	33.0 ± 12.15
			Tight selection		
$t\bar{t}$	51.89 ± 0.5	3.89 ± 0.14	19.48 ± 0.31	1.71 ± 0.09	1.46 ± 0.06
W + jets	18.64 ± 0.77	2.42 ± 0.27	8.76 ± 0.5	1.18 ± 0.12	1.14 ± 0.15
single top	2.29 ± 0.05	0.07 ± 0.01	0.78 ± 0.03	0.03 ± 0.01	0.02 ± 0.0
Drell-Yan	1.22 ± 0.22	0.08 ± 0.06	0.24 ± 0.1	0.0 ± 0.0	0.02 ± 0.01
QCD	2.73 ± 1.1	0.02 ± 0.01	0.27 ± 0.27	0.0 ± 0.0	0.0 ± 0.0
total SM MC	76.78 ± 1.45	6.48 ± 0.31	29.53 ± 0.65	2.92 ± 0.15	2.49 ± 0.14
data	80	4	30	2	1.5 ± 0.82

Table 5.4 shows similar Monte Carlo and data yields in the different regions and their predictions, but in the electron channel. The same conclusions that were made for the muon channel can be made in the electron channel. For the electron channel in the loose (tight) selection we observe 17 (2) events in the data while we predict $33.0 \pm 12.2 \pm 5.1$ ($1.5 \pm 0.8 \pm 0.3$) events.

Systematic uncertainties on the prediction in both the muon and the electron channel have been studied in detail and are discussed in Sec. 5.4.7.

Table 5.5: Muon channel: predicted (SM) backgrounds for the ABCD method with H_T and S_{MET} for events with exactly 3 jets. Table from Ref. [80].

sample	$N(A)$	$N(B)$	$N(C)$	$N(D)$	$N(D)_{\text{pred}}$
			Loose selection		
total SM MC	11.62 ± 0.49	19.52 ± 0.67	9.25 ± 0.44	15.42 ± 0.52	15.53 ± 1.13
data	5	18	15	17	54.0 ± 30.65
			Tight selection		
total SM MC	64.14 ± 1.17	3.0 ± 0.26	38.09 ± 0.85	1.82 ± 0.16	1.78 ± 0.16
data	61	3	44	1	2.16 ± 1.32

5.4.6 Cross-check of method using lower jet multiplicity

The previous section shows that the S_{MET} vs. H_T method works well in the Monte Carlo for each of the individual backgrounds and the total SM background. To ensure that this does not depend highly on the particular kinematic space we have chosen for the analysis we have some done some further tests of the method with different jet multiplicity. Although this analysis requires at least four jets, we check the behaviour of the method in a closely related orthogonal sample, requiring exactly three jets.

Tables 5.5 and 5.6 show the event yields of the S_{MET} vs. H_T method in the three jet bin for both the loose and tight selection and the muon and electron channel. We observe agreement between the predicted and observed yields in this sample and this provides a nice cross-check of the fundamental procedure of the method.

Table 5.6: Electron channel: predicted (SM) backgrounds for the ABCD method with H_T and S_{MET} for events with exactly 3 jets. Table from Ref. [80].

sample	$N(A)$	$N(B)$	$N(C)$	$N(D)$	$N(D)_{\text{pred}}$
			Loose selection		
total SM MC	19.99 ± 1.15	15.7 ± 0.59	17.32 ± 0.57	15.84 ± 0.52	13.6 ± 1.03
data	19	20	18	11	18.95 ± 7.54
			Tight selection		
total SM MC	53.87 ± 1.42	2.47 ± 0.24	29.7 ± 0.73	1.61 ± 0.15	1.36 ± 0.14
data	66.0	3.0	23.0	0.0	1.05 ± 0.65

5.4.7 Systematic uncertainties

The S_{MET} vs. H_T method provides a robust, inclusive way to determine the background in the signal region at high S_{MET} and high H_T. However, certain effects must be studied and quantified before making a final background prediction. This section looks quantitatively at many different systematic effects and assigns uncertainties to each of these effects. The figure of merit we use when studying systematic errors is $\kappa = [N(A)N(D)]/[N(B)N(C)]$, where A, B, C, and D are the regions defined in Sec. 5.4.2. If the variables are uncorrelated in the ABCD region, $\kappa = 1$. With all the backgrounds combined, the Monte Carlo prediction for κ in the muon channel is $\kappa = 1.08 \pm 0.04$ (0.98 ± 0.06) for the loose (tight) selection. For the electron channel the Monte Carlo prediction is $\kappa = 1.03 \pm 0.05$ (1.16 ± 0.08) for the loose (tight) selection. The κ values predicted from the Monte Carlo in some cases show a slight deviation from one

and this deviations is added as an additional systematic uncertainty.[14] In order to quantify other systematic uncertainties we probe different effects and see how much κ changes in each of these cases. The results of all the different systematic studies for both the muon and electron channel are presented in Table 5.7 and Table 5.8, for loose and tight selection respectively. We will now describe how each of the systematic uncertainties is estimated.

The first set of systematic studies we looked at were variations related to jet and $\not\!\!E_T$ reconstruction. These variations were studied in Monte Carlo simulation and include the jet energy scale (JES), the unclustered energy scale, the jet resolution, and the loss of a random jet in the detector (for whatever reason). All these variations can change both the H_T and $\not\!\!E_T$ in the event and thus move events around in the S_{MET} vs. H_T control and signal regions, possibly creating a correlation between the two variables. The variations on κ from these effects were found to be on the order of a few percent and are dominated by the uncertainty on the JES.

For the jet energy scale we applied a $\pm 5\%$ relative change in p_T to all jets that pass the jet identification criteria of the analysis. In addition, the change in the p_T's of all the jets in the event is propagated to a change in $\not\!\!E_T$ for each

[14] For instance, in the muon channel with the loose selection the predicted Monte Carlo κ is 1.08 ± 0.04. Thus, we apply an 8% systematic uncertainty on κ to reflect the fact that the predicted Monte Carlo κ is 1.08 not 1.00.

Table 5.7: Estimated systematic uncertainties on the background prediction for the ABCD method using the loose selection, expressed as variations on $\kappa = AD/BC$. The MC prediction is $\kappa = 1.08 \pm 0.04$ for the muon channel and $\kappa = 1.03 \pm 0.05$ for the electron channel, respectively. The observed variations of κ are at the limit of statistical significance. For all components the maximum deviation was assigned as a systematic error. Table from Ref. [80].

Source	Variation	Muon channel		Electron channel	
		$\Delta\kappa$	sys.err. [%]	$\Delta\kappa$	sys.err. [%]
Jet energy scale	+5%	0.03	3.2	0.01	9.4
	−5%	< -0.01		0.14	
Jet resolution	+10%	−0.02	1.9	0.03	2.9
	+20%	−0.02		< 0.01	
Unclustered energy	+10%	0.01	3.1	0.03	3.0
	−10%	0.03		−0.03	
Jet removal	5%	−0.01	1.1	−0.01	1.0
Lepton p_T scale	+0.5% (+2.5%)	0.01	0.6	< 0.01	2.3
	−0.5% (−2.5%)	< 0.01		−0.03	
Lepton rejection	5%	< 0.01	1.2	< 0.01	1.2
	10%	0.01		0.02	
Background composition		$< \pm 0.02$	1.6	$< \pm 0.02$	2.1
PDF uncertainties		$< \pm 0.01$	0.5	$< \pm 0.01$	0.1
$\kappa_{MC} \neq 1$			8.0		5.0
Total			9.7		12.0

Table 5.8: Estimated systematic uncertainties on the background prediction for the ABCD method using the tight selection, expressed as variations on $\kappa = AD/BC$. The MC prediction is $\kappa = 0.98 \pm 0.06$ for the muon channel and $\kappa = 1.16 \pm 0.08$ for the electron channel, respectively. The observed variations of κ are at the limit of statistical significance. For all components the maximum deviation was assigned as a systematic error. Table from Ref. [80].

Source	Variation	Muon channel		Electron channel	
		$\Delta\kappa$	sys.err. [%]	$\Delta\kappa$	sys.err. [%]
Jet energy scale	+5%	< 0.01	0.6	-0.02	7.8
	−5%	< 0.01		0.09	
Jet resolution	+10%	0.02	10.7	< -0.01	3.0
	+20%	0.10		-0.03	
Unclustered energy	+10%	-0.01	1.5	-0.04	4.1
	−10%	0.01		0.04	
Jet removal	5%	-0.02	1.8	< 0.01	0.1
Lepton p_T scale	+0.5% (+2.5%)	-0.01	1.5	< 0.01	0.4
	−0.5% (−2.5%)	-0.02		< -0.01	
Lepton rejection	5%	< 0.01	0.5	< 0.01	1.1
	10%	-0.01		-0.01	
Background composition		$< \pm 0.02$	4.6	$< \pm 0.02$	1.5
PDF uncertainties		$< \pm 0.01$	0.6	$< \pm 0.02$	1.8
$\kappa_{MC} \neq 1$			2.0		16.3
Total			12.2		19.0

event. This ±5% variation takes into account variations in the energy clustered in the calorimeters. We also looked at variations in the unclustered energy in the event and modified this unclustered energy by ±10%, which ends up having a negligible effect on κ because most of the visible energy is clustered into jets.

To vary the jet resolution we modified the nominal jet p_T of each jet in the event by comparing the reconstructed jet p_T to the generator level jet p_T and increasing the difference between the two by 10% and 20%. If a reconstructed jet did not have a generator level jet matched to it we applied a Gaussian random smearing of 15%. To simulate a possible extreme case of $\not\!\!E_T$, we also tested the effect of losing a jet by removing a random jet out of the four leading jets in 5% of all events.

The next systematic uncertainties studied were the lepton p_T scale and lepton efficiency. These effects are expected to be small since the $\not\!\!E_T$ and H_T have little dependence on the lepton in the event.[15] We performed two tests: first we scaled the lepton p_T by ±0.5% (±2.5%) for $|\eta| < 1$ ($|\eta| > 1$) and second we modeled lepton reconstruction efficiencies by rejecting leptons with a p_T dependent probability of $P_{rej}e^{-(p_T-20)/30}$, where $P_{rej} = 5\%$, 10% and is based on electron

[15]The H_T is not calculated with the lepton p_T and though the $\not\!\!E_T$ calculation should take into account the lepton p_T, the uncertainty on the lepton p_T is a much smaller effect than the jet scale uncertainty.

and muon efficiency measurements made in other related CMS analyses. The uncertainty from these lepton effects was very small, on the order of 1-2%.

Other effects that we looked into were variations in the parton distribution functions (PDF) and the relative amount of $t\bar{t}$ and W+jets in the event sample. For the PDF variations, in each event we applied alternative weights computed by the event generator [83] based on the CTEQ6.6 [84] PDF set. The PDF variations have a very small effect on the κ, $< 1\%$. To understand the effect from variations in the composition of our event sample we varied the cross section of our two largest backgrounds, $t\bar{t}$ and W+jets, by $\pm 30\%$ and 50%, respectively. Changes in the amount of $t\bar{t}$ and W+jets in the event sample should not produce a large effect since κ is close to one for both backgrounds and the method works well for each background individually (see Sec. 5.4.5). In the end the uncertainty from the $t\bar{t}$ and W+jets cross sections is on the order of a few percent.

Lastly, in addition to determining changes in the κ variable from different systematic effects, we also did a cross-check that the ratio of high to low S_{MET} (H_T) is approximately flat as a function of H_T (S_{MET}) in both MC and data. The definition of high and low follow the boundaries of the ABCD regions listed in Table 5.2. Figures 5.15 and 5.16 show exactly these ratios in the muon and electron channel respectively for both loose and tight selections. The ratios all look relatively flat in the Monte Carlo and in the data making us confident that

these variables in fact have a small correlation (though in the high H_T, S_{MET} bins there is lack of statistics in the data).

5.4.8 Systematic error due to QCD contamination

The selection of an isolated lepton and the cuts on H_T and S_{MET} provides a large suppression of the QCD background in the S_{MET} vs. H_T method. The Monte Carlo simulation predicts that the amount of QCD contribution in the A, B, C, and D regions of this method is very small. However, due to the large uncertainties of the QCD background and the fact that the QCD contribution can bias κ, and thus the background prediction, we do not rely on Monte Carlo simulation to predict this background. Instead we measure the QCD contribution to each of the A, B, C, and D regions using data-driven methods. Specifically we use a template method based on the distribution of the relative isolation of the lepton (defined in detail is Sec. 5.2.5). We first measure a relative isolation template in a QCD dominated region of low H_T and low S_{MET}. Once we have obtained the template we normalize it at high relative isolation, > 0.5, in a particular A, B, C, or D region. After normalizing we can predict the amount of QCD background in that region from the number of events that pass the relative isolation selection criteria in the template. This method assumes that

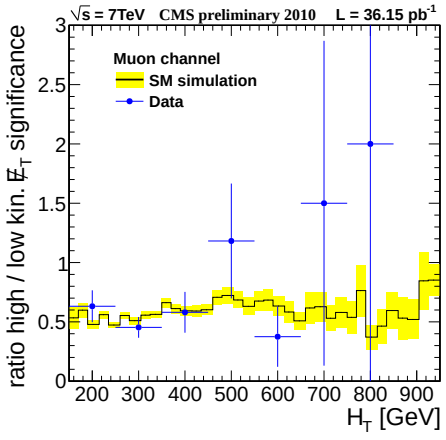

(a) Muon channel: ratio vs. H_T (loose)

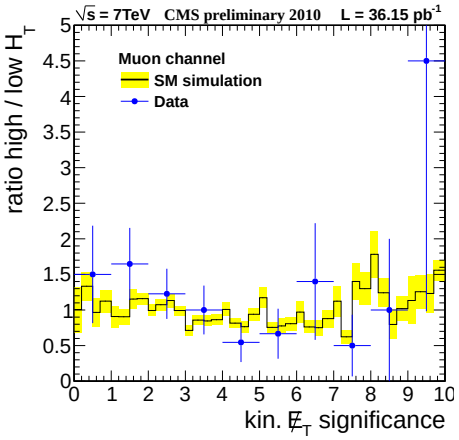

(b) Muon channel: ratio vs. S_{MET} (loose)

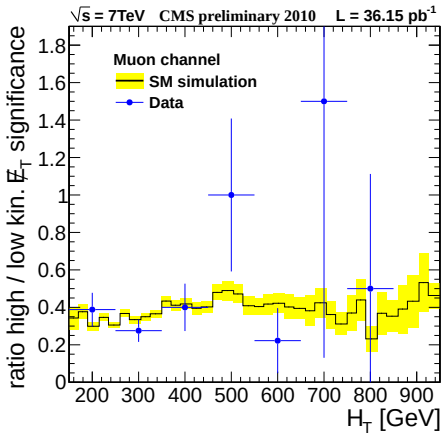

(c) Muon channel: ratio vs. H_T (tight)

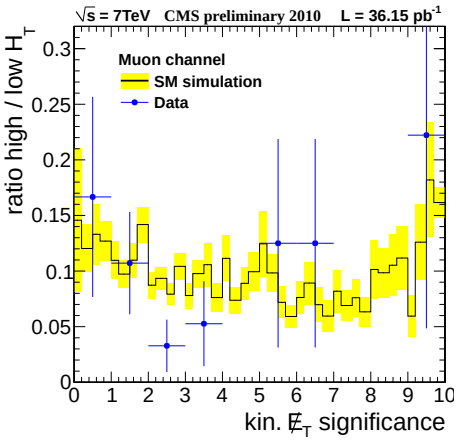

(d) Muon channel: ratio vs. S_{MET} (tight)

Figure 5.15: The ratio of events in the high and low regions in H_T (left) and S_{MET} (right) as a function of the second variable for the loose (top) and tight (bottom) selections in the μ channel. The points correspond to data while the lines and the shaded regions represent the SM MC predictions. These prediction have been normalized to data in the control region. These rescaling corrections were smaller than $\pm 25\%$. The definitions of the low (control) and high regions can be found in Table 5.2. Figures from Ref. [80].

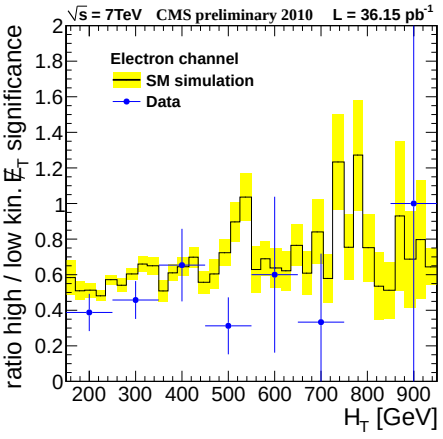

(a) Electron channel: ratio vs. H_T

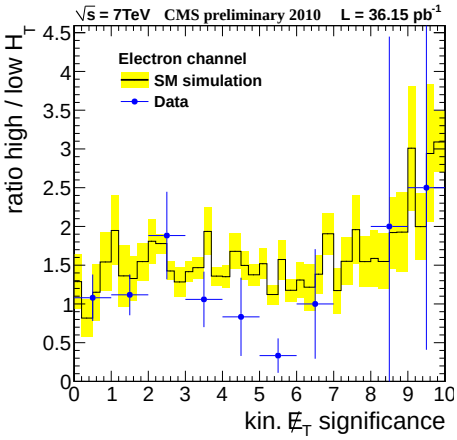

(b) Electron channel: ratio vs. S_{MET}

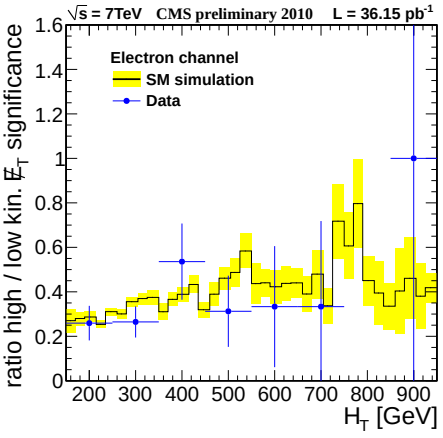

(c) Electron channel: ratio vs. H_T

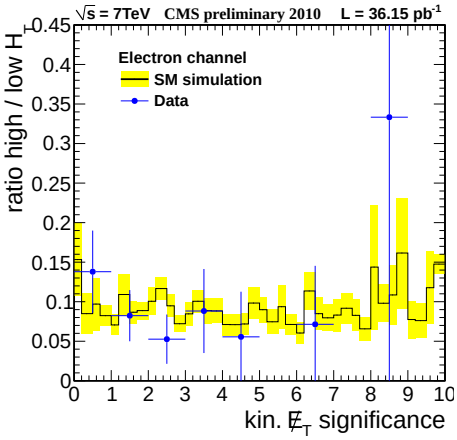

(d) Electron channel: ratio vs. S_{MET}

Figure 5.16: The ratio of events in the high and low regions in H_T (left) and S_{MET} (right) as a function of the second variable for the loose (top) and tight (bottom) selections in the electron channel. The points correspond to data while the lines and the shaded regions represent the SM MC predictions. These prediction have been normalized to data in the control region. These rescaling corrections were smaller than ±25%. The definitions of the low (control) and high regions can be found in Table 5.2. Figures from Ref. [80].

the relative isolation distribution is similar in the control region and each of the A, B, C, and D regions, which we have observed is the case in QCD simulation.

The control samples used to obtain the relative isolation template are chosen so QCD will dominate and so the electroweak contribution will be small. In the muon channel the control sample is defined to be $S_{MET} < 0.5$ and 150 GeV $< H_T <$ 250 GeV and in the electron channel the control sample is defined to be $S_{MET} < 1$ and 300 GeV $< H_T <$ 350 GeV. For the electron channel control sample the cut in H_T is raised due to trigger requirements. The triggers requiring a single electron object had requirements on the electron isolation to lower the trigger rate. To avoid the requirement on isolation for the electron QCD prediction we use triggers that require a certain amount of H_T in the event, but place no requirement on the electron. These triggers only became highly efficient above an offline H_T requirement of 300 GeV. For the muon channel there is not a similar problem, since no isolation requirement is made in any of the muon triggers used.

The distributions of the relative isolation variable for the control and analysis regions of both the muon and electron channel are shown in Figure 5.17, where the control sample is the low S_{MET}, low H_T region and the analysis regions is defined to be all the events in regions A, B, C, and D. The small electroweak contamination is not explicitly subtracted from the control sample but makes

Table 5.9: Results for the data-driven estimation of the QCD contribution to the regions in H_T and S_{MET} for the μ and e channels. The regions are defined in Table 5.2. Table from Ref. [80].

	Loose selection			
	Muon channel		Electron channel	
Region	Data	MC	Data	MC
A	0.7 ± 0.4	0.1 ± 0.1	1.55 ± 0.74	0.0
B	0.6 ± 0.4	0.1 ± 0.1	1.13 ± 0.56	1.51 ± 0.66
C	0.06 ± 0.04	0.0	0.14 ± 0.13	0.27 ± 0.27
D	0.1 ± 0.06	0.0	0.23 ± 0.18	0.0
	Tight selection			
	Muon channel		Electron channel	
Region	Data	MC	Data	MC
A	1.76 ± 0.99	0.3 ± 0.17	3.35 ± 1.46	2.73 ± 1.14
B	0.09 ± 0.05	0.0	0.23 ± 0.18	0.02 ± 0.01
C	0.08 ± 0.05	0.0	0.18 ± 0.16	0.27 ± 0.27
D	0.01 ± 0.01	0.0	0.02 ± 0.04	0.0

very little difference in the final result. In Table 5.9 the data-driven estimates in each of the four regions are compared to the predictions from simulation. The number of predicted QCD events in each region is very small, on the order of 0-4% of the total background in a particular region, and leads to small changes in the background prediction for region D. Ultimately the contributions are so small that we do not subtract the QCD contribution away in each of the regions, we just assign a conservative 10% error to the prediction from the QCD background. This 10% is added in quadrature with the totals from Tables 5.7 and 5.8.

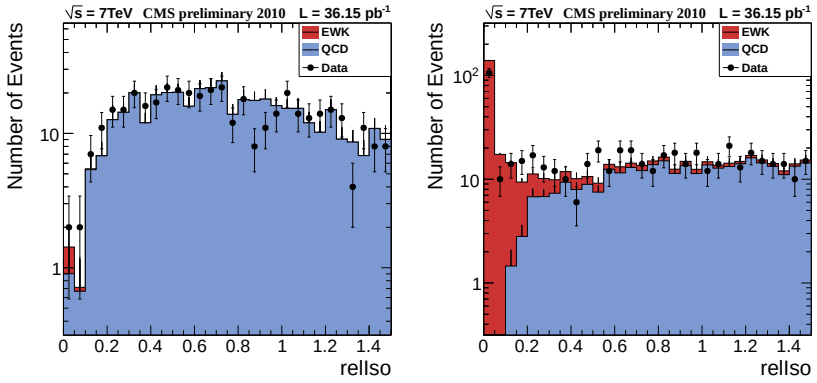

(a) control region, μ channel

(b) signal region, μ channel

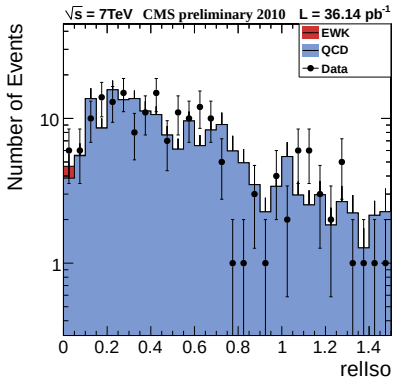

(c) control region, e channel

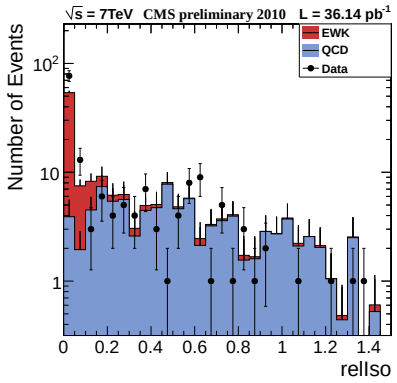

(d) signal region, e channel

Figure 5.17: Relative isolation distributions for QCD control and signal region. Figures from Ref. [80].

In the electron channel a second method was used to cross-check that the QCD contribution is in fact small. This method is also based on using the isolation of the lepton and it uses the same electron triggers as the previous method. In this second method we first obtain the ratio of well-isolated events to poorly isolated events in a QCD control region in data and then we multiply this ratio by the number of poorly isolated events in a particular A, B, C, or D region to predict the number of well-isolated leptons from QCD.

This method assumes that the relative isolation distribution in the control region and the signal region are the same. Figure 5.18(a) shows that the relative isolation distribution in the EB in the control and signal region agree well for QCD Monte Carlo simulation. The QCD control region is defined to be 300 GeV $< H_T <$ 400 GeV and $S_{MET} < 2$ and the signal region is the combined A, B, C, and D regions. Figure 5.18(b) shows that at high relative isolation, >0.2, the relative isolation distribution in the control and signal regions agrees well in the data.

The obtained ratio of well-isolated events to poorly isolated events for the control region in data is 0.049 ± 0.017 in the EB and 0.230 ± 0.076 in the EE, where the error includes statistical uncertainties and systematics uncertainties related to the subtraction of electroweak events. Table 5.10 summarizes the QCD estimates for the loose and tight selection criteria. The data-driven estimates

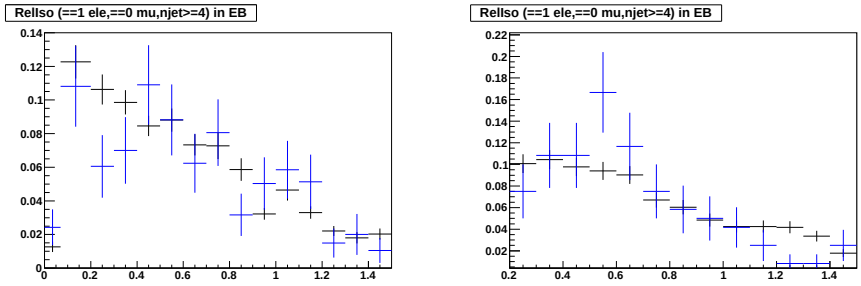

(a) QCD MC simulation (b) Data

Figure 5.18: RelIso distributions in the ECAL barrel region for the QCD control region (black) and the ABCD signal regions (blue). Left: distributions from QCD MC simulation. Right: Data for values of RelIso > 0.2. Figures from Ref. [80].

with this method are consistent with the numbers derived from the first QCD background method described in this section.

5.4.9 Summary of background prediction

We have performed a simple data-driven method that predicts the relevant number of standard model background events in the single-lepton channel at high S_{MET} and high H_T, where a SUSY signal should lie. To ensure that the method is robust we have tested this background prediction in many different kinematic regions in the Monte Carlo simulation and also performed many systematic studies of the procedure. The results of the method for the tight selection are summarized in Table 5.11 along with the expected number of events from

Table 5.10: QCD estimates from the alternative method for the loose and tight ABCD regions in the ECAl barrel and endcap and for the sum of both. The regions are defined in Table 5.2. Table from Ref. [80].

	Loose selection		
	Pred. QCD (EB)	Pred. QCD (EE)	Pred. QCD (Total)
Region A	1.08 ± 0.43	0.23 ± 0.24	1.31 ± 0.49
Region B	0.78 ± 0.33	0.23 ± 0.24	1.01 ± 0.41
Region C	0.20 ± 0.12	0	0.20 ± 0.12
Region D	0.24 ± 0.14	0	0.24 ± 0.14
	Tight selection		
	Pred. QCD (EB)	Pred. QCD (EE)	Pred. QCD (Total)
Region A	3.18 ± 1.15	0.69 ± 0.46	3.87 ± 1.24
Region B	0.05 ± 0.05	0	0.05 ± 0.05
Region C	0.15 ± 0.10	0	0.15 ± 0.10
Region D	0	0	0

Table 5.11: Summary of results in the tight selection for the S_{MET} vs. H_T background prediction. Numbers from Ref. [80].

Results	μ channel	e channel	total
LM0	12.2 ± 0.6	10.3 ± 0.3	22.5 ± 0.7
LM1	2.7 ± 0.1	2.0 ± 0.1	4.6 ± 0.1
predicted	$1.7 \pm 0.9 \pm 0.3$	$1.5 \pm 0.8 \pm 0.3$	$3.2 \pm 1.2 \pm 0.6$
observed	5	2	7

the two SUSY models LM0 and LM1. The result is compatible with a no-signal hypothesis.

5.5 Background determination using lepton spectrum method

The second data-driven background method, called the lepton spectrum method [85], relies on the intimate relationship between the lepton and the neutrino in the major background, $t\bar{t}$ and W+jets events with a single lepton from a W boson, to predict the $\not\!\!E_T$ tail in these events. The $\not\!\!E_T$ tail in the other smaller backgrounds is predicted in separate, compatible ways. Figure 5.19 shows the $\not\!\!E_T$ distribution for the different standard model backgrounds in this analysis. Deviations in the tail of this $\not\!\!E_T$ distribution could come from SUSY and a robust $\not\!\!E_T$ tail prediction for the different standard model background components is very important for any discovery.

5.5.1 Introduction to method

Two separate signal selection criteria are investigated, denoted loose and tight. The loose selection is the preselection with a lepton threshold of $p_T > 20$ GeV[16] and a $\not\!\!E_T$ requirement of 150 GeV. The tight selection is the preselection with a lepton threshold of $p_T > 20$ GeV, a H_T requirement of 500 GeV, and a $\not\!\!E_T$ requirement of 250 GeV. Figure 5.20 shows the standard model background

[16]For the preselection the muon p_T threshold is 15 GeV. Here it is raised to 20 GeV.

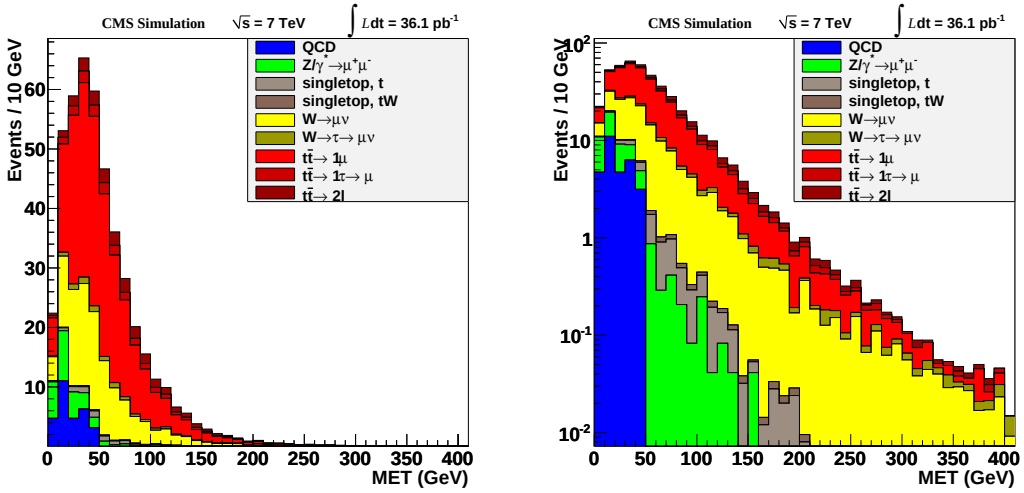

(a) linear scale

(b) log scale

Figure 5.19: Reconstructed $\not\!\!E_T$ distribution of different standard model processes in Monte Carlo simulation normalized to 36.1 pb^{-1}. The requirements for this plot are a reconstructed muon with $p_T > 20$ GeV, and at least 4 reconstructed jets with $p_T > 30$ GeV. Generator level information is used to classify the different contributions. The lepton spectrum method tries to predict the tail of this distribution for the different background components using data-driven methods. The dominant background is W+jets and $t\bar{t}$ events with a single lepton.

composition in the loose and tight selection. The main background, as described above, comes from $t\bar{t}$ and W+jets events where a single W boson decays to an electron or muon. This background is approximately 70% of the total SM background and the $\not\!\!E_T$ distribution is predicted using the lepton p_T spectrum (after applying suitable corrections). The other smaller backgrounds include events in $t\bar{t}$ and W+jets with a $\tau \to \mu$,e decay (15% of total background), and $t\bar{t}$ dilepton events (15% of total background), both of which are predicted using different control samples than the main background prediction. The other very small backgrounds include single top and Z+jets events, which are estimated from the Monte Carlo, and QCD, which is estimated using another data-driven method.

There are two main points that lead us to the conclusion that the lepton p_T spectrum can be used to predict the $\not\!\!E_T$ spectrum for the main SM background. The first is that in $t\bar{t}$ and W+jets, the $\not\!\!E_T$ tail comes mostly from high p_T neutrinos, as opposed to detector mismeasurement.[17] This is shown in Figure 5.21, which shows the reconstructed $\not\!\!E_T$ vs. the generator level $\not\!\!E_T$ (which is defined to be the $\not\!\!E_T$ from the neutrinos) in $t\bar{t}$ events. The second point is that the neutrino p_T distribution in single lepton background events is very similar to the lepton

[17]Though detector mismeasurement should be a small piece of the $\not\!\!E_T$ tail in this analysis, we take it into account using QCD templates from the data. This is all described in detail in Section 5.5.5.

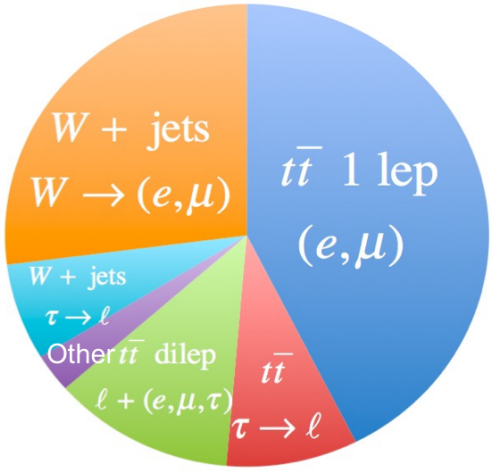

(a) loose selection: preselection, $\not{E}_T$>150 GeV.

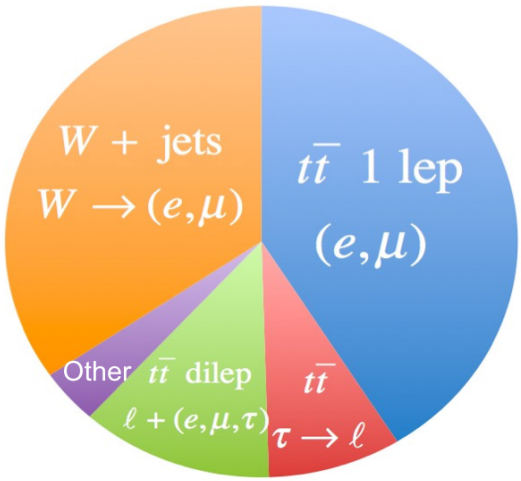

(b) tight selection: preselection, H_T >500 GeV,

$\not{E}_T$>250 GeV.

Figure 5.20: MC composition of background in loose and tight selection signal regions. The "Other" slice includes QCD, single top, and Z+jets.

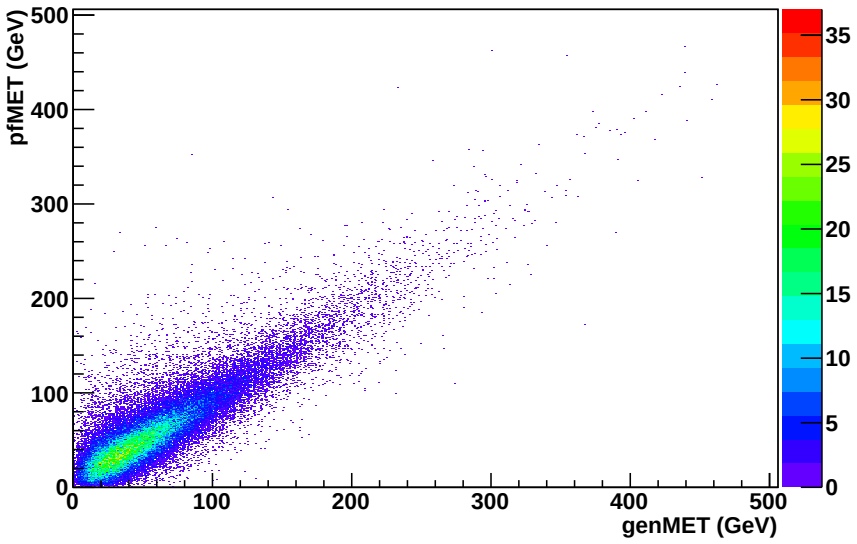

Figure 5.21: Monte Carlo $t\bar{t}$ events: reconstructed $\not\!\!E_T$ vs. generated $\not\!\!E_T$ from neutrinos. This plot demonstrated that for the event selection used in the single-lepton analysis, most of the reconstructed $\not\!\!E_T$ corresponds to true missing transverse momentum.

p_T distribution. This can be seen in Figure 5.22, which shows the generator level muon and neutrino p_T distributions in $t\bar{t}$ and W+jets events with exactly one muon and four reconstructed jets, with and without a p_T threshold on the muon (the details of effects from the p_T threshold will be discussed later). Since the $\not\!\!E_T$ spectrum in these events is dominated by high p_T neutrinos and the neutrino and lepton p_T distributions are similar, the lepton p_T and $\not\!\!E_T$ should be very similar, making it possible to predict the $\not\!\!E_T$ tail from the lepton p_T tail.

The fact that the lepton and neutrino p_T distributions are similar at generator level is a direct result of the two-body decay process of the W boson to a

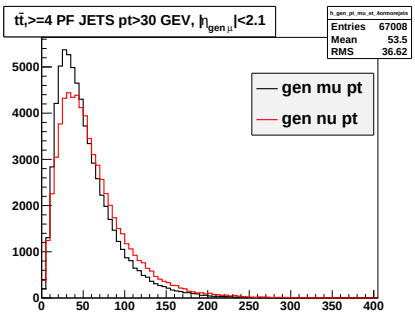

(a) $t\bar{t}$ no p_T threshold

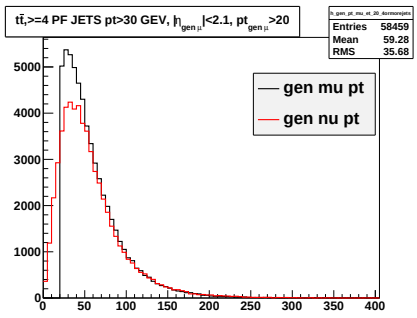

(b) $t\bar{t}$ with $p_T > 20$ GeV

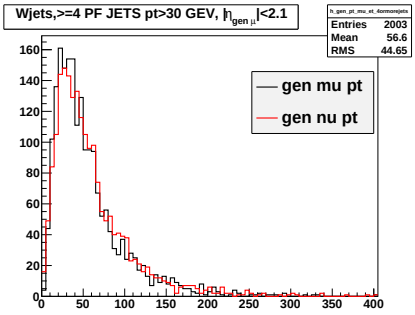

(c) W + jets, no p_T threshold

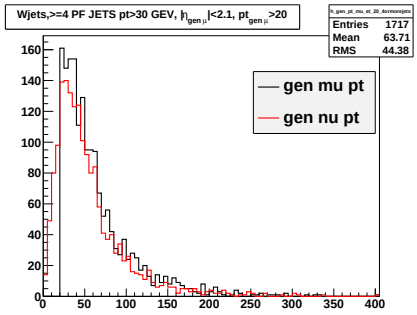

(d) W + jets, with $p_T > 20$ GeV threshold

Figure 5.22: Generator level μ and ν p_T distributions in $t\bar{t}$ and W+jets, with and without a $p_T(\mu)$ >20 threshold. Other requirements include at least 4 reconstructed jets and exactly 1 generator level muon from a W boson, where the geneartor muon must have $|\eta| < 2.1$. The neutrino and muon p_T distributions are very similar to each other in both $t\bar{t}$ and W+jets. The p_T threshold on the muon tends to remove events in the high $p_T(\nu)$ tail, while keeping the high $p_T(\mu)$ tail the same.

lepton and a neutrino in these events. In single lepton $t\bar{t}$ and W+jets events both the lepton and neutrino come from the same W boson decay; thus, on an event-by-event basis their momenta have the same magnitude in the W rest frame. When boosting the lepton and neutrino from the W rest frame to the lab frame these particles share the same sequence of Lorentz boosts which lead to different (and anti-correlated) momenta in the lab frame. The anti-correlation is evident in Fig 5.23(a) it arises because when one momentum vector is along the W flight direction the other will typically be against the W flight direction. Though the lepton and neutrino p_T in the lab frame are different in a single event, their summed distributions (i.e., their distribution over all events) will be the same if the angular distributions of the lepton and neutrino are identical. Differences in the angular distributions of the lepton and neutrino lead to their momenta spectra differing in the lab frame. However, the polarization of the W, which controls the lepton and neutrino angular distributions, is well understood, especially in $t\bar{t}$, and differences can be quantified.

In searching for SUSY this method relies on the fact that the lepton p_T distribution tends to be much softer than the $\not\!\!E_T$ distribution in the SUSY signal sample. If the SUSY signal had similar $\not\!\!E_T$ and lepton p_T distributions, the presence of SUSY would not be seen as an excess in the $\not\!\!E_T$ tail, since the SUSY lepton p_T spectrum would predict the extra events in the $\not\!\!E_T$ tail. However, since

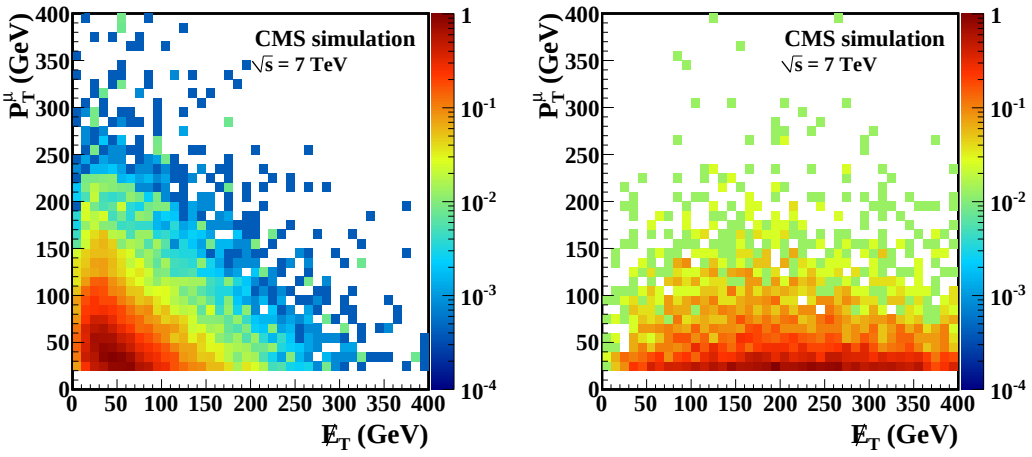

(a) MC: $t\bar{t}$ (b) MC: SUSY LM1

Figure 5.23: Distributions of muon p_T vs. $\not\!\!E_T$ in the μ channel for (a) Monte Carlo $t\bar{t}$ events and (b) the LM1 SUSY benchmark model. In $t\bar{t}$ events, the lepton p_T and $\not\!\!E_T$ in a given event are anticorrelated, but their distributions are very similar overall. In the LM1 benchmark model, which is typical of many SUSY models, the $\not\!\!E_T$ distribution is much harder than the lepton spectrum, since it is dominated by the production of two LSPs. Figures from Ref. [80].

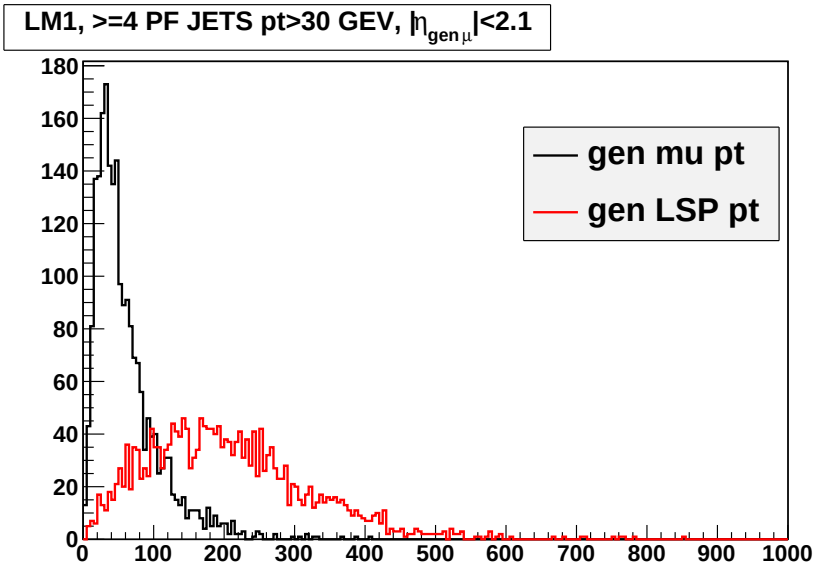

Figure 5.24: LM1: generator level lepton p_T distribution (black) and generator level $\not\!\!E_T$ (red), where the $\not\!\!E_T$ is calculated from the vector sum of the transverse momentum of the LSPs in the event. For these distributions no $p_T(\mu)$ threshold is required; however, the muon must have $|\eta|$ <2.1 and four reconstructed jets are also required.

most SUSY models have a much softer lepton p_T distribution, this method is very robust against signal contamination of the control region, the high lepton p_T tail which is used for the $\not\!\!E_T$ prediction. Figure 5.24 shows that the generator level lepton p_T distribution is much softer than the generator level $\not\!\!E_T$ distribution (vector sum of the p_T's of the LSPs in the event) in the case of the SUSY model LM1. In SUSY the correlation between the $\not\!\!E_T$ and the lepton p_T tends to be very different than the SM, as shown in Fig 5.23, because the $\not\!\!E_T$ is usually not from a W boson, but from the LSPs.

Before making a quantitative prediction of the $\not\!\!E_T$ tail using the lepton p_T distribution there are certain issues that must be addressed. The first, W polarization, was described briefly above, but needs to be studied in more detail. Another effect to understand is the fact that in this analysis a p_T threshold is applied to the lepton p_T spectrum but not the $\not\!\!E_T$ spectrum. This threshold can change the lepton p_T distribution with respect to the neutrino p_T, as shown in Figure 5.22. The W polarization and p_T threshold effects are discussed in detail in Sec. 5.5.3 and Sec. 5.5.4, respectively. The fact that the resolution of the $\not\!\!E_T$ and lepton p_T are quite different must also be taken into account and this is described in Section 5.5.5. Contamination of the single lepton control region by non-single lepton backgrounds and QCD backgrounds must be taken into account since these backgrounds are predicted using other more reliable data-driven methods. Contamination of the single lepton control region is described is Sec. 5.5.2. Sections 5.5.6 and 5.5.7 describe the separate data-driven background predictions for dilepton events, $\tau \to \ell$ events and QCD events.

Figure 5.25 shows a flow-chart of the different data-driven background pieces of the lepton spectrum method for the muon channel. For the electron channel the flow-chart is almost exactly the same if μ is interchanged everywhere with e. The one major difference is that in the electron channel the single muon control sample (not the single electron control sample) is used to predict the $\not\!\!E_T$ in

$W \to e$ events. This is described in Sec. 5.5.8 and is due to the single electron control sample having a large contamination from QCD events. The small single top and Z+jets backgrounds are not included in Figure 5.25 since they are determined from the MC. Sec. 5.5.9 describes the background determination of single top and Z+jets.

For all the data-driven methods except QCD, scale factors from the Monte Carlo are used to correct for known biases.[18] For instance, in the $W \to \ell$ prediction the scale factor corrects for the W polarization, $\not\!\!E_T$ scale, overlap with other predictions, and p_T threshold effects. These scale factors are described in detail in Sec. 5.5.10. The results for all the different background predictions in the lepton spectrum method are summarized in Sec. 5.5.11 and the systematic uncertainties associated with the predictions are discussed in Sec. 5.5.12.

[18]The statistics in the QCD MC sample is too small to obtain a meaningul scale factor.

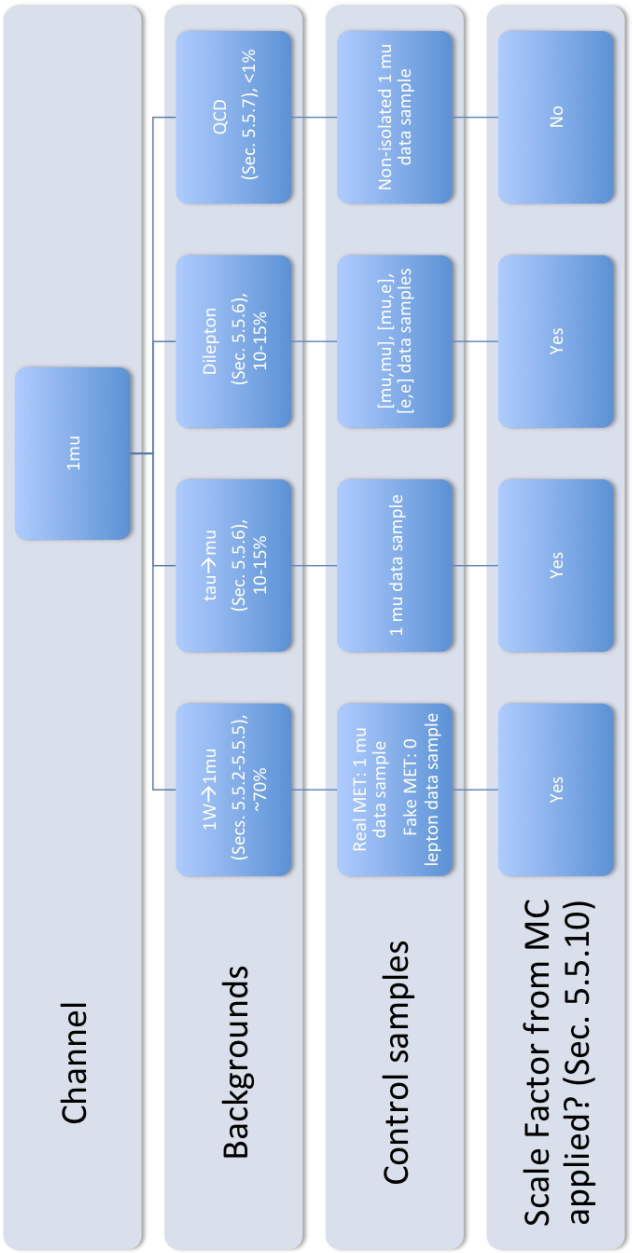

Figure 5.25: Flow-chart showing the different data-driven background determinations and the control samples used for each. The small Z+jets and single top contribution is not included in this flow-chart since it is very small and estimated from the MC. The last row of the flow-chart specifies whether a scale factor from the MC is applied to correct for known effects.

5.5.2 Description of signal and control regions for single lepton prediction

As specified in the previous section, the control sample used for the single lepton $\not\!\!E_T$ prediction is the lepton p_T distribution. This means that what we care about for the prediction is the number of events with lepton p_T greater than 150 GeV for the loose selection or 250 GeV for the tight selection. In this control sample there is no $\not\!\!E_T$ cut placed on the events, so an event with a lepton p_T of 300 GeV and $\not\!\!E_T$ of 10 GeV will be kept in our control sample. These high lepton p_T events are used to predict the number of events in the signal region, $\not\!\!E_T$>150 GeV in the loose selection, and $\not\!\!E_T$>250 GeV in the tight selection, where there is a cut on lepton p_T (20 GeV). As shown in Figure 5.23(a), most SM events that lie in the signal region (high $\not\!\!E_T$) do not lie in the control region (high lepton p_T), though in some rare cases a SM event can have both high $\not\!\!E_T$ and high lepton p_T.[19]

Table 5.12 shows the predicted number of events (lepton p_T > 150 GeV) vs. the actual number of events ($\not\!\!E_T$>150 GeV) in each of the backgrounds in this analysis for the loose selection. The background is broken up into all the different sub-processes and shown for both muons and electrons. For single lepton

[19]For the loose selection ($\not\!\!E_T$ > 150 GeV), roughly 5% of the Standard Model events ($t\bar{t}$ and W+jets) in the signal region also lie in the control region.

Table 5.12: Lepton spectrum method with loose cuts applied to Monte Carlo: tests of data-driven background determination. Pre-selection cuts are applied, and the signal region corresponds to $\not\!\!E_T > 150$ GeV. Note that the predictions for the dilepton feed-down and tau to lepton are underestimated by this method and are determined separately.

Background	$\ell = \mu$ true	$\ell = \mu$ predicted	$\ell = e$ true	$\ell = e$ predicted
$t\bar{t}$ 1ℓ	6.2 ± 0.2	6.4 ± 0.2	5.2 ± 0.2	5.5 ± 0.2
$t\bar{t}$ $\tau \to \ell$	1.3 ± 0.1	0.1 ± 0.02	1.2 ± 0.1	0.1 ± 0.02
$\ell + (e, \mu, \tau)$	1.8 ± 0.1	0.9 ± 0.1	1.6 ± 0.1	0.7 ± 0.1
$t\bar{t}$ total	9.3 ± 0.2	7.4 ± 0.2	8.0 ± 0.2	6.3 ± 0.02
W+jets 1ℓ	4.0 ± 0.5	5.6 ± 0.7	4.8 ± 0.6	4.8 ± 0.6
W+jets $\tau \to \ell$	1.0 ± 0.3	0.1 ± 0.1	0.7 ± 0.2	0.2 ± 0.1
W+jets total	5.0 ± 0.6	5.7 ± 0.7	5.6 ± 0.7	5.0 ± 0.6
Total $t\bar{t}$, W jets	14.3 ± 0.6	13.1 ± 0.7	13.6 ± 0.7	11.3 ± 0.6
Other SM	0.4 ± 0.1	1.4 ± 0.2	0.4 ± 0.07	4.2 ± 0.8
Total SM	14.7 ± 0.6	14.5 ± 0.7	14.0 ± 0.7	15.5 ± 1.0

$t\bar{t}$ and W+jets events the prediction works well since in these events the lepton p_T and $\not\!\!E_T$ distributions agree well. However, for the single tau and dilepton backgrounds the prediction from the lepton p_T distribution greatly underestimates the number of events in the $\not\!\!E_T$ tail. This is because the lepton p_T spectrum is much softer than the $\not\!\!E_T$ distribution in dilepton events and single τ events. Since the lepton p_T does not reliably estimate the $\not\!\!E_T$ tail in these events we use separate data-driven methods to estimate these backgrounds. However, the lepton p_T distribution does make a small prediction for these backgrounds, and this is corrected for.

In Table 5.12 "other SM" includes QCD, single top, and Z+jets. In the case of the muon channel the other SM contribution is dominated by Z+jets in both the signal and control sample. For the electron channel the "other SM" contribution is dominated by QCD in both the signal and control sample, and the control sample largely overestimates the amount of signal. In fact, there is such a large contamination in the high electron p_T tail from QCD that we use the muon p_T distribution to predict the $\not\!\!E_T$ in both the muon and electron channel. This is described in detail in Sec. 5.5.8.

Table 5.13 shows a similar breakdown of the SM backgrounds for the tight selection. Similar conclusions can be made as for the loose selection, with the major point that the single lepton high $\not\!\!E_T$ tail is predicted well by the high lepton p_T tail. One difference between the loose and tight selection is that in the tight selection the dilepton and single tau predictions from the single lepton p_T distribution are so small that there is essentially no overlap with the separate dilepton and single tau predictions described in Sec. 5.5.6.

5.5.3 Effect of W polarization in $t\bar{t}$ and W+jets

It is important to quantify differences in the lepton p_T and $\not\!\!E_T$ distributions due to the W polarization in $t\bar{t}$ and W+jets events. As stated previously the W polarization controls the angular distributions of the lepton and neutrino in $t\bar{t}$

Table 5.13: Lepton spectrum method with tight cuts applied to Monte Carlo: tests of data-driven background determination. Pre-selection cuts are applied, and the signal region corresponds to $\not{E}_T > 250$ GeV and $H_T > 500$ GeV. Note that the predictions for the dilepton feed-down and tau to lepton are underestimated by this method and are determined separately.

Background	$\ell = \mu$ true	$\ell = \mu$ predicted	$\ell = e$ true	$\ell = e$ predicted
$t\bar{t}$ 1ℓ	0.44 ± 0.05	0.27 ± 0.04	0.39 ± 0.04	0.24 ± 0.03
$t\bar{t}$ $\tau \to \ell$	0.09 ± 0.02	0	0.08 ± 0.02	0.01 ± 0.01
$\ell + (e, \mu, \tau)$	0.13 ± 0.03	0.02 ± 0.01	0.11 ± 0.02	0.07 ± 0.02
$t\bar{t}$ total	0.66 ± 0.06	0.30 ± 0.04	0.58 ± 0.09	0.32 ± 0.04
W+jets 1ℓ	0.37 ± 0.17	0.67 ± 0.22	0.60 ± 0.21	0.52 ± 0.20
W+jets $\tau \to \ell$	0	0	0.07 ± 0.07	0
W+jets total	0.37 ± 0.17	0.67 ± 0.22	0.67 ± 0.22	0.52 ± 0.20
Total $t\bar{t}$, W jets	1.03 ± 0.18	0.97 ± 0.22	1.25 ± 0.24	0.84 ± 0.20
Other SM	0.05 ± 0.04	0.08 ± 0.06	0.01 ± 0.003	0.38 ± 0.08
Total SM	1.08 ± 0.18	1.05 ± 0.23	1.26 ± 0.24	1.22 ± 0.20

and W+jets events and any differences in the angular distributions of the lepton and neutrino can can lead to their momenta differing in in the lab frame.

We first consider the W polarization in $t\bar{t}$ events, which is our largest background. In the standard model the top quark decays essentially 100%[20] of the time to a W^+ boson and a bottom quark. The W^+ boson from the top decay can be produced with helicity +1 (right-handed), -1 (left-handed), or zero (longitudinal).[21] In the limit that the mass of the bottom quark is zero, the +1 helicity component of the W^+ vanishes. This is because the $V-A$ interaction results in the bottom quark having left-handed chirality (in the limit of no mass its helicity is -1/2), and due to angular momentum conservation the W^+ boson cannot have +1 helicity if the bottom quark has -1/2 helicity. When the small mass of the bottom quark (relative to the top quark) is taken into account there is a very small +1 helicity component of the W^+ boson. Thus, the W^+ polarization is dominated by two helicity components, -1 (left-handed) and zero (longitudinal). The angular distribution of the positively charged lepton in the W^+ rest frame can be written as:

$$\frac{dN}{d\cos\theta^*_\ell} = f_{\lambda=+1}\frac{3}{8}(1+\cos\theta^*_\ell)^2 + f_{\lambda=-1}\frac{3}{8}(1-\cos\theta^*_\ell)^2 + f_{\lambda=0}\frac{3}{4}\sin^2\theta^*_\ell, \quad (5.5)$$

[20]This follows from V_{tb}, which is extremely close to unity (0.999), using the assumption of unitarity of the CKM quark-mixing matrix.

[21] Technically speaking helicity states are not eigenstates of chirality, which determines the handedness; however, in the relativistic limit where the particle mass is small compared to its momentum, the helicity states are essentially eigenstates of chirality. In this paper we will use helicity and chirality interchangebly.

where $f_{\lambda=+1}$, $f_{\lambda=-1}$, and $f_{\lambda=0}$ are the polarization fractions associated with the W-boson helicity +1, helicity +1, and helicity 0 amplitudes, respectively. The angle θ^*_ℓ is the polar angle of the charged lepton in the W^+ rest frame, measured with respect to a z axis that is collinear with the momentum direction of the W^+ in the top-quark rest frame. These polarization fractions determine the angular distribution of the lepton and neutrino in the W rest frame.

These polarization fractions have been theoretically determined [86] to high precision at NNLO:

$$\begin{aligned} f_{\lambda=0} &= 0.687 \pm 0.005, \\ f_{\lambda=-1} &= 0.311 \pm 0.005, \\ f_{\lambda=+1} &= 0.0017 \pm 0.0001 \end{aligned} \tag{5.6}$$

where the uncertainties are on the order of a percent. The errors on $f_{\lambda=-1}$ and $f_{\lambda=0}$ mostly come from the experimental error on the top mass and the error on $f_{\lambda=+1}$ mostly comes from the uncertainty in α_s, and a smaller amount from the uncertainty on m_b. In the case of $\bar{t}$ instead of t the angular distribution of the lepton is the same since the helicity of the W boson and lepton are both flipped. For a $\bar{t}$ decay, the resulting W^- boson is dominated by helicity +1 (right-handed) and 0 (longitudinal). The labels on the $\lambda = \pm 1$ coefficients in Eq. 5.5 and 5.6 would then be interchanged, but not their numerical values (leading to the same

angular distribution equation of the lepton). The angular distribution of the lepton in $t\bar{t}$ Monte Carlo is shown in Figure 5.26(a). When we fit this angular distribution to obtain the polarization fractions our results are extremely close, within one percent, to those given by theory.

The polarization fractions have also been determined experimentally at both the CDF and D0 experiments at the Tevatron. Each experiment measures the fractions $f_{\lambda=+1}$ and $f_{\lambda=0}$ simultaneously in a two-dimensional fit [87], [88]. The measured polarization fractions from CDF [87] are:

$$\begin{aligned} f_{\lambda=0} &= 0.88 \pm 0.11 \pm 0.06, \\ f_{\lambda=+1} &= -0.15 \pm 0.07 \pm 0.06. \end{aligned} \tag{5.7}$$

and the measured polarization fractions from D0 [88] are:

$$\begin{aligned} f_{\lambda=0} &= 0.669 \pm 0.078 \pm 0.065, \\ f_{\lambda=+1} &= 0.023 \pm 0.041 \pm 0.034. \end{aligned} \tag{5.8}$$

Both of these results are consistent within experimental uncertainties of the theoretical values given above. For this analysis we do not rely on the experimental values, since the theoretical values are a very precise prediction of standard model theory and any deviation from these values would be a sign of new physics.

Now that we have described in detail the different properties of the polarization fractions of the W boson in top decays and the resulting angular distribution

of the lepton, we can begin to understand the effect on the lepton and neutrino momenta spectrum in $t\bar{t}$ events. We first start with the angular distribution of the lepton at generator level. Figure 5.26(a) shows the angular distribution of the muon at generator level in $t\bar{t}$ Monte Carlo. This distribution is slightly asymmetric around $\cos(\theta^*) = 0$; there are more events with $\cos(\theta^*)$ close to -1 than 1. This means there are more muons against the W direction than along the W direction. However, since the neutrino will come out at an angle $\pi - \theta^*$, the angular distribution of the neutrino will be flipped around $\cos(\theta^*) = 0$. Thus, there will be more neutrinos with $\cos(\theta^*)$ close to 1 than -1, meaning there will be more events with a neutrino aligned along the W direction than muons aligned along the W direction. Due to these differences in the angular distributions of the lepton and neutrino, on average the muon p_T will be slightly lower than the neutrino p_T at generator level (before applying any cuts such as lepton threshold, number of jets, etc., which could effect these distributions). Figure 5.26(b) shows exactly this difference in the neutrino and muon p_T distributions at generator level in $t\bar{t}$ Monte Carlo.

Asymmetries in the angular distributions of the lepton and neutrino come purely from the left-handed (right-handed) piece of the W^+ (W^-) polarization, which is $1 - cos(\theta)$ for the lepton and $1 + cos(\theta)$ for the neutrino. If the W polarization were purely longitudinal (helicity = 0) with no left-handed or right-

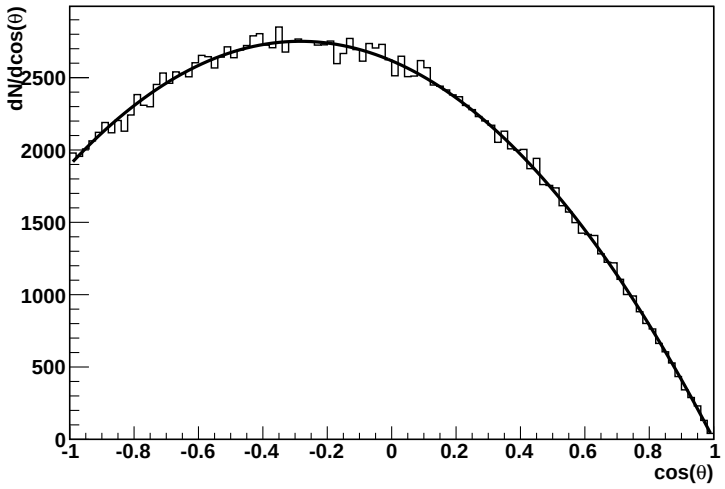

(a) MC: Nominal $dN/d\cos\theta^*_\ell$ in $t\bar{t}$.

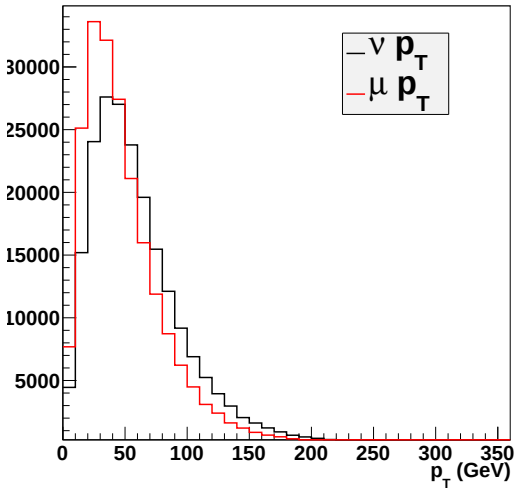

(b) MC: Generator-level lepton and neutrino p_T distributions in $t\bar{t}$.

Figure 5.26: Distributions plotted at generator level with requiring exactly 1 muon from a W boson and no other generator level or reco level requirements. The angular distribution of the muon results in a quantifiable difference in the muon and neutrino p_T distributions.

handed piece, the angular distribution of the lepton would be symmetric around $cos(\theta) = 0$ (the longitudinal term in Equation 5.5 is $sin^2(\theta)$) and, thus, the angular distribution of the neutrino would be the same as the lepton. The resulting lepton and neutrino p_T spectrum would then be essentially the same as both the lepton and neutrino would have an equal chance of being along the W direction or against the W direction in the top rest frame. Figure 5.27(a) shows the angular distribution of the lepton after reweighting at Monte Carlo level to a pure longitudinal polarization. The resulting p_T distributions of the lepton and neutrino after reweighting to pure longitudinal polarization, Figure 5.27(b), show that there are no longer any differences in the lepton and neutrino p_T. Thus, in the case of $t\bar{t}$ it is clear that the differences between the neutrino and lepton p_T spectrum at generator level arise from the W polarization.[22] Because this effect is well understood and modeled in the Monte Carlo, we quantify this effect using a scale factor for the prediction (in fact, this scale factor not only takes into account polarization effects but other effects such as the lepton p_T threshold, contamination of the control region by other backgrounds, etc.). The scale factor is described in detail in Sec. 5.5.12.

The W polarization in W+jets, our second largest background, is slightly more complicated than in $t\bar{t}$. In W+jets all three W polarization states are

[22]Other detector effects will be discussed later in detail.

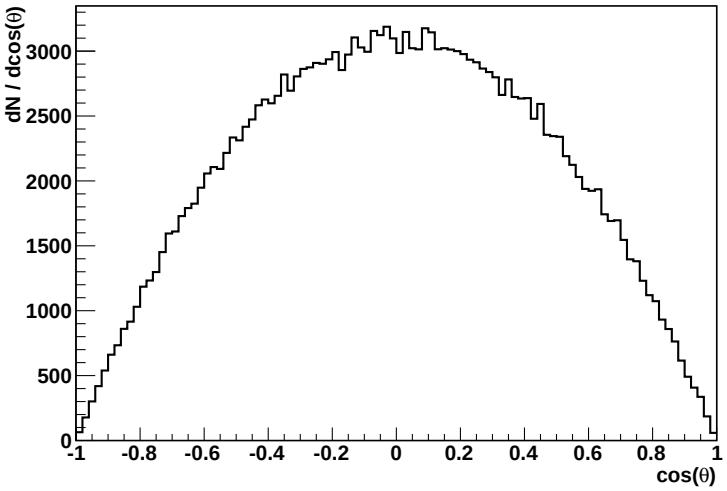

(a) MC: Re-weighted pure-longitudinal $dN/d\cos\theta^*_\ell$ $t\bar{t}$.

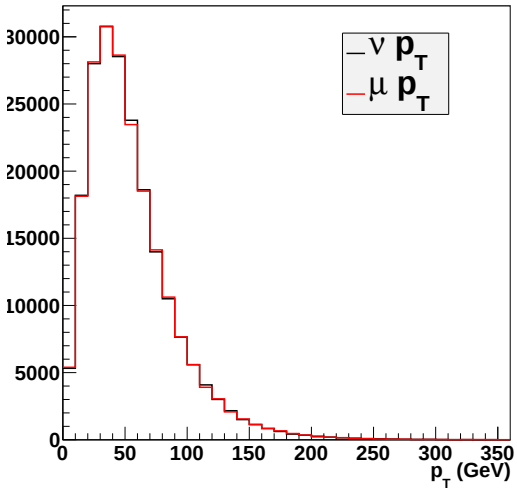

(b) MC: p_T spectrum from re-weighted $t\bar{t}$.

Figure 5.27: Test of re-weighting procedure for W polarization in $t\bar{t}$ events. Distributions plotted at generator level with requiring exactly 1 muon from a W boson and no other generator level or reco level requirements. Differences in the neutrino and muon p_T go away at generator level when reweighting the angular distribution to be purely longitudinal.

effectively present, the W polarization has a p_T dependence and the W polarization is somewhat different for W^+ and W^-. A first measurement of the W polarization at CMS has been reported [89] and is consistent with Alpgen and Madgraph simulations predicting that the W^+ and W^- are predominantly left-handed in W+jets events at high p_T. In the lepton spectrum method the large $\not\!\!E_T$ and lepton p_T requirements for the signal and control regions, respectively, make it so that the relevant W bosons have p_T greater than 100 GeV. Figure 5.28 shows the generator level $p_T(W)$ distribution after preselection requirements and also after an additional $\not\!\!E_T$ requirement. The additional $\not\!\!E_T$ requirement increases the $p_T(W)$ because large $\not\!\!E_T$ events come from neutrinos from high p_T W's.

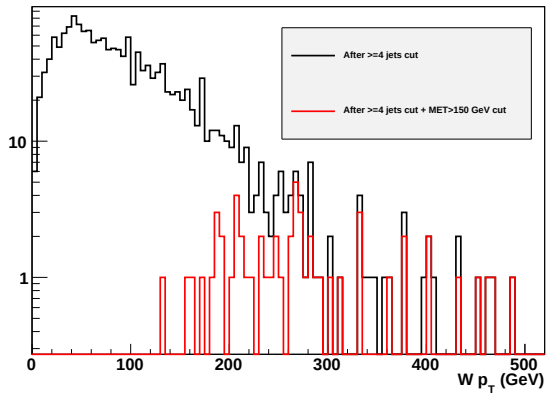

(a)

Figure 5.28: $p_T(W)$ after the preselection cuts (black) and after an additional $\not\!\!E_T$ cut (red), W+jets Madgraph MC.

There is also a new NLO QCD calculation [90] that has shown that the polarization fractions in W+jets events are stable with respect to QCD corrections. The polarization fractions are also quite stable over $p_T(W)$, with the left-handed piece on the order of 60% and rising with $p_T(W)$, the right-handed piece staying constant around 20-25%, and the remaining longitudinal fraction dropping towards zero as the $p_T(W)$ increases [90].

Figure 5.29 shows the angular distribution of the lepton in W^+ and W^- for $p_T(W)$ between 100 and 300 GeV. Since the polarization fractions are dominated by the left-handed piece in both W^+ and W^- the angular distributions have opposite asymmetries, with the W^+ angular distribution of the lepton peaking at $\cos(\theta^*) = -1$ and the W^- angular distribution of the lepton peaking at $\cos(\theta^*) = 1$. Thus, high p_T muons tend to come from W^- events and high p_T neutrinos tend to come from W^+ events. A cancellation in the asymmetries[23] would occur if the polarizations fractions were exactly the same in both W^+ and W^- and if the number of W^+'s was the same as the number of W^-'s. However, the cancellation in the asymmetries is not perfect because they are slightly different in W^+ as W^- and at the LHC the W^+ cross section is higher than the W^- cross section.[24] For events with a muon that is central ($|\eta < 2.1|$) and four jets, the

[23]Which would result in the same number of high p_T muons and high p_T neutrinos at generator level.

[24]This is because the LHC is a pp machine, and since there are two up quarks and only one down quark in the proton the W^+ production is much higher. This is not true at the Tevatron because it is a $p\bar{p}$ machine.

cancellation of the asymmetries is good enough that the neutrino and muon p_T distributions are very similar, see Figure 5.22(c). Differences between the two distributions are taken into account by the scale factor described in Sec. 5.5.10. The systematic uncertainties associated with these W polarization effects are discussed in Sec. 5.5.12.

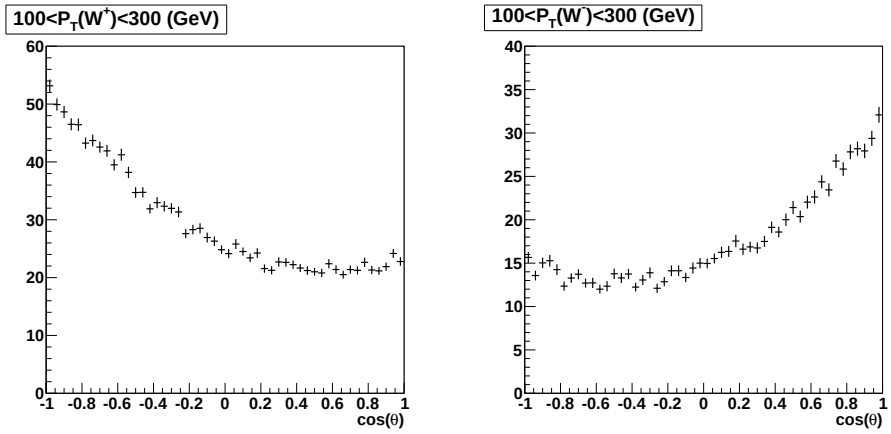

(a) W^+ (b) W^-

Figure 5.29: $dN/d\cos\theta^*_\ell$ (SM) in W + jets, $100 < p_T(W) < 300$ GeV, Alpgen MC. Distributions plotted at generator level, with requirement of exactly 1 muon from a W boson and no other requirements.

5.5.4 Effect of lepton p_T threshold

In this analysis a minimum p_T threshold is applied to the reconstructed muon or electron but no corresponding threshold is placed on the $\not\!\!E_T$. This creates an asymmetry between the two distributions that must be understood and taken

into account. The lepton p_T threshold requirement removes low p_T leptons in $t\bar{t}$ and W+jets events which tend to have high $\not\!\!E_T$. This is due to the anti-correlation between the two variables shown in Figure 5.23(a). However, since in the control sample the high p_T leptons easily pass the minimum p_T threshold and there is no $\not\!\!E_T$ requirement applied, there is no corresponding removal of high lepton p_T events, which are used for the $\not\!\!E_T$ prediction. This means the p_T threshold produces a bias toward an over-prediction of high $\not\!\!E_T$ events for the SM background. Figure 5.22 shows, for $t\bar{t}$ and W+jets MC, that some fraction of high p_T neutrinos are removed once a lepton p_T threshold is applied.

Though technically speaking we could apply a $\not\!\!E_T$ requirement in the lepton p_T control sample to get rid of this asymmetry between the $\not\!\!E_T$ and p_T samples, there are a few issues that make this difficult and risky. The first is that the $\not\!\!E_T$ and p_T have very different resolutions (which will be described in more detail in the next section). This means that a $\not\!\!E_T$ requirement of 20 GeV can be very different than a lepton p_T requirement of 20 GeV. Also, when looking at low $\not\!\!E_T$ events the $\not\!\!E_T$ is no longer dominated by the neutrino p_T, there is a larger relative contribution from detector effects, which means that a $\not\!\!E_T$ requirement of 20 GeV does not correspond to a neutrino requirement of 20 GeV (whereas a reconstructed p_T requirement of 20 GeV for the muon is very close to a generator level muon requirement of 20 GeV because the muon resolution is very good).

Without fully understanding resolution and detector effects on low $\not\!\!E_T$ events there is a risk that placing a low $\not\!\!E_T$ requirement on the control sample will produce effects in the high lepton p_T tail that we cannot quantify exactly. Thus, we have decided to avoid placing a $\not\!\!E_T$ requirement on the lepton p_T control sample. Instead, differences between the $\not\!\!E_T$ and lepton p_T distributions from the lepton p_T threshold are taken into account by the scale factor, discussed in Sec. 5.5.10.

5.5.5 Effect of $\not\!\!E_T$ resolution on background prediction

The resolution of the lepton p_T is on average better than the resolution of the $\not\!\!E_T$ because the $\not\!\!E_T$ is more sensitive to detector effects than the lepton reconstruction.[25] Thus, even if the energy scales of the lepton p_T and $\not\!\!E_T$ were the same, the poorer resolution of the $\not\!\!E_T$ would broaden the $\not\!\!E_T$ spectrum with respect to the lepton spectrum. We take into account differences in the $\not\!\!E_T$ and lepton resolutions by smearing the measured lepton momenta using $\not\!\!E_T$ templates from QCD data events. In these events the $\not\!\!E_T$ is predominantly from mismeasurement, not from high p_T neutrinos. This smearing essentially degrades the

[25]The reason the $\not\!\!E_T$ is more sensitive to detector effects is that it is not directly measured but rather infered from the measurement of all the objects in the event. So if any one of these many objects is reconstructed incorrectly it will effect the $\not\!\!E_T$. However, the lepton p_T is measured directly and not as dependent on a full event reconstruction. For more information on $\not\!\!E_T$ resolution in CMS, see Sec. A.

resolution of the lepton p_T measurement to match the $\not\!\!E_T$ resolution, in effect modeling the mismeasured portion of the $\not\!\!E_T$ (which again is the subdominant part of the total $\not\!\!E_T$ in our sample).

To obtain the $\not\!\!E_T$ templates we use samples of QCD multijet events (with no lepton requirement), which should have very little true $\not\!\!E_T$ and should be dominated by fake $\not\!\!E_T$ from detector effects. Single-jet triggers with a broad range of thresholds on the leading jet p_T are used to obtain QCD multijet events. Figure 5.30 shows the leading reconstructed jet p_T for different single-jet triggers used, where HLT_JetxxU means that the uncorrected jet p_T threshold of the trigger is xx GeV. Templates are made for different jet triggers, taking into account the HLT and L1 prescale values. In a given event, we choose the template depending on the leading jet p_T in the event, guaranteeing the most statistics in the templates. For larger leading jet p_T events the higher p_T jet triggers have more statistics since the lower p_T jet triggers have larger prescales. For smaller leading jet p_T in the event the lower p_T jet triggers have more statistics due to the threshold requirement of the high p_T jet triggers.[26]

The templates are created for events with >= 4 jets and are characterized by the H_T range of the event, since the $\not\!\!E_T$ resolution depends on H_T. Each

[26]For leading jet p_T between 30-70 GeV, 70-100 GeV, 100-170 GeV, and >170 GeV the triggers used for the templates are the HLT_Jet15U trigger, the HLT_Jet30U trigger, the HLT_Jet50U trigger, and the HLT_Jet100U trigger, respectively.

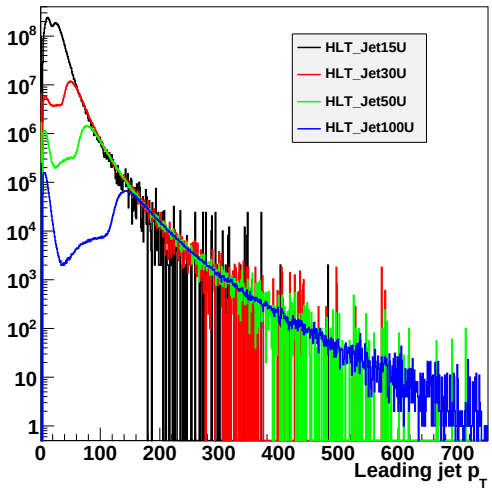

Figure 5.30: Leading jet p_T for different single-jet triggers.

template then serves as a resolution function and is sampled to obtain a random smearing of the lepton p_T. An example of two $\not\!\!E_T$ templates from the data used for the smearing is shown in Figure 5.31. For $0 < H_T < 1000$ GeV, the ΔH_T range for a given template is 10 GeV, whereas for $1000 < H_T < 2000$, the ΔH_T range for a given template is 100 GeV. A single template is created for events with $H_T >$2000 GeV. [27] The $\not\!\!E_T$ bins of the templates are 1 GeV wide.

The smearing template is applied as follows. For a single event with a particular lepton p_T, see Figure 5.32(a), the $\not\!\!E_T$ in each bin of the template is added to the lepton p_T at an angle θ in the transverse plane, with a weight corresponding

[27] We have studied changing the size of the template binning in H_T by factors of two and five and recomputed the resolution smearing in each case. The effects are negligible, demonstrating that the prediction is not highly sensitive to the details of the templates.

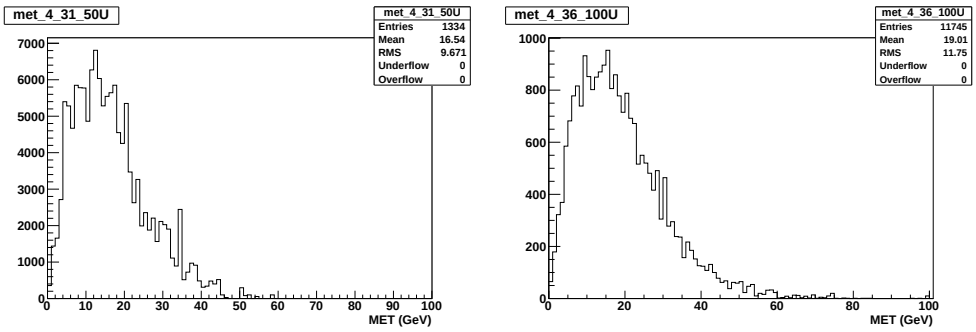

(a) (b)

Figure 5.31: Examples of $\not\!\!E_T$ templates from the data. The templates are produced in bins of H_T. Both these templates are for the ≥ 4 jet bin. Template (a) has $H_T = 310 - 320$ GeV and uses the Jet Trigger HLT_Jet50U. Template (b) has $H_T = 360 - 370$ GeV and Jet Trigger HLT_Jet100U.

to the number of entries in that particular $\not\!\!E_T$ bin. This is then done for 20 separate values of θ from 0-π, assuming that mismeasurements average over the full detector. For each value of θ and each bin in the $\not\!\!E_T$ template a new entry is made in the new smeared lepton p_T distribution. Thus, for a $\not\!\!E_T$ template with 50 bins filled (say from 0-50 GeV) there will be 1000 entries in the smeared distribution (20 θ angles x 50 $\not\!\!E_T$ bins). The smeared distribution is then normalized to one so that the weight of the smeared event will be the same as the unsmeared event. The lepton p_T in this single event is smeared to a distribution that peaks at the original value of the lepton p_T but with tails that mimic the resolution effects of the $\not\!\!E_T$ measurement. Figure 5.32 shows the result of smearing one event.

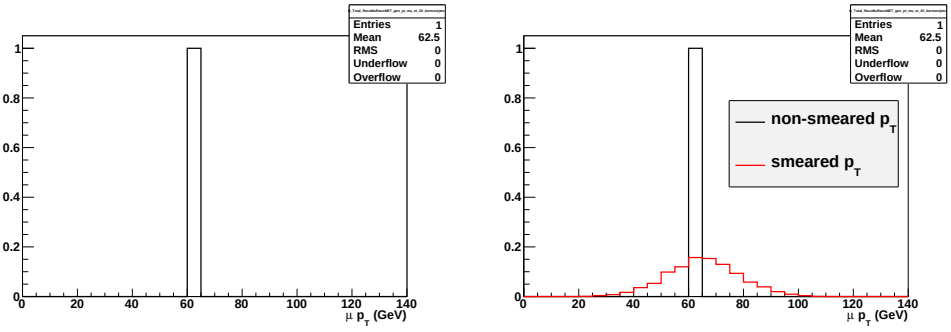

(a) Muon p_T of a single event.

(b) Muon p_T of a single event with and without smearing

Figure 5.32: Smearing effect on a single event.

The smeared distribution for this particular event is then combined with the smeared distributions of all the other events in the sample to obtain the full smeared lepton p_T spectrum. Figure 5.33 shows the effect of smearing the lepton p_T spectrum in the data. In the data the lepton p_T smearing increases the background prediction by about 10-15%. We have also studied the smearing in $t\bar{t}$ and W+jets Monte Carlo (using Monte Carlo QCD $\not\!\!E_T$ templates) and we see an increase in the background prediction of 5-10%, slightly smaller than in data.

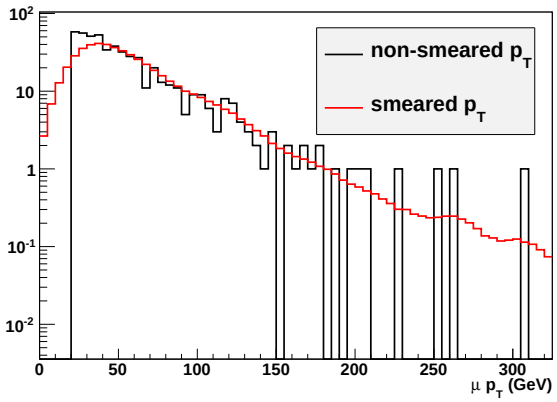

Figure 5.33: Smearing effect on the muon p_T distribution in 36 pb^{-1} of data.

5.5.6 Dilepton, single tau background predictions

As described in Sec. 5.5.2 the lepton p_T distribution does not accurately predict the $\not\!\!E_T$ tail from $t\bar{t}$ dilepton events and $t\bar{t}$ and W+jets events where a τ decays to a muon or electron. These backgrounds represent approximately 30% of the total background in the signal region and their contribution is estimated using separate data-driven techniques.

We categorize four types of $t\bar{t}$ dilepton events that can feed-down into the single lepton sample. These are:

- Lost leptons: second lepton is a muon or electron that falls outside the detector acceptance or is lost due to inefficiency of the reconstruction.

- Ignored leptons: second lepton is a muon or electron that has been reconstructed but does not pass the lepton requirements of the analysis.
- τ hadronic decay: second lepton is a τ that decays hadronically.
- τ leptonic decay: second lepton is a τ that decays to a muon or electron which does not pass the lepton criteria in the event.

Ignored leptons and τ hadronic decays tend to give the largest contribution to the dilepton feed-down. There are other dilepton feed-down events that are not listed above[28]; however, these events contribute a negligible amount to the signal sample in this analysis.

To estimate these dilepton backgrounds we use a control sample in the data which consists of reconstructed dilepton events with $2e$, 2μ, or $1e$ and 1μ. We take the $\not\!\!E_T$ from this control sample and after making some changes depending on the type of di-lepton event we are trying to predict we apply a Monte Carlo scale factor, defined to be the ratio of Monte Carlo events in the signal sample to the control sample, to estimate the number of dilepton feed-down events in the signal sample. This method is nice because it only takes a ratio from the Monte Carlo not an absolute rate, so a lot of uncertainties will cancel in this ratio. The actual shape of the $\not\!\!E_T$ distribution is taken from the data control sample and the

[28]For instance you could have an event where there is two tau decays, one leptonic, one hadronic.

absolute number of dilepton feed-down events in our signal sample is normalized to the number in the dilepton control sample.

In the case of ignored leptons since the second lepton was reconstructed in the detector the $\not\!\!E_T$ calculation properly takes it into account and the dilepton control sample $\not\!\!E_T$ shape can be used directly to model this contribution. For the case of lost leptons the second lepton is outside of detector acceptance or not reconstructed and the $\not\!\!E_T$ calculation does not take it into account. Because of this the $\not\!\!E_T$ shape must be modified to include the p_T of the missing lepton. Thus, for lost leptons the p_T of one of the observed leptons is added vectorially to the $\not\!\!E_T$ vector.

For τ hadronic and τ leptonic dilepton events the modification of the $\not\!\!E_T$ shape from the dilepton control sample is a little more complicated. For the case of a second lepton that is a τ decaying to a μ or e (where this μ or e does not pass the analysis requirements) a fraction of the p_T of one of the dilepton control sample leptons is added vectorially to the $\not\!\!E_T$ to model the additional neutrinos from the leptonic τ decay. The fraction is determined from 1-r_μ, where r_μ is a random number chosen from the tau-muon response function in $t\bar{t}$ Monte Carlo. The tau-muon response function tells you in a $\tau \to \ell$ decay the fraction of $p_T(\mu)$ to $p_T(\tau)$. So 1-r_μ should give the amount of neutrino p_T from the τ that should be added

to the $\not\!\!E_T$. Figure 5.34 shows the tau-muon response function in simulation and it shows that it does not depend on $p_T(\tau)$.

In τ hadronic events the τ lepton decays hadronically into a single jet or multiple jets, where additional neutrinos from this τ hadronic decay will contribute to the $\not\!\!E_T$. We treat this case similar to the τ leptonic case and take a fraction of the p_T of one of the dilepton control sample leptons and add it vectorially to the $\not\!\!E_T$. However, in this case the fraction is determined from a tau-jet response function, which should simulate how much of the $p_T(\tau)$ goes to the neutrinos and how much goes to the resulting jet(s). Figure 5.35 shows the tau-jet response function in $t\bar{t}$ Monte Carlo.

For each dilepton feed-down contribution we test the procedure in $t\bar{t}$ Monte Carlo. We apply a $\not\!\!E_T$ requirement of 40 GeV to the dilepton control sample to reduce contamination from off-shell Z's. Table 5.14 shows for the loose selection the true number of events, the prediction in the Monte Carlo and the prediction in the data. In both the muon and electron case the Monte Carlo predictions are within statistical uncertainties of the true number in Monte Carlo. Table 5.15 shows the same numbers but for the tight selection. In the tight selection the Monte Carlo prediction shows an overestimate with respect to the Monte Carlo true number of dilepton feed-down events. This overestimate is the result of many little effects, including the muon and jet response hypothesis, the kine-

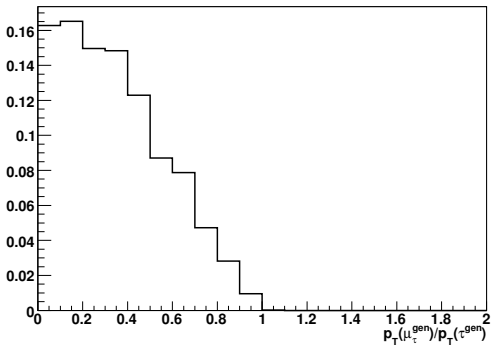

(a) 20 GeV< $p_T(\tau)$ <50 GeV

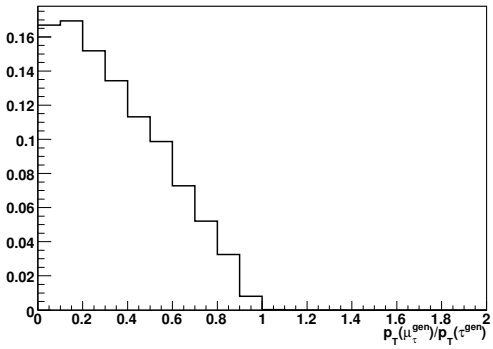

(b) 50 GeV< $p_T(\tau)$ <100 GeV

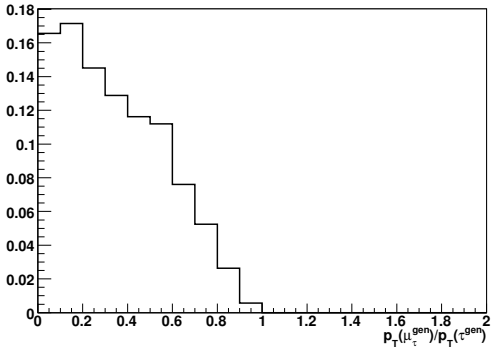

(c) $p_T(\tau)$ >100 GeV

Figure 5.34: The p_T response function for muons from τ decays, normalized to unity in $t\bar{t}$ MC. Figures from Ref. [80]

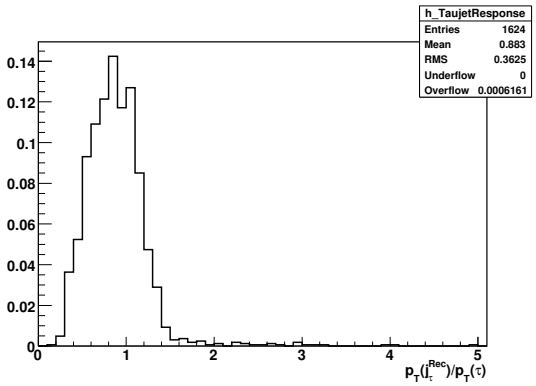

Figure 5.35: The p_T response function for jet(s) from τ decays with 20 GeV< $p_T(\tau)$ <50 GeV. Distribution normalized to unity in $t\bar{t}$ MC. Figure from Ref. [80].

Table 5.14: Loose Selection: Dilepton feed-down yields for Monte Carlo truth, Monte Carlo prediction, and data prediction. Only statistical uncertainties are shown. Numbers from Ref. [80].

Process	MC truth	MC prediction	data prediction
1μ	1.6 ± 0.1	1.8 ± 0.1	1.1 ± 0.6
$1e$	1.4 ± 0.1	1.5 ± 0.1	0.9 ± 0.5

matic cuts, the $\not\!\!E_T$ scale, among others. We correct for these effects using scale factors discussed in Sec. 5.5.10. Figure 5.36 shows the comparison of the actual $\not\!\!E_T$ distribution and the predicted $\not\!\!E_T$ distribution in dilepton feed-down events in $t\bar{t}$ Monte Carlo. Figure 5.37 shows the comparison of the predicted $\not\!\!E_T$ distribution in the data to the actual $\not\!\!E_T$ distribution of dilepton feed-down events in $t\bar{t}$ Monte Carlo.

Next we look at the background case where a single τ decays to a muon or electron in either $t\bar{t}$ or W+jets. These events will end up in our sample if

Table 5.15: Tight Selection: Dilepton feed-down yields for Monte Carlo truth, Monte Carlo prediction, and data prediction. Only statistical uncertainties are shown. Numbers from Ref. [80].

Process	MC truth	MC prediction	data prediction
1μ	0.11 ± 0.02	0.23 ± 0.03	$0.0^{+0.7}_{-0.0}$
$1e$	0.10 ± 0.02	0.18 ± 0.02	$0.0^{+0.5}_{-0.0}$

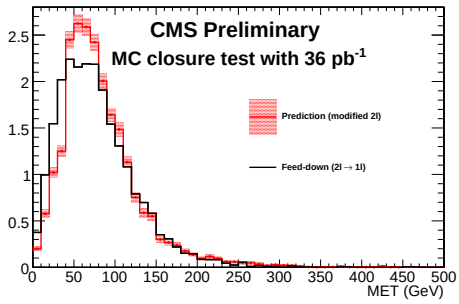

(a) Dilepton, muon MC, Loose Selection

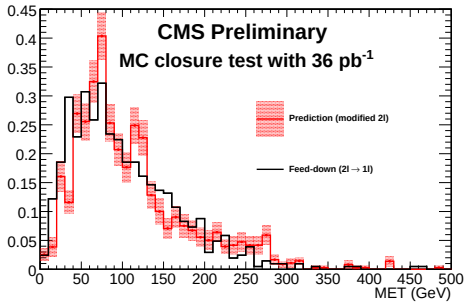

(b) Dilepton, muon MC, Tight Selection

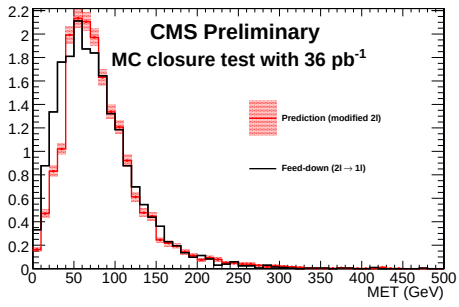

(c) Dilepton, electron MC, Loose Selection

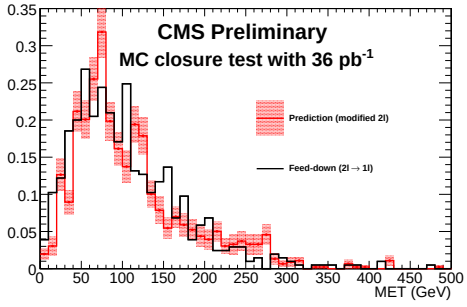

(d) Dilepton, electron MC, Tight Selection

Figure 5.36: Monte Carlo dilepton feed-down: comparison of actual $\not\!\!E_T$ distribution with prediction based on dilepton control sample. Figures from Ref. [80].

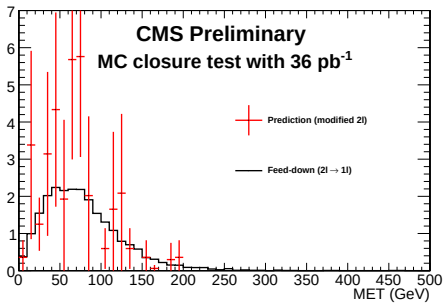

(a) Dilepton, muon data, Loose

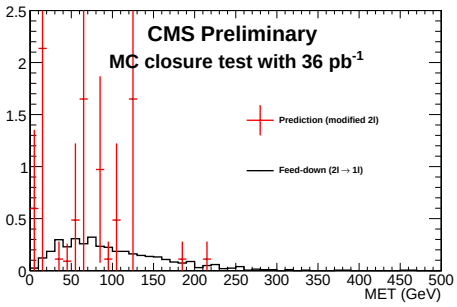

(b) Dilepton, muon data, Tight

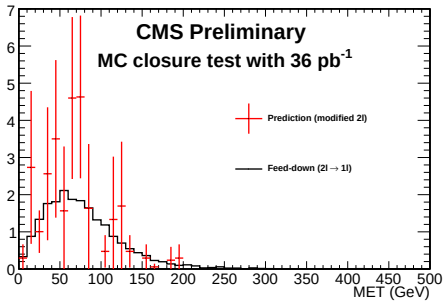

(c) Dilepton, electron data, Loose

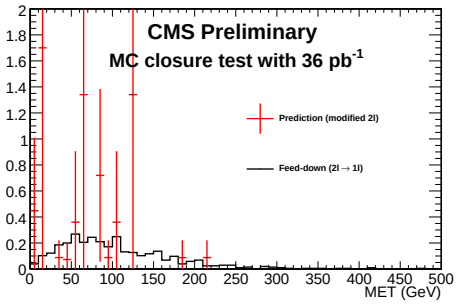

(d) Dilepton, electron data, Tight

Figure 5.37: Data dilepton feed-down: prediction of $\not\!\!E_T$ distribution based on dilepton control sample; comparison is with Monte Carlo dilepton background. Figures from Ref. [80].

the muon or electron passes all our lepton requirements. The control sample used for this sample is the single lepton sample (not the dilepton samples). The $\not\!\!E_T$ shape from this control sample is modified in the following way to predict this background contribution. A fraction of the lepton p_T is added vectorially to the $\not\!\!E_T$ to emulate the additional neutrinos in the τ decay. This fraction is taken from the same response function as for the dilepton leptonic τ decay background, Figure 5.35. In the electron channel an additional requirement of $0.26 < \delta\phi(\not\!\!E_T, j_1) < 3.05$ is made, where j_1 is the leading jet in the event. This cut is made to get rid of the QCD contamination in the electron channel, and is not made in the muon channel since the QCD contribution is very small.

Table 5.16 shows the true number of single τ events in the Monte Carlo and the resulting prediction in Monte Carlo and data for the loose selection. In both the muon and electron case the predicted number in Monte Carlo is within statistical uncertainties of the true number in Monte Carlo. Table 5.17 shows the same numbers but for the tight selection. As is the case for the dilepton feed-down, in the tight selection the prediction in the Monte Carlo overestimates the true number in the Monte Carlo and is taken into account by applying scale factors discussed in Sec.5.5.10. Figure 5.38 shows the Monte Carlo $\not\!\!E_T$ prediction and true $\not\!\!E_T$ for the single τ background. Figure 5.39 shows the $\not\!\!E_T$ prediction in data vs. the true $\not\!\!E_T$ distribution in Monte Carlo.

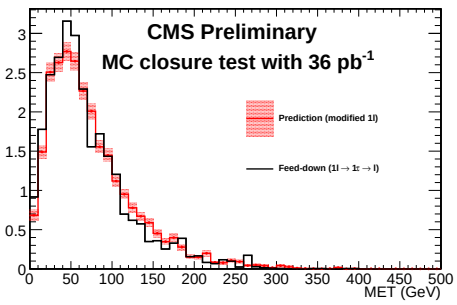

(a) tau, muon MC, Loose

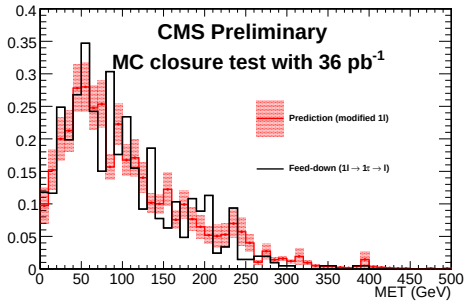

(b) tau, muon MC, Tight

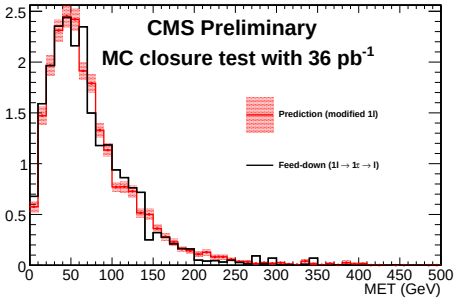

(c) tau, electron MC, Loose

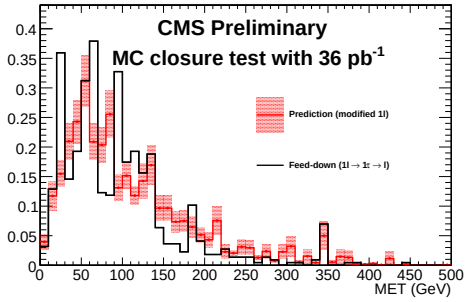

(d) tau, electron MC, Tight

Figure 5.38: Monte Carlo τ background: comparison of actual $\not\!\!E_T$ distribution with prediction based on single-lepton control sample. Figures from Ref. [80].

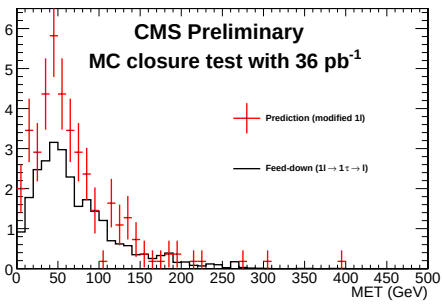

(a) tau, muon data, Loose

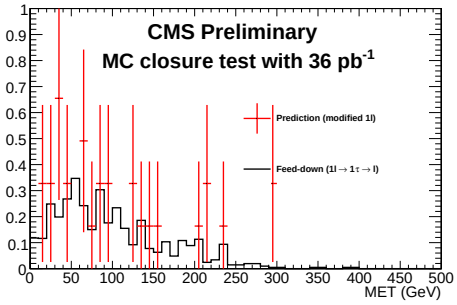

(b) tau, muon data, Tight

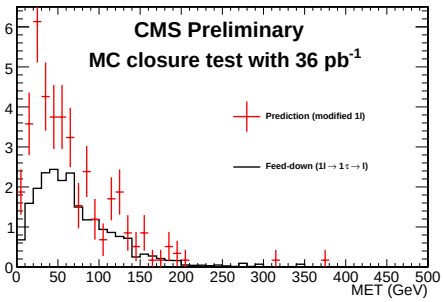

(c) tau, electron data, Loose

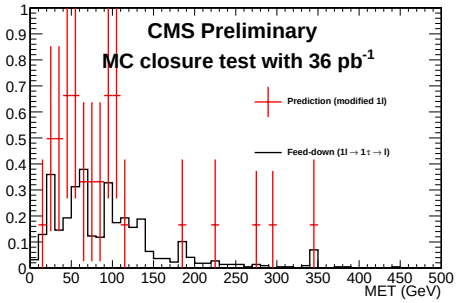

(d) tau, electron data, Tight

Figure 5.39: Data τ background: prediction of $\not\!\!E_T$ distribution based on single-lepton control sample; comparison is with Monte Carlo τ background samples. Figures from Ref. [80].

Table 5.16: Loose Selection: single $\tau \to \ell$ yields for Monte Carlo truth, Monte Carlo prediction, and data prediction. Only statistical errors are shown. Numbers from Ref. [80].

Process	MC truth	MC prediction	data prediction
1μ	2.3 ± 0.3	2.6 ± 0.1	2.4 ± 0.7
$1e$	1.7 ± 0.2	1.9 ± 0.1	2.6 ± 0.6

Table 5.17: Tight Selection: single $\tau \to \ell$ yields for Monte Carlo truth, Monte Carlo prediction, and data prediction. Only statistical errors are shown. Numbers from Ref. [80].

Process	MC truth	MC prediction	data prediction
1μ	0.09 ± 0.02	0.19 ± 0.02	0.3 ± 0.2
$1e$	0.14 ± 0.07	0.26 ± 0.04	0.5 ± 0.3

Data-driven methods for the dilepton feed-down and single $\tau \to \ell$ backgrounds have been described. These backgrounds are significantly less than that from $t\bar{t}$ and W+jets events with a single μ or e above threshold. For the tight selection less than one event is expected from the combined dilepton feed-down and single $\tau \to \ell$ backgrounds.

5.5.7 QCD background prediction in signal region

From Monte Carlo studies the QCD contribution to the signal region is expected to be very small, much less than the major backgrounds $t\bar{t}$ and W+jets and much less than one event. The relative isolation requirement and large $\not\!\!E_T$ requirement suppress the QCD background greatly. Because the QCD background

in the signal region is very small it is not necessary to estimate it precisely. We just want to confirm that it is much less than one event using data-driven methods instead of the Monte Carlo.

To predict the background from QCD processes, we use the two-dimensional distribution of $\not\!\!E_T$ and the relative lepton isolation (RelIso)[29]. Using a QCD dominated sample with $\not\!\!E_T$<25 GeV, we measure the ratio of the number of leptons passing the lepton isolation cut (RelIso< 0.10 for muons) to those in an isolation sideband (0.20 < RelIso < 0.50 for muons). Events that pass the $\not\!\!E_T$ requirement for the signal region, but are in the isolation sideband, are then scaled by this measured ratio, to obtain the number of events in the signal region (with small relative isolation and large $\not\!\!E_T$). A few things are crucial to this method: the first is that we understand the shape of the relative isolation distribution of the lepton and the second is that the relative isolation of the lepton and the $\not\!\!E_T$ are not strongly correlated.

Figure 5.40 shows the relative isolation distribution for muons in data and in Monte Carlo samples. The Monte Carlo samples are absolutely normalized to the luminosity using their respective nominal cross sections. The narrow peak in the region RelIso< 0.05 is produced by events with a prompt lepton from electroweak processes and $t\bar{t}$, while QCD completely dominates the sample for

[29]The relative isolation variable is described in detail in Sec. 5.2.5.

larger values of RelIso. The agreement in both the shape and normalization is good. We have investigated the relative isolation in the electron channel as well and find good agreement between data and Monte Carlo. Figure 5.41 shows the $\not\!\!E_T$ distribution in slices of relative isolation in QCD Monte Carlo events. The $\not\!\!E_T$ distribution does not depend significantly on the relative isolation slice used and, thus, we conclude that the correlation must be small.

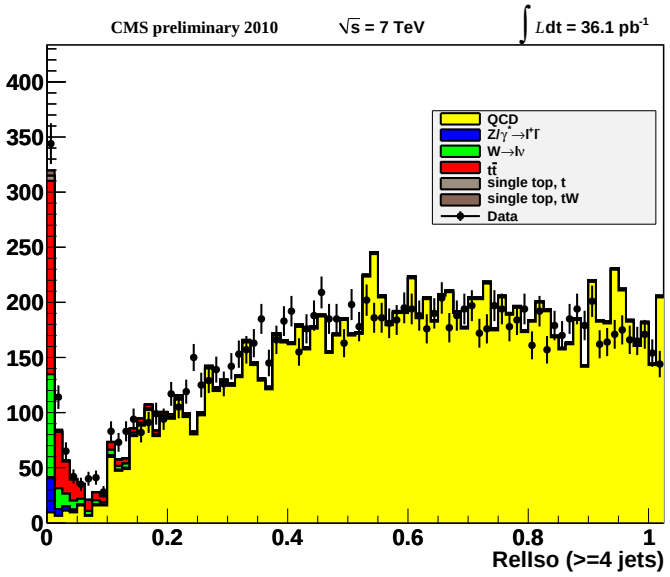

Figure 5.40: Relative isolation in data and SM Monte Carlo samples in events with $\geq 1\mu$, $0e$, and at least four jets with $p_T > 30$ GeV. The requirement that the muon satisfy $\Delta R > 0.3$ with respect to all jets above threshold is not applied here because it biases the distribution. This plot also uses lower muon p_T threshold, 15 GeV, to obtain a larger event sample in the low RelIso tail of the distribution.

We test the QCD background determination in the muon channel in the Monte Carlo. Figure 5.42 shows the two-dimensional distribution of relative

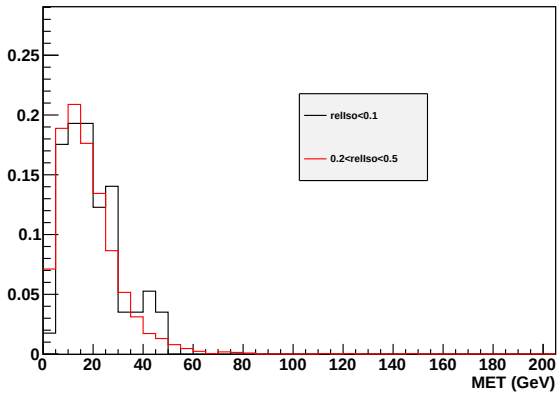

(a) Linear scale.

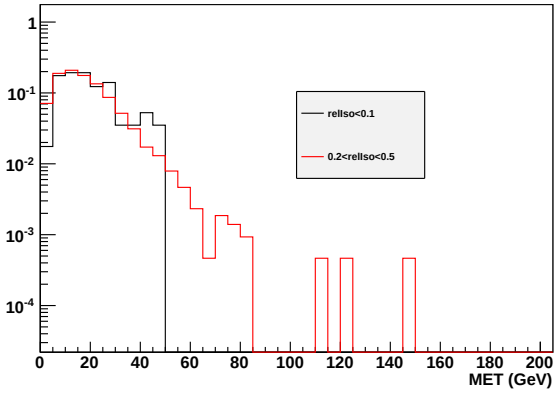

(b) Log scale.

Figure 5.41: QCD Monte Carlo: $\not\!\!E_T$ in slices of RelIso (RelIso<0.1 and $0.2 <$ RelIso < 0.5 for muons.

isolation vs. $\not\!\!E_T$ for QCD, electroweak, and $t\bar{t}$ Monte Carlo samples. Since the QCD Monte Carlo statistics run out at high $\not\!\!E_T$ we choose a signal region with a much looser $\not\!\!E_T$ requirement, $\not\!\!E_T$>25 GeV, than for the loose or tight selection. Table 5.18 shows the QCD Monte Carlo yields in different control regions, A, B, C, and the signal region D. Since the $\not\!\!E_T$ and relative isolation do not have a significant correlation, the predicted number of events in signal region D can be obtained from the control regions using the following procedure, $N(D)_{pred} = [N(B)/N(A)]N(C)$. The test in the Monte Carlo obtains a prediction that is within 100% of the actual number of events. This is sufficient given the very small contribution of this background.

In the data, we raise the $\not\!\!E_T$ threshold for the signal region to correspond to the loose and tight selection. Given that the high $\not\!\!E_T$ regions have some contamination from $t\bar{t}$ and W+jets events, this background prediction should be

Table 5.18: QCD background study in Monte Carlo using the two-dimensional distribution of RelIso vs. $\not\!\!E_T$. The regions are defined as A: 0.2<RelIso<0.5, $\not\!\!E_T$ <25 GeV, B: RelIso<0.1, $\not\!\!E_T$ <25 GeV, C: 0.2<RelIso<0.5, $\not\!\!E_T$ >25 GeV, D: RelIso<0.1, $\not\!\!E_T$ >25 GeV. Because there are so few QCD events in the signal region, even with the loose selection requirements, the test region D starts at $\not\!\!E_T > 25$ GeV, compared with $\not\!\!E_T > 150$ GeV for the loose selection and $\not\!\!E_T > 250$ GeV for the tight selection. Furthermore, we perform a test with a lower muon p_T threshold to gain additional statistics.

μ p_T threshold	Region A	Region B	Region C	Region D	Predicted D
$p_T > 15$ GeV	2635 ± 64	62.9 ± 9.9	745.1 ± 34.2	26.7 ± 6.5	17.8 ± 3.0
$p_T > 20$ GeV	1785 ± 53	26.7 ± 6.7	382.2 ± 24.5	12.6 ± 4.5	5.7 ± 1.4

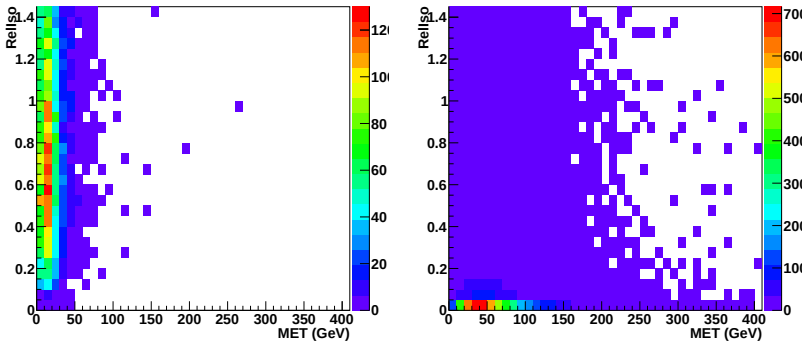

(a) QCD

(b) $t\bar{t}$

(c) W + jets

(d) Z + jets

Figure 5.42: Monte Carlo samples in the muon channel: relative isolation vs. $\not\!\!E_T$ distributions.

regarded as an overestimate. As noted earlier, our goal is simply to establish that the QCD background is much less than one event.

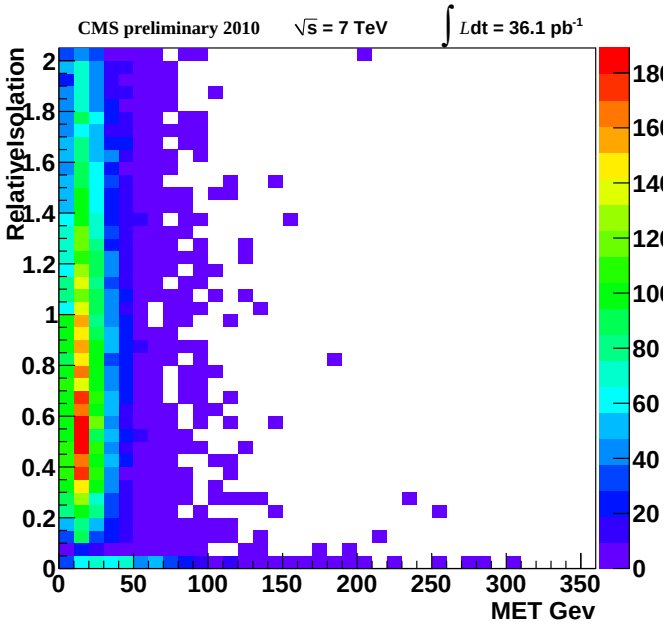

Figure 5.43: Distribution of muon relative isolation (RelIso) vs. $\not\!\!E_T$ in data (36 pb^{-1})

Figure 5.43 shows the relative isolation vs. $\not\!\!E_T$ distribution in the data for the muon channel after the loose selection. We obtain a prediction for the number of low RelIso events with $\not\!\!E_T$>150 GeV for the loose selection and $\not\!\!E_T$>250 GeV for the tight selection. Though the tight selection has an additional H_T requirement of 500 GeV, we do not place this requirement on the QCD estimate for the tight selection in order to have more statistics in the low $\not\!\!E_T$ region to calculate the ratio of high to low relative isolation events. With the H_T requirement removed

Table 5.19: Data (muon channel): QCD background determination in the space of RelIso vs. $\not\!\!E_T$ for loose and tight selections, 36 pb^{-1}.

	Region A	Region B	Region C	Region D
RelIso range	0.2 to 0.5	< 0.10	0.2 to 0.5	< 0.10
$\not\!\!E_T$ range (GeV) loose selection	0 to 25	0 to 25	> 150	> 150
Number events	1873	173	2	0.18 ± 0.13
$\not\!\!E_T$ range (GeV) tight selection	0 to 25	0 to 25	> 250	> 250
Number events	1873	173	1	$0.09^{+0.12}_{-0.09}$

for the tight selection the QCD prediction places an upper limit on the number of QCD events with $H_T > 500$ GeV. Table 5.19 shows the number of data events in each of control regions and the predicted number of events in the signal region D. The estimated QCD background for the loose (tight) selection is 0.18 ± 0.13 ($0.09^{+0.12}_{-0.09}$) events. As expected, the amount of QCD is much less than one event in the muon channel. Again these background estimates should be regarded as conservative since we do not subtract out the contamination from electroweak and $t\bar{t}$ events and in the case of the tight selection we do not require $H_T >$500 GeV. If the $t\bar{t}$ and electroweak backgrounds are subtracted from each of the control regions using the Monte Carlo prediction, the QCD background prediction in the muon channel for the tight selection drops to $0.04^{+0.05}_{-0.04}$.

In the electron channel we perform a similar analysis of relative isolation vs. $\not\!\!E_T$ to predict the number of QCD events at high $\not\!\!E_T$. The main differences with respect to the muon channel are the triggers used and the value of the relative

isolation requirements. In the single-electron triggers an isolation requirement was made after the first 8 pb^{-1} of data to keep the trigger rate at a low level as the luminosity of the LHC increased.[30] This isolation requirement biases any method using relative isolation. Thus, for the loose selection we take the QCD value predicted from the 8 pb^{-1} of data that did not have an isolation requirement and normalize it to the full 36 pb^{-1} to obtain a prediction for the full sample. In the tight selection it is possible to use the full 36 pb^{-1} of statistics to make a prediction using triggers that place requirements on the H_T in the event without any additional electron requirements. These are the same H_T triggers used for the QCD prediction in the electron channel for the S_{MET} vs. H_T method. However, these H_T triggers cannot be used for the loose selection since they are only fully efficient at $H_T > 300$ GeV, whereas the loose selection H_T requirement is at 120 GeV.

Figure 5.44(a) shows the relative isolation vs. $\not\!\!E_T$ distribution in the loose selection for the 8 pb^{-1} of data where the electron triggers do not have an isolation requirement. Table 5.20 defines the different control regions, A, B, C used to estimate the QCD contribution. Table 5.20 also specifies the signal region

[30]There are many different handles to lower the trigger rate in single electron trigger paths, including p_T, relative isolation and identification cuts. However, since the electron p_T requirement of the analysis is low (20 GeV), a trigger without a relative isolation cut requirement would require too high a p_T threshold on the electron at the trigger level.

Table 5.20: Data (electron channel), Loose Selection: QCD background determination in the space of RelIso vs. $\not\!\!E_T$. These numbers are for the 8 pb^{-1} of data with no isolation requirements on the single electron triggers. For the final prediction the number predicted in Region D is scaled from 8 pb^{-1} to 36 pb^{-1} to obtain $0.0^{+0.38}_{-0.0}$. Numbers from Ref. [80].

	Region A	Region B	Region C	Region D Predicted
RelIso range	0.2 to 0.5	< 0.07	0.2 to 0.5	< 0.07
$\not\!\!E_T$ range (GeV) tight selection	0 to 25	0 to 25	> 150	> 150
Number events	387	25	0	$0.0^{+0.08}_{-0.0}$

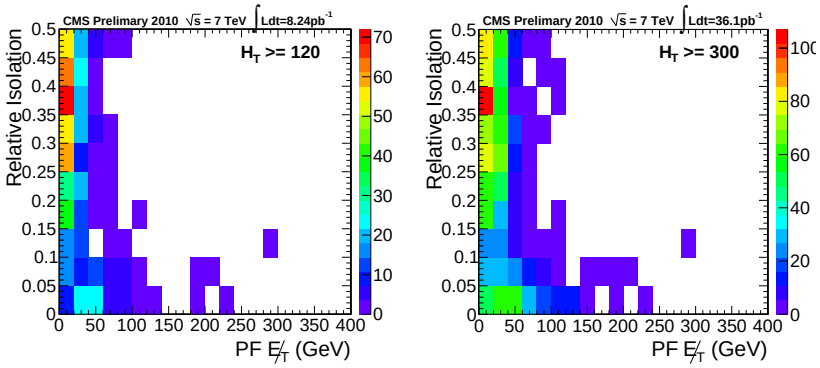

(a) 8 pb^{-1} and $H_T > 120$ GeV (b) 36 pb^{-1} and $H_T > 300$ GeV

Figure 5.44: Data in the electron channel: Relative isolation vs. $\not\!\!E_T$. (a) is used to make the QCD prediction in the loose selection, (b) is used to make the QCD prediction in the tight selection. Figures from Ref. [80].

for the estimate and the prediction in this signal region. The QCD background yield in the loose selection signal region is $0.0^{+0.38}_{-0.0}$.

Figure 5.44(b) shows the relative isolation vs. $\not\!\!E_T$ distribution in the data with an H_T requirement of 300 GeV for the H_T triggered sample. For the tight selection signal sample we make a prediction with H_T >300 GeV (where the H_T

Table 5.21: Data (electron channel), Tight Selection: QCD background determination in the space of RelIso vs. $\not\!\!E_T$. To calculate the uncertainty of the prediction we assume there is one event in Region C and assign a Poisson uncertainty to this one event, which we propagate to region D. The H_T requirement for the tight selection is loosened from 500 GeV to 300 GeV to gain more statistics in Regions A and B. With the loosened H_T requirement this prediction is more conservative. Numbers from Ref. [80].

	Region A	Region B	Region C	Region D Predicted
RelIso range	0.2 to 0.5	< 0.07	0.2 to 0.5	< 0.07
$\not\!\!E_T$ range (GeV) tight selection	0 to 25	0 to 25	> 250	> 250
Number events	625	79	0	$0.0^{+0.16}_{-0.0}$

triggers become fully efficient) and the result is taken as as an upper limit for the amount of QCD background with $H_T > 500$ GeV. Similarly to the muon channel, the H_T requirement is loosened to provide more statistics at low $\not\!\!E_T$ to measure the ratio of high-to-low relative isolation events. Table 5.21 defines the control regions A, B, C and the signal region D, and gives the yield in the data for each of the control regions and the prediction for the signal region. In the region of high relative isolation with high $\not\!\!E_T$, zero events are observed. We assign a Poisson uncertainty to zero events and then propagate this uncertainty to the prediction on the signal region using the ratio of high-to-low relative isolation obtained at low $\not\!\!E_T$. The QCD background yield in the tight selection signal region is $0.0^{+0.16}_{-0.0}$.

In conclusion, we estimate from data-driven methods, that the QCD background is small, much less than one event, in both the loose and tight signal regions and both the electron and muon channels.

5.5.8 QCD contamination to control regions

Although very few QCD background events are present in the signal regions, we must also investigate the control regions since there is no $\not\!\!E_T$ requirement for these samples. Without a $\not\!\!E_T$ requirement for the control samples, QCD events, which tend to lie at low $\not\!\!E_T$ when there is a lepton requirement, can contaminate the control samples. We could remove this QCD contamination in the control region by placing a modest $\not\!\!E_T$ requirement of 25 GeV. However, since the lepton p_T and $\not\!\!E_T$ variables are anti-correlated in $t\bar{t}$ and W+jets events, as shown in Fig. 5.23, a $\not\!\!E_T$ requirement in the control sample would remove high p_T lepton events, which are exactly the events used to predict the high $\not\!\!E_T$ tail.

In the muon channel the control sample requirement of $p_T(\mu)$ >150 (250) GeV for the loose (tight) selection is sufficient to remove QCD events with a muon from a $b, c \to \mu$ decay or a fake muon. Muons from $b, c \to \mu$ decays are usually at lower p_T and the muon reconstruction and identification requirements are sufficient to remove any high p_T fake muons. However, in the electron channel the p_T requirement does not remove the QCD contribution since the electron

reconstruction is more susceptible to fakes from QCD processes. In fact, in the electron channel there is also contamination from Z+jets events, since in some cases only one of the two electrons from the Z decay passes the electron reconstruction and identification criteria (for the muon channel the reconstruction and identification efficiency is higher and the Z+jets contamination is negligible).

To avoid the contamination of QCD and Z+jets in the electron control sample we use the muon control sample to predict both the rates for the electron and muon signal regions. We have evaluated a correction factor for the ratio $N(e)/N(\mu) = 0.70 \pm 0.15$ from the data. This ratio is obtained from fitting the data from $60 < \not\!\!E_T < 140$ GeV and is similar to that observed in Monte Carlo. Figure 5.45 shows the ratio of electron $\not\!\!E_T$ to muon $\not\!\!E_T$ in $t\bar{t}$ MC and in data. In $t\bar{t}$ Monte Carlo this ratio is very flat (we also find it to be very flat in W+jets Monte Carlo) and a fit gives the ratio $N(e)/N(\mu) = 0.82 \pm 0.01$. If both $t\bar{t}$ and W+jets Monte Carlo are considered, a fit to the ratio of electron $\not\!\!E_T$ to muon $\not\!\!E_T$ yields a ratio of $N(e)/N(\mu) = 0.84 \pm 0.01$. In the data this ratio does not stay flat at $\not\!\!E_T$ less than 50 GeV due to QCD and Z+jets contamination, which is significantly higher in the electron channel than the muon channel. This is why the fit range $60 < \not\!\!E_T < 140$ GeV is chosen. The error for the fit to the data is obtained from adding in quadrature the uncertainty from the fit and the variation of the fit mean when changing the fit region.

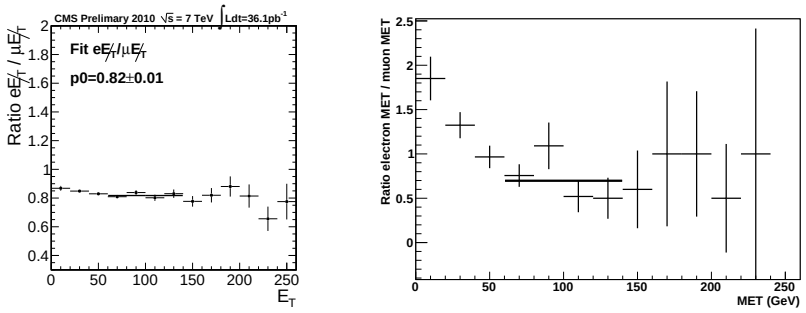

(a) $t\bar{t}$ MC. (b) Data, 36 pb^{-1}.

Figure 5.45: Distribution showing th ratio of $\not\!\!E_T$ in electron and muon channels. We fit this ratio in order to obtain a scale factor for using the muon p_T to predict the electron $\not\!\!E_T$. Figures from Ref. [80].

5.5.9 Single top and Z+jets background estimation

Since the single top and Z+jets backgrounds contribute very little to the signal regions and since we believe the Monte Carlo to be reasonably realiable for these samples (in contrast to QCD), we use the Monte Carlo to estimate their contribution to the signal sample.

The Z+jets contribution to the high $\not\!\!E_T$ tail is small for multiple reasons: first, the requirement of exactly one muon or electron in our selection criteria removes most of these events since the Z decays to either two leptons or zero leptons (ignoring fake leptons or leptons from QCD processes) and second, Z+jets tend to have a small amount of real $\not\!\!E_T$ since when the Z decays to a muon and an anti-muon or an electron and a positron since there are no high p_T neutrinos in

the event. One case where a Z+jets event could have a high p_T neutrino and only one reconstructed lepton is is if the Z boson decayed to a τ and an anti-τ and one of the τ's decayed hadronically and the other to a muon or electron. However, this case is still rare in our event sample.

The single top contribution is small because the cross section for these processes is much smaller, on the order of tens of pb, than the other relevant backgrounds ($t\bar{t}$ and W+jets), even though the kinematics are similar.[31]

In the loose selection the Monte Carlo predicts that the single top and Z+jets will contribute less than one event (0.4 ± 0.1 events in the muon channel and 0.4 ± 0.1 events in the electron channel) and only 2-3% of the total standard model background. For the tight selection the Monte Carlo predicts that the single top and Z+jets backgrounds will contribute significantly less than one event ($0.05^{+0.05}_{-0.04}$ events in the muon channel and 0.01 ± 0.003 in the electron channel) and still only 2-3% of the total standard model background.

5.5.10 Scale factors applied to predictions

In the case of the single lepton prediction and the dilepton feed-down and single $\tau \to \ell$ predictions we apply scale factors to the prediction to account for

[31]The kinematics are only roughly similar. The point here is that SUSY has small cross sections as well, but the kinematics tend to be very different than the backgrounds, especially for high mass SUSY models.

a specific set of effects. These scale factors take into account any differences between the predicted and true values obtained in Monte Carlo and are applied to the final data prediction.

For the single lepton background the $\not\!\!E_T$ prediction from the lepton p_T spectrum is effected by the W polarization, lepton p_T and the $\not\!\!E_T$ scale. In the case of the loose selection differences between the prediction and true values can also come from overlap between the dilepton/single τ predictions and the single lepton prediction and from contamination of the control sample by other standard model backgrounds (single top and Z+jets). For the tight selection the overlap of the predictions and other SM backgrounds have a negligible effect.

The scale factor, $S_{1\ell}$, for the single lepton prediction, is defined to be:

$$S_{1\ell} = \frac{\text{Number true 1 } W \to \ell \text{ events in signal region}}{\text{Number predicted 1 } W \to \ell \text{ events in signal region}}, \tag{5.9}$$

where for the loose selection the numerator is the number of 1 $W \to \ell$ events in $t\bar{t}$, W+jets Monte Carlo with $\not\!\!E_T > 150$ GeV and the denominator is the number of standard model Monte Carlo ($t\bar{t}$, W+jets, Z+jets, single top, QCD) events with $p_T(\mu) > 150$ GeV after smearing. For the tight selection the scale factor is defined to be the same except the thresholds on $\not\!\!E_T$ and muon p_T are 250 GeV and a $H_T > 500$ GeV cut is applied. Since we use the muon p_T spectrum for the electron $\not\!\!E_T$ prediction the denominator for the electron scale factor also includes an efficiency factor in going from muons to electrons.

For the loose selection the scale factors are 0.62 ± 0.02 (muons) and 0.70 ± 0.02 (electrons). For the tight selection the scale factors are close to unity, 0.88 ± 0.07 (muons) and 0.89 ± 0.08 (electrons). These scale factors are multiplied by the single lepton prediction in data to obtain the final result. The errors on the scale factors quoted here are statistical only. Systematic uncertainties are discussed in the Sec. 5.5.12.

For the dilepton and single τ predictions we apply scale factors to the separate predictions to take into account biases from effects such as the muon and jet response hypotheses, kinematic cuts, and the $\not\!\!E_T$ scale. In the loose selection these scale factors range from 0.86-0.94, with $\sim$10% uncertainty. For the tight selection, the scale factors are typically $\sim$0.5, with a large systematic uncertainty of $\sim$75%. The correction has little effect on the final result for both the loose or tight selection predictions, since for the loose selection the corrections are close to one and for the tight selection the background from these events is much less than one event.

Table 5.22 shows for the muon channel and tight selection exactly how the scale factors are calculated from the actual and predicted numbers in the Monte Carlo. Table 5.23 shows the same table but for the electron channel For the QCD background we do not apply any correction factors since we do not have enough Monte Carlo statistics to calculate known biases in the prediction.

Table 5.22: Muon channel: scale factors for single lepton, dilepton, and tau predictions. Numbers are for the tight selection and come from Monte Carlo. The errors on the actual and predicted numbers are statistical only. However, for the scale factor both statistical and systematic uncertainties are shown. See Sec. 5.5.12 for information on how the systematic uncertainties are determined. These numbers were calculated using the W+jets alpgen sample. The prediction for the single lepton component includes resolution smearing and the small overlap with the other predictions.

Background	Actual	Predicted	Scale Factor (Actual/Predicted)
$t\bar{t}$ & W+jets, 1μ	1.12 ± 0.05	1.27 ± 0.09	$0.88 \pm 0.07 \pm 0.39$
dilepton $t\bar{t}$	0.11 ± 0.02	0.23 ± 0.03	$0.48 \pm 0.11 \pm 0.52$
$\tau \to \mu$	0.09 ± 0.02	0.19 ± 0.02	$0.48 \pm 0.12 \pm 0.41$

Table 5.23: Electron channel: scale factors for single lepton, dilepton, and tau predictions. Numbers are for the tight selection and come from Monte Carlo. The errors on the actual and predicted numbers are statistical only. However, for the scale factor both statistical and systematic uncertainties are shown. See Sec. 5.5.12 for information on how the systematic uncertainties are determined. These numbers were calculated using the W+jets alpgen sample and the prediction is from the muon p_T spectrum. The prediction for the single lepton component includes resolution smearing and the small overlap with the other predictions.

Background	Actual	Predicted	Scale Factor (Actual/Predicted)
$t\bar{t}$ & W+jets, 1μ	0.95 ± 0.04	1.06 ± 0.07	$0.89 \pm 0.08 \pm 0.39$
dilepton $t\bar{t}$	0.10 ± 0.02	0.18 ± 0.02	$0.58 \pm 0.12 \pm 0.31$
$\tau \to \mu$	0.14 ± 0.02	0.26 ± 0.04	$0.55 \pm 0.11 \pm 0.40$

5.5.11 Results of background predictions

The predicted $\not\!\!E_T$ distribution for the single lepton background (using the lepton p_T spectrum) is shown along with the observed $\not\!\!E_T$ distribution in Figure 5.46 and Figure 5.47 for the loose and tight selection, respectively. Though the other additional background predictions are not shown in these plots the prediction for the single lepton background (the dominant background) is consistent with the $\not\!\!E_T$ in both the loose and tight selection and for both the muon and electron channel.

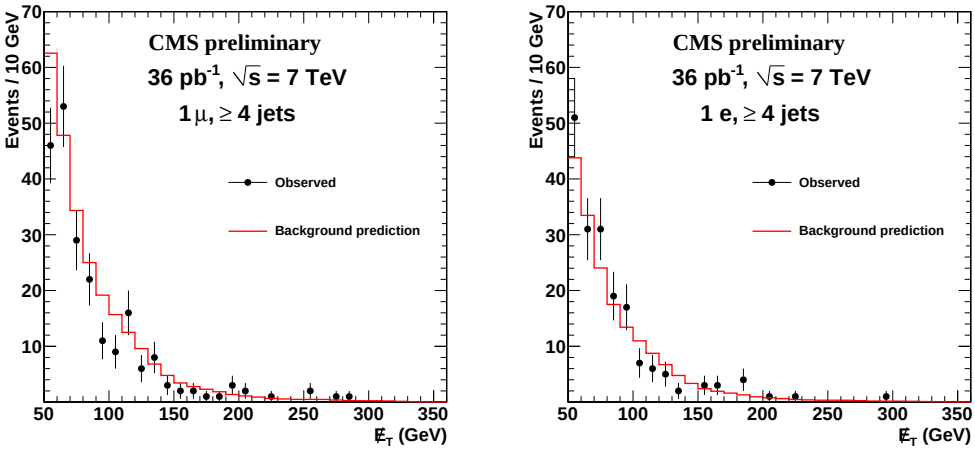

(a) muon channel: loose selection

(b) electron channel: loose selection

Figure 5.46: Measured vs. predicted $\not\!\!E_T$ distributions in muon and electron channels, with loose selections. The data are shown as points with error bars, while the prediction from the resolution-smeared lepton spectrum is shown as the red curve.

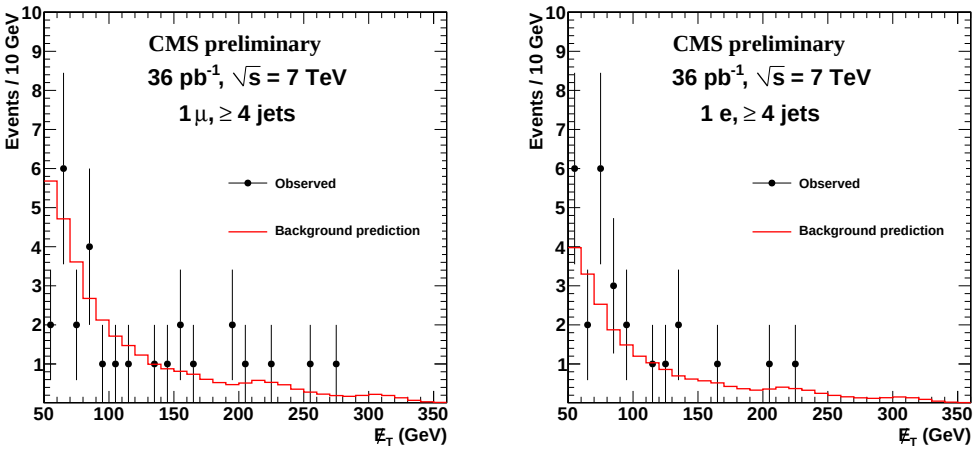

(a) muon channel: tight selection

(b) electron channel: tight selection

Figure 5.47: Measured vs. predicted $\not\!\!E_T$ distributions in muon and electron channels, with tight selections. The data are shown as points with error bars, while the prediction from the resolution-smeared lepton spectrum is shown as the red curve.

Table 5.24: Loose cuts applied to data: yield from data-driven background determination and yield in signal region. Pre-selection cuts are applied, and the signal region corresponds to $\not\!\!E_T > 150$ GeV.

Sample	$\ell = \mu$	$\ell = e$
Predicted SM 1 ℓ	$11.1 \pm 2.8 \pm 3.0$	$8.8 \pm 2.9 \pm 2.4$
Predicted SM dilepton	$1.0 \pm 0.6 \pm 0.1$	$0.8 \pm 0.5 \pm 0.03$
Predicted single τ	$2.1 \pm 0.6 \pm 0.2$	$2.2 \pm 0.5 \pm 0.3$
Predicted QCD background	0.18 ± 0.13	$0.0^{+0.38}_{-0.0}$
Predicted single top, Z+jets	0.4 ± 0.1	0.4 ± 0.1
Total predicted SM	$14.8 \pm 2.9 \pm 3.0$	$12.2 \pm 3.0 \pm 2.4$
Observed signal region	16	13

We combine the different background predictions to obtain a full prediction for the number of events at large $\not\!\!E_T$. Table 5.24 shows for the loose selection the number of background events predicted for the different backgrounds and the number of data events observed. The yield observed in data is consistent with the number predicted. For comparison, we note that the SUSY models LM0 and LM1 predict 64 and 8.7 events, respectively, in the loose selection.

Table 5.25 shows the different background predictions and observed data events in the tight selection. We observe two muon events with $\not\!\!E_T$ >250 GeV and no electron events above this threshold, both of which are consistent with our predictions. For comparison, the SUSY models LM0 and LM1 predict 11.2 and 4.2 events, respectively, in the tight selection. Event displays for the two muon events passing the tight selection are shown in Figure 5.48 and Figure 5.49.

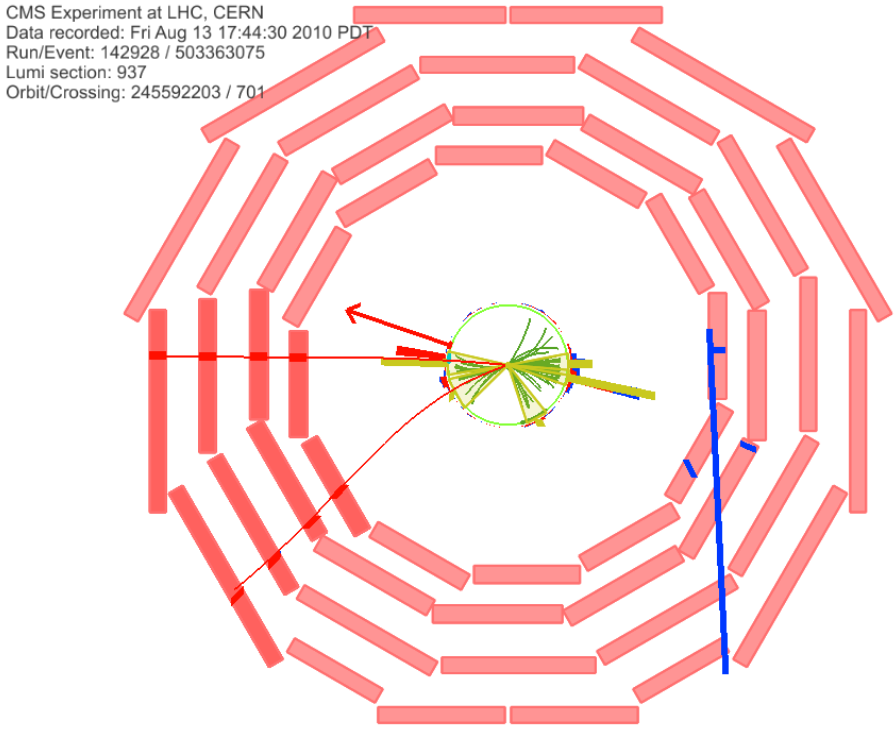

Figure 5.48: Display of muon event passing the tight selection.

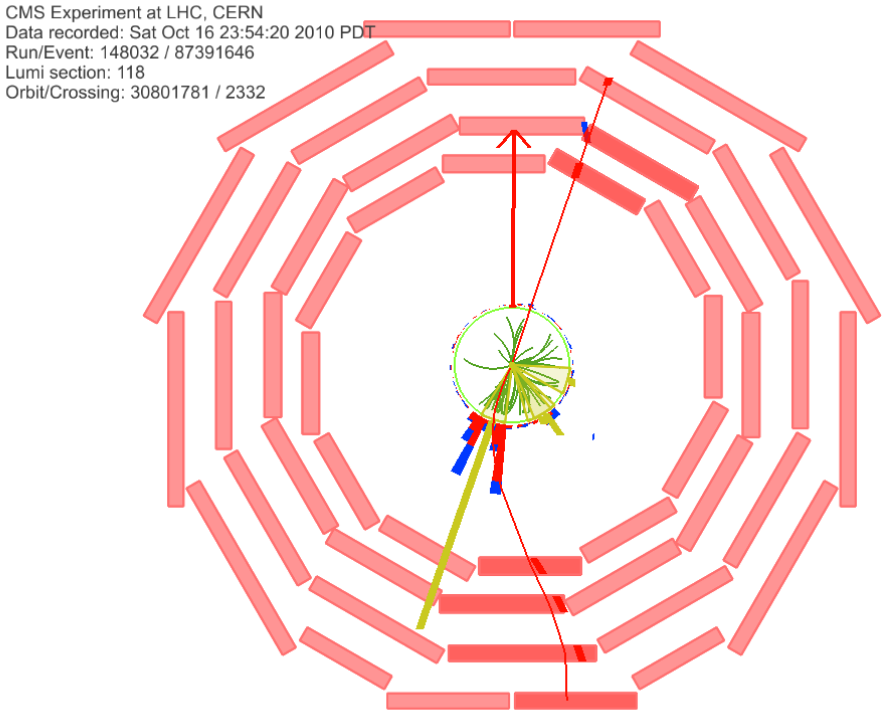

Figure 5.49: Display of muon event passing the tight selection.

Table 5.25: Tight cuts applied to data: yield from data-driven background determination and yield in signal region. Pre-selection cuts are applied, and the signal region corresponds to $\not\!\!E_T > 250$ GeV and $H_T > 500$ GeV.

Sample	$\ell = \mu$	$\ell = e$
Predicted SM 1 ℓ	$1.5 \pm 1.1 \pm 0.7$	$1.1 \pm 0.8 \pm 0.5$
Predicted SM dilepton	$0.0^{+0.3+0.23}_{-0.0-0.0}$	$0.0^{+0.4+0.14}_{-0.0-0.0}$
Predicted single τ	$0.16 \pm 0.10 \pm 0.20$	$0.27 \pm 0.20 \pm 0.20$
Predicted QCD background	$0.09^{+0.12}_{-0.09}$	$0.0^{+0.16}_{-0.0}$
Predicted single top, Z+jets	$0.05^{+0.05}_{-0.04}$	0.01 ± 0.003
Total predicted SM	$1.8 \pm 1.1 \pm 0.8$	$1.4 \pm 0.9 \pm 0.5$
Observed signal region	2	0

5.5.12 Systematics uncertainties

We test many different systematic effects that could impact the lepton spectrum method. Table 5.26 gives a summary of the different systematic studies made and the resulting error from each. The dominant systematic uncertainty for the lepton spectrum method is associated with the jet and $\not\!\!E_T$ energy scale. If the $\not\!\!E_T$ scale shifts relative to the lepton p_T scale, the observed number of events above a $\not\!\!E_T$ threshold will change while the prediction from the lepton p_T spectrum will stay the same. We apply a $\pm 5\%$ uncertainty to the jet energy scale and propagate this to the $\not\!\!E_T$ to obtain a systematic on the $\not\!\!E_T$ scale. This variation takes into account changes in the clustered energy in the event and its effect on the $\not\!\!E_T$. The 5% uncertainty on this scale propagates to a 22% uncertainty for the loose selection and a 37% uncertainty for the tight selection. We

Table 5.26: Systematic uncertainties for the lepton spectrum method. Each uncertainty is expressed as a change in the ratio of predicted to the true number of events (evaluated in Monte Carlo). The total uncertainty is the individual uncertainties summed in quadrature.

Source	$\Delta(N_{\text{predicted}}/N_{\text{true}})(\%)$ (Loose selection)	$\Delta(N_{\text{predicted}}/N_{\text{true}})(\%)$ (Tight selection)
$\not\!\!E_T$ and jet energy scale	22	37
W polarization in $t\bar{t}$	2	4
W polarization in W+jets	7	14
top p_T spectrum	5	7
$\sigma(t\bar{t})$ and $\sigma(W)$	12	16
lepton efficiency (μ) vs. p_T	4	4
lepton efficiency (e) vs. p_T	4	4
jet efficiency	< 2	< 2
Total (μ)	27	44
Total (e)	27	44

also looked at varying the unclustered energy in the event by $\pm 10\%$ and found this to have a negligible effect on the prediction.

Though the scale factor applied to the lepton spectrum method takes into account W polarization effects in $t\bar{t}$ and W+jets we have investigated how the uncertainties on the polarization will effect the method. For $t\bar{t}$, where the polarization is theoretically well known, polarization uncertainties have a negligible effect when propagated to the final background prediction. As a test, for muons from a top decay we applied a 5% variation to the helicity 0 polarization fraction and varied the helicity -1 component correspondingly, while leaving the helicity

+1 component at its 0 value (for muons from an anti-top decay the helicity -1 and +1 are switched). This 5% variation is roughly ten times larger than the theoretical errors on these polarization fractions and still only leads to a 2% (4%) effect in the loose (tight) selection. Figure 5.50 shows for $t\bar{t}$ Monte Carlo how the angular distribution of the lepton in the W frame is changed when applying this 5% variation.

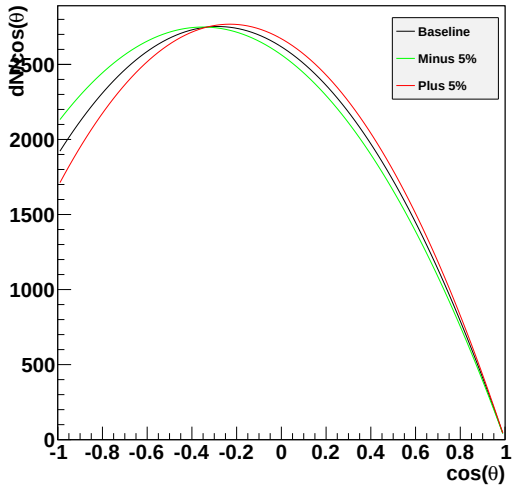

(a) $dN/d\cos\theta^*_\ell$ (SM) and $\pm 5\%$ polarization shifts

Figure 5.50: $dN/d\cos\theta^*_\ell$ (SM) and $\pm 5\%$ polarization shifts in $t\bar{t}$ Monte Carlo.

The W polarization in W+jets is more complicated and not as well known theoretically. To account for W polarization uncertainties we choose 3 conservative variations of the polarization fractions:

1. 100% variation to $f_{\lambda=-1} - f_{\lambda=+1}$ for both W^+ and W^- (this is equivalent to approximately a 30% variation of the individual polarization fractions).

2. 10% variation of $f_{\lambda=-1}$, $f_{\lambda=+1}$ for only W^+ or only W^-.

3. 100% variation to the longitudinal polarization fraction, $f_{\lambda=0}$, in both W^+ and W^-.

Each variation is applied in the same manner in three bins of $p_T(W)$: $50 < p_T < 100$ GeV, $100 < p_T < 300$ GeV, and $p_T > 300$ GeV. We do not vary the polarization of events with $p_T(W) < 50$ GeV since events with high p_T leptons or high $\not\!\!E_T$ result from boosted W's, with $p_T(W)$ >50 GeV. To find the total systematic error from W polarization in W+jets events we add the errors for each of the 3 variations listed above in quadrature. Of the three variations, 1) has the largest uncertainty on the final prediction, while 3) makes a very small impact. The reason the variation of 2) is smaller than 1) (10% vs. ∼30%) is that the W^+ polarization is somewhat constrained by the theory if you know the W^- polarization (and vice versa). If the variation of 1) and 2) were the same 2) would have a larger effect on the final background prediction because if the polarization is varied in just W^+ or W^- you will not get the cancelling effect that will occur if it is varied the same way in both. Variation 3) makes a small impact because f_0 is very small at high $p_T(W)$. Figure 5.51 shows exactly

the reweighting applied for variation 1) in the 100 GeV $< p_T(W) <$ 300 GeV bin for W^+ and W^-. The sum of the three variation in quadrature yields a 7% systematic uncertainty for the loose selection and a 14% uncertainty for the tight selection.

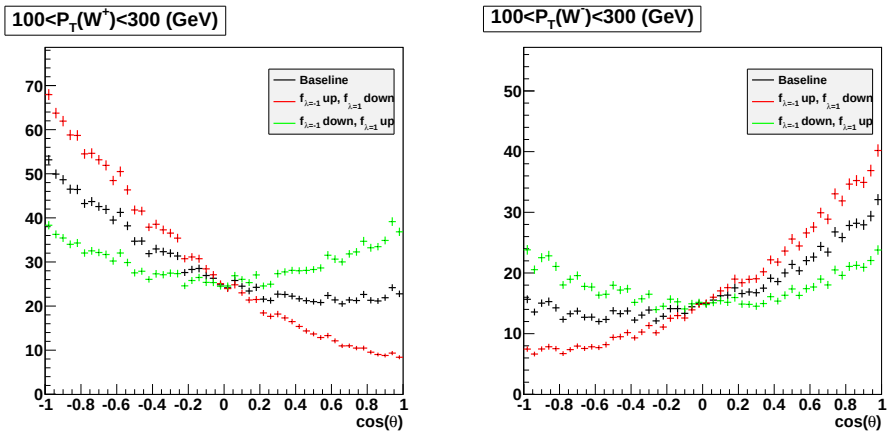

(a) W^+ (b) W^-

Figure 5.51: $dN/d\cos\theta^*_\ell$ (SM) and polarization shifts in W + jets from reweighting W polarization fractions, $100 < p_T(W) < 300$ GeV, Alpgen MC.

In $t\bar{t}$ events the top p_T spectrum can effect the boost of the W and thus effect the final $\not\!\!E_T$ and lepton p_T spectra if there is any differences between the polarization of the lepton and neutrino. To determine what variations of the top p_T spectrum to use we look at the $p_T(W)$ in data and Monte Carlo for single lepton events with at least 1 b-tag (the presence of a b-tag should provide a $t\bar{t}$

dominated sample with little W+jets contamination).[32] We then vary the top p_T spectrum to higher or lower values in the MC so that the $p_T(W)$ distribution no longer agrees between data and MC and take these as conservative systematic variations. Figure 5.52 shows the variations of the top p_T distribution used and also shows the $p_T(W)$ distribution for the data and MC and the effect of shifting the top p_T on the Monte Carlo distribution. Once we have the two shifted top p_T spectra we then test whether the correspondence between the lepton and neutrino fails to hold with these new spectra. The result of this procedure is a large shift in the both the lepton and neutrino spectra, but with the lepton spectrum continuing to track the neutrino spectrum. The variation of the top p_T leads to 5% (loose) and 7% (tight) uncertainties on the background yield.

The systematic uncertainty arising from the lepton reconstruction and identification efficiency p_T dependence is measured by varying the electron and muon efficiencies in the 20 to 40 GeV p_T range. We apply a change in the lepton efficiency starting with a 20% decrease of efficiency at 20 GeV and changing this linearly to a 0% decrease in efficiency at 40 GeV. This leads to a 4% uncertainty in the prediction in both the muon and electron channels. The systematic uncertainty due to mis-modeling jet reconstruction efficiencies is studied by removing

[32]The b-tagging algorithm we use identifies a jet as a b jet using the impact parameter significance (IP/σ_{IP}). If there are at least 3 tracks with an impact parameter significance above a certain value it signifies that most likely there was a displaced vertex from a b jet.

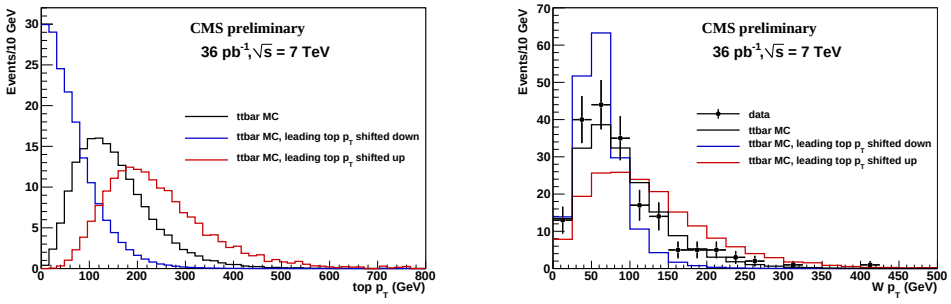

(a) top p_T, $t\bar{t}$ MC.

(b) $p_T(W)$, data and MC, with the nominal MC and the shifted top p_T in MC.

Figure 5.52: Determination of the variation of the MC top p_T that results in a MC $p_T(W)$ distribution that is no longer consistent with the data. Figures from Ref. [80].

a fraction of jets in the simulation and repeating the background prediction procedure. It is found to be small: less than 2% for a 5% change in the jet reconstruction efficiencies.

The systematic uncertainty from differences in the fraction of $t\bar{t}$ to W+jets in the final sample is investigated by varying the $t\bar{t}$ cross section by 30% and the W+jets cross section by 50%. The 30% variation of the $t\bar{t}$ cross section was taken from the uncertainty on early measurements on the top cross section measurement in the single lepton channel [81]. The 50% variation in W+jets events is chosen by studying Z+jets events in the $\geq$4 jet bin and observing that the difference between MC and data in this bin is at most 50%. The systematic

uncertainty from the $t\bar{t}$ and W+jets cross section variations is determined to be 12% in the loose selection and 16% in the tight selection.

The total systematic uncertainties on the single lepton background prediction are 27% for the loose selection and 44% for the tight selection. In the loose selection the statistical uncertainty is roughly the same size as the total systematic uncertainty. In the tight selection the statistical uncertainty dominates over the systematic uncertainty.

In addition to the studies listed in Table 5.26 we also investigated other effects that could bias the prediction. We looked at pileup effects in $t\bar{t}$ MC and found that they have less than a one percent effect on the final tight selection prediction. We also scanned all muon data events that fall into our loose signal region (preselection + $\not\!\!E_T > 150$ GeV) or loose control region (preselection + $\mu p_T > 150$ GeV) to look for any anomalies in muon reconstruction (that somehow passed our cuts) or any other weird effects. Tables 5.27 and 5.29 list several different muon quantities for data events that fall into the loose signal region and loose control region. We find no events where the muon tracker p_T is significantly different than the global fit p_T and no events where the error on the p_T is larger than 10%. Tables 5.28 and 5.30 show the charge and number of btags for data events in the signal and control regions for the loose selection. Looking at the charge of these events they are distributed pretty evenly between positive and

negative charge. When applying an anti-btag requirement (to try to focus on the W+jets background) the charge is still even between positive and negative (though the statistics is very low).

Table 5.27: Muon quantities in events in the loose signal region, $\not\!\!E_T > 150$ GeV. Events with * are those which are also in the tight signal region ($H_T > 500$ GeV and $\not\!\!E_T > 250$ GeV). $\Delta\phi$ is the angle between the muon and the $\not\!\!E_T$. Table from Ref. [80].

Run	Event	χ^2/n	$\lvert d_0\rvert$	$\lvert d_z\rvert$	$\frac{\Delta p_T}{p_T}$	$\frac{\sigma_{p_T}}{p_T}$	charge	Btags	$\Delta\phi$
140158	112262487	0.87	0.004	0.001	0	0.01	1	1	-1.07
*142928	503363075	0.99	0.002	0.002	0	0.02	-1	2	-0.21
142971	305903194	0.32	0.004	0.005	0	0.02	1	1	-0.45
143328	143543993	0.56	0.006	0.003	0	0.02	-1	1	-0.36
147115	144324244	0.67	0.002	0.0001	0	0.04	-1	1	0.49
*148032	87391646	0.28	0.002	0.006	0	0.04	1	1	0.30
148862	69953094	0.34	0.0008	0.002	0	0.02	1	1	-0.69
148862	969228778	0.28	0.003	0.002	0	0.01	1	0	-0.79
148864	334989072	0.30	0.007	0.003	0	0.03	-1	2	-0.85
149181	44293224	0.37	0.0006	0.02	0	0.03	-1	0	-0.65
149181	69628226	0.50	0.006	0.008	0	0.01	-1	1	0.36
149181	340730123	0.44	0.003	0.009	0	0.01	1	1	-0.33
149181	748592539	1.03	0.004	0.005	-0.005	0.056	1	1	0.19
149181	1671861307	0.41	0.005	0.01	0	0.02	1	1	-0.15
149182	210621275	0.54	0.001	0.008	0	0.03	1	0	-0.20
149291	506550588	0.89	0.009	0.006	0	0.02	-1	0	0.037

We also checked that the two data events passing the tight signal selection in the muon channel pass the Missing ECAL channel filters developed by the

Table 5.28: Distribution of charge and btag for data events in the muon channel with $\not\!\!E_T > 150$ GeV. Table from Ref. [80].

Tags:	μ^+	μ^-	Total:
0 Btags	2	2	4
1 Btag	7	3	10
2 Btags	0	2	2
Total:	9	7	16

Table 5.29: Muon quantities in events in the loose control region, $p_T(\mu) > 150$ GeV. Events with * are those which also are in the tight control region ($H_T > 500$ GeV and $p_T(\mu) > 250$ GeV). $\Delta\phi$ is the angle between the muon and the $\not\!\!E_T$. Table from Ref. [80].

Run	Event	χ^2/n	d_0	$\lvert d_z\rvert$	$\frac{\Delta p_T}{p_T}$	$\frac{\sigma_{p_T}}{p_T}$	charge	Btags	$\Delta\phi$
147043	65767167	0.78	0.002	0.0008	0	0.07	1	0	-0.028
147217	57270479	0.31	0.0004	5.0e-05	0	0.02	1	0	2.6
147754	391791578	0.48	0.002	0.001	0	0.03	-1	1	2.8
147926	33081405	0.65	0.001	0.002	0.005	0.04	1	0	0.35
148029	70481732	0.64	0.008	0.002	0	0.08	-1	1	-0.11
148029	252627992	0.28	0.001	0.006	0	0.04	-1	0	3.09
148032	87391646	0.28	0.002	0.006	0	0.04	1	1	0.30
148822	40702983	0.37	0.001	0.02	0	0.04	-1	0	-1.9
148822	236071642	0.92	0.003	0.0004	0	0.03	-1	1	-0.99
148822	364456282	0.42	0.003	0.01	0.04	0.07	-1	2	-1.4
148862	3843305	0.43	0.001	0.004	0	0.04	1	1	1.4
*148862	833474886	0.89	0.0004	0.0009	0.02	0.04	-1	0	0.17
148952	172873264	0.99	0.005	0.007	0	0.04	-1	0	-0.25
149181	552852359	0.58	0.001	0.008	0	0.04	-1	1	0.59
*149181	748592539	1.023	0.004	0.005	-0.005	0.06	1	1	0.19
149181	1189474551	0.22	0.005	0.007	-0.04	0.04	1	0	-2.7

Table 5.30: Distribution of charge and btag for data events in the muon channel with $p_T(\mu) > 150$ GeV. Table from Ref. [80].

Tags:	μ^+	μ^-	Total:
0 Btags	4	4	8
1 Btag	3	4	7
2 Btags	0	1	1
Total:	7	9	16

SUSY jets plus $\not\!\!E_T$ analysis effort [91].[33] These filters reject events where the signal from a single crystal or block of crystals in the ECAL is missing inside of a jet, oftentimes leading to large $\not\!\!E_T$. A single crystal or block of crystals can be missing because they are dead or deemed noisy. Though both our signal events pass this filter it turns out that for one of our signal events there is a missing 5x5 block of ECAL crystals within a jet, shown in Figure 5.53. This event passes the missing ECAL channel filter due to a small bug in the algorithm. This bug has since been fixed and this event would not pass the filter for 2011 data analysis.

The systematic uncertainties for the data-driven estimates of the dilepton and single τ backgrounds are determined separately using Monte Carlo simulation samples. For these backgrounds the systematic uncertainties are determined from investigating the deviation from unity of the dilepton and single τ scale factors described in Sec. 5.5.10. We attribute part of the deviation from unity

[33] In the electron channel there are no events passing the tight selection so we do not perform this check.

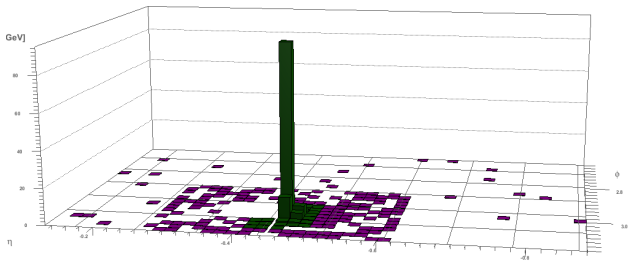

(a) lego view

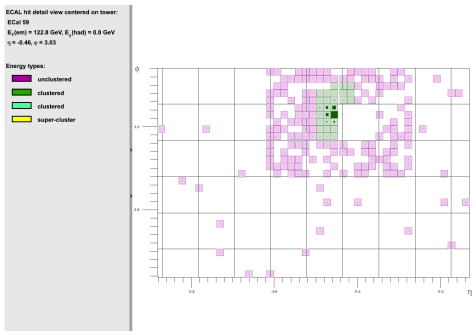

(b) 2-D view

Figure 5.53: Event display of the ECAL hits in an area surrounding one of the jets in Run 142928 Event 503363075 (one of our two signal events). Inside the jet there is a missing 5 x 5 ECAL crystal cluster that is either dead or masked out. It turns out that in this event the signal muon points very close to the jet axis (ϕ_μ =3.05, η_μ =0.52) but passes the relative isolation requirement. This happens because the crystals with the largest energy are within the inner veto cone of the muon isolation and the crystals outside the inner veto cone that would have the largest energy and make the muon fail the relative isolation requirement are either dead or masked out. Thus, this is a pathological event where dead or masked ECAL channels result in high $\not\!\!E_T$ and a lepton within a jet passing our relative isolation requirement. Algorithms were developed to remove events like this in the 2010 data. However, due to a bug in the algorithm this event actually passes this filter. This bug has been fixed and this event would be rejected in the 2011 data analysis.

to the $\not\!\!E_T$ scale and place a 100% uncertainty on this piece. On the remaining deviation from unity that we attribute to muon and jet response hypotheses, kinematic cuts, and other effects we also place a 100% uncertainty. These two errors are then added in quadrature.[34] Though this can be a large uncertainty in the tight selection (where the scale factors deviates from unity more than in the loose selection) it makes little difference on the final result as the dilepton and single τ contributions are small (much less than one event).

5.6 Signal efficiencies and uncertainties

In order to translate our predicted background numbers into upper limits on cross sections for new physics we must take into account acceptance and efficiency effects that could impact our signal samples. The acceptance and efficiencies are modeled well in the Monte Carlo, but differences between the data and Monte Carlo must be incorporated. In addition, systematic uncertainties on the acceptance and efficiency must be studied.

We measure the trigger and lepton reconstruction and identification efficiencies in data using a tag and probe method and compare to Monte Carlo. The

[34]For instance, in the tight selection $\tau \to e$ prediction the scale factor is 0.55 and when correcting for the $\not\!\!E_T$ scale it becomes 0.60. We put a 0.60-0.55=0.05 uncertainty due to the $\not\!\!E_T$ scale. The remaining deviation from unity, 1-0.60=0.40, is given a 100% error of 0.40. We then add the two errors in quadrature to obtain a total uncertainty of 0.40 on the scale factor, 0.55 ± 0.40(syst.). This uncertainty is propagated to the final result when the scale factor is applied to the prediction.

tag and probe method uses di-object resonances like $Z \to \ell\ell$ events to measure defined efficiencies. Specifically, the method looks at data events that have a di-lepton resonance at the Z mass, where one lepton passes a tight selection (tag) and the other lepton passes a loose selection (probe). The efficiency is then calculated by observing what fraction of the time the probe passes the particular cut(s) we are interested in. Efficiencies are usually dependent on p_T and η of the lepton and thus usually plotted as a function of these variables. However, in this study we have calculated overall efficiency factors for muons and electrons in the data. We compare this to the efficiency factors from the Monte Carlo and calculate scale factors from MC to data. The scale factors are:

$$\begin{aligned} \epsilon_{\text{data}}/\epsilon_{\text{MC}}(\mu) &= 96.2 \pm 0.5\% \\ \epsilon_{\text{data}}/\epsilon_{\text{MC}}(\text{e}) &= 95.0 \pm 0.7\% \end{aligned}$$

where the uncertainties on the scale factor are statistical only. These scale factors are applied to the MC signal before comparing the signal yield to the excluded yield calculated from the data.

To obtain the systematic uncertainties on the signal efficiency we model different effects in the simulation. The uncertainties come from the lepton and trigger and ID efficiences ($\pm 5\%$), the luminosity ($\pm 4\%$), the jet and $\not\!\!E_T$ energy scale ($\pm 17\%$ in the lepton spectrum method), and the possible variations of the

parton density functions (negligible). The total systematic uncertainty on the efficiency and acceptance is 20%.

5.7 Search results in terms of SUSY models

Since we see no significant excesses in either of our background predictions that could signify a signal, we set limits in the CMSSM framework plane of $m_{1/2}$ and m_0 for different values of $tan\beta$ and with $A_0 = 0$ and sign(μ)>0.[35] Next-to-leading order cross sections, determined from Prospino [92], are used for the signal points.

An issue that must addressed when obtaining limits is signal contamination to the control regions for different signal points. For the most accurate limit the signal contamination must be subtracted off from the control regions before obtaining the limit. Looking at our two background methods, S_{MET} vs. H_T has large signal contamination in the CMSSM while the lepton spectrum method has almost no signal contamination in the CMSSM (on average 0.05 events per signal point).[36] Because of the large signal contamination in the CMSSM for the S_{MET} vs. H_T method the reach of the limit is reduced by quite a bit with respect to the lepton spectrum method. For this reason we use the lepton spectrum method to

[35] The parameters of the CMSSM are described in detail in Sec. 2.3.

[36] The reason the signal contamination is so little for the lepton spectrum method is because most models in the CMSSM have soft leptons, regardless of $m_{1/2}$, m_0, or $tan\beta$.

obtain limits. However, since the range of SUSY models is large and the CMSSM is a very specific set of models both methods provide valuable information and a cross-check of each other. Since the signal contamination is so small for the lepton spectrum method we consider it negligible when calculating limits.

To interpret the results we combine yields from the electron and muon channels. For the tight selection the total combined number of observed events is 2 and the background prediction is 3.2 ± 2.3. For the loose selection the total combined number of observed events is 29 and the background prediction is 27.0 ± 7.9.

From these results we calculate upper limits on the number of signal events based on Neyman's construction [93] for confidence intervals with the ordering principle specified by Feldman-Cousins [94]. The Feldman-Cousins ordering principle fixes some inherent problems with the classical intervals, which can for instance give you unphysical or meaningless results if the number of observed events is signficantly less than expected from the backgrounds. The Feldman-Cousins ordering principle is based on the likelihood ratio

$$\lambda = \frac{f(x;\theta)}{f(x;\hat{\theta})}, \tag{5.10}$$

where x is the outcome of the experiment, θ is the unknown parameter (in our case θ would be the number of SUSY signal events), and $\hat{\theta}$ is the value of this unknown parameter which maximizes $f(x;\hat{\theta})$ [7]. This ordering principle is

motivated by the Neyman-Pearson lemma and the specification of the ordering is given in Ref. [94]. To take into account nuisance parameters this likelihood ratio is generalized to a profile likelihood ratio. The nuisance parameters in this analysis are the systematic uncertainties on the background and signal yields, and the expected number of background events. The input to the total likelihood function are the individual likelihood functions for the background predictions (single lepton prediction, dilepton prediction, tau prediction, QCD prediction, and single top/Z+jets prediction), the scale factors[37], and the signal prediction for a particular SUSY point. The likelihood functions for the signal and raw background predictions are Poisson-distributed probabilities and the likelihood functions for the scale factors are Gaussian-distributed probabilities.

Using the prescription described in the previous paragraph we calculate the 95% C.L. upper limit to be 3.8 (20.4) signal events for the tight (loose) selection. This means that any SUSY model with more predicted signal events than the upper limit will be excluded at 95% C.L. These upper limit numbers are then used to make exclusion curves in CMSSM parameter space. Figures 5.55, 5.57, and 5.59 show the exclusion curves for the lepton spectrum method tight selection with $\tan\beta = 3, 10, 50$, respectively. Figures 5.54, 5.56, and 5.58 show the exclu-

[37]These include the scale factors from MC described in Sec.5.5.10 and the correction factor from data described in Sec. 5.5.8 for using the muon p_T spectrum for the electron $\not\!\!E_T$ prediction.

sion curves for the lepton spectrum method loose selection with $\tan\beta = 3, 10, 50$, respectively.

Each plot shows the observed limit, the expected limit, and the expected $\pm 1\sigma$ limits. The expected limit is calculated using the data-driven background prediction and the observed limit is calculated using the observed background.[38] In the case of the loose selection because the predicted number of events is close to the observed number of events the expected limit curves and the observed limit curves are very similar. For the tight selection the observed limit curves are above the expected limit curves because we predict more events than we see. The loose selection has smaller $\pm 1\sigma$ bands, which means it can exclude the SUSY points at low $m_{1/2}$ and low m_0 better. However, the tight selection excludes a larger region for each of the $tan\beta$ points.

The total number of signal events passing the event selection and thus the exclusion curves are a function of the signal efficiency and the cross section. The signal efficiency is defined for each model as the number of events passing the reconstructed event selection, divided by the total number of SUSY events generated in the simulation, regardless of the decay chain. The efficiency decreases with $m_{1/2}$ but is relatively uniform as a function of m_0. In the tight selection, the efficiency in the combined e and μ channels is roughly 2% at $m_0 = 250$ GeV.

[38] Though this seems like a trivial point, one could in fact define the expected limit in different ways, such as using the prediction from MC instead of the prediction from data.

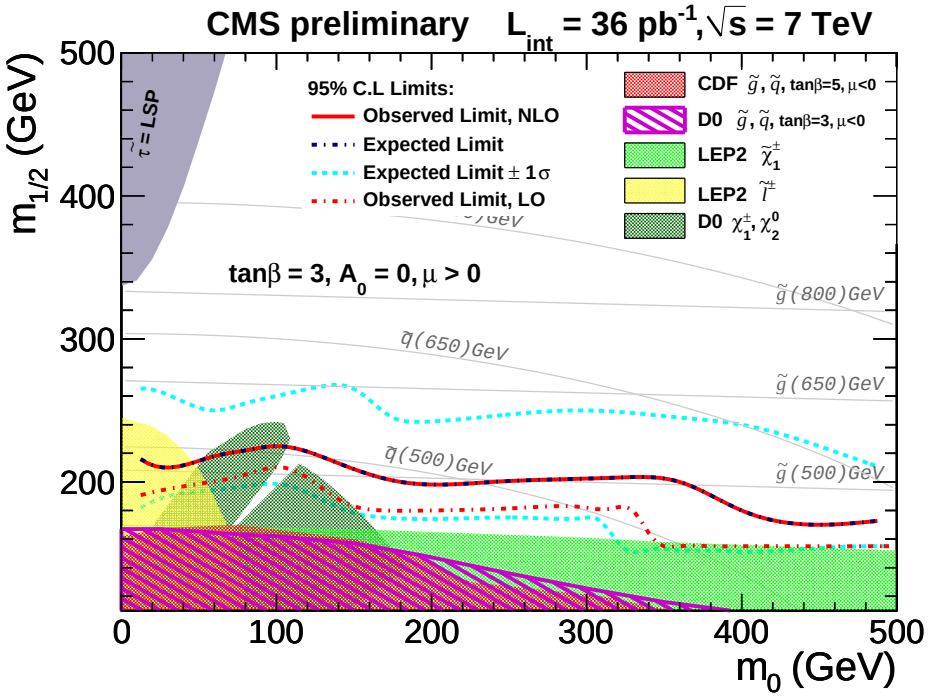

Figure 5.54: Exclusion region for $\tan\beta = 3$, loose selection, lepton spectrum method.

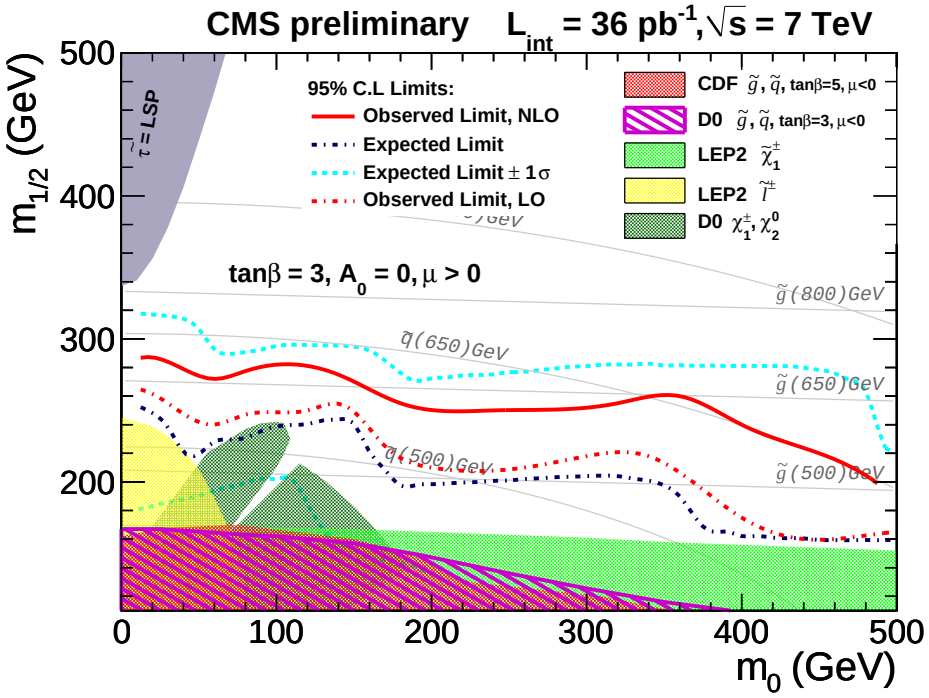

Figure 5.55: Exclusion region for $\tan\beta = 3$, tight selection, lepton spectrum method.

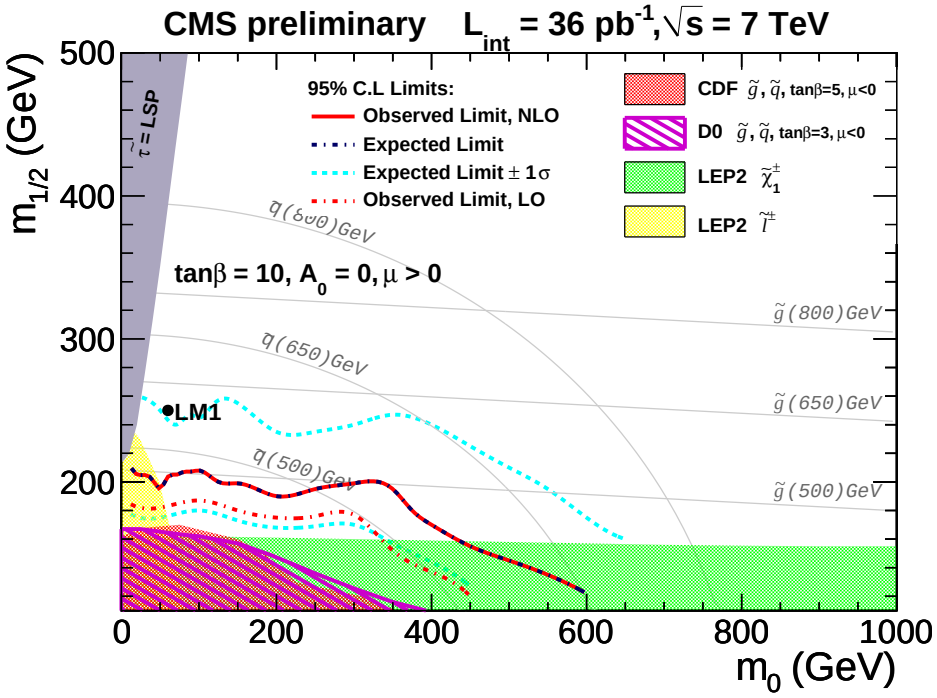

Figure 5.56: Exclusion region for $\tan\beta = 10$, loose selection, lepton spectrum method.

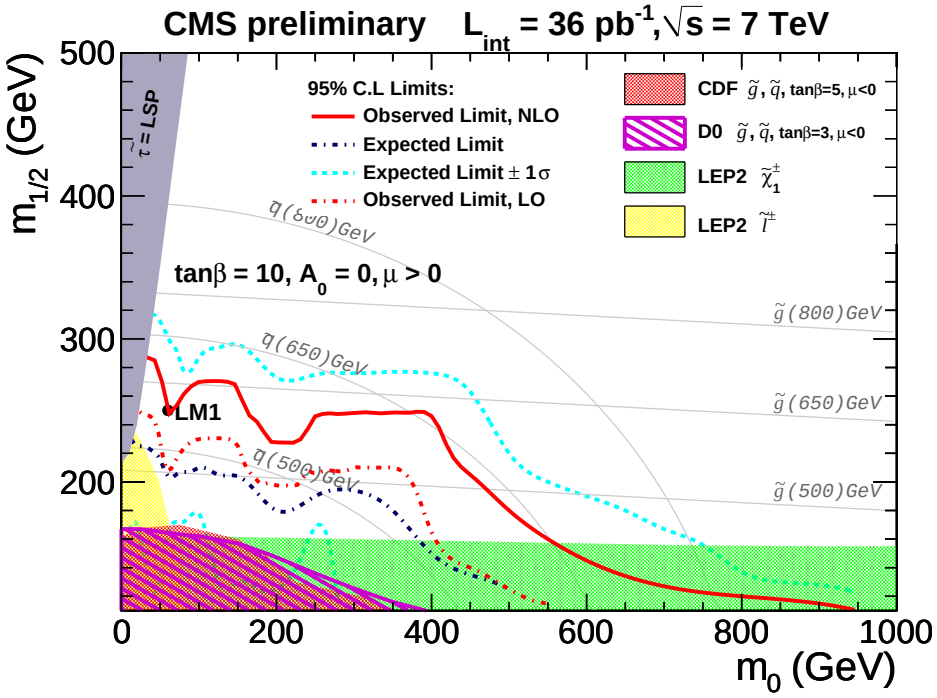

Figure 5.57: Exclusion region for $\tan\beta = 10$, tight selection, lepton spectrum method.

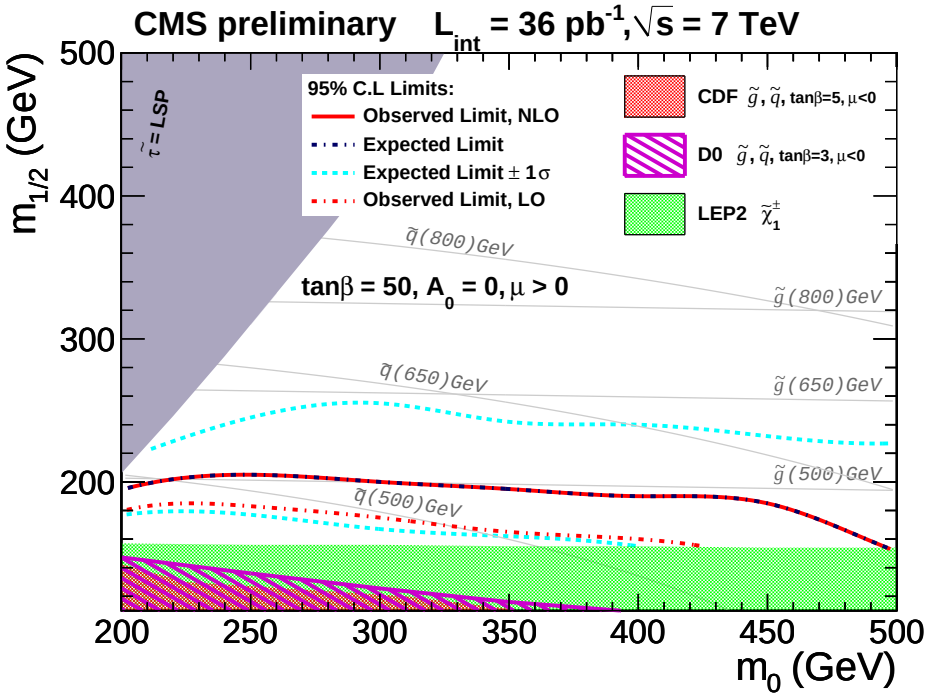

Figure 5.58: Exclusion region for $\tan\beta = 50$, loose selection, lepton spectrum method.

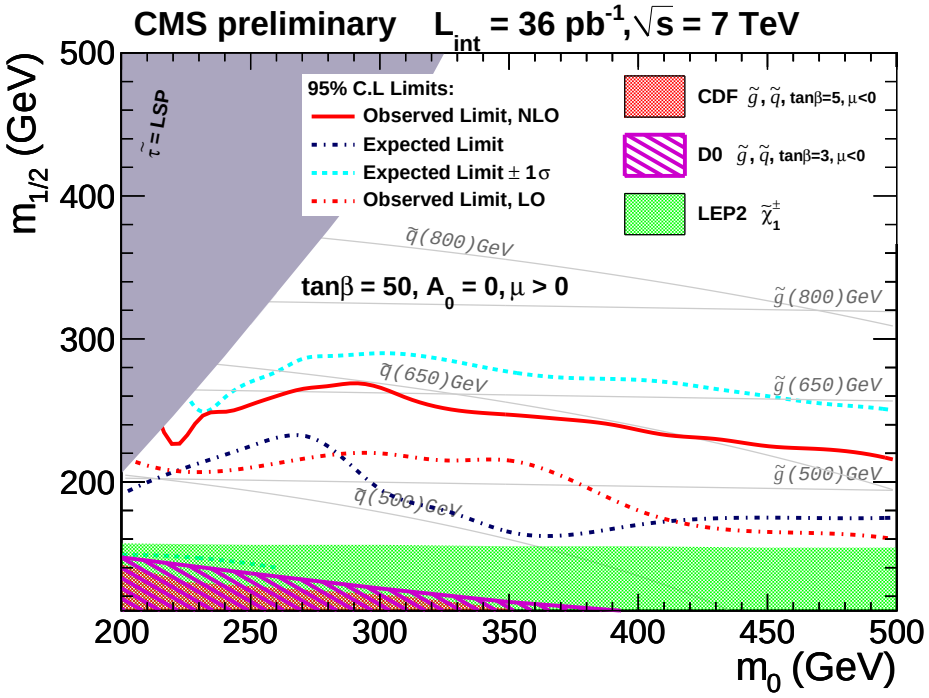

Figure 5.59: Exclusion region for $\tan\beta = 50$, tight selection, lepton spectrum method.

For the benchmark model LM0 (LM1), the efficiency is 3.2% (3.6%) in the loose selection and 0.6% (1.7%) in the tight selection.[39] A major reason that the signal efficiency is on the order of a few percent is that the efficiency for a signal model to have exactly one reconstructed lepton is somewhere between 5-15% (for LM1 it is 13%). The additional jet requirements and cuts on H_T and $\not\!\!E_T$ reduce this efficiency further to the final few percent number. The total signal cross section decreases as a function of $m_{1/2}$ and m_0 roughly following the contours of the squark mass shown in the exclusions plots.

For the $tan\beta = 10$ exclusion plots the small dips between $m_0 = 50 - 200$ GeV arise from corresponding dips in the efficiency curves; the falloff in the exclusion limits around $m_0 = 350 - 400$ GeV is due to the decrease in cross section. For $tan\beta = 3, 50$ the limit curves look slightly more flat vs. m_0. This is partly due to the fact that the x-axis is zoomed in to 0–500 GeV for these points and partly because the efficiency does not fluctuate as drastically. For $tan\beta = 10$ the tight selection excludes gluino masses below approximately 600 GeV for m_0 below about 400 GeV (in the context of the CMSSM framework).

[39] The efficiency is slightly higher in the muon channel than the electron channel as expected. For the loose selection the LM0 (LM1) muon efficiency is 1.7% (1.9%) and the electron efficiency is 1.5% (1.7%). For the tight selection the LM0 (LM1) muon efficiency is 0.3% (0.9%) and the electron efficiency is 0.3% (0.8%).

Chapter 6

Conclusion

This paper describes a SUSY search with a single isolated lepton, jets, and $\not\!\!E_T$ at CMS using 36 pb^{-1} of data. Though the requirement of an isolated lepton lowers the signal efficiency, it greatly reduces the QCD background, making it a sub-dominant background compared to electroweak and top processes. This is a nice feature because of the large uncertainties in QCD background events. In addition, anomalous events generally have a smaller chance of ending up in the signal sample (high $\not\!\!E_T$) with a requirement of a lepton. The lepton channel is also important because an isolated lepton signifies the electroweak decay of a heavy object. The jet requirements are motivated by the fact that many SUSY processes have large decay chains that can produce many jets. Lastly, the $\not\!\!E_T$ requirement is motivated by R-parity conserving SUSY models, where the two LSPs tend to give large $\not\!\!E_T$. This search signature is one of many different signatures at CMS and complements the other searches well.

The largest Standard Model backgrounds to this search are from $t\bar{t}$ and W+jets events with a single muon or electron. Smaller backgrounds come from dilepton $t\bar{t}$ events and $t\bar{t}$ and W+jets events with a tau decaying into a muon or electron. Other even smaller backgrounds that are on the order of a couple percent are QCD, single top, and Z +jets events.

To make background predictions data-driven techniques are used with minimal reliance on Monte Carlo simulation. The motivation for this is to be robust as possible in the event of a discovery. For this search two different data-driven methods are used for the background predictions. Each method focuses on slightly different event properties and they provide a cross-check of one another. The first, called S_{MET} vs H_T looks at the jets and $\not\!\!E_T$ in a signal region to see if they are consistent with predictions from the Standard Model. This method produces an inclusive prediction for all electroweak and top backgrounds while making a separate prediction for the small QCD background. The second method, called the lepton spectrum method, focuses on predicting the tail of the $\not\!\!E_T$ distribution in single lepton $t\bar{t}$ and W+jets events using the lepton p_T spectrum. In this method the other backgrounds such as dilepton $t\bar{t}$ events, $t\bar{t}$ and W+jets tau decay events, and QCD events are predicted by supplemental methods. For each method two different selections are chosen, called loose and tight. The loose selections are oriented towards having a larger number of events

to justify the background predictions. The tight selections are oriented towards having only a handful of background events left and they provide sensitivity to higher mass SUSY models compared with the loose selections.

Both methods make predictions in the the signal regions that are consistent with the Standard Model. For the S_{MET} vs H_T method the prediction in the combined muon and electron channel for the tight selection (H_T >650 GeV and S_{MET} >5.5) is 3.2 ± 1.3, compared to 7 observed data events. For the lepton spectrum method the prediction in the combined muon and electron channel for the tight selection ($\not\!\!E_T$ >250 GeV and H_T >500 GeV) is 3.2 ± 2.3, compared to 2 observed events. In addition to event yields being consistent with the Standard Model, the $\not\!\!E_T$ distribution is modeled well by the background predictions.

In the absence of a signal we proceed to set limits in the CMSSM parameter space. Specifically we plot exclusion limits in the $m_{1/2}$, m_0 plane for $\tan\beta = 3, 10, 50$ and $A_0 = 0$ and sign(μ)=0. The limits exceed searches at previous experiments at the Tevatron and LEP and are comparable to other SUSY searches at the LHC. For $\tan\beta = 10$ the tight selection excludes gluino masses below approximately 600 GeV for m_0 below about 400 GeV (in the context of the CMSSM framework).

Bibliography

[1] CMS Collaboration, "Search for new physics in proton-proton collisions at 7 TeV in events with a single lepton, jets, and missing transverse momentum", arXiv:1107.1870.

[2] S. L. Glashow, "Partial Symmetries of Weak Interactions", *Nucl. Phys.* **22** (1961) 579–588. doi:10.1016/0029-5582(61)90469-2.

[3] S. Weinberg, "A Model of Leptons", *Phys. Rev. Lett.* **19** (Nov, 1967) 1264–1266. doi:10.1103/PhysRevLett.19.1264.

[4] Salam, A., "Proc. 8th Nobel Symposium Stockholm 1968, edited by N. Svartholm (Almqvist and Wiksells, Stockholm 1968)", 367–377.

[5] Ellis, Stirling, and Webber, "QCD and Collider Physics". Cambridge, 1996.

[6] http://en.wikipedia.org/wiki/Standard_Model.

[7] K. Nakamura and P. D. Group, "Review of Particle Physics", *Journal of Physics G: Nuclear and Particle Physics* **37** (2010), no. 7A, 075021.

[8] F. Englert and R. Brout, "Broken Symmetry and the Mass of Gauge Vector Mesons", *Phys. Rev. Lett.* **13** (Aug, 1964) 321–323. doi:10.1103/PhysRevLett.13.321.

[9] P. W. Higgs, "Broken Symmetries and the Masses of Gauge Bosons", *Phys. Rev. Lett.* **13** (Oct, 1964) 508–509. doi:10.1103/PhysRevLett.13.508.

[10] G. S. Guralnik, C. R. Hagen, and T. W. B. Kibble, "Global Conservation Laws and Massless Particles", *Phys. Rev. Lett.* **13** (Nov, 1964) 585–587. doi:10.1103/PhysRevLett.13.585.

[11] J. L. Feng, "Dark Matter Candidates from Particle Physics and Methods of Detection", *Ann. Rev. Astron. Astrophys.* **48** (2010) 495, arXiv:1003.0904.

[12] F. Zwicky, "Spectral displacement of extra galactic nebulae", *Helv. Phys. Acta* **6** (1933) 110–127.

[13] V. C. Rubin and J. Ford, W. Kent, "Rotation of the Andromeda Nebula from a Spectroscopic Survey of Emission Regions", *Astrophys. J.* **159** (1970) 379–403. doi:10.1086/150317.

[14] V. C. Rubin, N. Thonnard, and J. Ford, W. K., "Rotational properties of 21 SC galaxies with a large range of luminosities and radii, from NGC 4605 /R = 4kpc/ to UGC 2885 /R = 122 kpc/", *Astrophys. J.* **238** (1980) 471. doi:10.1086/158003.

[15] Bosma, A., "The distribution and kinematics of neutral hydrogen in spiral galaxies of various morphological types", *PhD thesis* (1978).

[16] http://www.nasa.gov/vision/universe/starsgalaxies/dark_matter_proven.html.

[17] J. P. Ostriker and P. J. Steinhardt, "New Light on Dark Matter", *Science* **300** (2003) 1909–1913, arXiv:astro-ph/0306402. doi:10.1126/science.1085976.

[18] WMAP Collaboration, "Seven-Year Wilkinson Microwave Anisotropy Probe (WMAP) Observations: Cosmological Interpretation", *Astrophys. J. Suppl.* **192** (2011) 18, arXiv:1001.4538. doi:10.1088/0067-0049/192/2/18.

[19] S. P. Martin, "A Supersymmetry Primer", arXiv:hep-ph/9709356.

[20] J. Wess and B. Zumino, "Supergauge transformations in four dimensions", *Nuclear Physics B* **70** (1974), no. 1, 39 – 50. doi:10.1016/0550-3213(74)90355-1.

[21] H. P. Nilles, "Supersymmetry, supergravity and particle physics", *Physics Reports* **110** (1984), no. 1-2, 1 – 162. doi:10.1016/0370-1573(84)90008-5.

[22] H. E. Haber and G. L. Kane, "The search for supersymmetry: Probing physics beyond the standard model", *Physics Reports* **117** (1985), no. 2-4, 75 – 263. doi:10.1016/0370-1573(85)90051-1.

[23] R. Barbieri, S. Ferrara, and C. Savoy, "Gauge models with spontaneously broken local supersymmetry", *Physics Letters B* **119** (1982), no. 4-6, 343 – 347. doi:10.1016/0370-2693(82)90685-2.

[24] S. Dawson, E. Eichten, and C. Quigg, "Search for supersymmetric particles in hadron-hadron collisions", *Phys. Rev. D* **31** (Apr, 1985) 1581–1637. doi:10.1103/PhysRevD.31.1581.

[25] D. Alves et al., "Simplified Models for LHC New Physics Searches", arXiv:1105.2838.

[26] http://www.lhcnewphysics.org/.

[27] G. L. Kane, C. F. Kolda, L. Roszkowski et al., "Study of constrained minimal supersymmetry", *Phys. Rev.* **D49** (1994) 6173–6210, arXiv:hep-ph/9312272. doi:10.1103/PhysRevD.49.6173.

[28] https://twiki.cern.ch/twiki/bin/view/CMS/SUSYMassSpectra.

[29] http://atlas.ch/photos/lhc.html.

[30] CMS Collaboration, "CMS Physics Technical Design Report Volume I: Detector Performance and Software". Technical Design Report CMS. CERN, Geneva, 2006.

[31] http://en.wikipedia.org/wiki/Compact_Muon_Solenoid.

[32] http://cms.web.cern.ch/cms/Detector/FullDetector/index.html.

[33] S. Boreham, M. Brice, P. Ginter et al., "Photos from the CMS Photo Book". CMS Collection, Aug, 2008.

[34] http://abbaneo.web.cern.ch/abbaneo/cms/layout/whole.html.

[35] http://cms.web.cern.ch/cms/Media/Publications/CMStimes/2006/11_06/index.html.

[36] CMS Collaboration, "The Tracker Project Technical Design Report", *CERN/LHCC* **98-006** (1998).

[37] CMS Collaboration, "Addendum to the Tracker Project Technical Design Report", *CERN/LHCC* **2000-016** (2000).

[38] CMS Collaboration, "The Electromagnetic Calorimeter Technical Design Report", *CERN/LHCC* **97-033** (1997).

[39] CMS Collaboration, "Addendum to the Electromagnetic Calorimeter Technical Design Report", *CERN/LHCC* **2002-027** (2002).

[40] "Hadronic Calorimeter (HCAL) Calibration with Cosmics and Wire Source has started". CMS Collection, Oct, 2005.

[41] S. Abdullin et. al., "Design, performance, and calibration of CMS forward calorimeter wedges", *Eur. Phys. J. C.* **53** (2008) 139–166. doi:10.1140/epjc/s10052-007-0459-4.

[42] "Wedge Module of the Forward Hadron Calorimeter (HF)". CMS Collection, Apr, 2003.

[43] CMS Collaboration, "The Hadron Calorimeter Technical Design Report", *CERN/LHCC* **97-031** (1997).

[44] CMS Collaboration, "The Muon Project Technical Design Report", *CERN/LHCC* **97-032** (1997).

[45] CMS Collaboration, "Performance of muon identification in pp collisions at $\sqrt{s} = 7$ TeV", *CMS Physics Analysis Summary* **MUO-10-002** (2010).

[46] CMS Collaboration, "Photon reconstruction and identification at $\sqrt{s} = 7$ TeV", *CMS Physics Analysis Summary* **EGM-10-005** (2010).

[47] CMS Collaboration, "Isolated Photon Reconstruction and Identification at $\sqrt{s} = 7$ TeV", *CMS Physics Analysis Summary* **EGM-10-006** (2010).

[48] W. Adam, R. Frhwirth, A. Strandlie et al., "Reconstruction of electrons with the Gaussian-sum filter in the CMS tracker at the LHC", *Journal of Physics G: Nuclear and Particle Physics* **31** (2005), no. 9, N9.

[49] CMS Collaboration, "Commissioning of the Particle-flow Event Reconstruction with the first LHC collisions recorded in the CMS detector", *CMS Physics Analysis Summary* **PFT-10-001** (2010).

[50] CMS Collaboration, "Electron reconstruction and identification at $\sqrt{s} =$ 7 TeV", *CMS Physics Analysis Summary* **EGM-10-004** (2010).

[51] M. Cacciari, G. P. Salam, and G. Soyez, "The anti-kt jet clustering algorithm", *JHEP* **0804:063** (2008). doi:10.1088/1126-6708/2008/04/063.

[52] CMS Collaboration, "Commissioning of TrackJets in pp Collisions at $\sqrt{s} = 7$ TeV", *CMS Physics Analysis Summary* **JME-10-006** (2010).

[53] CMS Collaboration, "Particle-Flow Event Reconstruction in CMS and Performance for Jets, Taus, and Missing E_T", *CMS Physics Analysis Summary* **PFT-09-001** (2009).

[54] CMS Collaboration, "Commissioning of the Particle-Flow Reconstruction in Minimum-Bias and Jet Events from pp Collisions at 7 TeV", *CMS Physics Analysis Summary* **PFT-10-002** (2010).

[55] CMS Collaboration, "Calorimeter Jet Quality Criteria for the First CMS Collision Data", *CMS Physics Analysis Summary* **JME-09-003** (2009).

[56] CMS Collaboration, "Jet performance in pp Collisions at *sqrts* = 7 TeV", *CMS Physics Analysis Summary* **JME-10-003** (2010).

[57] CMS Collaboration, "Determination of Jet Energy Calibration and Transverse Momentum Resolution in CMS", `arXiv:1107.4277v1`.

[58] CMS Collaboration, "Missing transverse energy performance of the CMS detector", `arXiv:1106.5048v1`.

[59] CMS Collaboration, "Identification and Filtering of Uncharacteristic Noise in the CMS Hadron Calorimeter", *CMS Physics Analysis Summary* **CFT-09-019** (2009).

[60] CMS Collaboration, "HCAL performance from first collisions data", *CMS Detector Performance Summary* **DPS-2010/025** (2010).

[61] D0 Collaboration, "Search for associated production of charginos and neutralinos in the trilepton final state using 2.3 fb^{-1} of data", *Phys. Lett.* **B 680** (2009), no. 1, 34 – 43. `doi:10.1016/j.physletb.2009.08.011`.

[62] D0 Collaboration, "Search for squarks and gluinos in events with jets and missing transverse energy using 2.1 fb^{-1} of p$\bar{p}$ collision data at $\sqrt{s} = 1.96$ TeV", *Phys. Lett.* **B 660** (2008) 449, `arXiv:0712.3805`.

[63] CDF Collaboration, "The CDF exclusion region in the $m_{1/2}$ vs. m_0 plane", *Phys. Rev. Lett.* **102** (2009) 121801, `arXiv:011.2512`.

[64] ALEPH, DELPHI, L3 and OPAL Collaboration, "Joint SUSY Working Group", *Notes LEPSUSYWG/01-03.1 and 04-01.1.* http://lepsusy.web.cern.ch/lepsusy.

[65] CMS Collaboration, "Search for Supersymmetry in pp Collisions at 7 TeV in Events with Jets and Missing Transverse Energy", `arXiv:1101.1628`.

[66] CMS Collaboration, "Search for Supersymmetry in pp Collisions at $\sqrt{s}$ = 7 TeV in Events with Two Photons and Missing Transverse Energy", `arXiv:1103.0953`.

[67] CMS Collaboration, "Search for Physics Beyond the Standard Model in Opposite-sign Dilepton Events in pp Collisions at $\sqrt{s} = 7$ TeV", `arXiv:1103.1348`.

[68] CMS Collaboration, "Search for new physics with same-sign isolated dilepton events with jets and missing transverse energy at the LHC", `arXiv:1104.3168`.

[69] CMS Collaboration, "Search for supersymmetry using final states with one lepton, a photon, and large missing energy in pp collisions at $\sqrt{s} = 7$ TeV", `arXiv:1105.3152`.

[70] ATLAS Collaboration, "Search for supersymmetric particles in events with lepton pairs and large missing transverse momentum in $\sqrt{s} = 7$ TeV proton-proton collisions at the ATLAS experiment", `arXiv:1103.6214`.

[71] ATLAS Collaboration, "Search for supersymmetry using final states with one lepton, jets, and missing transverse momentum with the ATLAS detector in $\sqrt{s} = 7$ TeV pp collisions", `arXiv:1102.2357`.

[72] ATLAS Collaboration, "Search for supersymmetry in pp collisions at $\sqrt{s}$ = 7 TeV in final states with missing transverse momentum and b-jets", `arXiv:1103.4344`.

[73] ATLAS Collaboration, "Search for squarks and gluinos using final states with jets and missing transverse momentum with the ATLAS detector in $\sqrt{s} = 7$ TeV proton-proton collisions", `arXiv:1102.5290`.

[74] J. Alwall et al., "MadGraph/MadEvent v4: The New Web Generation", *JHEP* **09** (2007) 028, `arXiv:0706.2334`.

[75] M.L. Mangano, M. Moretti, F. Piccinini, R. Pittau and A. Polosa, "ALPGEN, a generator for hard multiparton processes in hadronic collisions", *JHEP* **0307:001** (2003).

[76] T. Sjöstrand, S. Mrenna, and P. Z. Skands, "PYTHIA 6.4 Physics and Manual; v6.420, tune D6T", *JHEP* **05** (2006) 026, arXiv:hep-ph/0603175.

[77] GEANT4 Collaboration, S. Agostinelli et al., "GEANT4: A simulation toolkit", *Nucl. Instrum. Meth.* **A 506** (2003) 205–303.

[78] R. Field, "Early LHC underlying event data – findings and surprises", arXiv:1010.3558.

[79] CMS Collaboration, "MET performance in pp collisions at 7 TeV", *CMS Physics Analysis Summary* **JME-10-009** (2010).

[80] Adam, W. et. al., "Search for supersymmetry in proton-proton collisions at $\sqrt{s} = 7$ TeV in events with a single lepton, jets, and missing transverse momentum", *CMS Analysis Note* **AN-2010/419** (2010).

[81] CMS Collaboration, "Measurement of the $t\bar{t}$ Pair Production Cross Section at $\sqrt{s} = 7$ TeV using the Kinematic Properties of Lepton + Jets Events", *CMS Physics Analysis Summary* **TOP-10-002** (2010).

[82] CMS Collaboration, "Search for Physics Beyond the Standard Model in Opposite-sign Dilepton Events in pp Collisions at $\sqrt{s} = 7$ TeV", arXiv:1103.1348.

[83] M. R. Whalley, D. Bourilkov, and R. C. Group, "The Les Houches Accord PDFs (LHAPDF) and Lhaglue", arXiv:0508110.

[84] P. M. Nadolsky et al., "Implications of CTEQ global analysis for collider observables", *Phys. Rev. D* **78** (2008) 013004, arXiv:0802.0007. doi:doi:10.1103/PhysRevD.78.013004.

[85] V. Pavlunin, "Modeling missing transverse energy in V+jets at CERN LHC", *Phys.Rev.* **D81** (2010) 035005, arXiv:0906.5016. doi:10.1103/PhysRevD.81.035005.

[86] A. Czarnecki, J. Korner, and J. Piclum, "Helicity fractions of W bosons from top quark decays at next-to-next-to leading order in QCD", *Phys. Rev.* **D 81** (2010) 111503(R).

[87] CDF Collaboration, "Measurement of W-Boson Polarization in Top-quark Decay in $p\bar{p}$ Collisions at $\sqrt{s} = 1.96$ TeV", *Phys. Rev. Lett.* **105** (2010) 042002, arXiv:1003.0224.

[88] D0 Collaboration, "Measurement of the W boson helicity in top quark decays using 5.4 fb^{-1} of $p\bar{p}$ collision data", *Phys. Rev.* **D83** (2011) 032009, arXiv:1011.6549. doi:10.1103/PhysRevD.83.032009.

[89] CMS Collaboration, "First Measurement of the Polarization of W Bosons with Large Transverse Momentum in W + Jets Events at a pp Collider", *CMS Physics Analysis Summary* **EWK-10-014** (2010).

[90] Z. Bern et al., "Left-handed W bosons at the LHC", arXiv:1103.5445.

[91] Beaudette, F. et. al., "Fake missing transverse momentum in the RA2 analysis", *CMS Analysis Note* **AN-2010/383** (2010).

[92] Beenakker, W. and Hopker, R. and Spira, M., and others, "Squark and gluino production at hadron colliders", *Nucl. Phys. B* **492** (1997) 51–103.

[93] J. Neyman, "Outline of a theory of statistical estimation based on the classical theory of probability", *Philos. Trans. Roy. Soc. London. Ser. A* **236** (1937) 333–380.

[94] G. Feldman and R. Cousins, "A Unified Approach to the Classical Statistical Analysis of Small Signals", *Phys. Rev.* **D 57** (1998) 3873–3899.

[95] CMS Collaboration, "Missing Transverse Energy Performance in Minimum-Bias and Jet Events from Proton-Proton Collisions at $\sqrt{s} = 7$ TeV", *CMS Physics Analysis Summary* **JME-10-004** (2010).

[96] T. Sjostrand, S. Mrenna, and P. Z. Skands, "A Brief Introduction to PYTHIA 8.1", *Comput. Phys. Commun.* **178** (2008) 852–867, arXiv:0710.3820. doi:10.1016/j.cpc.2008.01.036.

[97] P. Z. Skands, "The Perugia Tunes", arXiv:0905.3418.

[98] CMS Collaboration, "HCAL performance from first collisions data", *CMS Detector Performance Summary* **DPS-2010/025** (2010).

[99] CMS Collaboration, "Electromagnetic calorimeter commissioning and first results with 7 TeV data", *CMS Note* **2010/012** (2010).

[100] CMS Collaboration, "CMS Jet Performance in pp Collisions at $\sqrt{s} = 7$ TeV", *CMS Physics Analysis Summary* **JME-10-003** (2010).

[101] N. Akchurin, J. Damgov, S.W. Lee, E. Yazgan, "MET scale validation with Photon + Jet Events", *CMS Analysis Note* **AN-2010/132** (2010).

Appendices

Appendix A

$\not\!\!E_T$ resolution in CMS

In this appendix we perform a detailed study of $\not\!\!E_T$ resolution as a function of the scalar sum of the transverse energy (ΣE_T) using minimum bias event samples from data and Monte Carlo at $\sqrt{s} = 7$ TeV. Four different $\not\!\!E_T$ algorithms are investigated: type I calo$\not\!\!E_T$, pf$\not\!\!E_T$, tc$\not\!\!E_T$, and type II calo$\not\!\!E_T$.[1] Because the $\not\!\!E_T$ and ΣE_T values computed by each algorithm have different energy scales, comparison of the results of different algorithms is non-trivial. We use a $\not\!\!E_T$ calibration based on MC photon plus jets and a ΣE_T calibration based on MC truth in minimum bias events. We also investigate the generator dependence of the ΣE_T calibrations.

A.1 Samples and event requirements

The data sets used for this study were collected from approximately two months of data taking starting at the end of March 2010, and they correspond to an integrated luminosity of 11.7 nb^{-1}. Only runs with all the CMS subdetectors working properly are used for this study and a minimum-bias trigger was used to collect the data. The minimum-bias trigger requires that a signal in the Beam Scintillation Counter (BCS) is coincident with a signal from either of the two Beam Pick-up Timing eXperiment (BPTX) devices [95]. Due to the large bandwidth of the minimum-bias trigger it was prescaled for some of the data taking.

The main Monte Carlo sample used was a 7 TeV minimum bias sample produced with Pythia 8.1 [96].[2] Two additional minimum bias pythia tunes, TuneP0 [97] and TuneD6T [76], were used to look at the generator dependence

[1] The different $\not\!\!E_T$ algorithms used are described in Sec. 4.4.

[2] We will refer to this as pythia8 from now on.

of the ΣE_T calibrations.[3] The generator events are passed through the CMS detector simulation based on GEANT4 [77].

For this study cleaning cuts are made to remove instrumental anomalies and beam-induced backgrounds. The removal of anomalous signals in the calorimeters is done based on studies documented in Ref. [98] for the HCAL and Ref. [99] for the ECAL. For beam-induced backgrounds there are dedicated beam halo triggers that we veto on to remove this background. Additional event cleaning is made on the primary vertex and tracker. We require that in each event there be at least one good primary vertex. A primary vertex is defined to be good if its z position is less than 15 cm away from the nominal center of the detector and its transverse distance, ρ, is less than 2 cm away from the nominal center of the detector. These requirements ensure that the particles coming from the interaction of the protons are contained within the detector. Requirements on tracking quantities were made to remove anomalous beam scraping events that shower one side of the silicon tracker with hundreds of tracks. Any event with more than 10 tracks and less than 25% "high purity" tracks[4] was vetoed.

The anti-kt jet algorithm [51] with a ΔR cone of 0.5 was used for jet reconstruction. The calorimeter based jets were used though cross-checks were performed using particle-flow jets.[5] Jet corrections were applied to the raw jet energies to take into account differences across the detector and scale differences. Jet identification criteria [100] were used to remove fake jets from detector effects. In addition to the jet id requirements for this study the following cuts were used:

- $p_T^{jet} > 25$ GeV
- $|\eta| < 3$

Events with two or more calojets passing the above jet criteria were considered.

When investigating generator level $\not\!\!E_T$, generator particles with $|\eta| < 5$ are considered. For the rest of this study we will refer to the generator level $\not\!\!E_T$ as gen$\not\!\!E_T$ and generator level ΣE_T as genΣE_T.

[3] The different pythia tunes have a different number of low momentum tracks in the detector and thus different amount of ΣE_T.

[4] "High purity" means there are requirements made on the track quality.

[5] For more information on jet reconstuction and the different types of jet reconstruction see Sec.??.

A.2 $\not\!\!E_T$ resolution vs. ΣE_T without calibrations

Before investigating the $\not\!\!E_T$ resolution of different algorithms it is important to look at the basic $\not\!\!E_T$ and ΣE_T distributions to understand how each algorithm reconstructs these quantities. Figure A.1 shows the genΣE_T, type I caloΣE_T, type II caloΣE_T, pfΣE_T, and tcΣE_T distributions in MC minimum bias events. As this plot shows, every algorithm underestimates the generator ΣE_T. Type I calo$\not\!\!E_T$ underestimates the generator ΣE_T the most of any of the algorithms. This is because type I calo$\not\!\!E_T$ makes no corrections to the unclustered energy[6], which has a large contribution in this sample. The other $\not\!\!E_T$ algorithms all make some type of corrections for the unclustered energy in the calorimeter and come closer to reproducing the generator ΣE_T distribution. Of all the algorithms, type II comes the closest to reproducing the genΣE_T distribution.

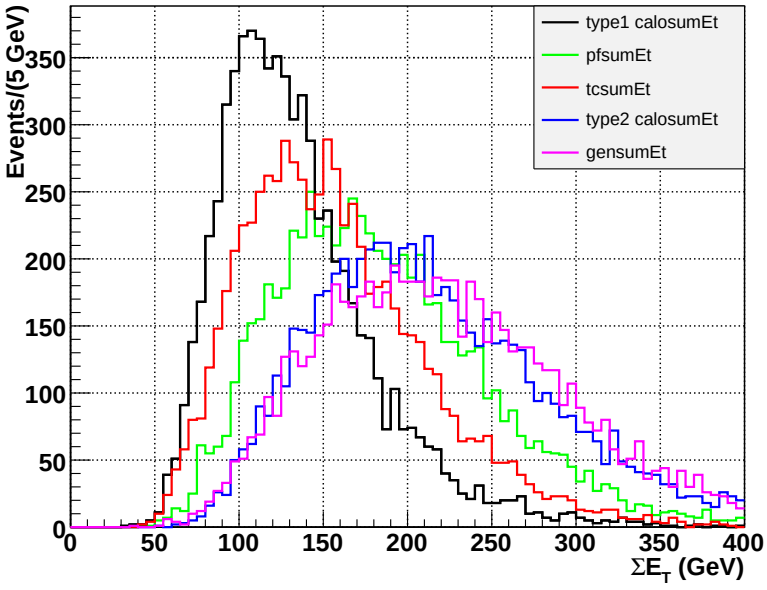

Figure A.1: Minimum bias MC ΣE_T for different $\not\!\!E_T$ algorithms (pythia 8).

Figure A.2 shows the $\not\!\!E_T$ distribution for gencalo$\not\!\!E_T$, type I calo$\not\!\!E_T$, type II calo$\not\!\!E_T$, pf$\not\!\!E_T$, and tc$\not\!\!E_T$. As expected the generator level $\not\!\!E_T$ peaks much lower than any of the reconstructed $\not\!\!E_T$ algorithms. In minimum bias events the real $\not\!\!E_T$ should be very low and the tails of the reconstructed $\not\!\!E_T$ distributions should

[6]The unclustered energy is the energy in the calorimeter that isn't clustered inside a jet.

come from mismeasurement. The pf$\not\!\!E_T$ and tc$\not\!\!E_T$ algorithms have the smallest $\not\!\!E_T$ tail in this sample.

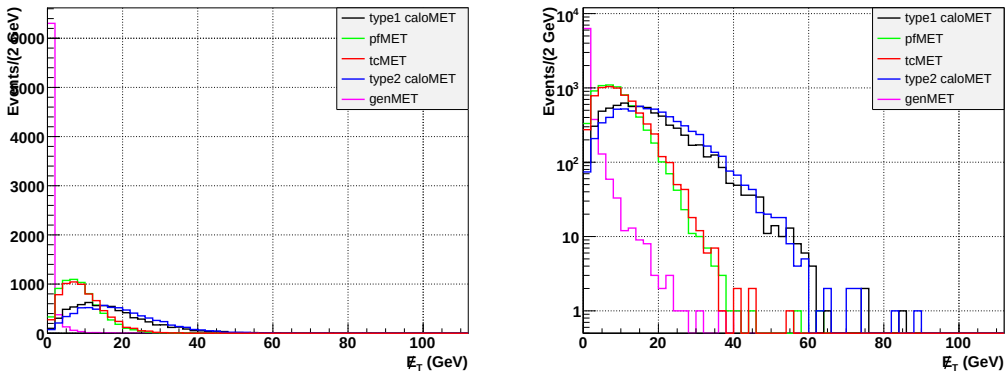

Figure A.2: Minimum bias MC $\not\!\!E_T$ for different $\not\!\!E_T$ algorithms (pythia 8). The plot on the left is linear and the plot on the right is log.

Figure A.3 shows the $\not\!\!E_T$ resolution versus ΣE_T for minimum bias MC and data. The resolution was calculated by taking the RMS of the $\not\!\!E_{x,y}$ distribution. For all algorithms and also for different Monte Carlo generators the resolution tends to be slightly better in MC than data.

All the $\not\!\!E_T$ resolution plots shown so far were made with the requirement of two calojets of $p_T > 25$ in order to compare all algorithms in the same exact events. However, we must be careful that no bias was introduced by looking at pf$\not\!\!E_T$ in events with a requirement of two calojets since the pfjet reconstruction is quite different than the calojet reconstruction. To investigate this in more detail we applied the criteria of two particle flow jets and replotted the $\not\!\!E_T$ resolution vs. ΣE_T for pf$\not\!\!E_T$. Figure A.4 shows the pf$\not\!\!E_T$ resolution vs. pfΣE_T for the case of calojet requirements (left plot) and pfjet requirements (right plot). For the plot on the right at least two particle flow jets with the following criteria were required:

- $p_T^{jet} > 25GeV$
- $|\eta| < 3$
- particle-flow specific identification requirements to remove fake jets

Figure A.4 shows that for this study it makes little difference for the pf$\not\!\!E_T$ plots whether the jet requirements were made on calojets or pfjets. For the rest of this study only the calojet requirements were used.

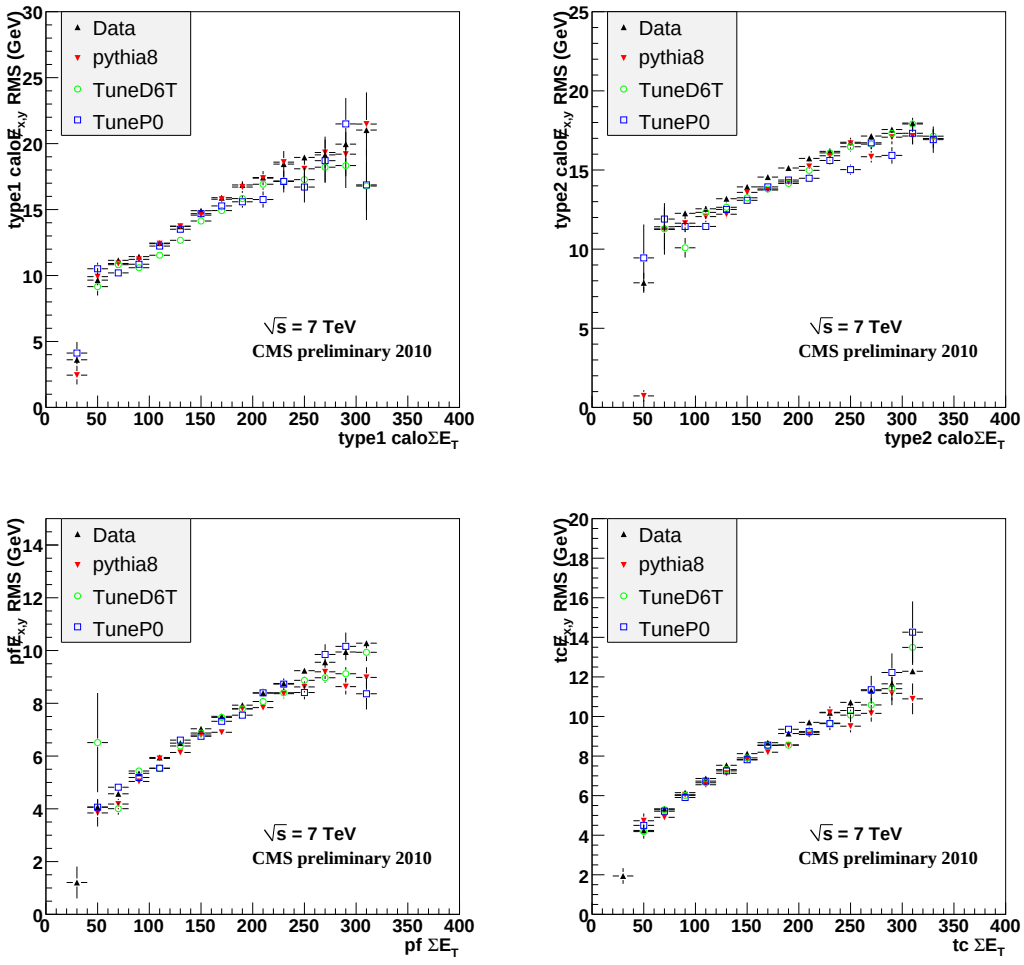

Figure A.3: $\not\!\!E_T$ Resolution from RMS versus ΣE_T in data and MC for different $\not\!\!E_T$ algorithms. The upper left plot shows for type I calo$\not\!\!E_T$. The upper right plot shows for type II calo$\not\!\!E_T$. The lower left plot shows for pf$\not\!\!E_T$. The lower right plot shows for tc$\not\!\!E_T$.

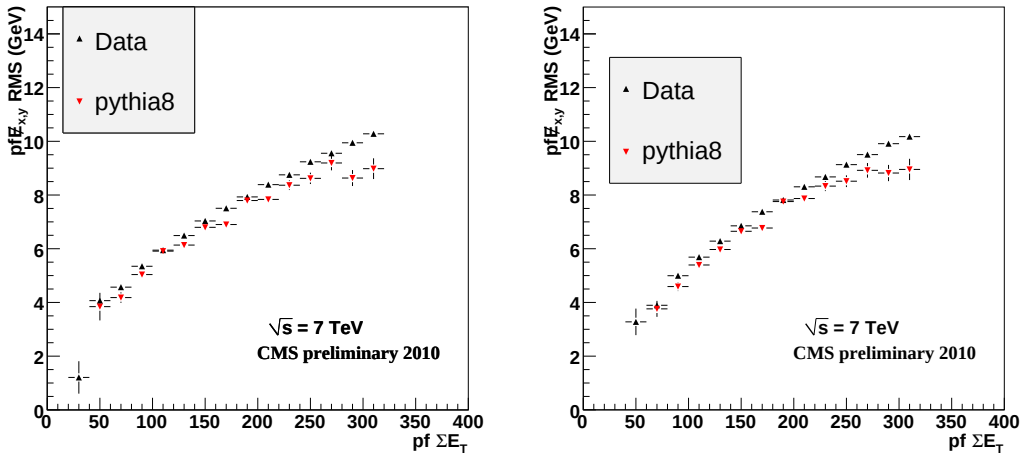

Figure A.4: $\not\!\!E_T$ Resolution vs. ΣE_T for pf$\not\!\!E_T$ in the case of requiring two calojets (left) and in the case of requiring two pfjets (right).

Figure A.5 shows the $\not\!\!E_T$ resolution versus ΣE_T as well, but in this case the $\not\!\!E_T$ resolution was calculated by doing a gaussian fit instead of taking the RMS of the $\not\!\!E_{x;y}$ The resolution curves from a gaussian fit are very similar to the resolution curves from taking the RMS. One plotting difference is that the gaussian curves do not go to as high values of ΣE_T as the RMS curves. This is because at high ΣE_T the statistics becomes very small and causes some of the gaussian fits to perform very poorly. However, it is still possible to obtain a reasonable RMS value with very low statistics. Figure A.5 shows that the type1calo $\not\!\!E_T$ distribution has the lowest statistics at high ΣE_T and cuts off at the lowest value of ΣE_T. This is due to the type1 calo$\not\!\!E_T$ having the lowest response of all the algorithms.

In order to compare the resolution of different $\not\!\!E_T$ algorithms it is not possible to overlay the different distributions in Figure A.3 or Figure A.5. This is because each algorithm reconstructs the ΣE_T and $\not\!\!E_T$ very differently and calibrations to the ΣE_T and $\not\!\!E_T$ must be applied before any comparison is made. In the next section calibrations for the $\not\!\!E_T$ and ΣE_T are investigated.

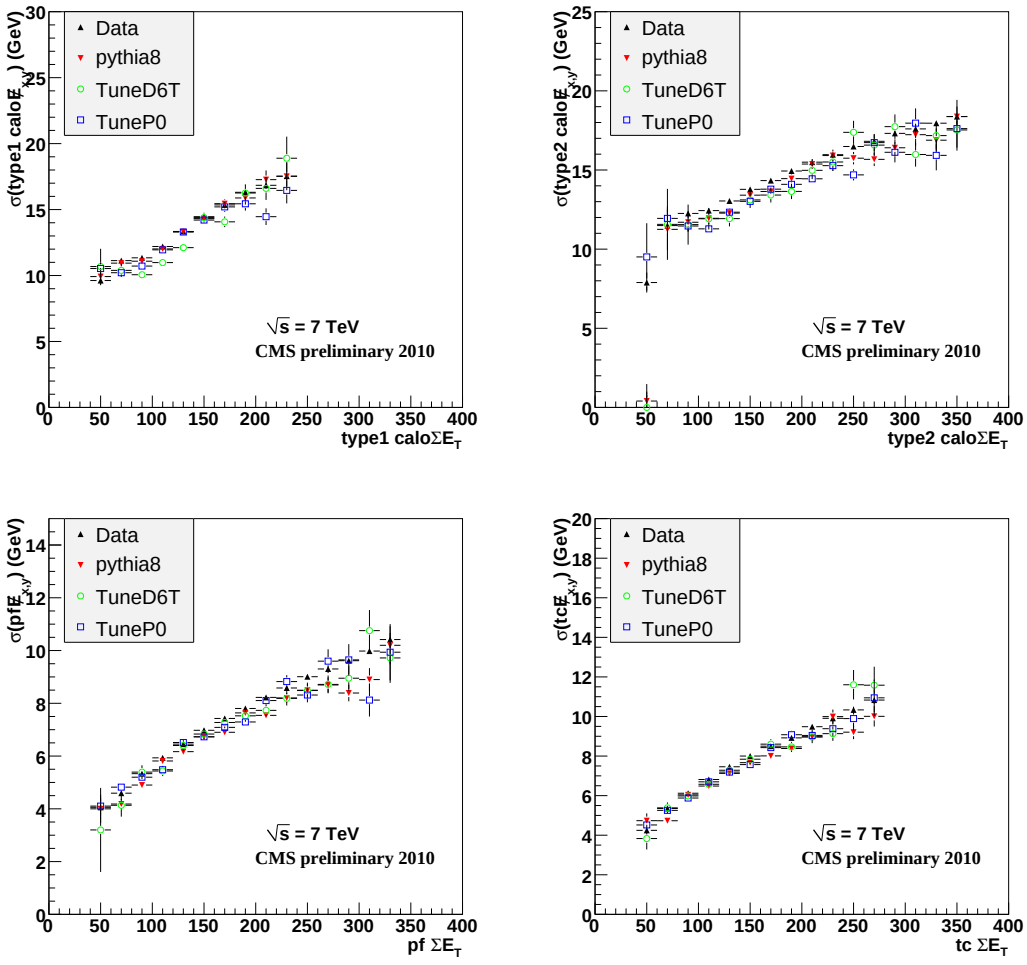

Figure A.5: $\not\!\!E_T$ Resolution from gaussian fit versus ΣE_T in data and MC for different $\not\!\!E_T$ algorithms. The upper left plot shows for type I calo$\not\!\!E_T$. The upper right plot shows for type II calo$\not\!\!E_T$. The lower left plot shows for pf$\not\!\!E_T$. The lower right plot shows for tc$\not\!\!E_T$.

A.3 Calibrated $\not\!\!E_T$ resolution vs. calibrated ΣE_T

In order to compare the $\not\!\!E_T$ resolution vs. ΣE_T for different algorithms we tried to calibrate the $\not\!\!E_T$ and ΣE_T for each $\not\!\!E_T$ algorithm. Different scaling factors were applied for ΣE_T and $\not\!\!E_T$. The minimum bias MC pythia8 sample was used to correct the ΣE_T after applying all the requirements in Sec. A.1. The scalar E_T is thus the sum over the underlying event and the two jets. The correction was done by rescaling the reco ΣE_T to what the generator level ΣE_T should be. Figure A.6 shows the scatter plot of reco ΣE_T versus genΣE_T for the different algorithms. Figure A.7 shows the mean reco ΣE_T versus genΣE_T distributions for the different algorithms. For each algorithm we preformed a linear fit to the mean reco ΣE_T versus genΣE_T distribution to obtain an equation for the ΣE_T correction. All distributions show a slight to moderate deviation from linearity at high generator ΣE_T.

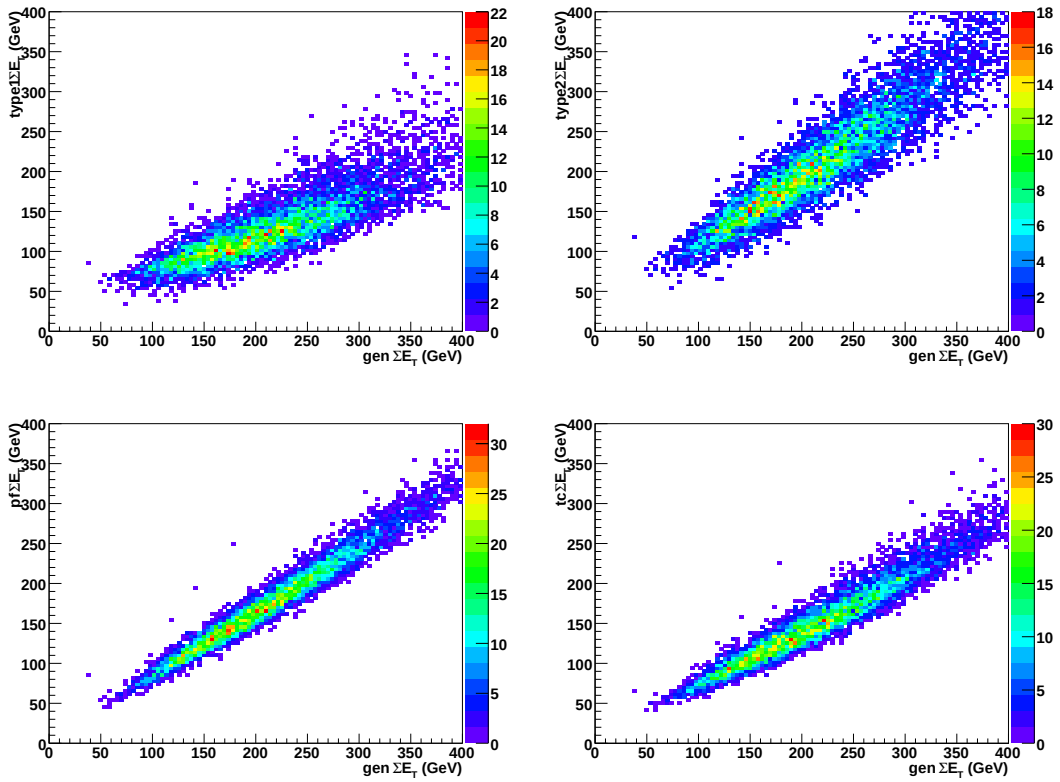

Figure A.6: Scatter plots of reco ΣE_T vs. gen ΣE_T for different algorithms.

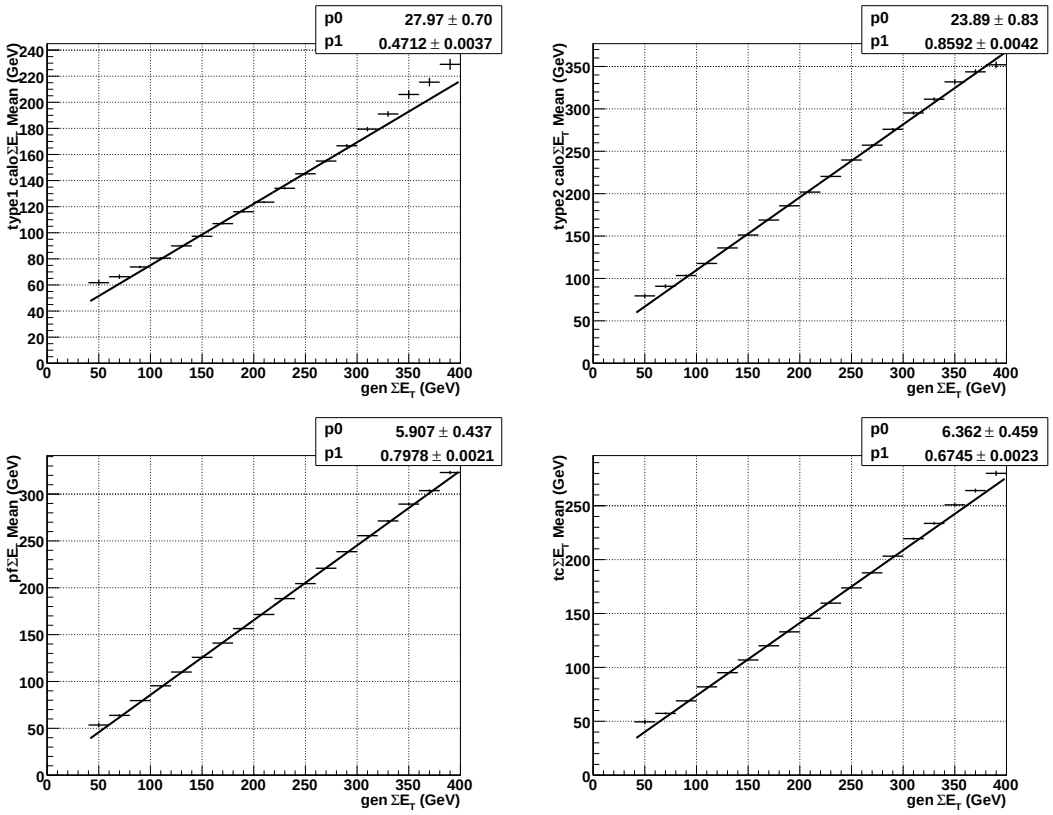

Figure A.7: Mean reco ΣE_T vs. gen ΣE_T for different algorithms. Each distribution is fitted to a linear shape.

For the $\not\!\!E_T$ correction, the Monte Carlo photon plus jets sample was used, and the correction factor was taken from Ref. [101]. In this case, the correction factor is obtained from looking at the $\not\!\!E_T$ component along the photon axis, and as the underlying event cancels (since it is just a component, and the underlying event is a symmetric component) what is left is the sum over the jet.

There are two different sources for the ΣE_T scale and the $\not\!\!E_T$ scale. For the ΣE_T the source is the underlying event scale and for the $\not\!\!E_T$ the source is the jet scale. Due to the calorimeter non-linearity, the underlying event scale is smaller than the jet scale. Figure A.8 shows the $\not\!\!E_T$ and ΣE_T correction factors as a function of the average dijet p_T in the event. These plots show that the correction factor for ΣE_T is larger than the correction factor for $\not\!\!E_T$. This makes sense since if the scale is smaller for ΣE_T the expected correction factor should be larger. In Figure A.8 we see that the scale factors are approximately 1.55 for tcΣE_T,1.35 for tc$\not\!\!E_T$, 1.25 for pfΣE_T and 1.10 for pf$\not\!\!E_T$. If we take the ratio of the ΣE_T correction over the $\not\!\!E_T$ correction for pf$\not\!\!E_T$ and tc$\not\!\!E_T$, this ratio is $\sim$1.15 for both tc$\not\!\!E_T$ and pf$\not\!\!E_T$. This is approximately the ratio of scales for quark versus gluon jets. Thus, this difference of the scale factors can most likely be explained by the different makeup of the samples. The photon plus jets sample should be dominated by quark jets, whereas the minimum bias sample should be dominated by gluon jets.

To compare the resolution of different algorithms, intially we plotted each algorithms calibrated $\not\!\!E_T$ resolution versus its own calibrated ΣE_T (i.e., calibrated tc$\not\!\!E_T$ versus calibrated tcΣE_T). However, when comparing this distribution for each algorithm to the calibrated $\not\!\!E_T$ resolution versus genΣE_T distribution we saw some discrepancies for the typeI and typeII algorithms. Figure A.9 shows that for the typeI algorithm the calibrated ΣE_T curve is larger than the genΣE_T curve at low ΣE_T. For the typeII algorithm distribution there is a small discrepancy at low ΣE_T and some larger discrepancy at high ΣE_T, where the genΣE_T is larger than the calibrated ΣE_T. We believe these discrepancies come from the fact that the 2-D scatter plot distributions of recoΣE_T vs. genΣE_T, shown in Figure A.6, are very broad for typeI and typeII. So even though the fits to the mean recoΣE_T vs. genΣE_T distributions for typeI and typeII (shown in Figure A.7) are approximately linear the calibration can be quite off because the dispersion of the reco ΣE_T vs. genΣE_T distributions is very broad. Another reason for not plotting each algorithm versus its own calibrated ΣE_T is that when comparing different algorithms a particular bin will not necessarily have the same number of events.

To get around the issues described in the previous paragraph we plotted each algorithms calibrated $\not\!\!E_T$ resolution vs. calibrated pfΣE_T. Figure A.10

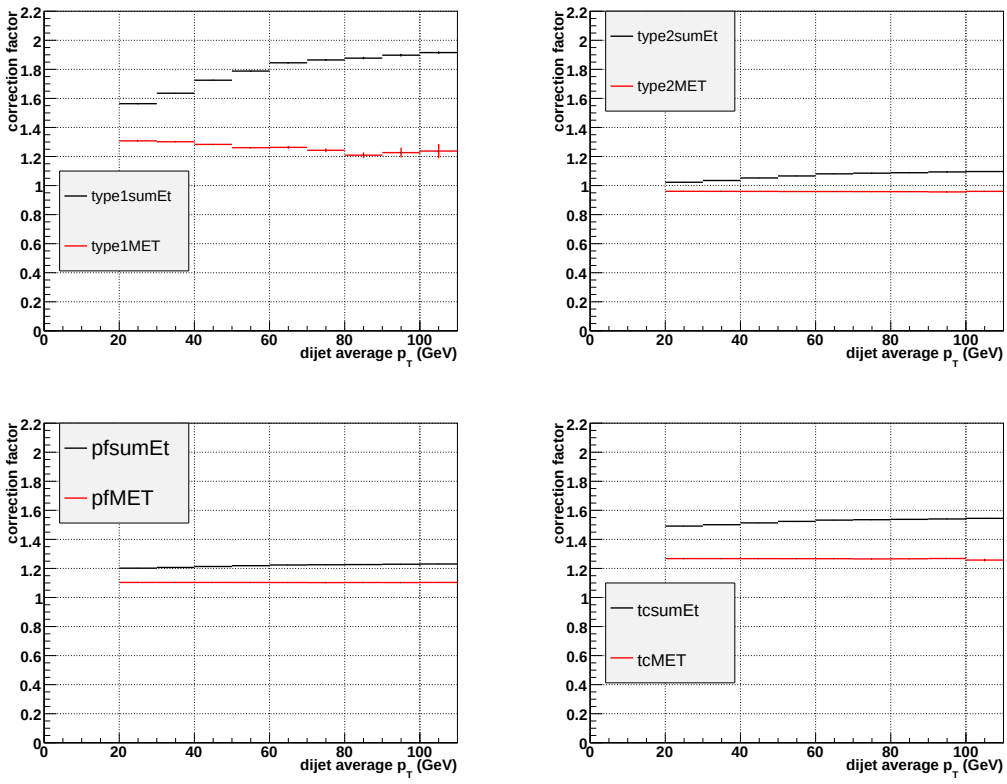

Figure A.8: Correction factors for $\not\!\!E_T$ and ΣE_T in MC (pythia), versus average dijet p_T. The upper left plot shows for type I calo$\not\!\!E_T$. The upper right plot shows for type II calo$\not\!\!E_T$. The lower left plot shows for pf$\not\!\!E_T$. The lower right plot shows for tc$\not\!\!E_T$.

shows that the discrepancy between the calibrated pfΣE_T distributions and the genΣE_T distributions is very small. Also, since we are plotting each algorithm versus calibrated pfΣE_T the x-axis is exactly the same for each algorithm and there is the same number of events in each bin.

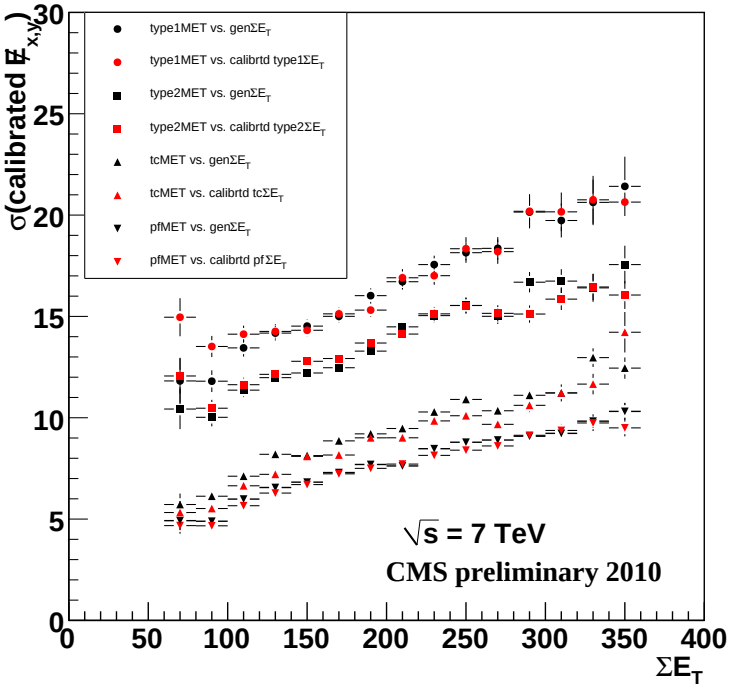

Figure A.9: Calibrated $\not\!\!E_T$ resolution vs. calibrated ΣE_T compared to calibrated $\not\!\!E_T$ resolution vs. genΣE_T. The black points are vs. genΣE_T, the red points are vs. calibrated ΣE_T. The circles are for type1, the squares are for type2, the right side up triangles are for tc$\not\!\!E_T$ and the upside down triangles are for pf$\not\!\!E_T$.

Figure A.11 shows a comparison of the different algorithm's calibrated $\not\!\!E_T$ resolution versus calibrated pfΣE_T for data (points) and MC (lines). The data has a slightly larger resolution than the MC. Another point to notice is that the type II algorithm has improved resolution compared to the type I algorithm. Figure A.12 shows the ratio of the calibrated pf$\not\!\!E_T$, tc$\not\!\!E_T$, and type II $\not\!\!E_T$ resolution to the calibrated typeI $\not\!\!E_T$ resolution. For pf$\not\!\!E_T$, the resolution is on average about 45% of the typeI resolution. For tc$\not\!\!E_T$, the resolution is on average about 55%

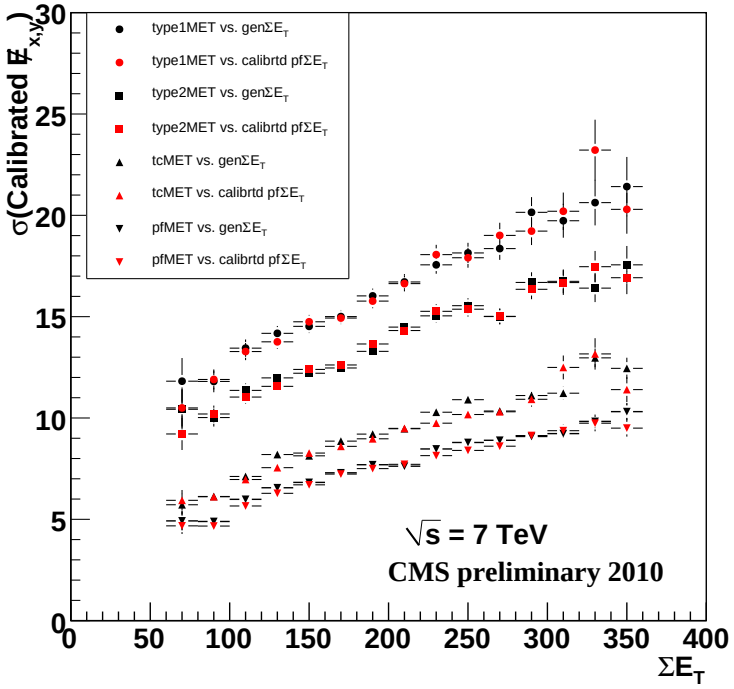

Figure A.10: Calibrated $\not\!\!E_T$ resolution vs. calibrated particle flow ΣE_T compared to calibrated $\not\!\!E_T$ resolution vs. genΣE_T. The black points are vs. genΣE_T, the red points are vs. particle flow calibrated ΣE_T. The circles are for type1, the squares are for type2, the right side up triangles are for tc$\not\!\!E_T$ and the upside down triangles are for pf$\not\!\!E_T$.

of the type I resolution. For type II $\not\!\!E_T$, the resolution is on average about 85% of the type I resolution.

In order to compare the calibrated $\not\!\!E_T$ resolution of all the different types of calo$\not\!\!E_T$, we also investigated the raw calo$\not\!\!E_T$. Figure A.13 shows the calibrated $\not\!\!E_T$ resolution of raw calo$\not\!\!E_T$, type I calo$\not\!\!E_T$, and type II calo$\not\!\!E_T$. The resolution of the raw calo$\not\!\!E_T$ is very similar to the resolution of type II calo$\not\!\!E_T$ and both raw calo$\not\!\!E_T$ and type II calo$\not\!\!E_T$ show improvement in resolution compared to type I calo$\not\!\!E_T$.

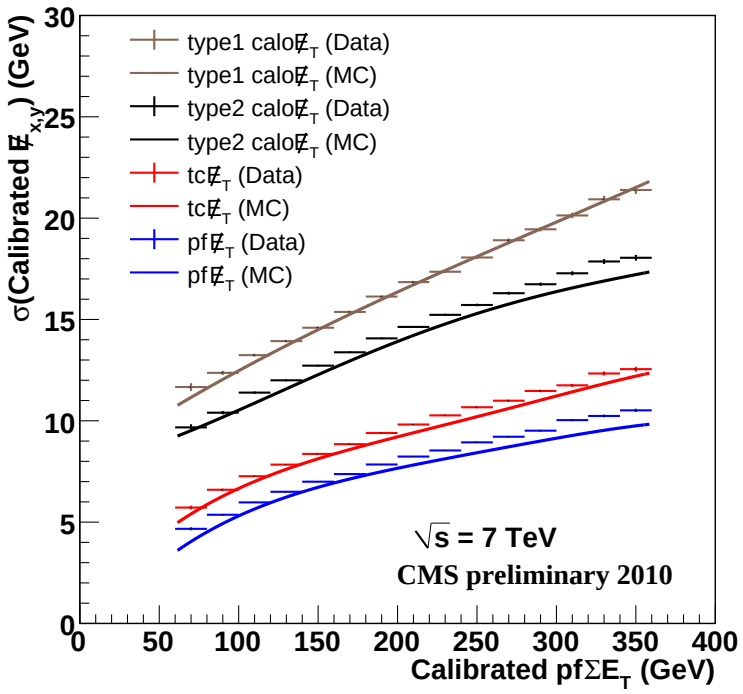

Figure A.11: Calibrated $\not\!\!E_T$ resolution vs. calibrated pfΣE_T for the different algorithms in data (points), MC (lines).

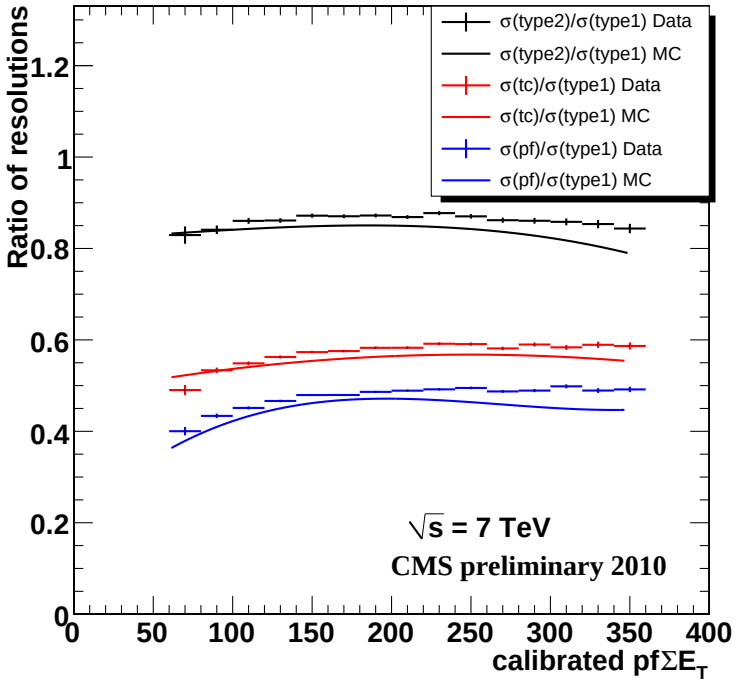

Figure A.12: Ratio of calibrated type II, pf, and tc $\not\!\!E_T$ resolution to type I $\not\!\!E_T$ resolution as a function of calibrated pfΣE_T, for data (points) and MC (lines).

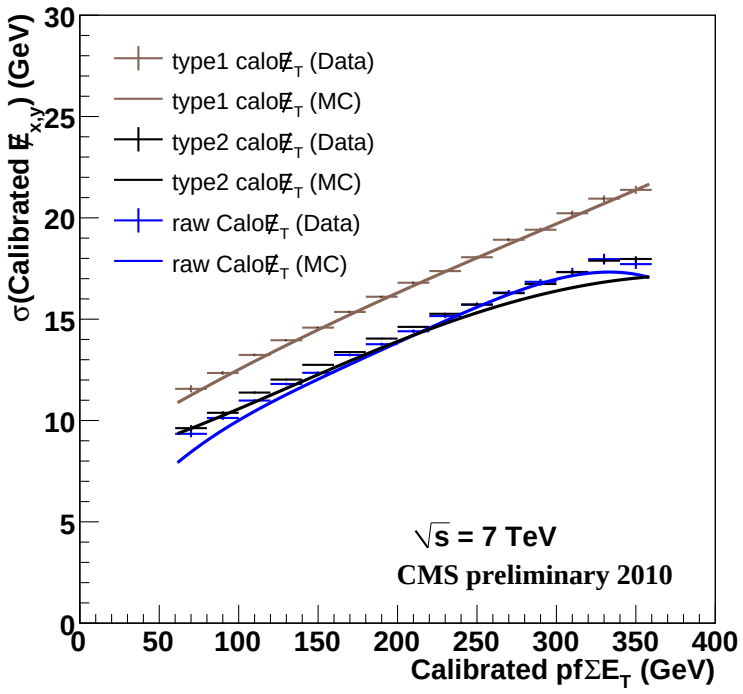

Figure A.13: Calibrated $\not\!\!E_T$ resolution vs. calibrated pfΣE_T for raw calo$\not\!\!E_T$, typeI calo$\not\!\!E_T$, and typeII calo$\not\!\!E_T$. The points are for data and the lines are for MC.

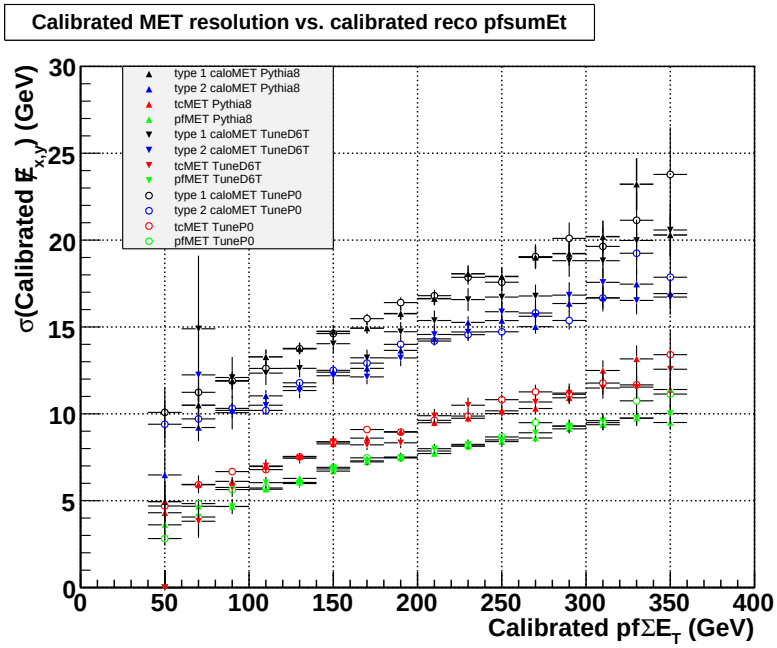

Figure A.14: Calibrated $\not\!\!E_T$ resolution vs. calibrated pfΣE_T for different pythia samples and different $\not\!\!E_T$ algorithms. The different colors represent different algorithms, and the different style points represent different minimum bias MC samples.

A.4 Monte Carlo generator dependence of ΣE_T calibration

The calibration of the ΣE_T will be a function of the p_T spectrum of the generator-level particles and thus depend on the generator used. To try to understand the dependence of the generator used, we investigated two different MC minimum bias tunes in addition to the baseline pythia8 sample. The two tunes used were TuneP0 and TuneD6T. Figure A.14 shows the calibrated $\not\!\!E_T$ resolution versus calibrated ΣE_T for the three different pythia samples and the four different $\not\!\!E_T$ algorithms. For each different pythia sample the calibration of the ΣE_T was recalculated using fits similar to those shown in Figure A.7. The $\not\!\!E_T$ rescaling was not changed for different pythia samples. From Figure A.14 we see that the general picture of calibrated $\not\!\!E_T$ resolution versus calibrated ΣE_T for the different algorithms does not change much as you vary the generator. Figure A.15 shows the relative difference of the $\not\!\!E_T$ resolution from pythia8 and the $\not\!\!E_T$ resolution from the different tunes.

A.5 Conclusion

We have presented a study of $\not\!\!E_T$ resolution versus ΣE_T for different $\not\!\!E_T$ algorithms in both data and Monte Carlo. In this study calibrations were applied to the $\not\!\!E_T$ and the ΣE_T in order to get rid of the scale dependence of the different $\not\!\!E_T$ algorithms. By applying these calibrations we were able to compare the $\not\!\!E_T$ resolution versus ΣE_T on the same footing for the different algorithms.

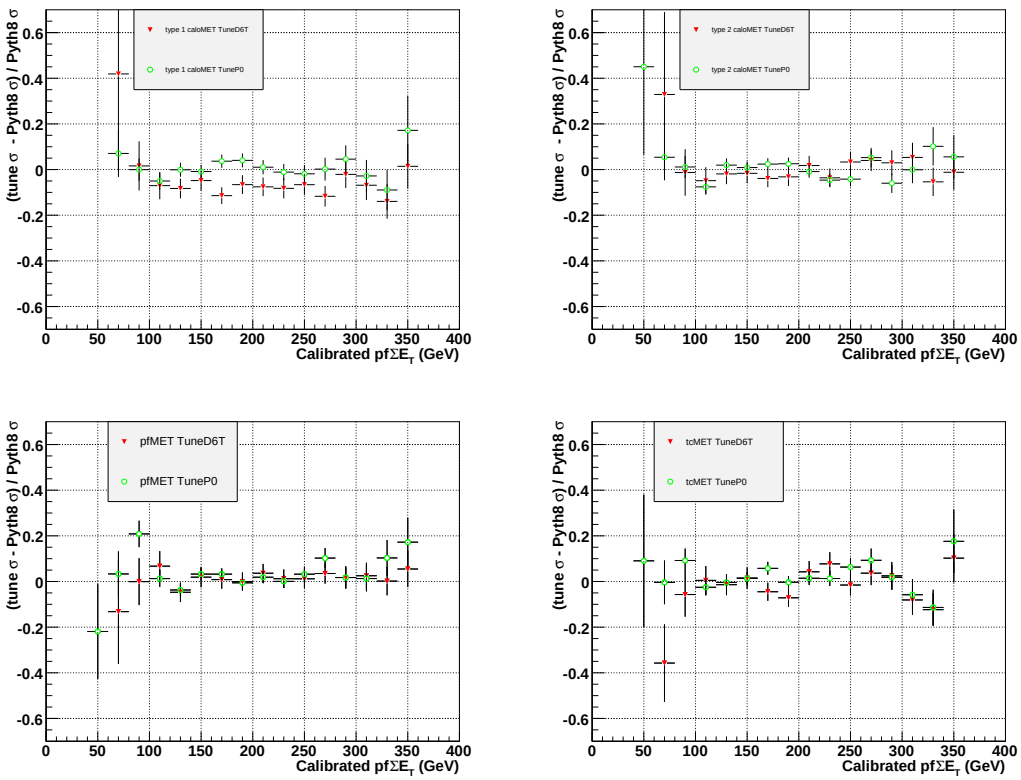

Figure A.15: Difference of pythia tunes calibrated $\not\!\!E_T$ resolution and pythia8 calibrated $\not\!\!E_T$ resolution vs. calibrated pfΣE_T for different algorithms.